University of Southampton

Faculty of Physical Sciences and Engineering

Phenomenological aspects of elementary and composite Higgs models

by

Emine Yildirim

Presented for the degree of

Doctor of Philosophy

September 2017

ABSTRACT

UNIVERSITY OF SOUTHAMPTON
FACULTY OF PHYSICAL SCIENCES AND ENGINEERING
School of Physics and Astronomy

Doctor of Philosophy

PHENOMENOLOGICAL ASPECTS OF ELEMENTARY AND COMPOSITE HIGGS MODELS

by Emine Yildirim

This thesis presents the phenomenological analysis of the charged Higgs sector in 3-Higgs Doublet Models (3HDMs) and that of heavy Higgs bosons in Composite 2-Higgs Doublet Models (C2HDMs). In the first chapter, the main properties of five types of 3HDMs are summarised. In addition, the constraints from the measurements of the $B \to X_s\gamma$ decay rate on the parameter space of 3HDMs are considered at the next-to-leading order in QCD and then limits from direct searches for $H_1^\pm$ and $H_2^\pm$ at colliders are discussed. In the other chapters, we move on to the investigation of a C2HDM framework based on the spontaneous breakdown of a global symmetry $SO(6) \to SO(4) \times SO(2)$ at the compositeness scale f. The motivations and the main properties of it are summarised. By requiring C2HDMs to fulfil perturbative unitarity at energies, we obtain constraints on its parameters. We also study the Large Hadron Collider (LHC) phenomenology of C2HDMs of various Yukawa types by concentrating on the modifications from Standard Model (SM) couplings of the discovered Higgs state (h) in addition to the production cross sections and Branching Ratios (BRs) of additional Higgs bosons. We find that, even if the same deviation in the hVV ($V = W^\pm, Z$) coupling is established in both a C2HDM and Elementary 2-Higgs Doublet Model (E2HDM), one can disentangle the two scenarios due to the structure of the Yukawa couplings by using the production and decay properties of additional Higgs bosons. Finally, we study single- and double-h production at future e^+e^- colliders in C2HDMs and E2HDMs. In particular, we study the differences in the cross sections between the two hypotheses when the deviation in the hVV ($V = W^\pm, Z$) coupling is set to be the same value in both scenarios.

Contents

List of Figures

List of Tables

Declaration of Authorship

I, Emine Yildirim, declare that this thesis, entitled 'phenomenological aspects of elementary and composite Higgs models' and the work presented in it are my own. I confirm the following.

- This work was done wholly or mainly while in candidature for a research degree at this university.
- Where any part of this thesis has previously been submitted for a degree or any other qualification at this University or any other institution, this has been clearly stated.
- Where I have consulted the published work of others, this is always clearly attributed.
- Where I have quoted from the work of others, the source is always given. With the exception of such quotations, this thesis is entirely my own work.
- I have acknowledged all main sources of help.
- Where the thesis is based on work done by myself jointly with others, I have made clear exactly what was done by others and what I have contributed myself.
- Work contained in this thesis has previously been published in Refs. [30-33].

Signed:

Date:

Acknowledgements

First and foremost, I will thank my supervisor Prof. Stefano Moretti for guiding me on this path: regular support, constructive collaboration and encouragements to take part in conferences to present my work to the physics communities have enabled me to grow in confidence. I would like to give Dr. Kei Yagyu a special thanks. I express my gratitude to him for the valuable lessons, his patient explanations and discussions. He has taught me a lot as a post-doc. I would also like to thank my collaborators Dr. Stefania De Curtis and Dr. Andrew Akeroyd for their valuable advice and help. It is my pleasure to thank my mother, father, brother and sisters for never letting me miss their support. I thank The Ministry of National Education of Turkey for funding my PhD. Finally, a special thanks goes to all my friends in Southampton for their help while I was abroad.

Chapter 1

Introduction

1.1 Overview

The Standard Model (SM) of particle physics is so far our best understanding of Nature at the fundamental level. This theory unifies the strong, Electro-Magnetic (EM) and weak forces and specifies the fundamental building blocks of the Universe. Over the last few decades, all particles predicted by the SM and their properties have been confirmed by several experiments, for example, the Large Electron Positron (LEP) collider, Tevatron and the Large Hadron Collider (LHC). The Higgs boson, which has been discovered by the ATLAS and CMS experiments at the LHC in 2012 [1], is a crucial part of the SM. It arises as a last piece of the mechanism of Electro-Weak Symmetry Breaking (EWSB) [2–7], which gives mass to gauge bosons and fermions and is essential for the consistency of the theory. This discovery implies that EWSB occurs in the real world and indicates the beginning of a new era in particle physics.

Even though the SM is a successful theory and agrees with experimental data, it is still filled with problems and puzzles such as neutrino masses and oscillations, Dark Matter (DM), the baryon-antibaryon asymmetry of the Universe, inflation, fine-tuning problems and so forth. These are all motivations to broaden ideas and look for physics beyond the SM. One of the most important problems regarding the Higgs sector is the fine-tuning problem. In the SM, the EW symmetry is broken by hand because of a negative mass-squared term, so it is inevitable to accept fine tuning of the Higgs mass parameter. However, it is expected that EWSB must be defined by some mechanism naturally. In order to describe the Higgs sector naturally at the EW scale, we have to consider a theory at the TeV scale (and beyond) to substitute the SM. It is believed that the SM cannot be a complete description of Nature precisely because of this shortcoming. Many models identifying extensions of the SM are available in the literature. The two best candidates to solve the fine-tuning problem of the SM are Supersymmetry and Composite Higgs Models (CHMs), particularly the Composite 2-Higgs Doublet Model (C2HDM), which will be our focus for much of this thesis.

Although the Higgs sector (a minimal Higgs sector) in the SM is formulated by only one isospin doublet field, this is not supported by a fundamental principle. There is no specific reason why there should be only one Higgs doublet in Nature. The possibility of the existence of more Higgs doublets still remains an open question. Models with non-minimal Higgs sectors represent a common direction in theoretical exploration of physics opportunities beyond the SM. Enlarged scalar sectors ease difficulties of the SM and lead to a rich spectrum of characteristic collider signatures. Such new models are searched for by means of both direct and indirect measurements. One is direct measurement, by which the collisions at the LHC give rise to a new physics particle on-shell and its decay products are measured. And another is indirect evidence, this method looks for deviations from SM predictions. We will discuss extended Higgs sectors, namely, the C2HDM with two isospin doublets and the 3-Higgs Doublet Model (3HDM) with three isospin doublets, in the remainder of this thesis.

1.2 The SM

Herein, we will briefly discuss the SM. Detailed materials are available in [8–10]. In the 1960s, Glashow [11], Weinberg [12] and Salam [13] unified EM interactions, based on the Quantum Electro-Dynamics (QED) theory [14], and weak interactions into EW interactions. The EW theory $SU(2)_L \times U(1)_Y$ describes all the EW interactions between matter fields. $SU(3)_C$ is the group of the strong colour forces of Quantum Chromo-Dynamics (QCD) [15]. The SM is finally achieved by the combination of the EW and strong interactions based on the symmetry group $SU(3)_C \times SU(2)_L \times U(1)_Y$. The massless and electrically-neutral photon (γ) is the mediator of the EM interactions, whereas the neutral Z boson and the two charged $W^{\pm}$ bosons are the massive mediators of the weak interactions. The gluons are the mediators of the strong interactions, eight massless spin-one gauge bosons, self-interacting and with a colour charge. All force mediators of the SM are classified as spin-one gauge bosons. These gauge bosons except the photon and gluons get a mass via Spontaneous Symmetry Breaking (SSB), i.e., the Higgs mechanism, [2–7], without violating the EW gauge symmetry. In the SM, the mechanism of SSB applied to the EW interactions (the aforementioned EWSB) is performed by adding to the gauge boson and fermion spectrum of the SM a complex scalar Higgs doublet generating a new scalar particle, the Higgs boson, which interacts with particles proportionally to their masses: the more massive is the particle, the stronger is its coupling with the Higgs boson.

In addition to SM bosons, Gell-Mann [16] and Zweig [17] postulated that there are fundamental matter fields (fermions) with a spin quantum number 1/2, which are divided into leptons and quarks. Quarks and leptons are classified in three generations. The second and third generation are essentially heavier than the first one. Each quark flavour is a colour triplet and carries both colour and EW charge including electric charges of $+2/3$ and $-1/3$, where the first case corresponds to the up-type quarks (up, charm, top) and the second to the down-type quarks (down, strange,

bottom), thus they are involved in the strong as well as in the EW interactions. Leptons are colourless and thus do not feel the strong force. Electrons, muons and tau leptons have electric charge -1, while neutral leptons, the neutrinos ν_e, ν_μ and ν_τ, are electrically neutral. The respective anti-fermions have opposite sign electric charge.

Precision studies have been carried over in multiple experiments especially during the past 30 years at lepton (LEP, SLAC Linear Collider (SLC)), lepton-hadron (Hadron-Electron Ring Accelerator (HERA)) and hadron colliders (Tevatron, LHC). Every feature of the SM is confirmed with precision measurements by experiments. Discovery of the properties of W and Z bosons, the existence of a third family of quarks and the Higgs boson, the latest achievement of the SM, prove its success. Fig. 1.1 summarises the recent result of EW precision measurements. Currently, the features of the Higgs boson, especially its couplings to the other SM particles, are investigated by the LHC.

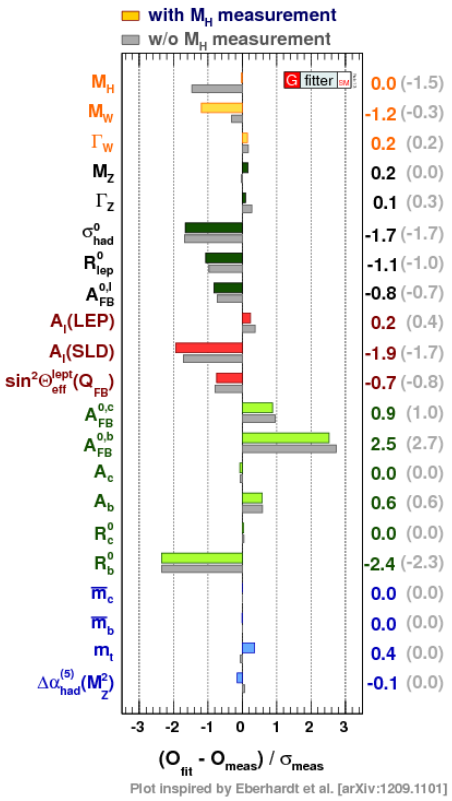

Figure 1.1: This figure shows differences between the SM fit and direct measurements with (coloured bars) and without (grey bars) mass of the Higgs boson in units of the experimental uncertainty. The image is taken from [18].

1.2.1 The Higgs mechanism in the SM

Let us examine how the Higgs mechanism is defined analytically. The Higgs scalar field, arising from a complex $SU(2)$ doublet, can be described in the Lagrangian as

$$\phi = \begin{pmatrix} \phi^+ \\ \phi^0 \end{pmatrix} = \frac{1}{\sqrt{2}} \begin{pmatrix} \phi_1 + i\phi_2 \\ \phi_3 + i\phi_4 \end{pmatrix}. \tag{1.1}$$

The Higgs potential is

$$V(\phi) = \mu^2 \phi^\dagger \phi + \lambda (\phi^\dagger \phi)^2, \tag{1.2}$$

where $\phi_{1,2,3,4}$ is a complex scalar field, μ is a mass factor and λ is a self-interaction parameter of the scalar doublet. A $SU(2)$ doublet has weak hypercharge $Y = +1$. By choosing $\mu^2 < 0$ and $\lambda > 0$ the potential of the Higgs field V has a minimum value at

$$|\phi^+ \phi| = \frac{\mu^2}{2\lambda} \equiv \frac{v_{\mathrm{SM}}^2}{2}, \tag{1.3}$$

where v_{SM} is the Vacuum Expectation Value (VEV)[1]. When the real part of the neutral component of the complex doublet field ϕ_3 gets a VEV, the $SU(2)_L \times U(1)_Y$ symmetry is spontaneously broken to the EM gauge symmetry $U(1)_{\mathrm{EM}}$ surviving as a symmetry of the ground state. Therefore, the ground state of the scalar field is nonzero and can be defined as:

$$\langle \phi \rangle = \frac{1}{\sqrt{2}} \begin{pmatrix} 0 \\ v_{\mathrm{SM}} \end{pmatrix}. \tag{1.4}$$

Expanding the field around the true minimum of the theory, in the unitary gauge, ϕ becomes

$$\phi = \frac{1}{\sqrt{2}} \begin{pmatrix} 0 \\ v_{\mathrm{SM}} + h \end{pmatrix}. \tag{1.5}$$

Substituting this field in the Higgs potential in Eq. (1.2), one can obtain the self-interaction terms of the h field and a new physical state (the Higgs boson) with a mass given by:

$$m_h = v_{\mathrm{SM}} / \sqrt{2\lambda}. \tag{1.6}$$

Before SSB of the EW gauge symmetry group we are left with 4 degrees of freedom. Longitudinal polarisation states of the $W^\pm$ and Z bosons absorb 3 degrees of freedom of the scalar field, so the bosons get their masses, while the photon remains massless. The remaining degree of freedom relates to a physical scalar particle, i.e., the Higgs boson. Additionally, the masses of the fermions can be generated by couplings with the Higgs field h via Yukawa interactions [19]. As a result, the

[1] The Fermi constant G_F, which results in $v_{\mathrm{SM}} = 1/\sqrt{\sqrt{2} G_F} = 246.22$ GeV, fixes the scale of EWSB.

mass of elementary particles arises from the Higgs boson.

1.2.2 Theoretical perspective on Higgs physics

In this section, some theoretical features of Higgs physics are discussed. Since the Higgs field emerging from EWSB is the only scalar field in the SM, its theoretical features are diverse and significant to study. Moreover, they are important in the investigation of new physics since the Higgs sector of extended models could alter these features.

1.2.2.1 Perturbative unitarity

Unitarity ensures consistency of the theory through the application of the conservation of probability. In quantum field theory the unitarity of the S-matrix is expressed as $S^\dagger S = SS^\dagger = 1$. From this simple idea, limits on the partial wave amplitudes and cross sections for different scattering processes can be developed. One can employ these bounds at any order in perturbation theory to control the consistency of the perturbative calculations.

It has been first explained by Lee, Quigg and Thacker [20] that the unitarity of the S-matrix can give an upper bound on the Higgs boson mass in the SM. The amplitudes of elastic scattering fulfil the below relation for each partial wave amplitude

$$a_J^I = \lambda(\frac{m_x}{\sqrt{s}}, \frac{m_y}{\sqrt{s}})|a_J^R + ia_J^I|^2, \tag{1.7}$$

$$\lambda(\frac{m_x}{\sqrt{s}}, \frac{m_y}{\sqrt{s}}) = \sqrt{(1-(\frac{m_x}{\sqrt{s}}+\frac{m_y}{\sqrt{s}})^2)(1-(\frac{m_x}{\sqrt{s}}-\frac{m_y}{\sqrt{s}})^2)}\ , \tag{1.8}$$

where s and $(a_J^I)a_J^R$ stand for the squared Center of Mass (CM) energy and the (imaginary) real part of the partial wave amplitude, respectively. Partial waves are described with the Legendre polynomials $P_a(x)$ and the scattering angle $\Delta = 0$ as follows

$$\mathcal{M}(\cos\Delta) = 16\pi \sum_{J=0}^{\infty}(2J+1)a_J P_J(\cos\Delta), \tag{1.9}$$

$$\int_{-1}^{1} dx P_a(x) P_J(x) = \frac{2}{2J+1}\delta_{aJ}. \tag{1.10}$$

Eq. (1.7) stands for the equation of a circle with radius $\frac{1}{2\lambda}$ and center of coordinate $(0, \frac{1}{2\lambda})$. When the radius of the circle reaches the maximum, the masses of the generated particles can be ignored in the high energy limit. Therefore, partial wave amplitudes require $a_J^R \in \left[-\frac{1}{2}, \frac{1}{2}\right]$ and $a_J^I \in [0,1]$ at the tree level.

The classical example of perturbative unitarity bounds on the mass of the Higgs boson studied

by [20] was considered from the tree level scattering of the longitudinal W bosons, $W_LW_L \to W_LW_L$. Without the Higgs boson, the contribution to the amplitude comes from the s- and t-channel mediation of the photon and Z boson plus the four-point contact interaction diagrams as follows

$$M(W_LW_L \to W_LW_L)_{\text{gauge}} = \\ -\frac{s}{2v_{\text{SM}}^2}(1-\cos\Delta) - \frac{g_z^2}{4}\left[(2\cos^2\theta_W - 1)(1+\cos\Delta) - 2\tan^2\frac{\Delta}{2}\right] + \mathcal{O}(s^{-1}), \tag{1.11}$$

where θ_{W} is the Weinberg angle. Without the Higgs boson mediation, the amplitude has a squared-energy dependence, thus tree level unitarity would be violated around $E \simeq 1.7$ TeV by applying the unitarity bound

$$|Re(a_J \leq 1/2)|. \tag{1.12}$$

However, in the SM, the Higgs boson can be exchanged in s- and t-channel and the total amplitude is given by

$$M(W_LW_L \to W_LW_L)_{\text{Higgs}} = \frac{s}{2v_{\text{SM}}^2}(1-\cos\Delta) - \frac{2}{v_{\text{SM}}^2}m_h^2 + \mathcal{O}(s^{-1}), \tag{1.13}$$

where m_h is the mass of the physical neutral Higgs boson. Hence, the s- dependence in the total amplitude vanishes and the total amplitude is given by

$$M(W_LW_L \to W_LW_L)_{\text{tot}} = -\frac{2}{v_{\text{SM}}^2}m_h^2 - \frac{g_z^2}{4}(2\cos^2\theta_W - 1)(1+\cos\Delta) - 2\tan^2\frac{\Delta}{2}. \tag{1.14}$$

The leading order $J = 0$ partial wave amplitude for this process is written as

$$a_0 = \frac{1}{32\pi}\int_{-1}^{1} d\cos\Delta M = -\frac{1}{32\pi}\int_{\pi}^{0} d\Delta \sin\Delta M, \tag{1.15}$$

$$a_0(W_LW_L \to W_LW_L) = -\frac{m_h^2}{8\pi v_{\text{SM}}^2}. \tag{1.16}$$

From Eq. (1.12), by applying the unitarity bound to this amplitude, it is obtained that

$$m_h^2 \leq 4\pi v_{\text{SM}}^2. \tag{1.17}$$

One can thus impose a restriction on the Higgs boson mass from the unitarity constraint:

$$m_h^2 \leq (871\ \text{GeV})^2. \tag{1.18}$$

The strongest bound can be given by all other scattering processes with the same charge in the initial (final) states. Let us investigate other charge neutral states, namely, $\frac{1}{\sqrt{2}}Z_LZ_L, \frac{1}{\sqrt{2}}hh,\ hZ_L$. In the high energy limit, according to the equivalence theorem [21], the scattering process of the

longitudinal component of the massive gauge bosons can be taken over from the analogue Nambu-Goldstone Boson (NGB) mode. The matrix of the scattering amplitudes for $J = 0$ has the form

$$a_0 = -\frac{m_h^2}{8\pi v_{\rm SM}^2} \begin{pmatrix} 1 & \frac{1}{\sqrt{8}} & \frac{1}{\sqrt{8}} & 0 \\ \frac{1}{\sqrt{8}} & \frac{3}{4} & \frac{1}{4} & 0 \\ \frac{1}{\sqrt{8}} & \frac{1}{4} & \frac{3}{4} & 0 \\ 0 & 0 & 0 & \frac{1}{2} \end{pmatrix}. \tag{1.19}$$

The strongest bound comes from the largest eigenvalue. By imposing the unitarity condition Eq. (1.12), we attain

$$m_h^2 < (710 \text{ GeV})^2. \tag{1.20}$$

However, any deviations from the SM predictions in the Higgs boson self-couplings or Higgs boson couplings to vector bosons (and fermions as well) could violate perturbative unitarity in certain energy regions. We will exploit precisely this phenomenon in the rest of the thesis.

1.2.2.2 Custodial symmetry

The Higgs sector has an approximate global symmetry given by

$$SU(2)_L \times SU(2)_R \simeq SO(4). \tag{1.21}$$

If we build a potential by introducing this symmetry, we write the Higgs field Φ as a 2×2 matrix, composed of ϕ^* and ϕ

$$\Phi = (i\sigma_2\phi^*, \phi) = \begin{pmatrix} \phi^{0*} & \phi^+ \\ -\phi^- & \phi^0 \end{pmatrix}, \tag{1.22}$$

which transforms under $SU(2)_L \times SU(2)_R$ as

$$\Phi \to U_L \Phi U_R. \tag{1.23}$$

Here, $U_{L,R}$ are the relevant unitarity $SU(2)_{L,R}$ transformation matrices. When the Higgs field acquires a non-zero VEV

$$\langle \Phi \rangle = \frac{1}{\sqrt{2}} \begin{pmatrix} v & 0 \\ 0 & v \end{pmatrix} \tag{1.24}$$

the $SO(4) \cong SU(2)_L \times SU(2)_R$ symmetry is broken spontaneously to the diagonal subgroup $SO(3) = SU(2)_V$, called a custodial symmetry, giving rise to the relation $\rho \equiv m_W^2/(m_Z^2 \cos\theta_W^2) = 1$, that has been probed to high precision. Here $m_{W,Z}$ are the masses of the gauge bosons. The Higgs

potential can be written as

$$\mathcal{L}_V = \mu^2 \mathrm{Tr}[\Phi^\dagger \Phi] - \lambda \mathrm{Tr}[\Phi^\dagger \Phi \Phi^\dagger \Phi]. \tag{1.25}$$

The Lagrangian above is obviously invariant under the transformation of Eq. (1.23). We also consider the Higgs kinetic term. The covariant derivative D_μ in the kinetic Lagrangian is given by

$$D_\mu \Phi = \partial_\mu \Phi + \frac{1}{2} i g W_\mu^a \tau_a \Phi - \frac{1}{2} i g' B_\mu \Phi \tau_3, \tag{1.26}$$

with $a \in \{1, 2, 3\}$. This covariant derivative is gauged if $g' = 0$, otherwise the coupling with B_μ violates the global $SU(2)_R$ symmetry. Setting $g' = 0$, the covariant derivative is invariant under the transformation in Eq. (1.21) and W_μ^a transforms as a triplet under $SU(2)_L$ (because of the three matrices τ^a) and a singlet under $SU(2)_R$. The covariant derivative in the vacuum is then written as

$$D_\mu \langle \Phi \rangle = \frac{gv}{2\sqrt{2}} \begin{pmatrix} W_\mu^3 & W_\mu^1 - i W_\mu^2 \\ W_\mu^1 + i W_\mu^2 & - W_\mu^3 \end{pmatrix}. \tag{1.27}$$

The gauge field mass term reads as

$$\frac{1}{2} Tr[(D_\mu \langle \Phi \rangle)^T D^\mu \langle \Phi \rangle] = \frac{g^2 v^2}{4} \frac{W_\mu^a W^{a\mu}}{2}. \tag{1.28}$$

The gauge boson masses are equal to $m_W = m_Z \cos\theta_W$ at tree level. If we allow $g' \neq 0$, the custodial symmetry is spoiled since the $SU(2)_R$ and $U(1)_Y$ generators do not commute. The Yukawa Lagrangian also violates the custodial symmetry since their top and bottom quark contributions are relatively large because of their mass difference. The covariant derivative in the vacuum is introduced as

$$D_\mu \langle \Phi \rangle = \frac{gv}{2\sqrt{2}} \begin{pmatrix} W_\mu^3 - \frac{g'}{g} B_\mu & W_\mu^1 - i W_\mu^2 \\ W_\mu^1 + i W_\mu^2 & - W_\mu^3 + \frac{g'}{g} B_\mu \end{pmatrix}. \tag{1.29}$$

From this definition, $m_W = m_Z \cos\theta_W$ remains valid (at tree level). Despite the symmetry is broken at loop level, the effect is not important due to the smallness of the hypercharge coupling. Notably, radiative corrections from loop diagrams must be proportional to g' to protect the mass relation in $m_W = m_Z \cos\theta_W$. Thus, it is important to obtain the above custodial symmetry to construct Higgs physics beyond the SM, as it guarantees the relation $\rho \equiv m_W^2/(m_Z^2 \cos\theta_W^2) = 1$.

1.2.2.3 Vacuum stability

A lower limit on the Higgs mass is given by the vacuum stability bound. The Higgs couplings λ grows with the particle mass and hence the important contributions will arise from the top quarks. In order to obtain the running coupling λ, the one-loop Renormalisation Group Equation (RGE) can be employed [22]

$$\frac{d\lambda}{\mathrm{dlog}Q^2} \equiv \frac{3}{4\pi^2}[\lambda^2 + \frac{1}{2}\lambda y_t^2 - \frac{1}{4}y_t^4 - \frac{1}{8}\lambda(3g^2 + g'^2) + \frac{1}{64}(3g^4 + 2g^2g'^2 + g'^4)], \tag{1.30}$$

where Q is the energy scale and y_t is the top quark Yukawa coupling. Since top-loop corrections decrease λ for increasing top-Yukawa coupling, λ develops negative value if the top mass gets too large. In this case, the ground state becomes unstable because of the absence of a minimum in the Higgs potential. A stable vacuum [23–25] is ensured, if $\lambda >> g,\ g',\ y_t$. This gives a lower bound on the mass of the Higgs boson as a function of the cut-off value Λ.

1.2.2.4 The hierarchy problem of the Higgs sector

In standard quantum field theories, the one-loop radiative corrections to the masses of scalar fields have quadrical sensitivity to the cut-off scale of the model. If there is new physics at higher scales such as the Grand Unified Theory (GUT) scale (10^{16} GeV) or Planck scale (10^{19} GeV), one would naively expect the Higgs mass to be close to the GUT or Planck scale because of the absence of a symmetry to protect the Higgs mass from radiative corrections via 1-loops diagrams. At loop level, the Higgs mass gets corrections from self interactions, gauge loops, and fermion loops (particularly the top quark) [22]

$$m_{h,\mathrm{phys}}^2 = m_{h,\mathrm{bare}}^2 + \frac{3\Lambda^2}{8\pi^2 v_{SM}^2}[m_{h,\mathrm{phys}}^2 + 2m_W^2 + m_Z^2 - 4m_t^2], \tag{1.31}$$

where Λ is the cut-off the theory, $m_{h,\mathrm{phys}}$ is the Higgs boson mass with measured value 125 GeV, $m_{h,\mathrm{bare}}$ is the Higgs boson bare mass parameter of the unrenormalised Lagrangian and m_t is the top quark mass. The unexpected smallness of the Higgs mass with respect to the Planck scale is called the hierarchy (also called naturalness or fine-tuning) problem. These corrections to the Higgs mass demand an enormous fine tuning to obtain the theoretical value compatible with the observed value. In general, one would expect that there must be some new dynamics, not much above the weak scale $\sim$ TeV, to stabilise the Higgs mass. Present collider experiments are now exploring energies at and above the TeV scale and have yet to lead to any solid discoveries of new physics.

There are two main proposals to solve the hierarchy problem of the SM. Namely, weakly coupled and strongly coupled theories. Those based on Supersymmetry are an example of weakly coupled

theories assuming the presence of new symmetries relating fermions and bosons. The Higgs boson is an elementary particle. In such theories, the quadratic divergence due to a certain particle in the loop is killed by the contribution from a superpartner particle. A characteristic example of strongly coupled models is CHMs assuming new interactions. The Higgs boson is here a composite particle. In this case, strong dynamics will cause, through other bound states, a Pseudo Nambu-Goldstone Boson (PNGB) with the quantum numbers of the Higgs which breaks the EW symmetry by obtaining a VEV. The PNGB nature of this Higgs particle will ensure its lightness since all the radiative corrections modifying its mass will be saturated at the compositeness scale, that is, its mass will not receive radiative corrections above such a scale. Therefore, if the hierarchy problem is solved by some CHMs, one anticipates the emergence of new resonances, particularly fermionic ones, around the TeV scale, to stabilise the Higgs mass [26–28]. Another typical example of strongly coupled theories is Technicolour [29] where the Higgs boson is strongly interacting and the Higgs mass is at the TeV scale, which is inspired by chiral symmetry breaking in QCD.

1.3 Why beyond SM physics

Various beyond the SM scenarios have been introduced which are motivated in order to overcome the SM problems. Beyond the SM (BSM) scenarios generally contain the SM with further fields and possibly further symmetries of the Lagrangian. In addition, many BSM constructions introduce a Higgs sector which is more complicated than that of the SM. We will not discuss all the different BSM constructions here. Instead, we focus on two realisations corresponding to the research presented later in this thesis. The first topic is 3HDMs which propose the existence of two extra scalar doublets [30]. Especially, we focus on the phenomenology of charged Higgs bosons in this model. The second is C2HDMs [31–33]. After the discovery of a Higgs boson, it is therefore crucial to study BSM physics by concentrating on the Higgs sector.

1.3.1 3HDMs

Although the Higgs sector in the SM is developed from only one isospin doublet field, the possibility of the existence of more Higgs doublets is still acceptable. In fact, it is often the case in BSM scenarios that more than one Higgs multiplet is permitted, or even demanded. There exist various types of 3HDMs in the literature, depending on the symmetries implemented in the scalar potential [34–36]. Features of an enlarged Higgs sector clearly depend on the new physics scenario embedding it, so that the investigation of the true Higgs boson dynamics is highly crucial to derive information on the new physics model. Particularly, if a multi-doublet structure is chosen for the Higgs sector, what is the mass scale of the extra scalar bosons? How can we derive information on the total number of doublet fields? The direct method to examine a multi-doublet structure is discovering additional scalar bosons at collider experiments and measuring their properties, e.g., the mass, couplings, production cross sections and decay rates.

One of the most important features of models with multi-Higgs doublets is the existence of physical extra scalar bosons such as a charged pair $H^{\pm}$, two CP-even h, H and one CP-odd A Higgs bosons. Particularly, the features of extra Higgs states strongly depend on the structure of the Higgs sector, e.g., the symmetries of the model, the actual number of doublets, the mass spectrum, etc. In addition, models with a multi-doublet structure have also been discussed based upon several physics motivations, e.g., to introduce a DM candidate [37], neutrino mass models [38] and extra CP violating phases for the definition of the baryon-antibaryon asymmetry of Universe [39]. Thus, testing the existence of additional doublet fields is very important to investigate new physics scenarios beyond the SM.

We will make a phenomenological analysis of the charged Higgs bosons, namely, $H_1^{\pm}$ and $H_2^{\pm}$, in our 3HDM in the remainder of the thesis [30]. In a first step, we introduce the theoretical aspects of this model. Particularly, we will show five types of Yukawa interactions, Higgs potential and mass eigenstates of the model. We will display Branching Ratios (BRs) of the charged Higgs bosons in five Yukawa types. In particular, we will concentrate on the parameter space of 3HDMs by enforcing constraints from the measurement of the $B \to X_s\gamma$ decay rate at the next-to-leading order in QCD. We will see that in all Yukawa types of 3HDMs both masses of the two charged Higgs bosons $m_{H_1^{\pm}}$ and $m_{H_2^{\pm}}$ can be less than the top mass m_t while agreeing with the constraints from $B \to X_s\gamma$. We will finally also introduce collider limits on light charged Higgs bosons from LEP2, Tevatron and LHC.

1.3.2 The composite Higgs boson idea

It is often argued that elementary scalars cannot be light in the absence of a mechanism that protects their masses from quantum corrections. In the 1980s, Georgi and Kaplan pointed out that a composite Higgs boson can be naturally lighter than other resonances [40]. In CHMs, a light Higgs boson is not an elementary field, rather it emerges as the bound state of a strong dynamics at some energy scale f, the analogue of the pion decay constant, higher than the EW scale (approximately the TeV scale). A light spinless particle, which is the lightest particle of the strong sector, is obtained if the Higgs appears as a NGB emerging from the spontaneous breaking of a global symmetry G of the strong sector. After the global symmetry G is broken explicitly by couplings to the SM gauge bosons and fermions, NGBs become PNGBs getting a potential at the loop-level [41]. A composite Higgs state deals with the hierarchy problem since its mass is not sensitive to radiative corrections above the compositeness scale. In CHMs, additional parameters control the Higgs properties which then deviate from the SM ones, thus these deviations have effects on the searches for the Higgs boson at colliders [42].

The minimal model of a Higgs as a PNGB in which the EW symmetry is broken dynamically via top loop effects is presented in [43, 44]. The minimal CHM based on a $SO(5) \to SO(4)$ coset structure delivers the minimum number of PNGB as Higgs fields. Furthermore, $SO(4)$ is isomorphic

to $SU(2)_L \times SU(2)_R$, while $SO(4) \times U(1)_X$ includes the SM EW group $SU(2)_L \times U(1)_Y$, therefore hypercharge is determined as $Y = T^{3R} + X$. The coset $SO(5)/SO(4)$ yields four real NGBs transforming as the SM Higgs doublet H which must contain a custodial $SO(4)$-symmetry to protect ρ or the T-parameter. Therefore, in the following subsections, we will introduce the general ideas of C2HMs (Subsection 1.3.2.1) and concentrate on the low-energy theory definition of the Higgs sector through the Coleman, Weinberg, Wess and Zumino (CCWZ) prescription (Section 1.3.3).

1.3.2.1 C2HDMs

Among the CHMs present in literature, in this thesis we will concentrate upon the C2HDMs of [31–33, 45] based on the spontaneous breakdown of a global symmetry $SO(6) \to SO(4) \times SO(2)$ at the compositeness scale f. The eight PNGBs arising from such a dynamics are classified as two isospin doublet Higgs fields. In order to define them as PNGBs, a specific symmetry breaking structure consisting of multiple PNGBs is imposed explicitly by the couplings of the SM fields to the strong sector. The C2HDM results in five physical composite Higgs bosons: three neutral (h, H, and A) and two charged ($H^{\pm}$), while the minimal CHM generates only one physical composite Higgs boson h. We will study the predictions from this structure of the (pseudo)scalar spectrum and the deviations of their couplings from those of a generic Elementary 2-Higgs Doublet Model (E2HDM).

In the minimal CHM [43,44], the composite version of the SM Higgs doublet, the only light scalar is classified as a PNGB (the lightest state of the composite resonances, both spin-1/2 and spin-1). Thus, one expects that the new (pseudo)scalars Higgs states of a C2HDM are also PNGBs. A C2HDM can also provide a DM candidate which is given by the neutral light states of extra Higgs doublets with no VEV nor couplings to quarks and leptons [31, 45]. Furthermore, light PNGBs are introduced as a possible composite DM candidate in Ref. [37, 46, 47]. We construct the corresponding non-linear effective Lagrangian in the usual CCWZ formulation, the details are given in later sections of this chapter. The Higgs potential is produced by radiative corrections and, at the lowest order, is determined by the free parameters relevant to the top sector [45]. Here, we will not adopt the Higgs potential generated at the loop level. Instead, we construct a Higgs potential of the same form as in the E2HDM with a Z_2 symmetry, enforced in order to avoid Flavour Changing Neutral Currents (FCNCs) at the tree level [48]. This approach allows us to study the phenomenology of C2HDM in a rather model independent way.

In our analysis, we first investigate unitarity properties of a C2HDM based on the coset $SO(6) \to SO(4) \times SO(2)$ [31]. We will calculate the S-wave amplitude for all possible two-to-two body elastic (pseudo)scalar boson scatterings at energy scales $\sqrt{s}$ obtainable at the LHC (see Ref. [31]) and discuss the perturbative unitarity bounds on its parameter space. In fact, while the E2HDM is renormalisable, the C2HDM is a low-energy effective theory, which includes dimension six derivative interactions emerging from the kinetic term in the Lagrangian. These interactions lead to modifications of the Higgs couplings to matter with respect to the E2HDM case. In addi-

tion, these interactions make a contribution to scattering among longitudinal massive gauge bosons through the equivalence theorem and force non-vanishing s-dependence of the scattering amplitudes. Hence, cross sections of these processes become larger and larger as energy increases. As a result, the C2HDM violates unitariy for energies above a critical value or, put another way, other new physics (e.g., new composite fermions and gauge bosons) contributions need to be taken into account to make the model unitarity above that energy scale. Thus, it is effective to compare the limits on the additional Higgs masses in the energy region where the E2HDM and C2HDM are both unitarity.

Next, we investigate the phenomenology of C2HDMs of numerous Yukawa types based on the global symmetry breaking $SO(6) \to SO(4) \times SO(2)$ [32]. We introduce the relevant effective kinetic and Yukawa Lagrangian. Phenomenological differences between E2HDMs and C2HDMs are discussed by studying departures from the SM couplings of the discovered Higgs state (h) besides the production cross sections and BRs at the LHC of extra Higgs bosons. Despite the same value of deviations in the hVV ($V = W, Z$) couplings are constructed in both scenarios, the structure of the Yukawa couplings leads to important discriminations between E2HDMs and C2HDMs. This means that these two scenarios can be identified by using production and decay features of extra Higgs bosons.

We also analyse single- and double-h, the discovered SM-like Higgs boson, production at future e^+e^- colliders in C2HDMs based on the coset $SO(6) \to SO(4) \times SO(2)$ [33]. We then discuss differences between E2HDMs and C2HDMs in single- and double-h production cross sections. The single-h production modes are effective to extract the hZZ coupling, while the double-h production modes are effective to extract hZZ, $ht\bar{t}$ and the triple Higgs boson coupling λ_{hhh}. We will show that C2HDMs generate significant deviations in the Higgs couplings which cannot be explained in E2HDMs. We indicate that the differences between the two scenarios can be even larger than 50% for double Higgs production process by assuming the same values of deviation in the hVV ($V = W,\ Z$) couplings from the SM value in both scenarios.

1.3.3 The CCWZ prescription for Goldstone bosons

In this section we give some details about the most common prescription introduced by CCWZ [49, 50] to write down a low energy effective Lagrangian for a CHM, wherein the NGBs are parametrised as fields ϕ_a taking values in the coset space G/H. This method starts by introducing a useful quantity, the Maurer-Cartan form, given by

$$\Xi_\mu = iU^\dagger \partial_\mu U, \quad U = e^{i\pi T^{\hat{a}}/f}, \quad \text{with} \quad \pi = \phi_a T^{\hat{a}}, \tag{1.32}$$

where $T^{\hat{a}}$ are the generators of a coset G/H and T^a are the generators of G. The dimensionful parameter f has been defined inside the exponential to have correct mass dimension. A non-linear

transformation of U is defined as

$$U \to gUh^\dagger,\ g = Uh,\ g \in G,\ h \in H. \tag{1.33}$$

We can define Ξ as the sum of two parts, in terms of the generators of H and G/H,

$$\Xi_\mu \equiv E_u^a T^a + d_\mu^a T^{\hat{a}}, \tag{1.34}$$

and the terms $E_\mu = E_\mu^a T^a$ and $d_\mu = d_\mu^a T^{\hat{a}}$ transform as

$$E_\mu \to h(E_\mu + d_\mu)h^\dagger, \tag{1.35}$$

$$d_\mu \to h d_\mu h^\dagger. \tag{1.36}$$

The G-invariant kinetic Lagrangian can be constructed by using d_μ (the field E_μ transform like a connection)

$$\mathcal{L} \propto f^2 Tr[d^\mu d_\mu] \propto f^2 (\partial_\mu \Phi)^\dagger (\partial^\mu \Phi) \tag{1.37}$$

$$\tag{1.38}$$

with

$$\Phi = \exp(i\pi^{\hat{a}} T^{\hat{a}}/f)\phi_0 \quad \phi_0 = (0, 0, .., 1), \tag{1.39}$$

then

$$\begin{aligned}
&(\partial_\mu \Phi)^\dagger (\partial^\mu \Phi) = (\partial_\mu (U\phi_0))^\dagger (\partial^\mu (U\phi_0)) = \\
&= \phi_0^T (\partial_\mu U)^\dagger (\partial^\mu U)\phi_0 = \phi_0^T (U^\dagger \partial_\mu U)^\dagger (U^\dagger \partial^\mu U)\phi_0 = \\
&= \phi_0^T d_\mu^\dagger d^\mu \phi_0 = \phi_0^T (E_\mu^a T^a + d_\mu^{\hat{a}} T^{\hat{a}})(E^{\mu b} T^b + d^{\mu \hat{b}} T^{\hat{b}})\phi_0 = \\
&= \phi_0^T (d_\mu^{\hat{a}} T^{\hat{a}})^\dagger (d^{\mu \hat{b}} T^{\hat{b}})\phi_0 = \\
&= d_\mu^{\hat{a}} d^{\mu \hat{b}} \delta^{\hat{a}\hat{b}} = \\
&= \frac{1}{2} \mathrm{Tr}[d_\mu d^\mu].
\end{aligned} \tag{1.40}$$

According to the CCWZ prescription, the Lagrangian giving the dynamics of the NGB correspond to coset G/H at the level of two derivatives reads as

$$\mathcal{L} = \frac{f^2}{4} \mathrm{Tr}[d_\mu d^\mu]. \tag{1.41}$$

If we perform gauge theories with some gauged subgroup of H, partial derivatives ∂_μ are replaced with covariant derivatives D_μ in the definition of Ξ in Eq. (1.32). However, the form of d_μ depends on the specific groups G and H. It is important to construct the main object d_μ in non-linear σ

models.

To conclude, this thesis performs studies of Higgs bosons properties in extended Higgs models both elementary and composite ones. It proposes methods to infer what the structure of BSM physics can be and could provide the guidance towards searching for some new physics at experiments, either directly or indirectly.

1.4 Outline of the thesis

This thesis is organised as follows. In Chapter 2, we discuss the accessible parameter space of 3HDMs yielding light charged $H^{\pm}_{1,2}$ Higgs states by enforcing bounds from the measurement of the $B \to X_s\gamma$ decay rate at the next-to-leading order in QCD and direct searches at colliders [30]. In Chapter 3, we discuss perturbative unitarity bounds in C2HDMs [31]. In chapter 4, LHC phenomenology of C2HDMs is discussed [32]. In chapter 5, we discuss single- and double-h, the discovered SM like Higgs boson, production at future e^+e^- colliders in C2HDMs and E2HDMs [33]. This thesis concludes in Chapter 6. In the appendices we introduce additional information. Appendix A gives the analytic expressions for the mass matrices of the scalar states in the Higgs basis of 3HDMs. Appendix B presents input parameters for numerical calculations in 3HDMs. In Appendix C, the kinetic Lagrangian of C2HDMs is given in detail. Appendix D introduces the antisymmetric representation, $\Sigma(15)$, in C2HDMs. Appendix E represents the Feynman rules in C2HDMs. Appendix F shows a list of tables containing Higgs data patterns from the LHC. Appendix G presents the list of publications.

Chapter 2

Light charged Higgs bosons scheme in 3HDMs

2.1 Overview

The presence of a second Higgs doublet is strongly expected when we study physics BSM. One of the specific features of extended Higgs models is the existence of charged Higgs bosons, thus their detection can be considered as direct evidence of such structures. Particularly in multi-doublet models, singly charged scalar bosons can have impact on various flavour observables such as B-meson relevant processes. For example, a lower limit on the mass and Yukawa couplings of charged Higgs bosons is given by $B \to X_s\gamma$ data. In Refs. [51–54], the BR of $B \to X_s\gamma$ has been evaluated at the Next-to-Leading Order (NLO) in QCD in the context of 2-Higgs Doublet Models (2HDMs) with a softly-broken Z_2 symmetry. In Refs. [55, 56] the calculation has been extended to Next-to-NLO (NNLO). In Ref. [56], the lower limit on the mass of a charged Higgs boson $m_{H^\pm}$ is found to be about 480 GeV at 95% CL in the Type-II 2HDM when $\tan\beta$, which is the ratio of the Higgs VEVs of the two doublets, is set to be larger than 2. Conversely, a milder constraint from $B \to X_s\gamma$ is obtained from the Type-I 2HDM, e.g., $m_{H^\pm} \gtrsim 100$ and 200 GeV in the case of $\tan\beta = 2.5$ and 2, respectively [55], with the lower bound on $m_{H^\pm}$ weakening with growing $\tan\beta$.

In this chapter, we study the phenomenology of charged Higgs bosons in 3HDMs [30]. Two softly-broken discrete Z_2 symmetries are enforced in order to realise the Natural Flavour Conserving (NFC) hypothesis, where only one of the three doublets couples to each type of fermion in order to prevent FCNCs at the tree level. Under these Z_2 symmetries, we present five independent types of Yukawa interactions similarly to the four types of Yukawa interactions in Z_2 symmetric 2HDMs. In 3HDMs two physical charged Higgs bosons exist (indicated by $H_1^\pm$ and $H_2^\pm$, with $m_{H_1^\pm} < m_{H_2^\pm}$) and more parameters determine the phenomenology of the charged Higgs sector than in 2HDMs. In Refs. [57–60], the phenomenology of $H_1^\pm$ in 3HDMs has been investigated with decoupled $H_2^\pm$ in

	Φ_1	Φ_2	Φ_3	u_R	d_R	e_R	Q_L, L_L	Φ_u	Φ_d	Φ_e
Type-I	$(+,+)$	$(+,-)$	$(-,+)$	$(+,-)$	$(+,-)$	$(+,-)$	$(+,+)$	Φ_2	Φ_2	Φ_2
Type-II	$(+,+)$	$(+,-)$	$(-,+)$	$(+,-)$	$(+,+)$	$(+,+)$	$(+,+)$	Φ_2	Φ_1	Φ_1
Type-X	$(+,+)$	$(+,-)$	$(-,+)$	$(+,-)$	$(+,-)$	$(+,+)$	$(+,+)$	Φ_2	Φ_2	Φ_1
Type-Y	$(+,+)$	$(+,-)$	$(-,+)$	$(+,-)$	$(+,+)$	$(+,-)$	$(+,+)$	Φ_2	Φ_1	Φ_2
Type-Z	$(+,+)$	$(+,-)$	$(-,+)$	$(+,-)$	$(+,+)$	$(-,+)$	$(+,+)$	Φ_2	Φ_1	Φ_3

Table 2.1: Charge assignments under the $Z_2 \times \tilde{Z}_2$ symmetry, e.g. $(+,-)$ indicates Z_2-even and $\tilde{Z}_2$-odd. A similar table is seen in Ref. [30].

terms of effective Yukawa couplings for the down-type quark, up-type quark and charged lepton, which are defined by a function of four independent parameters [59] in the framework of NFC. It has been indicated that $H_1^\pm$ can be lighter than the top quark whereas fulfilling bounds from $B \to X_s\gamma$ even for the case with Type-II like Yukawa couplings. Furthermore, it was discussed in Refs. [57, 58, 60, 61] that the decay channel $H_1^\pm \to cb$ can obtain a large BR (up to 80%) in a 3HDM. Even though such a value is possible in the Type-Y 2HDM for $m_{H^\pm} < m_t - m_b$, the bound $m_{H^\pm} > 480$ GeV from $B \to X_s\gamma$ excludes this scenario. Thus a large BR($H_1^\pm \to cb$) is a distinguishing signature of 3HDMs.

However, there are some significant shortcomings in the previous method where the heavier charged Higgs boson is decoupled from the theory. When one adopts the decoupling limit of the heavier charged Higgs boson, then the mixing angle between the two charged Higgs bosons asymptotically approaches zero due to the structure of the charged scalar mass matrix. Finally, this situation makes the predictions in 3HDMs same to those in 2HDMs. Namely, the effective coupling approach [57–60] is completely assuming that a cancellation is arising between the contributions of the two charged Higgs bosons to $B \to X_s\gamma$, and the heavier charged Higgs boson should not be too heavy in order for enough cancellation to happen. Hence in this chapter, we explain the 3HDM phenomenology with a non-decoupled $H_2^\pm$ and, as a result, the effect of $H_2^\pm$ on flavour physics and its typical collider signatures. We calculate the BR of $B \to X_s\gamma$ at NLO in QCD in 3HDMs by considering both $H_1^\pm$ and $H_2^\pm$ loops, in which the dependence of the relevant five independent parameters, i.e., $m_{H_1^\pm}$, $m_{H_2^\pm}$, two ratios of VEVs and a mixing angle between $H_1^\pm$ and $H_2^\pm$, is explicitly presented with a fixed type of Yukawa interaction. We then concentrate on the phenomenology of $H_1^\pm$ and $H_2^\pm$ at the LHC in the parameter space allowed by $B \to X_s\gamma$ and by the direct searches for charged Higgs bosons via $t \to H^\pm b$ with $H^\pm \to \tau\nu/cs$ at the Tevatron and LHC in addition to pair production H^+H^- at LEP 2. We remind the fact that present LHC searches for $H^\pm$ is not sensitive to the region $80\,\text{GeV} < m_{H^\pm} < 90$ GeV provided that $H^\pm$ has a substantial BR to cs and/or cb, and LEP2 searches did not exclude the possibility of a $H^\pm$ in this region. We also interface these consequences to the standard hadro-production mode $gg, q\bar{q} \to t\bar{b}H^- + \text{c.c.}$ studied in [62], where analytical formulae can be found.

	Factor for $\tilde{H}_1$, $\tilde{A}_1$ and $\tilde{H}_1^\pm$			Factor for $\tilde{H}_2$, $\tilde{A}_2$ and $\tilde{H}_2^\pm$		
	R_{u2}/R_{u1}	R_{d2}/R_{d1}	R_{e2}/R_{e1}	R_{u3}/R_{u1}	R_{d3}/R_{d1}	R_{e3}/R_{e1}
Type-I	$\cot\beta$	$\cot\beta$	$\cot\beta$	0	0	0
Type-II	$\cot\beta$	$-\tan\beta$	$-\tan\beta$	0	$-\tan\gamma/\cos\beta$	$-\tan\gamma/\cos\beta$
Type-X	$\cot\beta$	$\cot\beta$	$-\tan\beta$	0	0	$-\tan\gamma/\cos\beta$
Type-Y	$\cot\beta$	$-\tan\beta$	$\cot\beta$	0	$-\tan\gamma/\cos\beta$	0
Type-Z	$\cot\beta$	$-\tan\beta$	$-\tan\beta$	0	$-\tan\gamma/\cos\beta$	$\cot\gamma/\cos\beta$

Table 2.2: Factors emerging in Eq. (2.16) for each type of Yukawa interaction. A similar table is seen in Ref. [30].

2.2 Models

We study extensions of the SM Higgs sector with three isospin doublet Higgs fields Φ_i (i = 1-3), where all the Higgs fields have non-zero VEVs. In general, each of these Higgs doublets would couple to all three types of fermions, i.e., up- and down-type quarks and charged leptons. However, this framework induces FCNCs at the tree level, as is well known in the general 2HDM without discrete Z_2 symmetries. The easiest way to suppress FCNCs is to take into account a Yukawa Lagrangian where each of the three Higgs doublets couples to at most one of the fermion types, and such a Lagrangian is introduced as follows:

$$-\mathcal{L}_Y = Y_u \bar{Q}_L (i\sigma_2)\Phi_u^* u_R + Y_d \bar{Q}_L \Phi_d d_R + Y_e \bar{L}_L \Phi_e e_R + \text{h.c.}, \tag{2.1}$$

where $\Phi_{u,d,e}$ are either Φ_1, Φ_2 or Φ_3.

We can naturally realise the above Lagrangian by enforcing two discrete symmetries Z_2 and $\tilde{Z}_2$ on the Higgs sector. In general, we can also present soft-breaking Z_2 and $\tilde{Z}_2$ terms in the Higgs potential without losing the key property of the absence of FCNCs at tree level. Depending on the charge assignment of the Z_2 and $\tilde{Z}_2$ symmetries, we can describe five independent types of Yukawa interactions[1] as listed in Tab. 2.1. Note that the Type-Z corresponds to the Yukawa interaction of the 3HDM studied in Ref. [59] which is entitled therein as the 'democratic 3HDM'.

The most general form of Higgs potential under the $SU(2)_L \times U(1)_Y \times Z_2 \times \tilde{Z}_2$ symmetry is

[1]We can also describe extra four types by interchanging $\Phi_1 \leftrightarrow \Phi_3$. However, these types are physically the same as the last four types defined in Tab. 2.1.

defined by

$$
\begin{aligned}
V(\Phi_1,\Phi_2,\Phi_3) = & \sum_{i=1}^{3}\mu_i^2\Phi_i^\dagger\Phi_i - (\mu_{12}^2\Phi_1^\dagger\Phi_2 + \mu_{13}^2\Phi_1^\dagger\Phi_3 + \mu_{23}^2\Phi_2^\dagger\Phi_3 + \text{h.c.}) \\
& + \frac{1}{2}\sum_{i=1}^{3}\lambda_i(\Phi_i^\dagger\Phi_i)^2 + \rho_1(\Phi_1^\dagger\Phi_1)(\Phi_2^\dagger\Phi_2) + \rho_2|\Phi_1^\dagger\Phi_2|^2 + \frac{1}{2}[\rho_3(\Phi_1^\dagger\Phi_2)^2 + \text{h.c.}] \\
& + \sigma_1(\Phi_1^\dagger\Phi_1)(\Phi_3^\dagger\Phi_3) + \sigma_2|\Phi_1^\dagger\Phi_3|^2 + \frac{1}{2}[\sigma_3(\Phi_1^\dagger\Phi_3)^2 + \text{h.c.}] \\
& + \kappa_1(\Phi_2^\dagger\Phi_2)(\Phi_3^\dagger\Phi_3) + \kappa_2|\Phi_2^\dagger\Phi_3|^2 + \frac{1}{2}[\kappa_3(\Phi_2^\dagger\Phi_3)^2 + \text{h.c.}],
\end{aligned} \tag{2.2}
$$

where the μ_{12}^2, μ_{13}^2 and μ_{23}^2 terms represent the soft-breaking terms for Z_2 and $\tilde{Z}_2$. In general, μ_{ij}^2, ρ_3, σ_3 and κ_3 are complex parameters but throughout the chapter we adopt them as real parameters for simplicity, therefore achieving avoidance of explicit CP-violation. There are the 18 free parameters in the 3HDM scalar potential. Two of them are fixed by the mass of the W boson and the mass of the discovered neutral Higgs boson. Theoretical constraints imposed on the 16 remaining parameters are stability of the vacuum, absence of charge breaking minima, compliance with unitarity of scattering processes etc. Such constraints are well-known in the 2HDM (e.g. see [63] for a recent study) and have also been investigated for the scalar potential in 3HDMs [34,36,64–66]. We do not impose these constraints in our phenomenological study because they only exclude specific regions of the parameter space of 16 variables, which might not contain the region what we are interested in for the phenomenological study concentrating on the charged Higgs sector. It will be seen below, the phenomenology in the charged Higgs sector depends on only 5 parameters (which we consider as unconstrained parameters), and we will assume that the freedom in the other 11 parameters can be used to obey the above theoretical bounds. To justify this approach we note that two parameters in the charged Higgs sector ($m_{H^\pm}$ and $\tan\beta$) are not constrained by the associated constraints on the scalar potential in 2HDMs due to the freedom in the remaining four parameters (for the case of a 2HDM scalar potential with a softly broken Z_2 symmetry).

The three Higgs doublet fields can be parametrised by

$$
\Phi_i = \begin{bmatrix} \omega_i^+ \\ \frac{1}{\sqrt{2}}(h_i + v_i + iz_i) \end{bmatrix}, \quad (i = 1, ...3), \tag{2.3}
$$

where the v_i's represent the VEVs of the Φ_i's with the sum rule $\sum_i v_i^2 \equiv v_{\rm SM}^2 = 1/(\sqrt{2}G_F) \simeq (246\ \text{GeV})^2$. It is convenient to introduce the so-called Higgs basis in 3HDMs, in which only one of the three doublets includes the VEV $v_{\rm SM}$ and the Nambu-Goldstone (NG) bosons.

This can be described by presenting the orthogonal 3×3 matrix R as

$$\begin{pmatrix} \Phi_1 \\ \Phi_2 \\ \Phi_3 \end{pmatrix} = R \begin{pmatrix} \Phi \\ \Psi_1 \\ \Psi_2 \end{pmatrix}. \tag{2.4}$$

The R matrix is indicated in terms of the three VEVs:

$$\begin{aligned} R &= \begin{pmatrix} \frac{v_1}{v} & -\frac{v_2 v_1}{v_{13} v} & -\frac{v_3}{v_{13}} \\ \frac{v_2}{v} & \frac{v_{13}}{v} & 0 \\ \frac{v_3}{v} & -\frac{v_2 v_3}{v_{13} v} & \frac{v_1}{v_{13}} \end{pmatrix} = \begin{pmatrix} \cos\gamma & 0 & -\sin\gamma \\ 0 & 1 & 0 \\ \sin\gamma & 0 & \cos\gamma \end{pmatrix} \begin{pmatrix} \cos\beta & -\sin\beta & 0 \\ \sin\beta & \cos\beta & 0 \\ 0 & 0 & 1 \end{pmatrix} \\ &= \begin{pmatrix} \cos\beta\cos\gamma & -\sin\beta\cos\gamma & -\sin\gamma \\ \sin\beta & \cos\beta & 0 \\ \cos\beta\sin\gamma & -\sin\beta\sin\gamma & \cos\gamma \end{pmatrix}, \end{aligned} \tag{2.5}$$

where we presented the two ratios of the VEVs in the following expressions

$$\tan\beta \equiv \frac{v_2}{v_{13}}, \quad \tan\gamma \equiv \frac{v_3}{v_1}, \quad \text{with} \quad v_{13} \equiv \sqrt{v_1^2 + v_3^2}. \tag{2.6}$$

Using this notation, each of the VEVs is defined by

$$v_1 = v_{13}\cos\gamma = v\cos\beta\cos\gamma, \quad v_2 = v\sin\beta, \quad v_3 = v_{13}\sin\gamma = v\cos\beta\sin\gamma. \tag{2.7}$$

We note that these definitions differ from those employed in Ref. [59]. In the Higgs basis, the three doublets Φ, Ψ_1 and Ψ_2 are defined by

$$\Phi = \begin{pmatrix} G^+ \\ \frac{v+\tilde{h}+iG^0}{\sqrt{2}} \end{pmatrix}, \quad \Psi_a = \begin{pmatrix} \tilde{H}_a^+ \\ \frac{\tilde{H}_a+i\tilde{A}_a}{\sqrt{2}} \end{pmatrix} \quad \text{with} \quad a = 1, 2, \tag{2.8}$$

where $G^\pm$ and G^0 are the NG bosons which are absorbed into the longitudinal components of W and Z, respectively. In Eq. (2.8), two singly-charged states $\tilde{H}_a^\pm$, two CP-odd states $\tilde{A}_a$ and three CP-even states $\tilde{h}$ and $\tilde{H}_a$ are not given in general the mass eigenstates. The mass eigenstates for the singly-charged ($H_1^\pm$ and $H_2^\pm$) and the CP-odd states (A_1 and A_2) are expressed by

$$\begin{pmatrix} \tilde{H}_1^\pm \\ \tilde{H}_2^\pm \end{pmatrix} = \begin{pmatrix} \cos\theta_C & -\sin\theta_C \\ \sin\theta_C & \cos\theta_C \end{pmatrix} \begin{pmatrix} H_1^\pm \\ H_2^\pm \end{pmatrix}, \quad \begin{pmatrix} \tilde{A}_1 \\ \tilde{A}_2 \end{pmatrix} = \begin{pmatrix} \cos\theta_A & -\sin\theta_A \\ \sin\theta_A & \cos\theta_A \end{pmatrix} \begin{pmatrix} A_1 \\ A_2 \end{pmatrix}, \tag{2.9}$$

where the mixing angles θ_C and θ_A are defined in terms of the mass matrix elements for the singly charged states ($\mathcal{M}_C^2$) and those for the CP-odd states ($\mathcal{M}_A^2$) in the Higgs basis (see Appendix A):

$$\tan 2\theta_C = \frac{2(\mathcal{M}_C^2)_{12}}{(\mathcal{M}_C^2)_{11} - (\mathcal{M}_C^2)_{22}}, \quad \tan 2\theta_A = \frac{2(\mathcal{M}_A^2)_{12}}{(\mathcal{M}_A^2)_{11} - (\mathcal{M}_A^2)_{22}}. \tag{2.10}$$

The squared mass eigenvalues for the singly-charged and CP-odd Higgs bosons are defined by

$$m^2_{H_1^\pm} = (\mathcal{M}_C^2)_{11}\cos^2\theta_C + (\mathcal{M}_C^2)_{22}\sin^2\theta_C + (\mathcal{M}_C^2)_{12}\sin 2\theta_C, \tag{2.11}$$

$$m^2_{H_2^\pm} = (\mathcal{M}_C^2)_{11}\sin^2\theta_C + (\mathcal{M}_C^2)_{22}\cos^2\theta_C - (\mathcal{M}_C^2)_{12}\sin 2\theta_C, \tag{2.12}$$

$$m^2_{A_1} = (\mathcal{M}_A^2)_{11}\cos^2\theta_A + (\mathcal{M}_A^2)_{22}\sin^2\theta_A + (\mathcal{M}_A^2)_{12}\sin 2\theta_A, \tag{2.13}$$

$$m^2_{A_2} = (\mathcal{M}_A^2)_{11}\sin^2\theta_A + (\mathcal{M}_A^2)_{22}\cos^2\theta_A - (\mathcal{M}_A^2)_{12}\sin 2\theta_A. \tag{2.14}$$

For the CP-even states, three physical states exist, so that we need to diagonalise the 3×3 mass matrix to attain the mass eigenvalues. The mass eigenstates are given by introducing the 3×3 orthogonal matrix R_H as

$$\begin{pmatrix} \tilde{h} \\ \tilde{H}_1 \\ \tilde{H}_2 \end{pmatrix} = R_H \begin{pmatrix} h \\ H_1 \\ H_2 \end{pmatrix}. \tag{2.15}$$

Amongst the three mass eigenstates, one of them must be specified as the discovered Higgs boson at the LHC with a mass of about 125 GeV, which in our case is the h state. The mass matrix for the CP-even states in the Higgs basis $(\tilde{h}, \tilde{H}_1, \tilde{H}_2)$ is also presented in Appendix A. The Yukawa interaction terms can be defined in the Higgs basis as

$$\begin{aligned} -\mathcal{L}_Y =& \sum_{f=u,d,e} \frac{m_{f^i}}{v}\bar{f}^i \left[\left(\tilde{h} + \frac{R_{f2}}{R_{f1}}\tilde{H}_1 + \frac{R_{f3}}{R_{f1}}\tilde{H}_2\right) - 2I_f\left(\frac{R_{f2}}{R_{f1}}\tilde{A}_1 + \frac{R_{f3}}{R_{f1}}\tilde{A}_2\right)\gamma_5\right] f^i \\ &+ \frac{\sqrt{2}}{v}\left[\bar{u}^j V_{ji} m_{d^i}\left(\frac{R_{d2}}{R_{d1}}\tilde{H}_1^+ + \frac{R_{d3}}{R_{d1}}\tilde{H}_2^+\right) P_R d^i - \bar{u}^i m_{u^i} V_{ij}\left(\frac{R_{u2}}{R_{u1}}\tilde{H}_1^+ + \frac{R_{u3}}{R_{u1}}\tilde{H}_2^+\right) P_L d^j\right] + \text{h.c.} \\ &+ \frac{\sqrt{2}}{v}\bar{\nu}^i m_{e^i}\left(\frac{R_{e2}}{R_{e1}}\tilde{H}_1^+ + \frac{R_{e3}}{R_{e1}}\tilde{H}_2^+\right) P_R e^i + \text{h.c.} \end{aligned} \tag{2.16}$$

where $I_f = +1/2\,(-1/2)$ for $f = u\,(d,e)$ and V_{ij} is the Cabibbo-Kobayashi-Maskawa (CKM) matrix element. The ratios of the matrix elements R_{f2}/R_{f1} and R_{f3}/R_{f1} $(f = u,d,e)$ are listed in Tab. 2.2 for each of the five types of Yukawa interactions. Herein, it is useful to display the agreement between the X_a, Y_a and Z_a couplings employed in Refs. [57–60] and the above couplings. When we determine these couplings by

$$-\mathcal{L}_Y = \frac{\sqrt{2}}{v}\sum_{a=1,2}\left(\bar{u}^j V_{ji} m_{d^i} X_a P_R d^i + \bar{u}^i m_{u^i} V_{ij} Y_a P_L d^j + \bar{\nu}^i m_{e^i} Z_a P_R e^i\right) H_a^+ + \text{h.c.}, \tag{2.17}$$

we obtain

$$X_1 = \frac{R_{d2}}{R_{d1}}c_C + \frac{R_{d3}}{R_{d1}}s_C,\ Y_1 = -\frac{R_{u2}}{R_{u1}}c_C - \frac{R_{u3}}{R_{u1}}s_C,\ Z_1 = \frac{R_{e2}}{R_{e1}}c_C + \frac{R_{e3}}{R_{e1}}s_C, \tag{2.18}$$

$$X_2 = -\frac{R_{d2}}{R_{d1}}s_C + \frac{R_{d3}}{R_{d1}}c_C,\ Y_2 = \frac{R_{u2}}{R_{u1}}s_C - \frac{R_{u3}}{R_{u1}}c_C,\ Z_2 = -\frac{R_{e2}}{R_{e1}}s_C + \frac{R_{e3}}{R_{e1}}c_C, \tag{2.19}$$

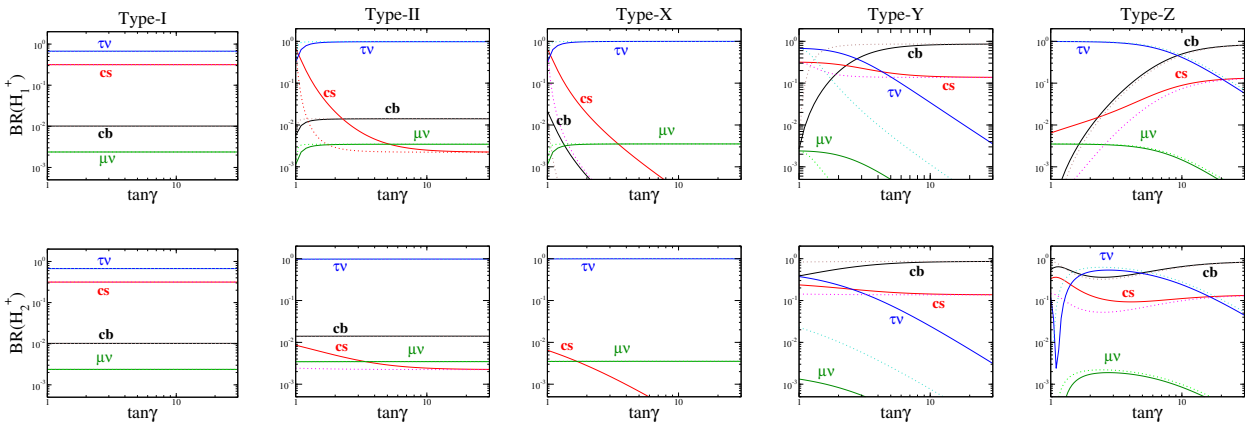

Figure 2.1: BRs of $H_1^\pm$ (upper panels) and $H_2^\pm$ (lower panels) as a function of $\tan\gamma$ in the Type-I, II, X, Y and Z 3HDM from the left to right panels. We set $m_{H_1^\pm} = 100$ GeV, $m_{H_2^\pm} = 150$ GeV and $\theta_C = -\pi/4$. The value of $\tan\beta$ is fixed to be 2 (5) for the solid (dotted) curves. A similar figure is seen in Ref. [30].

where $s_C = \sin\theta_C$ and $c_C = \cos\theta_C$. In this chapter, we particularly concentrate on the physics related to the charged Higgs bosons $H_1^\pm$ and $H_2^\pm$, for which the number of relevant (new physics) parameters are five, namely,

$$m_{H_1^\pm},\ m_{H_2^\pm},\ \tan\beta,\ \tan\gamma,\ \text{and}\ \theta_C. \tag{2.20}$$

A sixth parameter [59], which is a complex phase δ of the mass matrix $\mathcal{M}_C^2$, is fixed to be zero as we have already employed the CP-invariance of the Higgs sector.

We now display the BRs of $H_1^\pm$ and $H_2^\pm$ in the Type-I, Type-II, Type-X, Type-Y and Type-Z 3HDMs. For simplicity, we set all the masses of additional neutral Higgs bosons ($H_{1,2}$ and $A_{1,2}$) to be larger than those of the charged Higgs bosons and adopt the alignment limit $R_H \to I_{3\times3}$, where the CP-even states in the Higgs basis $\tilde{h}$ and $\tilde{H}_{1,2}$ correspond to the mass eigenstates. In this case, the decays of the charged Higgs bosons such as $H_a^\pm \to W^{(*)\pm} A_a/H_a/h$ ($a = 1, 2$) do not emerge nor do the $H_2^\pm \to H_1^\pm H_a/h$ ($a = 1, 2$) ones either[2]. Therefore, only the charged Higgs boson decays into fermion pairs need to be considered. The leading order formulae for the partial widths of $H_1^\pm$

[2]There is no $H_1^\pm H_2^\mp Z$ vertex at tree level because both charged Higgs bosons arise from Higgs fields with similar $SU(2)_L \times U(1)_Y$ charge. Hence, there is no $H_2^\pm \to H_1^\pm Z^{(*)}$ decay at the tree level either. We also recall that $H_1^\pm H_2^\mp \gamma$ vertex does not exist in any models with singly charged Higgs bosons at any order of perturbation theory because of a Ward identity.

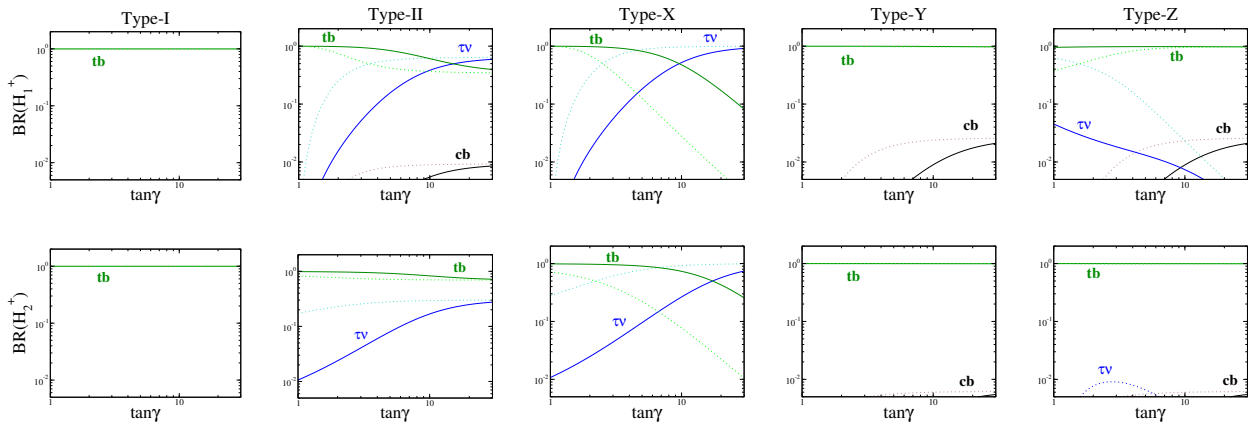

Figure 2.2: BRs of $H_1^\pm$ (upper panels) and $H_2^\pm$ (lower panels) as a function of $\tan\gamma$ in the Type-I, II, X, Y and Z 3HDM from the left to right panels. We set $m_{H_1^\pm} = 200$ GeV, $m_{H_2^\pm} = 250$ GeV and $\theta_C = -\pi/4$. The value of $\tan\beta$ is fixed to be 2 (5) for the solid (dotted) curves. A similar figure is seen in Ref. [30].

and $H_2^\pm$ decaying to fermions are defined by:

$$\Gamma(H_a^\pm \to \ell^\pm \nu) = \frac{G_F m_{H_a^\pm}}{4\pi\sqrt{2}} m_\ell^2 Z_a^2 \left(1 - \frac{m_\ell^2}{m_{H_a^\pm}^2}\right)^2, \tag{2.21}$$

$$\Gamma(H_a^\pm \to ud) = \frac{3G_F|V_{ud}|^2 m_{H_a^\pm}}{4\pi\sqrt{2}} \times \left[(\bar{m}_d^2 X_a^2 + \bar{m}_u^2 Y_a^2)(1 - x_u^a - x_d^a) - 4\bar{m}_u\bar{m}_d\sqrt{x_u^a x_d^a} X_a Y_a\right] \lambda^{1/2}(x_u, x_d), \tag{2.22}$$

where $\bar{m}_u$ and $\bar{m}_d$ are the running quark masses assessed at the scale of the mass of the charged Higgs bosons. When calculating the running masses we take the scale to be 100 GeV, since using the actual charged Higgs boson masses only causes small numerical distinctions from the values obtained when fixing the scale to be 100 GeV. The parameters $m_u^{\rm pole}$ and $m_d^{\rm pole}$ are the pole masses of quarks, and $x_u^a = (m_u^{\rm pole})^2/m_{H_a^\pm}^2$ and $x_d^a = (m_d^{\rm pole})^2/m_{H_a^\pm}^2$. The values of all these quark masses are provided in Appendix B. In the above formula, λ stands for the two body phase space function defined by $\lambda(x,y) = 1 + x^2 + y^2 - 2x - 2y - 2xy$.

In Fig. 2.1 displays the BRs of $H_1^\pm$ (upper panels) and $H_2^\pm$ (lower panels) as a function of $\tan\gamma$. In these plots, we set $m_{H_1^\pm} = 100$ GeV, $m_{H_2^\pm} = 150$ GeV and $\theta_C = -\pi/4$. The solid and dotted curves display the case for $\tan\beta = 2$ and 5, respectively. It can be seen that, in the Type-I, Type-II and Type-X 3HDM, the decays of the charged Higgs bosons into $\tau\nu$ pairs are dominant. Conversely, in the Type-Y and Type-Z 3HDM, the decay into cb can be dominant in the large $\tan\gamma$ region. As indicated in [57,58,60], the parameter space of a large BR of the cb channel corresponds to $|X_a| \gg |Y_a|, |Z_a|$ (see Eq. (2.21) and Eq. (2.22)) and we have indicated that this condition can only be achieved in the Type-Y and Type-Z 3HDM.

We exhibit similar plots in Fig. 2.2, but we here set $m_{H_1^\pm} = 200$ GeV, $m_{H_2^\pm} = 250$ GeV and $\theta_C = -\pi/4$. Apart from the Type-X 3HDM, the decay of the charged Higgs bosons into tb is dominant in wide regions of the parameter space. In the Type-Y and Type-Z 3HDM, the BR of the cb mode can reach at the few percent level in the large $\tan\gamma$ region.

From these results, we see that the charged Higgs boson decay into cb can be significant in the Type-Y and Type-Z 3HDMs, particularly when the charged Higgs boson masses are less than the top mass. We would finally like to emphasise that the $H^\pm_{1,2} \to cb$ decay can be a helpful tool to disentangle 3HDMs from 2HDMs due to the following reason. In practice, in the 2HDM with a softly-broken Z_2 symmetry, the $H^\pm \to cb$ decay can be dominant in the case $m_{H^\pm} < m_t - m_b$ and $\tan\beta \gtrsim 3$ for the Type-Y case [58, 67]. However, such a light charged Higgs boson is ruled out by the $B \to X_s\gamma$ data. In our model, the bound from $B \to X_s\gamma$ is instead avoidable using a cancellation between the contributions from the loops including $H_1^\pm$ and $H_2^\pm$ as we will explain in the succeeding section.

2.3 Bounds from $B \to X_s\gamma$ and direct searches

In this section, we first investigate the bounds on the parameter space of the five types of 3HDMs from measurements of $B \to X_s\gamma$. Then we proceed to discuss bounds from direct searches for $H_1^\pm$ and $H_2^\pm$ at colliders.

2.3.1 Limits from the flavour sector

We compute the branching fraction of the radiative $B \to X_s\gamma$ decay process at NLO in QCD. In our model, besides the $W^\pm$ boson loop contribution, $H_1^\pm$ and $H_2^\pm$ also participate in this process at the same perturbative level. The decay rate of $B \to X_s\gamma$ can be defined as a sum of the following three parts: i) the b quark decay process $b \to s\gamma$ ($\Gamma_{b\to s\gamma}$); ii) the gluon bremsstrahlung process $b \to s\gamma g$ ($\Gamma_{b\to s\gamma g}$); iii) non-perturbative effects due to the mesonic processes ($\Gamma_{\text{non-pert.}}$). Hence,

$$\Gamma(B \to X_s\gamma) = \Gamma_{b\to s\gamma} + \Gamma_{b\to s\gamma g} + \Gamma_{\text{non-pert.}}. \tag{2.23}$$

The first and the second contribution depend on the new physics parameters, for example, the charged Higgs boson masses and their couplings to quarks, whereas the third contribution does not. The decay rates $\Gamma_{b\to s\gamma}$ and $\Gamma_{b\to s\gamma g}$ are computed employing the Wilson coefficients at a scale μ [68]:

$$C_i^{\text{eff}}(\mu, m_{H_1^\pm}, m_{H_2^\pm}) = C_{i,\text{SM}}^{\text{eff}}(\mu) + \sum_{a=1,2}\left[(X_aY_a^*)C_{i,XY}^{\text{eff}}(\mu, m_{H_a^\pm}) + |Y_a|^2 C_{i,YY}^{\text{eff}}(\mu, m_{H_a^\pm})\right], \tag{2.24}$$

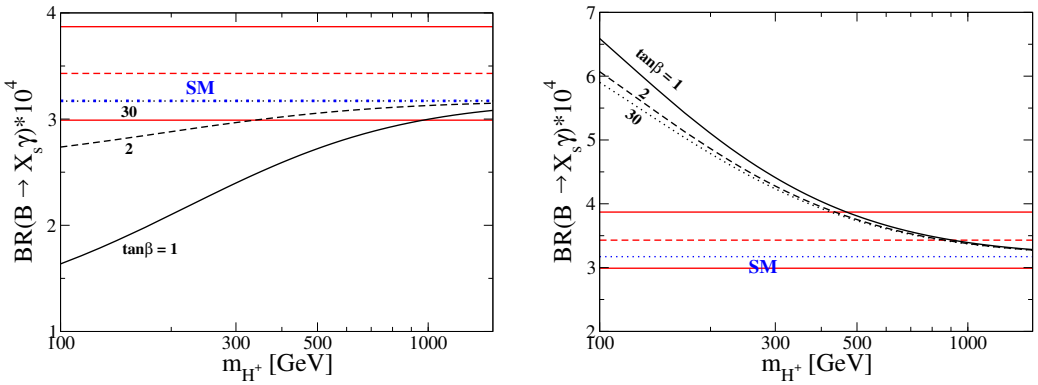

Figure 2.3: Predictions for the BR of the $B \to X_s\gamma$ process in the Type-I (left) and Type-II 2HDM (right) as a function of $m_{H^\pm}$. We set $\tan\beta = 1$ (solid), 2 (dashed) and 30 (dotted). The red solid (dashed) lines represent the 2σ allowed region (central value) of the experimental result. The blue dotted line represents the SM prediction. A similar figure is seen in Ref. [30].

where $i = 1, \ldots 8$ while X_a and Y_a $(a = 1, 2)$ are defined in Eqs. (2.18) and (2.19). Note that one can obtain the results of the 2HDMs by setting the limit of $\theta_C \to 0$ or $m_{H_2^\pm} \to m_{H_1^\pm}$. The latter holds due to the sum rule:

$$\sum_{a=1,2} X_a Y_a = X_1 Y_1\Big|_{\theta_C=0}, \quad \sum_{a=1,2} |Y_a|^2 = |Y_1|^2\Big|_{\theta_C=0}. \tag{2.25}$$

The structure of the quark Yukawa couplings is identical in Type-II, Type-Y and Type-Z 3HDMs and so the same constraint from $B \to X_s\gamma$ applies equally to these three models. Similarly, the constraint from $B \to X_s\gamma$ applies equally to the Type-I and Type-X 3HDMs. To get $\Gamma_{b\to s\gamma}$ and $\Gamma_{b\to s\gamma g}$, we fix the scale μ emerging in Eq. (2.24) to be the bottom quark mass scale μ_b. All the Wilson coefficients that are calculated at the corresponding scale $\mu = \mu_W$ have to be evaluated at μ_b by solving the renormalisation group equations. In Ref. [53], all the relevant Wilson coefficients at $\mu = \mu_b$ at LO and NLO are introduced in terms of those at $\mu = \mu_W$ and we use them for our numerical evaluations. Using the decay rate and BR of the semi-leptonic decay of the B meson, we can show the BR of the $B \to X_s\gamma$ process as

$$\mathrm{BR}(B \to X_s\gamma) = \frac{\Gamma(B \to X_s\gamma)}{\Gamma(B \to X_c\ell\nu)}\mathrm{BR}(B \to X_c\ell\nu). \tag{2.26}$$

The measured value of the BR is defined [69] as

$$\mathrm{BR}(B \to X_s\gamma) = (3.43 \pm 0.22) \times 10^{-4}. \tag{2.27}$$

All the SM input parameters for the numerical calculations are provided in Appendix B, and we set $\mu_b = m_b^{\rm pole}$ and $\mu_W = m_{W^\pm}$.

In order to compare the predictions in 2HDMs with those in 3HDMs, we first display the

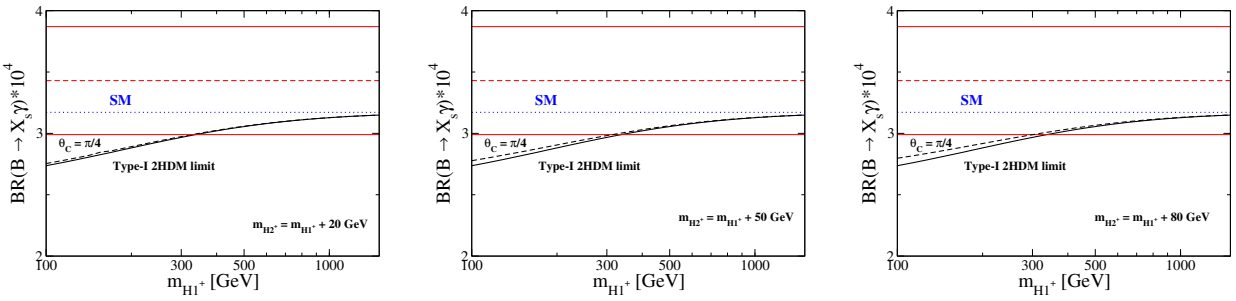

Figure 2.4: Prediction of the BR of $B \to X_s\gamma$ in the Type-I 3HDM (black dashed curve) in the case of $\tan\beta = 2$ and $\theta_C = \pi/4$ as a function of $m_{H_1^\pm}$. As a comparison, we also display the results in the Type-I 2HDM with $\tan\beta = 2$ as the black solid curve. The left, centre and right panels represent the case for $m_{H_2^\pm} - m_{H_1^\pm} = 20$, 50 and 80 GeV, respectively. The same results are produced in the Type-X 3HDM. A similar figure is seen in Ref. [30].

results in the former case where there is only one pair of charged Higgs bosons $H^\pm$. Fig. 2.3 displays the prediction of the BR of $B \to X_s\gamma$ in the Type-I (left) and Type-II (right) 2HDM as a function of the mass of the charged Higgs boson $m_{H^\pm}$. The blue dotted line represents the SM prediction. Horizontal red solid lines represent the 2σ bounds from the experimental data. The black curves represent the results in 2HDMs with several fixed values of $\tan\beta$. It can be seen that the $H^\pm$ contribution interferes destructively (constructively) with the SM contribution in the Type-I (Type-II) 2HDM. Furthermore, in Type-I, when we choose a large $\tan\beta$ value, the $H^\pm$ contribution gets quite small because all the $H^\pm$ couplings to quarks are proportional to $\cot\beta$. Conversely, in the Type-II case, even if we choose a large $\tan\beta$ value, the $H^\pm$ loop effect does not disappear. This can be realised by noting that the coupling product $X_1 Y_1^*$ with $\theta_C \to 0$ arising in the Wilson coefficient is equal to unity in the Type-II 2HDM. Therefore, in Type-I, a strict lower limit on $m_{H^\pm}$ is only achieved for small values of $\tan\beta$, with the bound being around $m_{H^\pm} > 1$ TeV with $\tan\beta = 1$. In Type-II, when $\tan\beta \gtrsim 2$, we attain $m_{H^\pm} \gtrsim 450$ GeV independently of $\tan\beta$[3].

Next, we present the numerical results of $\mathrm{BR}(B \to X_s\gamma)$ in 3HDMs. In Fig. 2.4, the black dashed curve represents the $m_{H_1^\pm}$ dependence of $\mathrm{BR}(B \to X_s\gamma)$ in the Type-I 3HDM. The prediction in the Type-I 2HDM is also displayed as the solid curve for comparison. In these plots, we set $\tan\beta = 2$ and $\theta_C = \pi/4$. The mass difference $m_{H_2^\pm} - m_{H_1^\pm}$ is fixed to be 20 (left panel), 50 (centre panel) and 80 GeV (right panel). It can be seen that the difference between the prediction in the Type-I 3HDM and the Type-I 2HDM gets slightly bigger as the mass difference $m_{H_2^\pm} - m_{H_1^\pm}$ grows, but, even when $m_{H_2^\pm} - m_{H_1^\pm} = 80$ GeV, these two results are nearly the same. Note that $\tan\gamma$ does not have impact on $\mathrm{BR}(B \to X_s\gamma)$ in the Type-I 3HDM, because $\tan\gamma$ is not participating in the quark Yukawa couplings as displayed in Tab. 2.2. Moreover, We note that the prediction in the

[3]In Ref. [56], the calculation at NNLO in QCD has been studied in the Type-II 2HDM and the slightly more severe limit $m_{H^\pm} \gtrsim 480$ GeV has been obtained at 95% CL.

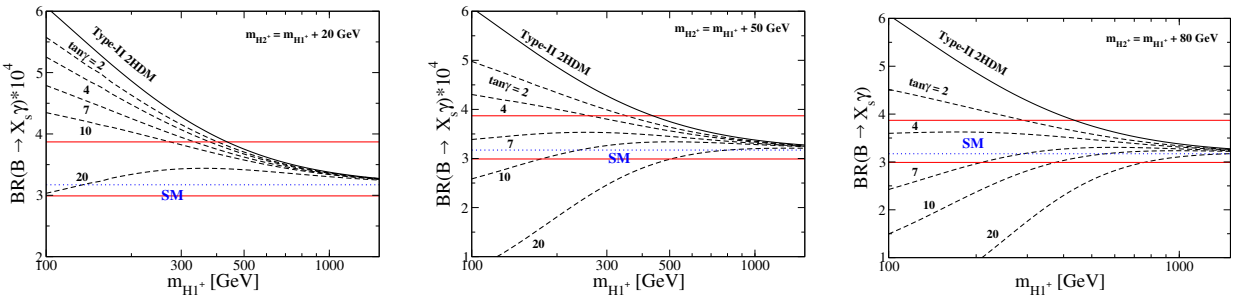

Figure 2.5: Prediction of the BR of $B \to X_s\gamma$ in the Type-II 3HDM with several values of $\tan\gamma$. We set $\tan\beta = 2$ and $\theta_C = -\pi/4$. As a comparison, we also display the results in the Type-II 2HDM with $\tan\beta = 2$ as the black solid curve. The left, centre and right panels represent the case for $m_{H_2^\pm} - m_{H_1^\pm} = 20$, 50 and 80 GeV, respectively. The same results are produced in the Type-Y and Type-Z 3HDM. A similar figure is seen in Ref. [30].

Type-I 3HDM does not depend on the sign of θ_C.

In Fig. 2.5, black dashed curves represent the $m_{H_1^\pm}$ dependence of $\mathrm{BR}(B \to X_s\gamma)$ in the Type-II 3HDM for several fixed values of $\tan\gamma$. The prediction in the Type-II 2HDM is also displayed as the solid curve for comparison. In these plots, we set $\tan\beta = 2$ and $\theta_C = -\pi/4$. The mass difference $m_{H_2^\pm} - m_{H_1^\pm}$ is fixed to be 20, 50 and 80 GeV in the left, centre and right panel, respectively. It is clear that the prediction in the 3HDM becomes smaller when we adopt a larger value of $\tan\gamma$. This tendency becomes more clear with larger mass differences. Therefore, we can find that cases where both charged Higgs boson masses of $\mathcal{O}(100)$ GeV are permitted by setting appropriate values for $\tan\gamma$ and their mass difference.

We here discuss the bound on the parameter space from the other observables in flavour physics according to Ref. [59]. Note that the bounds studied in Ref. [59] are based on a 3HDM with $H_2^\pm$ decoupled, so that we cannot simply use them to our case. In the succeeding, we use these bounds to obtain the limit on each of the couplings for $H_1^\pm$ and $H_2^\pm$, which means that we do not consider the interference effect of the two charged Higgs boson contributions.

From R_b measured from the $Z \to b\bar{b}$ decay, we get

$$|Y_a| \leq 0.72 + 0.24 \left(\frac{m_{H_1^\pm}}{100\ \mathrm{GeV}} \right) \quad \text{at } 95\%\ \mathrm{CL}, \tag{2.28}$$

under $|X_a| < 50$ $(a = 1, 2)$. This can be easily prevented by fixing $\tan\beta \gtrsim 1$ for $m_{H_1^\pm} = 100$ GeV. The constraint on the charged lepton coupling Z_1 is achieved from the leptonic τ decay as

$$Z_a \leq 40 \left(\frac{m_{H_1^\pm}}{100\ \mathrm{GeV}} \right) \quad \text{at } 95\%\ \mathrm{CL}. \tag{2.29}$$

This corresponds to the constraint on $\tan\gamma \lesssim 32(15)$ for $\tan\beta = 2(5)$ with $m_{H_1^\pm} = 100$ GeV and

$\theta_C = -\pi/4$ in the Type-II and Type-X 3HDMs. For the other types, this does not fix an upper limit on $\tan\gamma$ unless we adopt $\tan\beta \gg 1$ and/or $m_{H_1^\pm} \ll 100$ GeV. Finally, from the measurement of $B \to \tau\nu$, we attain

$$|X_a Z_a| \leq 1080 \left(\frac{m_{H_1^\pm}}{100 \text{ GeV}} \right)^2 \quad \text{at } 95\% \text{ CL.} \tag{2.30}$$

This yields a significant bound on the parameters only in the Type-II 3HDM, because both X_1 and Z_1 are increased by enhancing $\tan\beta$ and $\tan\gamma$. For example, $\tan\gamma \gtrsim 22(11)$ is ruled out in the case of $\tan\beta = 2(5)$, $m_{H_1^\pm} = 100$ GeV and $\theta_C = -\pi/4$. We checked that the numerical analysis presented in the following sections satisfies all these above bounds.

2.3.2 Limits from colliders

As investigated in the previous subsection, in 3HDMs, we can set the charged Higgs boson masses to be $\mathcal{O}(100)$ GeV without conflict with the $B \to X_s\gamma$ data. In this subsection, we consider this hypothesis at the LHC as a characteristic manifestation of a 3HDM, especially for the Type-Y and Type-Z cases, because the specific decay of the charged Higgs bosons $H_{1,2}^\pm \to cb$ can be dominant.

When we discuss the case for $m_{H_{1,2}^\pm} < m_t - m_b$, we need to consider the bounds from direct searches for $H^\pm$ states from the top quark decay $t \to H^\pm b$ at the LHC. In Ref. [70], ATLAS perform a search for the decay $H^\pm \to \tau\nu$ employing the data taken with 8 TeV of collision energy and 19.5 fb^{-1} of integrated luminosity. From the non-observation of an excess above the SM prediction, the 95% CL lower limit on $\text{BR}(t \to H^\pm b) \times \text{BR}(H^\pm \to \tau^\pm\nu)$ has been assigned to be between 0.23% and 1.3% in the range 80 GeV $< m_{H^\pm} <$ 160 GeV. Similar constraints are obtained from the CMS search in [71]. CMS has also performed the search for $H^\pm$ with decay into cs in [72] by employing 8 TeV data and 19.7 fb^{-1} of integrated luminosity. The 95% CL lower limit on $\text{BR}(t \to H^\pm b) \times \text{BR}(H^\pm \to cs)$ has been assigned to be between 1.2% and 6.5% in the range 90 GeV $< m_{H^\pm} <$ 160 GeV. Similar bounds are derived in the ATLAS search for $H^\pm \to cs$ in [73]. Note that a local excess of 2.4σ about $m_{H^\pm} = 150$ GeV exists in the CMS search in [72], with a best-fit branching fraction of $t \to H^\pm b = 1.2 \pm 0.2\%$, assuming $\text{BR}(H^\pm \to cs) = 100\%$.

In order to evaluate the limit from these LHC direct searches in our 3HDMs, the following conditions are required as the strongest limit of which meaning is defined below:

$$\sum_{a=1,2} \text{BR}(t \to H_a^\pm b) \times \text{BR}(H_a^\pm \to \tau^\pm\nu) < 0.23\%, \tag{2.31}$$

$$\sum_{a=1,2} \text{BR}(t \to H_a^\pm b) \times [\text{BR}(H_a^\pm \to cs) + \text{BR}(H_a^\pm \to cb)] < 1.2\%, \tag{2.32}$$

where one can apply these bounds to the case of 90 GeV $< m_{H_{1,2}^\pm} <$ 160 GeV. Concerning the second equation, we include the cb mode because no flavour tagging was used in Ref. [72], see

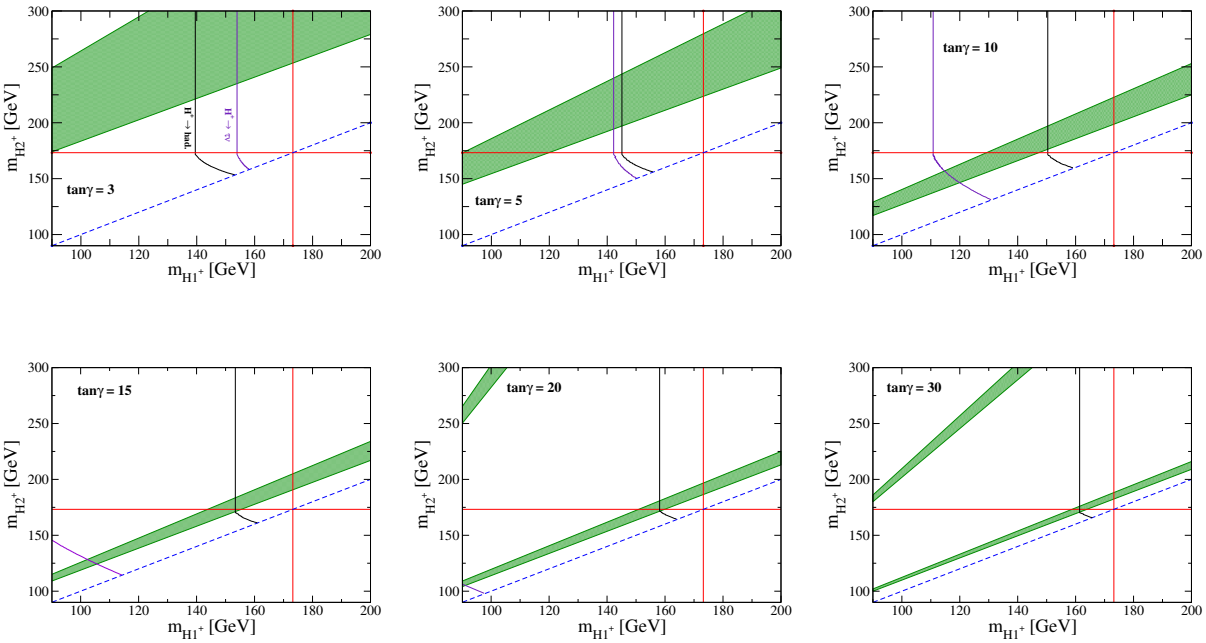

Figure 2.6: Green shaded regions show the 2σ allowed region by the $B \to X_s\gamma$ data in the Type-Y 3HDM with $\tan\beta = 2$ and $\theta_C = -\pi/4$. The value of $\tan\gamma$ is fixed to be 3, 5, 10, 15, 20 and 30 from the upper left to lower right panel. The right region from the black and purple curve is allowed by the constraint from the $t \to H^\pm_{1,2} b \to q\bar{q}'b$ (cs and cb) and $t \to H^\pm_{1,2} b \to \tau\nu b$ processes at the LHC. The BR of $H^\pm_1 \to cb$ is around 43%, 68%, 82%, 84%, 85% and 86% for the case with $\tan\gamma = 3$, 5, 10, 15, 20 and 30, respectively, and $m_{H^\pm_1} < m_t$. A similar figure is seen in Ref. [30].

also [60, 74]. Note that one should not sum the two charged Higgs boson contributions if the mass difference between $H^\pm_1$ and $H^\pm_2$ is set to be larger than the detector resolution. If we do not sum these two contributions, then we should obtain a milder constraint than that derived in Eqs. (2.31) and (2.32). Hence, the meaning of "strongest bound" is taking the strongest limit on the product of two branching fractions (the top decay and the charged Higgs boson decay) in the given mass range and summing two charged Higgs boson contributions.

Fig. 2.6 displays the allowed parameter space on the $m_{H^\pm_1}$-$m_{H^\pm_2}$ plane in the Type-Y 3HDM in the case of $\tan\beta = 2$ and $\theta_C = -\pi/4$. The green shaded region is allowed from $B \to X_s\gamma$ data and the right region from the purple and the black curve fulfils the requirement defined in Eqs. (2.31) and (2.32), respectively. The value of $\tan\gamma$ is set to be 3, 5, 10, 15, 20 and 30 as shown in each panel of the figure. Note that the region below the dashed curve, $m_{H^\pm_1} > m_{H^\pm_2}$, is ruled out by definition. It is seen that the bound from $H^\pm_{1,2} \to q\bar{q}'$ gets stronger as compared to that from $H^\pm_{1,2} \to \tau\nu$ when we adopt a larger value of $\tan\gamma$, because of the enhancement of $\mathrm{BR}(H^\pm_{1,2} \to cb/cs)$, as we already recognised in Fig. 2.1. Therefore, the case with $m_{H^\pm_1} < m_t - m_b$ and $m_{H^\pm_2} < m_t - m_b$ is extremely restricted from $B \to X_s\gamma$ and the direct search at the LHC. However, we can obtain allowed regions with $m_{H^\pm_1} < m_t - m_b$ and $m_{H^\pm_2} > m_t - m_b$ and also those with $m_{H^\pm_1} > m_t - m_b$ and $m_{H^\pm_2} > m_t - m_b$. The former case induces a very interesting phenomenological result, because

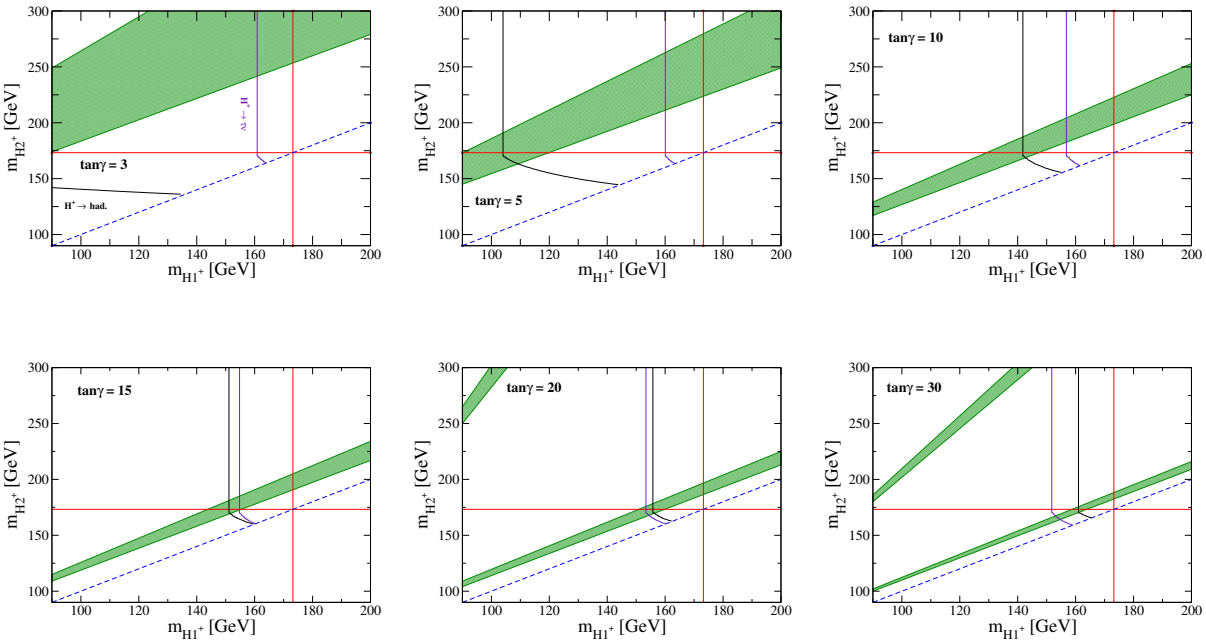

Figure 2.7: Same as Fig. 2.6, but for the case of Type-Z 3HDM. The BR of $H_1^\pm \to cb$ is around 4%, 16%, 50%, 67%, 75% and 81% for the case with $\tan\gamma = 3$, 5, 10, 15, 20 and 30, respectively, and $m_{H_1^\pm} < m_t$. A similar figure is seen in Ref. [30].

the lighter charged Higgs boson $H_1^\pm$ can essentially decay into the cb final state. The BR of the $H_1^\pm \to cb$ mode is displayed in the caption of Fig. 2.6, and is mainly established only by the value of $\tan\gamma$ for a fixed value of $\tan\beta$ and θ_C when $m_{H_1^\pm} < m_t$.

In Fig. 2.7, we also display a similar plot for the Type-Z 3HDM, where the bound from $B \to X_s\gamma$ is precisely the same as that in the Type-Y 3HDM because of the same form of the quark Yukawa couplings. The difference can be noticed in the relative strength of the bound from Eqs. (2.31) and (2.32) as compared to the Type-Y case. Similarly to the Type-Y case, the hypothesis with both charged Higgs boson masses smaller than $m_t - m_b$ is extremely restricted by $B \to X_s\gamma$ and LHC direct searches, but at least one of the charged Higgs bosons can be lighter than the top quark. In analogy with Fig. 2.6, we give the value of the BR of $H_1^\pm \to cb$ in the caption of this figure.

It is especially interesting to study the case with a charged Higgs boson mass between 80 GeV and 90 GeV, and $H^\pm$ decaying dominantly to cs/cb. In this case, the limit from direct searches at the LHC cannot be applied to rule out any parameter space since there is no sensitivity in this mass region. The reason is that the background from $t \to W^\pm b$ is overpowering in this region and the invariant mass cut on the jets originating from $H^\pm$ would lose its effect of exceedingly suppressing the background when $m_{H^\pm}$ is close to m_W. However, searches for $H^\pm$ from LEP2 and the Tevatron are some sensitive to this region of charged Higgs boson mass between 80 GeV and 90 GeV and we add these constraints in our analysis. In Ref. [75], the excluded region in the $m_{H^\pm}$-BR($H^\pm \to \tau\nu$) plane has been obtained by employing the combined LEP2 data from all four experiments. If we

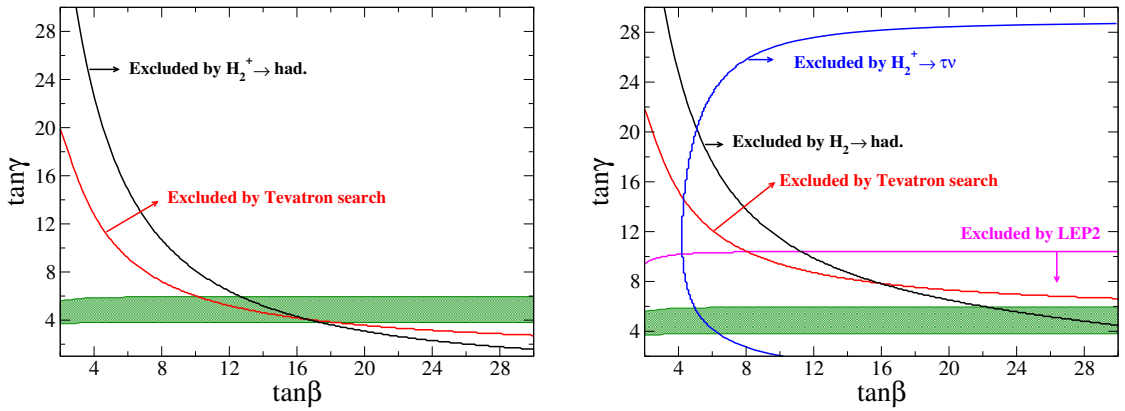

Figure 2.8: Allowed parameter space by several bounds on the $\tan\beta$-$\tan\gamma$ plane in the Type-Y (left) and Type-Z (right) 3HDM with $m_{H_1} = 83$ GeV, $m_{H_2^\pm} = 160$ GeV and $\theta_C = -\pi/4$. The right region from the blue, black and red curve is ruled out by Eq. (2.31), Eq. (2.32) and the Tevatron data, respectively. The region below the magenta curve is also ruled out by the LEP2 data. The green shaded region is allowed by the measurement of $B \to X_s\gamma$. A similar figure is seen in Ref. [30].

set $m_{H_1^\pm} = 83$ GeV, we can derive the bound $\mathrm{BR}(H_1^\pm \to \tau\nu) \lesssim 0.45$ at the 95% CL, with the exact bound depending on the choice of $m_{H_1^\pm}$ i.e. there is a substantial region of unexcluded parameter space where $\mathrm{BR}(H_1^\pm \to cs/cb)$ is substantial and $80\,\mathrm{GeV} < m_{H_1^\pm} < 90$ GeV. Note that the results of the LEP2 search in Ref. [75] display that there exist some regions of $\mathrm{BR}(H_1^\pm \to cs/cb)$ and $80\,\mathrm{GeV} < m_{H_1^\pm} < 90$ GeV where there exist fluctuations in excess of 2σ above the background. In Ref. [76], we can also derive the bound $\mathrm{BR}(t \to H^+b) \times \mathrm{BR}(H_1^\pm \to q\bar{q}') \lesssim 0.2$ at the 95% CL from the data gathered at the Tevatron with 1.0 fb^{-1}. The reason why this Tevatron search is sensitivite to charged Higgs masses between 80 GeV and 90 GeV is because no invariant mass cut is employed, and instead a disappearance search is performed. So far this search strategy has not been used by the LHC searches.

By enforcing these two bounds (from LEP2 and Tevatron) for $H_1^\pm$ and those from Eqs. (2.31) and (2.32) for $H_2^\pm$, we attain the excluded region on the $\tan\beta$-$\tan\gamma$ plane given in Fig. 2.8. In this figure, we set $m_{H_1^\pm} = 83$ GeV, $m_{H_2^\pm} = 160$ GeV and $\theta_C = -\pi/4$. The left and right panel display the case in the Type-Y and Type-Z 3HDM, respectively. The allowed green shaded region comes from the $B \to X_s\gamma$ data. As we can see, in the Type-Z 3HDM, region satisfying all the constraints mentioned above does not exist. Conversely, we can obtain allowed regions in the Type-Y case, namely, when $4 \lesssim \tan\gamma \lesssim 6$ and $\tan\beta <$ 10-18.

	$(m_{H_1^\pm}, m_{H_2^\pm}, \tan\gamma)$	$\mathrm{BR}(H_1^\pm \to X)_\mathrm{Y}$	$\mathrm{BR}(H_2^\pm \to X)_\mathrm{Y}$	$\mathrm{BR}(H_1^\pm \to X)_\mathrm{Z}$	$\mathrm{BR}(H_2^\pm \to X)_\mathrm{Z}$
BM1:	$(83, 160, 5)$	$cb : 68, cs : 17$	$cb : 77, cb : 16$	-	-
BM2:	$(160, 250, 3)$	$cb : 43, \tau\nu : 34$	$tb : 99.7, cb : 0.17$	$\tau\nu : 94, cb : 4.0$	$tb : 99.7, ts : 0.17$
BM3:	$(160, 225, 5)$	$cb : 68, cs : 17$	$tb : 99.6, cb : 0.21$	$\tau\nu : 80, cb : 16$	$tb : 99.4, cb : 0.21$
BM4:	$(160, 200, 10)$	$cb : 82, cs : 15$	$tb : 98, cb : 1.3$	$cb : 50, \tau\nu : 41$	$tb : 98, cb : 1.3$
BM5:	$(160, 180, 20)$	$cb : 85, cs : 14$	$tb : 67, cb : 28$	$cb : 75, \tau\nu : 13$	$tb : 66, cb : 27$
BM6:	$(200, 250, 10)$	$tb : 99.0, cb : 0.89$	$tb : 99.5, cb : 0.29$	$tb : 98, cb : 0.89$	$tb : 99.4, cb : 0.29$

Table 2.3: Predictions of the biggest two values of $\mathrm{BR}(H_{1,2}^\pm \to X)$ in the Type-Y and Type-Z 3HDM for the six benchmark points (BM1-BM6) which are allowed by $B \to X_s\gamma$ and direct searches at LEP2, Tevatron and LHC. We set $\tan\beta = 2$ and $\theta_C = -\pi/4$. The values of $m_{H_1^\pm}$ and $m_{H_2^\pm}$ are shown in GeV whereas those for the BRs are in %. For BM1, only the Type-Y is allowed, therefore we do not indicate the predictions in the Type-Z 3HDM. A similar table is seen in Ref. [30].

2.4 Phenomenology of 3HDM charged Higgs bosons at the LHC

The collider phenomenology of a charged Higgs boson can be categorised into two methods depending on its mass $m_{H^\pm}$: (i) $m_{H^\pm} < m_t - m_b$ (light) and (ii) $m_{H^\pm} > m_t - m_b$ (heavy). For case (i), charged Higgs bosons can be generated through the top quark decay, thus the main production process at the LHC is $gg, q\bar{q} \to t\bar{t} \to H^+ b\bar{t}$. For case (ii), the main production mode is the top quark associated process, i.e., $gb \to H^\pm t$ + c.c. As intimated, see Fig. 2.9, we will adopt the $gg \to t\bar{b}H^-$ + c.c. subprocess (at LO) in our Monte Carlo (MC) analysis, which captures both (i) (limited to the gg channel) and (ii) along with their interference, which is significant in the threshold region $m_{H^\pm} \approx m_t - m_b$ [77,78]. (Indeed, we will also be emulating the subleading contribution from $q\bar{q} \to t\bar{b}H^-$ + c.c. too.) Recall that, on the other hand, in the narrow width approximation of the top quark one has that $\sigma(gg, q\bar{q} \to t\bar{b}H^-) \equiv \sigma(gg, q\bar{q} \to t\bar{t}) \times \mathrm{BR}(\bar{t} \to \bar{b}H^-)$ (limited to the diagrams in which the H^- is emitted by the t antiquark) and, on the one hand, the b-quark in the initial state arises from a gluon splitting inside the proton, as clarified in [77,78].

In order to motivate phenomenological studies for the charged Higgs bosons at the LHC, we show six benchmark parameter sets, BM1–BM6, allowed by the $B \to X_s\gamma$ data and direct searches at LEP2, Tevatron and LHC in Tab. 2.3. Here, the biggest two values of BRs for $H_1^\pm$ and $H_2^\pm$ comes from the Type-Y and Type-Z 3HDM for each of the six benchmark points. In particular, we will use BM1, BM4 and BM6 in the Type-Y case for our next MC analysis, as illustrative of the three situations appeared so far: of a light, mixed and heavy charged Higgs mass spectrum, respectively, with respect to the top quark mass. Whereas we refer to the Type-Y 3HDM case in the rest of our study, we confirm that the subsequent phenomenology is not different in the Type-Z 3HDM case (except for BM1 which is not allowed herein).

For the MC study the following signal (S) and (irreducible) background (B) processes have

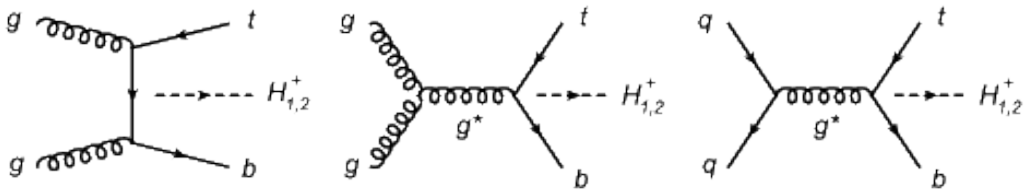

Figure 2.9: Topologies of the Feynman diagram for the $gg \to \bar{t}bH^+_{1,2}$ (left and middle) and $q\bar{q} \to \bar{t}bH^+_{1,2}$ (right) processes. The charged Higgs bosons can be emitted from the final state quark current at 3 (left) and 2 (middle and right) different points. For the topology on the left, gluon permutations are also needed. In total, there are 8(2) diagrams for the $gg(q\bar{q})$-induced process (at fixed q flavour). A similar figure is seen in Ref. [30].

been computed, respectively:

$$\text{a. } gg, q\bar{q} \to t\bar{b}H^-_{1,2} + \text{c.c} \to t\bar{b}jj + \text{c.c},$$
$$\text{b. } gg, q\bar{q} \to t\bar{b}W^- + \text{c.c.} \to t\bar{b}jj + \text{c.c.},$$

where the di-jet system jj is tagged via a single b-tag, as recommended in [60]. We recall the reader here that employing such a b-tag would enhance sensitivity to $H^\pm_{1,2} \to cb$ decays extremely, since the background from $W \to cb$ has a very small rate. This is made explicit by taking a b-tagging efficiency $\epsilon_b = 0.5$, a c-quark mistagging rate $\epsilon_c = 0.1$ and a light quark (u, d, s) mistagging rate $\epsilon_j = 0.01$. It succeeds that the estimate gain in sensitivity according to the case in which the di-jet system is untagged is then:

$$\frac{[S/\sqrt{B}]_{\text{btag}}}{[S/\sqrt{B}]_{\not{\text{b}}\text{tag}}} \sim \frac{\epsilon_b\sqrt{2}}{\sqrt{(\epsilon_j + \epsilon_c)}} \sim 2.13. \tag{2.33}$$

In Fig. 2.10, we display the di-jet mass distribution for S and B at 13 TeV based on cross section for BM1, BM4 and BM6. Even before imposing any selection cuts, it is clear the LHC potential in reaching these peculiar 3HDM signatures during Run 2. Two caveats should be borne in mind herein though. On the other hand, we have not permitted for full combinatorial effects in the di-jet mass reconstruction, as we have assumed that each of the three b-jets present in the final state can be accurately assigned to its parent heavy particle (i.e., t, $\bar{t}$ and $H^\pm_{1,2}$). On the one hand, BM1, BM4 and BM6 are the very best points for our aims, those with highest BR, whereas one actually ought to test the whole parameter space of 3HDMs sampled over the inputs θ_C, $\tan\beta$, $\tan\gamma$, $m_{H^\pm_1}$ and $m_{H^\pm_2}$.

Ultimately, we briefly explain the phenomenology of the extra neutral Higgs bosons $H_{1,2}$ and $A_{1,2}$ in the 3HDMs. When we take into account the case with the masses of $H^\pm_{1,2}$ to be $\mathcal{O}(100)$ GeV, the neutral Higgs bosons cannot be so heavy due to the limits from EW precision observables such as the S and T parameters [80] and from perturbative unitarity [66]. If we take into account

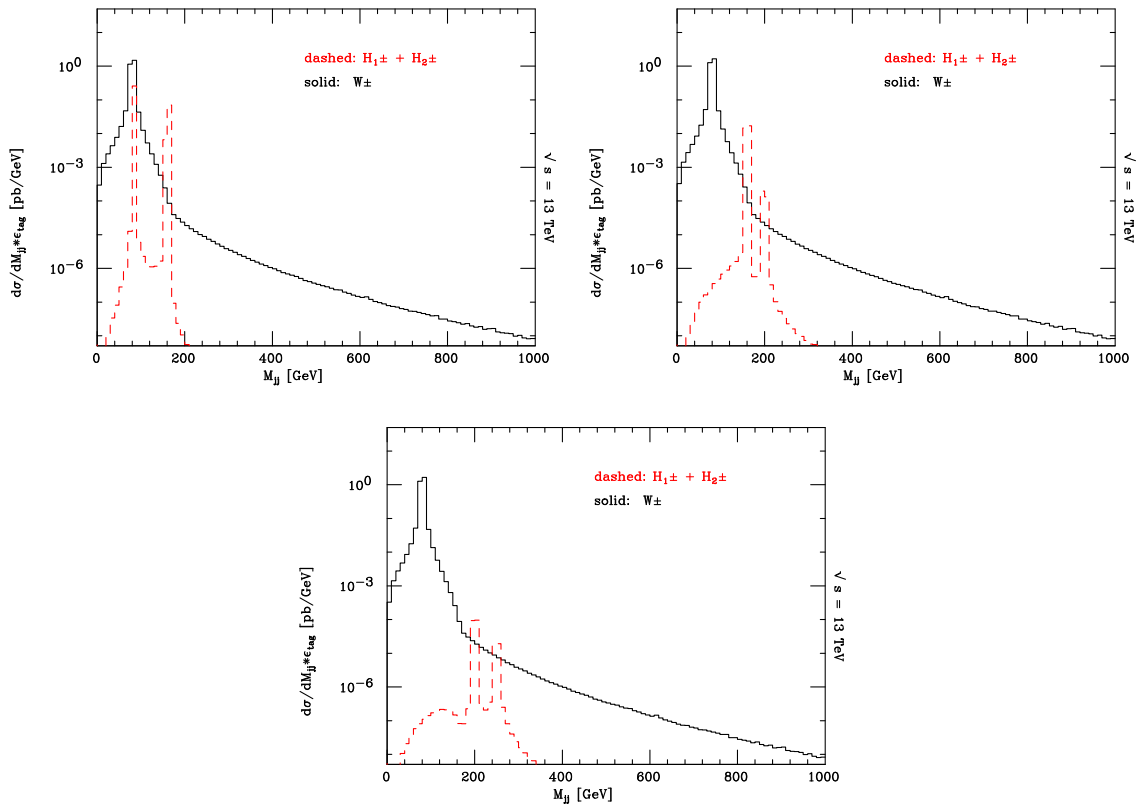

Figure 2.10: Differential distributions in the di-jet invariant mass of processes a (red dashed) and b (black solid) for the BM1 (top-left), BM4 (top-right) and BM6 (bottom) at the LHC with $\sqrt{s} = 13$ TeV. Tagging efficiencies are employed as explained in the text. CTEQ(4L) with $Q = \mu = \sqrt{\hat{s}}$ is adopted [79]. A similar figure is seen in Ref. [30].

the case where masses of these neutral Higgs bosons are larger than the charged Higgs bosons, then there are no extra decay modes of the charged Higgs bosons beyond those given in this chapter. However, in this situation, the decay channels $H_{1,2}/A_{1,2} \to H^{\pm}_{1,2} W^{(*)\mp}$ can be dominant depending on the mass difference between the neutral Higgs states and the charged Higgs states, and the numerical values of the X_a, Y_a and Z_a parameters given in Eqs. (2.17)-(2.19). These cascade decay channels would be extra production modes of $H^{\pm}_{1,2}$ beyond those discussed in this section, even though they would require a separate signal-background study in order to evaluate the detection prospects.

2.5 Conclusions

We have investigated the phenomenology of charged Higgs bosons in fully active 3HDMs with two softly-broken discrete Z_2 symmetries which are enforced to prevent FCNCs at tree level. Under these Z_2 symmetries, we have determined five types of Yukawa interactions. We have then displayed that the decay branching fractions of $H^{\pm}_{1,2} \to cb$ can be dominant in the Type-Y and Type-Z 3HDM

when the masses of the charged Higgs bosons are set to be below $m_t - m_b$. The $H^\pm \to cb$ decay can also be dominant in the Type-Y 2HDM when $m_{H^\pm} < m_t - m_b$, but such a light charged Higgs boson hypothesis is ruled out by the constraint from $B \to X_s\gamma$. Conversely, in 3HDMs, the scenario with masses of $\mathcal{O}(100)$ GeV for the charged Higgs bosons is allowed by $B \to X_s\gamma$ due to a cancellation between the individual contributions from the $H_1^\pm$ and $H_2^\pm$ loop diagrams. As a result, one can distinguish 3HDMs from 2HDMs through the search for a light charged Higgs boson decaying into cb.

We then have computed the branching fraction of the $B \to X_s\gamma$ process at NLO in QCD in 3HDMs in order to verify how the cancellation occurs numerically. We noticed that it occurs particularly in the Type-II, Type-Y and Type-Z 3HDMs when there is a non-zero mixing and a mass difference between $H_1^\pm$ and $H_2^\pm$. In the Type-I and Type-X 3HDMs, the numerical values of $\mathrm{BR}(B \to X_s\gamma)$ are not much different from the predictions in Type-I and Type-X 2HDMs.

We also have considered the bounds from direct searches at the LHC of charged Higgs bosons from the top quark decays $t \to H^\pm b \to \tau\nu b$ and $t \to H^\pm b \to q\bar{q}'b$ with the 8 TeV data. We have seen that, in the Type-Y and Type-Z 3HDM, the hypothesis with both $H_1^\pm$ and $H_2^\pm$ lighter than $m_t - m_b$ is extremely restricted from $B \to X_s\gamma$ and the LHC direct searches, whereas the scenario with only $H_1^\pm$ lighter than $m_t - m_b$ is allowed. However, the specific case $m_{H_1^\pm} \approx m_{W^\pm}$ with $m_{H_2^\pm} < m_t$ is allowed (also by Tevatron and LEP2), despite only in the Type-Y 3HDM. We remarked to the fact that the region of $80\,\mathrm{GeV} < m_{H_1^\pm} < 90$ GeV is not constrained by present LHC searches for $t \to H^\pm b$ followed by dominant decay $H^\pm \to cs/cb$, and this parameter space is only weakly restricted from LEP2 and Tevatron searches. Any future signal in this region could be easily accommodated by $H_1^\pm$ from a 3HDM.

Ultimately, upon running a MC simulation to compare the output of the $H_{1,2}^\pm$ signals and $W^\pm$ background via the production processes $gg, q\bar{q} \to t\bar{b}H_{1,2}^-$ + c.c and $gg, q\bar{q} \to t\bar{b}W^-$ + c.c, respectively, succeeded by the corresponding di-jet decays $H_{1,2}^\pm \to jj$ and $W^\pm \to jj$, we have displayed that the aforementioned charged Higgs boson signals should be reachable at Run 2 of the LHC over an appropriate region of the 3HDM parameter space, provided that b-tagging is imposed so as to single out the cb component above the cs one. As a result, these (multiple) charged Higgs boson signatures can be employed not only to discriminate between 2HDMs and 3HDMs but also to recognise the types realising the latter.

Chapter 3

Perturbative unitarity constraints in C2HDMs

3.1 Overview

Despite the obvious far-reaching consequences of a discovery of even a single additional scalar, the presence of another Higgs would not be, by itself, an evidence for the naturalness of the weak scale: such a defining situation would still be pending upon the whole subject. Just like for the case of a single Higgs doublet, for which the hierarchy problem can be explained by its PNGB nature, we would like to link the presence of extra Higgs particles to natural theories of the Fermi scale. In particular, we have in mind CHMs, where the mass of the lightest Higgs state is kept naturally lighter than a new strong scale around $\sim$ TeV by an approximate global symmetry [81], broken by SM interactions in the *partial compositeness* paradigm [82, 83].

In the minimal CHM [43, 44], the only light scalar in the spectrum is a PNGB, surrounded by spanned composite resonances roughly heavier by a loop factor. The underlying symmetries protect the Higgs mass from quantum corrections thus giving a simple solution to the hierarchy problem. The only robust way to expect new light (pseudo)scalars in the spectrum is to make them also PNGBs. Even in the case they are not expected to be as light as the SM Higgs, it is interesting to find a mechanism for describing all the Higgses as PNGBs and to explain their mass differences. Last, but not least for importance, in the case of extra Higgs doublets with no VEV nor couplings to quark and leptons, one could also have the possibility to describe neutral light states as possible composite DM candidates [84].

In this chapter, we aim at identifying among the lightest scalars at least two Higgs doublets as this would lead to a C2HDM [31,45]. To include them as PNGBs, one has basically two different and complementary approaches: (i) to write down an effective Lagrangian (e.g., *a la* Strongly Interacting Light Higgs (SILH) [85]) invariant under SM symmetries for light composite $SU(2)$ Higgses; (ii)

to explicitly impose a specific symmetry breaking structure containing multiple PNGBs. We take here the second approach. In particular, we will study in detail models based on the spontaneous global symmetry breaking of $SO(6) \to SO(4) \times SO(2)$ [45]. We will focus on their predictions for the structure of the (pseudo)scalar spectrum and the deviations of their couplings from those of a generic renormalisable E2HDM. In the $f \to \infty$ limit the PNGB states are in fact identified with the physical Higgs states of doublet scalar fields of the E2HDM[1]. Deviations from the E2HDM are parametrised by $\xi = v_{\rm SM}^2/f^2$, with $v_{\rm SM}$ the SM Higgs VEV.

Here we will focus on the unitarity properties of a C2HDM[2], namely, we will derive the bounds on the parameters of the model by requiring perturbative unitarity to hold at the energies reachable by the LHC [31]. In fact, contrarily to the E2HDM, which is renormalisable, the C2HDM is an effective theory. The PNGB nature of the Higgses leads to a modification of their couplings to matter with respect to the E2HDM case and, as a consequence, forces to a non-vanishing s-dependence of the scattering amplitudes. This means that the C2HDM is not unitary for energies above a critical value. Since the fermion content of the model is not playing a role in the present investigation, we will not specify the fermion representation and we will not calculate the Higgs potential generated by the radiative corrections. Instead, we will assume the same general form of the Higgs potential as in the E2HDM with a Z_2 symmetry, the latter imposed in order to avoid FCNCs at the tree level [48]. Therefore, in the energy region where the E2HDM and C2HDM are both unitary, it is interesting to compare the bounds on the additional Higgs masses. In fact, due to a compensation amongst mass- and energy-dependent contributions, we find that regions not allowed in the E2HDM are instead permitted in the C2HDM for the most general configuration of their parameter spaces.

3.2 The composite $SO(6)/SO(4) \times SO(2)$ model

3.2.1 Higgs bosons as PNGBs

We first consider how two isospin scalar doublets can be obtained from the spontaneous breakdown of the global symmetry, i.e., $SO(6) \to SO(4) \times SO(2)$. In order to explain this, we present the following fifteen $SO(6)$ generators:

$$
\begin{aligned}
&T^a_{L,R} = -\frac{i}{2}\left[\frac{1}{2}\epsilon^{abc}(\delta^b_i\delta^c_j - \delta^b_j\delta^c_i) \mp (\delta^a_i\delta^4_j - \delta^a_j\delta^4_i)\right], \\
&T_S = -\frac{i}{\sqrt{2}}(\delta^5_i\delta^6_j - \delta^5_j\delta^6_i), \\
&T^{\hat{a}}_1 = -\frac{i}{\sqrt{2}}(\delta^{\hat{a}}_i\delta^5_j - \delta^{\hat{a}}_j\delta^5_i), \quad T^{\hat{a}}_2 = -\frac{i}{\sqrt{2}}(\delta^{\hat{a}}_i\delta^6_j - \delta^{\hat{a}}_j\delta^6_i), \\
&\text{with} \quad (a,b,c = \text{1-3}), \quad (i,j = \text{1-6}), \quad (\hat{a} = \text{1-4}).
\end{aligned} \tag{3.1}
$$

[1] For an updated review of the theory and phenomenology of E2HDMs see [86].
[2] For the discussion of unitarity in minimal CHMs see [87].

The above generators are categorised into the seven unbroken generators $T^a_{L,R}$ and T_S and the eight broken generators $T^{\hat{a}}_1$ and $T^{\hat{a}}_2$. We can confirm that $T^a_{L,R}$ and T_S are the subalgebras which generate the $SO(4) \times SO(2)$ subgroup by looking at the following commutation relations:

$$[T^a_L, T^b_L] = i\epsilon^{abc}T^c_L, \quad [T^a_R, T^b_R] = i\epsilon^{abc}T^c_R, \quad [T^a_L, T^b_R] = [T^a_L, T_S] = [T^a_R, T_S] = 0, \tag{3.2}$$

$$[T^a_L, T_{\Phi_\alpha}] = -\frac{1}{2}\sigma^a T_{\Phi_\alpha}, \quad [T^3_R, T_{\Phi_\alpha}] = -\frac{1}{2}T_{\Phi_\alpha}, \tag{3.3}$$

where

$$T_{\Phi_\alpha} = \begin{pmatrix} T^2_\alpha + iT^1_\alpha \\ T^4_\alpha - iT^3_\alpha \end{pmatrix}, \quad \alpha = 1, 2. \tag{3.4}$$

Eq. (3.2) tells us that the commutation relations among $T^a_{L,R}$ and T_S are closed plus that T^a_L (T^a_R) generates the $SU(2)_L$ ($SU(2)_R$) subgroup of $SO(4)$ which is identified as the custodial symmetry of the SM Higgs sector. Furthermore, Eq. (3.3) shows that T_{Φ_α} transforms as the $SU(2)_L$ doublet with charge $+1/2$[3]. Therefore the broken generators are associated with the PNGBs, transforming as a (**4**,**2**) of $SO(4) \times SO(2)$.

We then introduce the following two $SU(2)_L$ doublet scalar fields associated with T_{Φ_α} as PNGBs:

$$\Phi_\alpha \equiv \frac{1}{\sqrt{2}}\begin{pmatrix} h^2_\alpha + ih^1_\alpha \\ h^4_\alpha - ih^3_\alpha \end{pmatrix} \equiv \begin{pmatrix} \omega^+_\alpha \\ \frac{v_\alpha + h_\alpha + iz_\alpha}{\sqrt{2}} \end{pmatrix}, \tag{3.5}$$

where the v_α's are the VEVs of Φ_α. The relation among v_1, v_2 and the Fermi constant G_F will be discussed in Section 3.2.2. Notice that, in order to assign the right hypercharge to fermions, one has to introduce also an extra $U(1)_X$. The electric charge Q will be then defined as usual by $Q = T^3_L + Y$ with the hypercharge Y given by $Y = T^3_R + X$ where X is the $U(1)_X$ charge. In this chapter, we do not discuss the fermion sector which is not relevant to the following analysis, so we can omit to include this extra $U(1)_X$ group.

3.2.2 Effective kinetic Lagrangian

In general, once the coset space has been chosen, the low-energy Lagrangian is fixed at the two-derivative level, the basic ingredient being the PNGB matrix which transforms non-linearly under the global group.

The kinetic invariant Lagrangian under the $SO(6)$ symmetry can be formulated through the

[3]The overall minus sign is a conventional as the T^3_R charge should be $+1/2$ to get $Y = +1/2$ and $Q = +1$ for the upper component of the Higgs doublet.

analogue of the formalism in non-linear sigma models, as discussed in Section 1.3.3 as

$$\mathcal{L}^{kin} = \frac{f^2}{4}(d_\alpha^{\hat{a}})_\mu (d_\alpha^{\hat{a}})^\mu, \tag{3.6}$$

where

$$(d_\alpha^{\hat{a}})_\mu = i\,\mathrm{tr}(U^\dagger D_\mu U T_\alpha^{\hat{a}}). \tag{3.7}$$

Here U is the PNGB matrix:

$$U = \exp\left(i\frac{\Pi}{f}\right), \quad \text{with} \quad \Pi \equiv \sqrt{2}h_\alpha^{\hat{a}} T_\alpha^{\hat{a}} = -i \begin{pmatrix} 0_{4\times 4} & h_1^{\hat{a}} & h_2^{\hat{a}} \\ -h_1^{\hat{a}} & 0 & 0 \\ -h_2^{\hat{a}} & 0 & 0 \end{pmatrix}. \tag{3.8}$$

In Eq. (3.7), the covariant derivative D_μ is given by

$$D_\mu = \partial_\mu - igT_L^a W_\mu^a - ig' Y B_\mu. \tag{3.9}$$

The expressions for $(d_\alpha^{\hat{a}})_\mu$ up to $\mathcal{O}(1/f)$ are given in Appendix C.

In order to see how the gauge boson masses are generated, let us consider the fourth components of the Higgs fields:

$$h_1^{\hat{a}} = (0,0,0,\tilde{h}_1), \quad h_2^{\hat{a}} = (0,0,0,\tilde{h}_2), \tag{3.10}$$

with

$$\tilde{h}_1 = h_1 + v_1, \quad \tilde{h}_2 = h_2 + v_2. \tag{3.11}$$

In this case, the matrix U defined in Eq. (3.8) takes a simple form,

$$U = \begin{pmatrix} 1_{4\times 4} - (1-\cos\frac{\tilde{h}}{f})_{44} & \frac{\tilde{h}_1^{\hat{a}}}{\tilde{h}}\sin\frac{\tilde{h}}{f} & \frac{\tilde{h}_2^{\hat{a}}}{\tilde{h}}\sin\frac{\tilde{h}}{f} \\ -\frac{\tilde{h}_1^{\hat{a}}}{\tilde{h}}\sin\frac{\tilde{h}}{f} & 1-\frac{\tilde{h}_1^2}{\tilde{h}^2}(1-\cos\frac{\tilde{h}}{f}) & -\frac{\tilde{h}_1\tilde{h}_2}{\tilde{h}^2}(1-\cos\frac{\tilde{h}}{f}) \\ -\frac{\tilde{h}_2^{\hat{a}}}{\tilde{h}}\sin\frac{\tilde{h}}{f} & -\frac{\tilde{h}_1\tilde{h}_2}{\tilde{h}^2}(1-\cos\frac{\tilde{h}}{f}) & 1-\frac{\tilde{h}_2^2}{\tilde{h}^2}(1-\cos\frac{\tilde{h}}{f}) \end{pmatrix}, \tag{3.12}$$

where

$$\tilde{h} \equiv \sqrt{\tilde{h}_1^2 + \tilde{h}_2^2}. \tag{3.13}$$

The two-gauge-boson terms are extracted from Eqs. (3.6), (3.7) and (3.12) as

$$\mathcal{L}_{\rm kin}^{\rm mass} = \frac{f^2}{8}(2g^2 W_\mu^+ W^{-\mu} + g_Z^2 Z_\mu Z^\mu)\sin^2\frac{\tilde{h}}{f}, \tag{3.14}$$

and thus the gauge boson masses are given by

$$m_W^2 = \frac{g^2}{4} f^2 \sin^2 \frac{v}{f}, \quad m_Z^2 = \frac{g_Z^2}{4} f^2 \sin^2 \frac{v}{f}, \tag{3.15}$$

where $v^2 \equiv v_1^2 + v_2^2$ and $g_Z = g/\cos\theta_W$ with θ_W being the weak mixing angle. Notice here that the VEV v is different from the one $v_{\rm SM}$ in the SM as long as we take a finite value of f. The relationship among v, $v_{\rm SM}$ and G_F is expressed as follows:

$$v_{\rm SM}^2 \equiv \frac{1}{\sqrt{2} G_F} = f^2 \sin^2 \frac{v}{f} \simeq (246\ {\rm GeV})^2. \tag{3.16}$$

The ratio of the two VEVs is defined by $\tan\beta = v_2/v_1$.

Similarly to the E2HDM, we can define the so-called Higgs basis [88] in which only one of the two doublet fields contains the VEV v and the NG states $G^\pm$ and G^0 absorbed into the longitudinal components of $W^\pm$ and Z bosons, respectively:

$$\begin{pmatrix} \Phi_1 \\ \Phi_2 \end{pmatrix} = R(\beta) \begin{pmatrix} \Phi \\ \Psi \end{pmatrix}, \quad R(x) = \begin{pmatrix} \cos x & -\sin x \\ \sin x & \cos x \end{pmatrix}, \tag{3.17}$$

where

$$\Phi = \begin{pmatrix} G^+ \\ \frac{v + h_1' + iG^0}{\sqrt{2}} \end{pmatrix}, \quad \Psi = \begin{pmatrix} H^+ \\ \frac{h_2' + iA}{\sqrt{2}} \end{pmatrix}. \tag{3.18}$$

In the above expressions, $H^\pm$ and A are the physical charged and CP-odd neutral Higgs boson, respectively, while h_1' and h_2' are the CP-even Higgs bosons which in general can be mixed with each other. In this basis, the two-derivative terms for scalar bosons are extracted up to $\mathcal{O}(1/f^2)$:

$$\mathcal{L}_{\rm kin}^{\text{2-der}} = \left(1 - \frac{\xi}{3}\right) \left[|\partial_\mu G^+|^2 + \frac{1}{2}(\partial_\mu G^0)^2 + \frac{1}{2}(\partial_\mu h_2')^2 \right] + |\partial_\mu H^+|^2 + \frac{1}{2}(\partial_\mu A)^2 + \frac{1}{2}(\partial_\mu h_1')^2, \tag{3.19}$$

where

$$\xi = \frac{v_{\rm SM}^2}{f^2}. \tag{3.20}$$

We see that the kinetic terms for $G^\pm$, G^0 and h_2' are not in canonical form and we need to rescale the fields:

$$G^+ \to \left(1 - \frac{\xi}{3}\right)^{-1/2} G^+, \quad G^0 \to \left(1 - \frac{\xi}{3}\right)^{-1/2} G^0, \quad h_2' \to \left(1 - \frac{\xi}{3}\right)^{-1/2} h_2'. \tag{3.21}$$

After this shift, we can define the mass eigenstates for the CP-even scalar bosons by introducing

the mixing angle θ as:

$$\begin{pmatrix} h_1' \\ h_2' \end{pmatrix} = R(\theta) \begin{pmatrix} h \\ H \end{pmatrix}, \tag{3.22}$$

where h is assumed to be the observed Higgs boson with a mass of 125 GeV. The mixing angle θ is determined by the mass matrix for the CP-even states calculated from the Higgs potential, which will be discussed in the next subsection.

3.2.3 Higgs potential

The Higgs potential is generated through the Coleman-Weinberg (CW) mechanism [89] at loop levels. There are two types of contributions to the potential, coming from gauge boson loops and fermion loops. The former contribution can be calculated without any ambiguities and it generates a positive squared mass term in the potential [90]. Thus, EW symmetry breaking does not occur by the gauge loops alone. Fermion loops can provide a negative contribution to the squared mass term, so their effect is essentially important to trigger EW symmetry breaking. However, the contribution from fermion loops depends on the choice of the representation of fermions.

The structure of the Higgs potential in the $SO(6)/SO(4) \times SO(2)$ model has been studied in Ref. [45] assuming several representations of fermion fields. They also assume that the explicit breaking of the global symmetry is associated with the couplings of the strong sector to the SM fields, that is, gauge and Yukawa interactions. This assumption, dictated by minimality, allows one to parametrise the Higgs potential, at each given order in the fermion and gauge couplings, in terms of a limited number of coefficients. If this assumption is relaxed, the parameter space of the C2HDM could be significantly enlarged. The form of the potential they obtain is given by the general E2HDM one, but each of the parameters is expressed in terms of those in the strong sector (mainly associated to the top dynamics). In this thesis, however, we do not explicitly calculate the CW potential and we do not specify the fermion representations, making our analysis applicable to different choices of them. In fact, while the coupling of the vector bosons is fixed by gauge invariance, more freedom exists in the fermion sector and, to specify the model, one must fix the quantum numbers of the strong sector operators which mix with the SM fermions, in particular with the top quark. The CW potential clearly depends on these choices. Instead of performing the explicit calculation, we assume here the same form of the Higgs potential as that in the E2HDM. Our results on the unitarity properties of the C2HDM will be expressed as bounds on the masses of the Higgses which are free parameters in the E2HDM. Once the model is explicitly specified, we will have the possibility to check, by calculating the CW potential, if the composite Higgs spectrum of that particular configuration satisfies the unitarity bounds.

In order to avoid FCNCs at the tree level, a discrete Z_2 symmetry [48] is often imposed onto

the potential, which is what we also do here[4]. Under the Z_2 symmetry, the two doublet fields are transformed as $(\Phi_1, \Phi_2) \to (+\Phi_1, -\Phi_2)$. This symmetry can also avoid a large contribution to the EW T-parameter which could emerge in C2HDMs from the dimension-six operator in the kinetic Lagrangian[5]. Depending on the nature of the Z_2 symmetry, i.e., softly-broken or unbroken, the properties of the Higgs bosons can drastically change. In the following, we first discuss the softly-broken Z_2 case and then we consider the unbroken case. For the latter case, the VEV of Φ_2 must be taken to be zero to avoid the spontaneously breakdown of the Z_2 symmetry. In analogy with the E2HDM we will refer to the former scenario as the active C2HDM, while the latter describes the inert C2HDM.

3.2.3.1 Active C2HDM

The Higgs potential under the gauge symmetry $SU(2)_L \times U(1)_Y$ with the softly-broken Z_2 symmetry introduced as follows

$$\begin{aligned} V(\Phi_1, \Phi_2) = {} & m_1^2 \Phi_1^\dagger \Phi_1 + m_2^2 \Phi_2^\dagger \Phi_2 - m_3^2 (\Phi_1^\dagger \Phi_2 + \text{h.c.}) + \frac{1}{2}\lambda_1 (\Phi_1^\dagger \Phi_1)^2 + \frac{1}{2}\lambda_2 (\Phi_2^\dagger \Phi_2)^2 \\ & + \lambda_3 (\Phi_1^\dagger \Phi_1)(\Phi_2^\dagger \Phi_2) + \lambda_4 |\Phi_1^\dagger \Phi_2|^2 + \frac{1}{2}\lambda_5 [(\Phi_1^\dagger \Phi_2)^2 + \text{h.c.}], \end{aligned} \tag{3.23}$$

where m_3^2 and λ_5 are generally complex, but we assume them to be real for simplicity. It is useful to rewrite the soft-breaking Z_2 parameter m_3^2 through M^2 [91] as follows:

$$M^2 = \frac{m_3^2}{s_\beta c_\beta}, \tag{3.24}$$

where $s_\beta = \sin\beta$ and $c_\beta = \cos\beta$. In the following, we use the shorthand notations $s_X = \sin X$ and $c_X = \cos X$ for an arbitrary angle X.

The tadpole conditions for h_1 and h_2 fields, assuming $v_1 \neq 0$ and $v_2 \neq 0$, are given by

$$m_1^2 + \frac{1}{2}v^2 \left(\lambda_1 c_\beta^2 + \lambda_{345} s_\beta^2\right) - M^2 s_\beta^2 = 0, \tag{3.25}$$

$$m_2^2 + \frac{1}{2}v^2 \left(\lambda_2 s_\beta^2 + \lambda_{345} c_\beta^2\right) - M^2 c_\beta^2 = 0, \tag{3.26}$$

where $\lambda_{345} = \lambda_3 + \lambda_4 + \lambda_5$. The mass matrices for the charged states $M_\pm^2$ in the basis of $(\omega_1^\pm, \omega_2^\pm)$ and the CP-odd scalar states M_{odd}^2 in the basis of (z_1, z_2) are diagonalised as

$$R^T(\beta) M_\pm^2 R(\beta) = \text{diag}(0, m_{H^\pm}^2), \quad R^T(\beta) M_{\text{odd}}^2 R(\beta) = \text{diag}(0, m_A^2), \tag{3.27}$$

[4] In Ref. [45], the Z_2 symmetry ($\Phi_1 \to +\Phi_1$ and $\Phi_2 \to -\Phi_2$) is referred as the C_2 symmetry whose transformation can be expressed by a diagonal 6×6 matrix form acting on the 6×6 PNGB matrix given in Eq. (3.8).

[5] The issue of anomalous contribution to the T-parameter and to FCNCs in C2HDMs is faced also in [92] where they discuss T-safe models based on different cosets, in particular SO(9)/SO(8).

where $m^2_{H^\pm}$ and m^2_A are the squared masses of $H^\pm$ and A:

$$m^2_{H^\pm} = M^2 - \frac{v^2}{2}(\lambda_4+\lambda_5), \quad m^2_A = M^2 - v^2\lambda_5. \tag{3.28}$$

The massless states correspond to the modes $G^\pm$ and G^0. The mass matrix for the CP-even scalar states is also calculated in the basis of (h'_1, h'_2) as

$$M^2_{\rm even} = \begin{pmatrix} (M_{\rm even})^2_{11} & (M_{\rm even})^2_{12} \\ (M_{\rm even})^2_{12} & (M_{\rm even})^2_{22} \end{pmatrix}, \tag{3.29}$$

where each of matrix elements is expressed by

$$(M_{\rm even})^2_{11} = v^2(\lambda_1 c^4_\beta + \lambda_2 s^4_\beta + 2\lambda_{345}c^2_\beta s^2_\beta), \tag{3.30}$$

$$(M_{\rm even})^2_{22} = \left(1+\frac{\xi}{3}\right)[M^2 + v^2(\lambda_1+\lambda_2-2\lambda_{345})s^2_\beta c^2_\beta], \tag{3.31}$$

$$(M_{\rm even})^2_{12} = v^2\left(1+\frac{\xi}{6}\right)\left[-\lambda_1 c^2_\beta + \lambda_2 s^2_\beta + c_{2\beta}\lambda_{345}\right] s_\beta c_\beta. \tag{3.32}$$

This matrix can be diagonalised by the rotation $R(\theta)$ introduced in Eq. (3.22) as

$$m^2_h = c^2_\theta (M_{\rm even})^2_{11} + s^2_\theta (M_{\rm even})^2_{22} + 2s_\theta c_\theta (M_{\rm even})^2_{12}, \tag{3.33}$$

$$m^2_H = s^2_\theta (M_{\rm even})^2_{11} + c^2_\theta (M_{\rm even})^2_{22} - 2s_\theta c_\theta (M_{\rm even})^2_{12}, \tag{3.34}$$

$$\tan 2\theta = \frac{2(M_{\rm even})^2_{12}}{(M_{\rm even})^2_{11} - (M_{\rm even})^2_{22}}. \tag{3.35}$$

Now, we can rewrite all the λ_i parameters of the potential (3.23) in terms of the masses of the physical Higgs bosons and the mixing angle θ as follows:

$$\lambda_1 = \frac{1}{v^2 c^2_\beta}\left[m^2_h c^2_{\beta+\theta} + m^2_H s^2_{\beta+\theta} - M^2 s^2_\beta + \frac{\xi}{3}s_\beta(m^2_h c_{\beta+\theta}s_\theta - m^2_H s_{\beta+\theta}c_\theta)\right], \tag{3.36}$$

$$\lambda_2 = \frac{1}{v^2 s^2_\beta}\left[m^2_h s^2_{\beta+\theta} + m^2_H c^2_{\beta+\theta} - M^2 c^2_\beta - \frac{\xi}{3}c_\beta(m^2_h s_{\beta+\theta}s_\theta + m^2_H c_{\beta+\theta}c_\theta)\right], \tag{3.37}$$

$$\lambda_3 = \frac{1}{v^2}\left[\frac{2s_{\beta+\theta}c_{\beta+\theta}}{s_{2\beta}}(m^2_h - m^2_H) + 2m^2_{H^\pm} - M^2 - \frac{\xi}{3s_{2\beta}}(m^2_h s_\theta c_{2\beta+\theta} - m^2_H c_\theta s_{2\beta+\theta})\right], \tag{3.38}$$

$$\lambda_4 = \frac{1}{v^2}(M^2 + m^2_A - 2m^2_{H^\pm}), \tag{3.39}$$

$$\lambda_5 = \frac{1}{v^2}(M^2 - m^2_A). \tag{3.40}$$

In total, there are nine independent parameters which can be introduced as m_H, m_A, $m_{H^\pm}$, $\cos\theta$, $\tan\beta$, M^2, ξ (or f), v and m_h. The latter two parameters will be fixed in our analysis by requiring $m_h = 125$ GeV and $v_{\rm SM} = 246$ GeV.

3.2.3.2 Inert C2HDM

The Higgs potential is given as in Eq. (3.23) without the m_3^2 term. Because of the absence of the VEV of Φ_2, we have only one tadpole condition for m_1, and the m_2 parameter will set the scale for the mass of the inert Higgs. Thus, the mass relations are the following:

$$m_{H^\pm}^2 = m_2^2 + \frac{v^2}{2}\lambda_3, \tag{3.41}$$

$$m_A^2 = {m_2}^2 + \frac{v^2}{2}(\lambda_3 + \lambda_4 - \lambda_5), \tag{3.42}$$

$$m_H^2 = \left(1 + \frac{\xi}{3}\right)\left({m_2}^2 + \frac{v^2}{2}\lambda_{345}\right), \tag{3.43}$$

$$m_h^2 = \lambda_1 v^2. \tag{3.44}$$

From the above four relations, the λ_1, λ_3, λ_4 and λ_5 parameters can be rewritten in terms of the four mass parameters and m_2^2:

$$\lambda_1 = \frac{m_h^2}{v^2}, \tag{3.45}$$

$$\lambda_3 = \frac{2}{v^2}(m_{H^\pm}^2 - m_2^2), \tag{3.46}$$

$$\lambda_4 = \frac{1}{v^2}\left[m_A^2 - 2m_{H^\pm}^2 + m_H^2\left(1 - \frac{\xi}{3}\right)\right], \tag{3.47}$$

$$\lambda_5 = \frac{1}{v^2}\left[m_H^2\left(1 - \frac{\xi}{3}\right) - m_A^2\right]. \tag{3.48}$$

We note that the λ_2 parameter is not determined in terms of the Higgs masses, just like the m_2^2 parameter.

The eight independent parameters in the potential can be expressed as m_H, m_A, $m_{H^\pm}$, m_2^2, λ_2 and ξ (or f), v and m_h. Similar to the active case, m_h and v will be fixed by 125 GeV and by requiring $v_{\rm SM} = 246$ GeV, respectively.

3.3 Unitarity constraints

In this section, we discuss the bound from perturbative unitarity in our C2HDM. We consider all possible two-to-two-body bosonic elastic scatterings. The procedure to obtain the unitarity bound is similar to that in elementary models such as the SM [20] and E2HDM [93–97]. Namely, we compute the S-wave amplitude matrix, derive its eigenvalues x_i and then impose the following criterion [98] for each of these:

$$|\mathrm{Re}(x_i)| \leq 1/2. \tag{3.49}$$

The most important difference between the unitarity bound in elementary models and that in composite models is that there is a squared energy dependence in the S-wave amplitude for the latter. This is exactly canceled in elementary models among the diagrams with the gauge boson mediation, the Higgs boson mediation and the contact interactions. In composite models, however, this cancellation does not work, because the sum rule of the Higgs-Gauge-Gauge type couplings is modified from that in the elementary ones. For example, in the E2HDM, the squared sum of the hVV and HVV ($V = W, Z$) couplings is the same as the squared $h_{\rm SM}VV$ coupling in the SM, while in the C2HDM, that is modified by the factor $(1 - \xi)$. The energy dependence of the S-wave amplitudes leads to unitarity violation and asks for an Ultra-Violet (UV) completion of the C2HDM. The study of the unitarity bounds in this effective theory therefore gives an indication of the scale at which the onset of other effects of the strong sector become relevant.

3.3.1 The $W_L^+W_L^- \to W_L^+W_L^-$ scattering process

In order to clearly indicate the difference of perturbative unitarity properties in the E2HDM and those in the C2HDM, let us calculate the elastic scattering of the longitudinal component of the W boson scattering, i.e., $W_L^+W_L^- \to W_L^+W_L^-$, in the active case.

The contribution from the diagrams without the Higgs bosons is calculated as in the SM,

$$\begin{aligned}&\mathcal{M}(W_L^+W_L^- \to W_L^+W_L^-)_{\rm gauge}\\ &= \frac{s}{2v_{\rm SM}^2}(1 - c_\phi) - \frac{g_Z^2}{4}\left[(2\cos^2\theta_W - 1)(1 + c_\phi) - 2\tan^2\frac{\phi}{2}\right] + \mathcal{O}(s^{-1}),\end{aligned} \tag{3.50}$$

where ϕ is the scattering angle and s is the squared CM energy. The contribution from the Higgs boson mediation (h and H) is defined by

$$\begin{aligned}&\mathcal{M}(W_L^+W_L^- \to W_L^+W_L^-)_{\rm Higgs}\\ &= -\frac{s}{2v_{\rm SM}^2}(1 - c_\phi)(1 - \xi) - \frac{2}{v_{\rm SM}^2}(1 - \xi)(m_h^2c_\theta^2 + m_H^2s_\theta^2) + \mathcal{O}(s^{-1}).\end{aligned} \tag{3.51}$$

As a result, in the total amplitude the s dependence appears which vanishes in the limit of $\xi \to 0$:

$$\mathcal{M}(W_L^+W_L^- \to W_L^+W_L^-)_{\rm tot} = \frac{s\xi}{2v_{\rm SM}^2}(1 - c_\phi) - \frac{2}{v_{\rm SM}^2}(m_h^2c_\theta^2 + m_H^2s_\theta^2)(1 - \xi) + \mathcal{O}(g^2, s^{-1}). \tag{3.52}$$

The S-wave amplitude a_0, defined by

$$a_0 = \frac{1}{32\pi}\int_{-1}^{1} d\cos\phi\,\mathcal{M} = -\frac{1}{32\pi}\int_{\pi}^{0} d\phi\sin\phi\,\mathcal{M}, \tag{3.53}$$

is calculated for the $W_L^+W_L^- \to W_L^+W_L^-$ process as

$$a_0(W_L^+W_L^- \to W_L^+W_L^-) = \frac{s}{32\pi v_{\rm SM}^2}\xi - \frac{1}{8\pi v_{\rm SM}^2}(m_h^2 c_\theta^2 + m_H^2 s_\theta^2)(1-\xi) + \mathcal{O}(g^2, s^{-1}). \tag{3.54}$$

Thus, S-matrix unitarity is broken at a certain energy scale as long as we take $\xi \neq 0$.

We expect that exactly the same result as in Eq. (3.54), up to $\mathcal{O}(s^0)$, is obtained by using the equivalence theorem [99], in which the $W_L^\pm$ mode is replaced by the NG mode $G^\pm$. Let us check this. There are three relevant diagrams for the amplitude ($G^+G^- \to G^+G^-$), i.e., the contact diagram (denoted by $\mathcal{M}_c$), and the s- and t-channel diagrams (denoted by $\mathcal{M}_s$ and $\mathcal{M}_t$, respectively) with the h and H exchanges. Each of these diagrams is calculated as

$$\mathcal{M}_c(G^+G^- \to G^+G^-) = \frac{s}{2}(1-c_\phi)(g_{G^\pm G^\pm, G^\mp G^\mp} - g_{G^+G^-,G^+G^-}) + \lambda_{G^+G^-G^+G^-}, \tag{3.55}$$

$$\mathcal{M}_s(G^+G^- \to G^+G^-) = -\sum_{\varphi=h,H}\frac{1}{s-m_\varphi^2}\left[\frac{s}{2}(2g_{G^\pm\varphi,G^\mp} - g_{G^+G^-,\varphi}) + \lambda_{G^+G^-\varphi}\right]^2, \tag{3.56}$$

$$\mathcal{M}_t(G^+G^- \to G^+G^-) = -\sum_{\varphi=h,H}\frac{1}{t-m_\varphi^2}\left[\frac{t}{2}(2g_{G^\pm\varphi,G^\mp} - g_{G^+G^-,\varphi}) + \lambda_{G^+G^-\varphi}\right]^2. \tag{3.57}$$

In the above expressions, we introduced the scalar trilinear λ_{abc} and quartic λ_{abcd} couplings from the potential as well as the scalar trilinear $g_{ab,c}$ and quartic $g_{ab,cd}$ couplings with two derivatives coming from the kinetic Lagrangian. They are given by

$$\lambda_{abcd} \equiv -\frac{\partial^4 V}{\partial a \partial b \partial c \partial d}, \quad \lambda_{abc} \equiv -\frac{\partial^3 V}{\partial a \partial b \partial c} \tag{3.58}$$

and

$$g_{ab,cd} \equiv \frac{\partial^4 \mathcal{L}_{\rm kin}}{\partial(\partial_\mu a)\partial(\partial^\mu b)\,\partial c\,\partial d}, \quad g_{ab,c} \equiv \frac{\partial^3 \mathcal{L}_{\rm kin}}{\partial(\partial_\mu a)\partial(\partial^\mu b)\,\partial c}. \tag{3.59}$$

While $g_{ab,cd}$ and $g_{ab,c}$ are proportional to $\xi/v_{\rm SM}^2$, the λ_{abcd} and λ_{abc} couplings contain ξ^0 terms plus corrections proportional to ξ. These scalar couplings emerging in Eqs. (3.55)–(3.57) are defined by

$$\lambda_{G^+G^-G^+G^-} = -\frac{2}{v_{\rm SM}^2}\left(1+\frac{\xi}{3}\right)(m_h^2 c_\theta^2 + m_H^2 s_\theta^2), \tag{3.60}$$

$$\lambda_{G^+G^-h} = -\frac{m_h^2}{v_{\rm SM}}\left(1+\frac{\xi}{6}\right)c_\theta, \quad \lambda_{G^+G^-H} = \frac{m_H^2}{v_{\rm SM}}\left(1+\frac{\xi}{6}\right)s_\theta,, \tag{3.61}$$

$$g_{G^+G^-,G^+G^-} = -\frac{\xi}{3v_{\rm SM}^2}, \quad g_{G^\pm G^\pm,G^\mp G^\mp} = \frac{2\xi}{3v_{\rm SM}^2}, \tag{3.62}$$

$$g_{G^+G^-,h} = -\frac{2\xi}{3v_{\rm SM}}c_\theta, \quad g_{G^\pm h,G^\mp} = \frac{\xi}{3v_{\rm SM}}c_\theta, \tag{3.63}$$

$$g_{G^+G^-,H} = \frac{2\xi}{3v_{\rm SM}}s_\theta, \quad g_{G^\pm H,G^\mp} = -\frac{\xi}{3v_{\rm SM}}s_\theta. \tag{3.64}$$

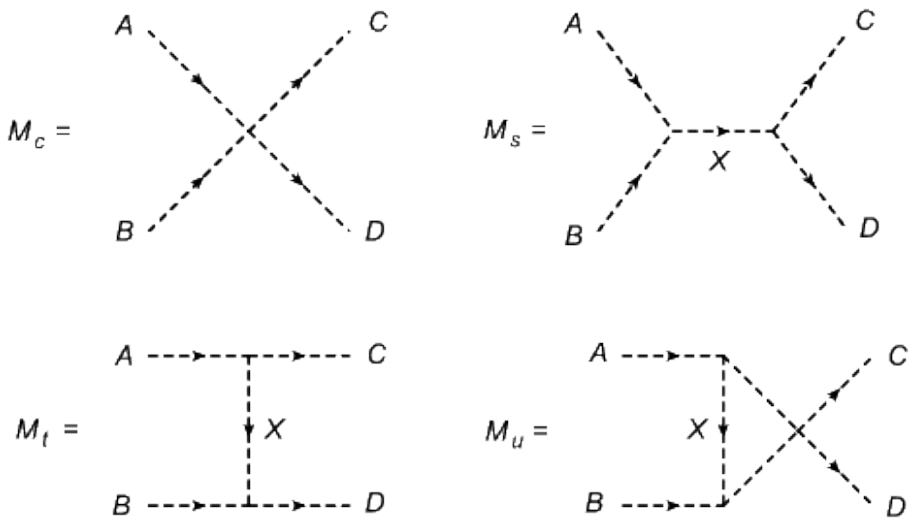

Figure 3.1: Feynman diagrams for the two-to-two-body (pseudo)scalar boson scatterings. The arrow with each dashed line indicates the momentum flow for each particle. A similar figure is seen in Ref. [31].

By substituting in Eqs. (3.55)–(3.57), we find that the total amplitude of the $G^+G^- \to G^+G^-$ process is exactly the same as that of the $W_L^+W_L^- \to W_L^+W_L^-$ one given in Eq. (3.52). In the following, we calculate all the other two-to-two-body scattering channels using the equivalence theorem.

3.3.2 Generic formulae for the two-to-two body (pseudo)scalar boson scatterings

We discuss here the general two-to-two-body scattering process denoted by $A\,B \to C\,D$ with A, B, C and D being (pseudo)scalar bosons. There are contributions from contact $\mathcal{M}_c$, s-channel $\mathcal{M}_s$, t-channel $\mathcal{M}_t$ and u-channel $\mathcal{M}_u$ diagrams as shown in Fig. 3.1. Each of the amplitudes is

calculated in the following way:

$$\begin{aligned}\mathcal{M}_c(AB \to CD) &= -(g_{AB,CD}\, p_{AB} + g_{CD,AB}\, p_{CD}) \\ &\quad + g_{AC,BD}\, p_{AC} + g_{BD,AC}\, p_{BD} + g_{AD,BC}\, p_{AD} + g_{BC,AD}\, p_{BC} + \lambda_{ABCD}, \qquad (3.65)\\ \mathcal{M}_s(AB \to X \to CD) &= -\frac{1}{s - m_X^2}\left(g_{XA,B}\, p_{XA} + g_{BX,A}\, p_{BX} - g_{AB,X}\, p_{AB} + \lambda_{ABX}\right) \\ &\quad \times \left(g_{XC,D}\, p_{XC} + g_{DX,C}\, p_{DX} - g_{CD,X}\, p_{CD} + \lambda_{CDX}\right), \qquad (3.66)\\ \mathcal{M}_t(AB \to X \to CD) &= -\frac{1}{t - m_X^2}\left(g_{AC,X}\, p_{AC} + g_{XA,C}\, p_{XA} - g_{CX,A}\, p_{CX} + \lambda_{ACX}\right) \\ &\quad \times \left(g_{BD,X}\, p_{BD} - g_{XB,D}\, p_{XB} + g_{DX,B}\, p_{DX} + \lambda_{BDX}\right), \qquad (3.67)\\ \mathcal{M}_u(AB \to X \to CD) &= -\frac{1}{u - m_X^2}\left(g_{AD,X}\, p_{AD} + g_{XA,D}\, p_{XA} - g_{DX,A}\, p_{DX} + \lambda_{ADX}\right) \\ &\quad \times \left(g_{BC,X}\, p_{BC} - g_{XB,C}\, p_{XB} + g_{CX,B}\, p_{CX} + \lambda_{BCX}\right), \qquad (3.68)\end{aligned}$$

where $p_{ij} = p_i \cdot p_j$. In the above formulation, λ_{abc} and λ_{abcd} are given in Eq. 3.58, whereas $g_{a,bc}$ and $g_{ab,cd}$ are given in Eq 3.59. The four-momenta of the particles A, B, C and D are defined by

$$p_i^\mu = (E_i, \vec{p}_i), \quad (i = A,\ B,\ C,\ D), \qquad (3.69)$$

with E_i and $\vec{p}_i$ being the energy and three-momentum of the particle i, respectively. In the CM frame, these quantities are expressed by

$$E_A = \frac{\sqrt{s}}{2}(1 + x_A - x_B), \quad E_B = \frac{\sqrt{s}}{2}(1 + x_B - x_A), \qquad (3.70)$$

$$E_C = \frac{\sqrt{s}}{2}(1 + x_C - x_D), \quad E_D = \frac{\sqrt{s}}{2}(1 + x_D - x_C), \qquad (3.71)$$

$$\vec{p}_A = (0, 0, p_{\rm in}), \quad \vec{p}_C = (p_{\rm out} s_\phi, 0, p_{\rm out} c_\phi), \quad \vec{p}_B = -\vec{p}_A, \quad \vec{p}_D = -\vec{p}_C, \qquad (3.72)$$

and

$$p_{\rm in} = \frac{\sqrt{s}}{2}\lambda^{1/2}(x_A, x_B), \quad p_{\rm out} = \frac{\sqrt{s}}{2}\lambda^{1/2}(x_C, x_D), \quad x_i = \frac{m_i^2}{s}. \qquad (3.73)$$

The 2-body phase space function λ is defined by

$$\lambda(x, y) = 1 + x^2 + y^2 - 2xy - 2x - 2y. \qquad (3.74)$$

In the massless limit of the external particles, i.e., $x_i \to 0$, we obtain the simpler form

$$\begin{aligned}
\mathcal{M}_c \to & -\frac{s}{2}\Big[g_{AB,CD} + g_{CD,AB} - \frac{1-c_\phi}{2}(g_{AC,BD} + g_{BD,AC}) \\
& - \frac{1+c_\phi}{2}(g_{AD,BC} + g_{BC,AD})\Big] + \lambda_{ABCD}, \qquad (3.75) \\
\mathcal{M}_s \to & -\frac{s^2}{4(s-m_X^2)}\left(g_{XA,B} + g_{BX,A} - g_{AB,X} + \frac{2}{s}\lambda_{ABX}\right) \times (A \to C,\, B \to D)\,, \\
= & -\frac{1}{2}\left(g_{XA,B} + g_{BX,A} - g_{AB,X}\right)\lambda_{CDX} + [(A,B) \leftrightarrow (C,D)] + \mathcal{O}(s^{-1}), \qquad (3.76) \\
\mathcal{M}_t \to & -\frac{t^2}{4(t-m_X^2)}\left(g_{AC,X} - g_{XA,C} - g_{CX,A} - \frac{2}{t}\lambda_{ACX}\right) \times (A \to B,\, C \to D)\,, \\
= & -\frac{1}{2}\left(g_{AC,X} - g_{XA,C} - g_{CX,A}\right)\lambda_{BDX} + [(A,C) \leftrightarrow (B,D)] + \mathcal{O}(s^{-1}), \qquad (3.77) \\
\mathcal{M}_u \to & -\frac{u^2}{4(u-m_X^2)}\left(g_{AD,X} - g_{XA,D} - g_{DX,A} - \frac{2}{u}\lambda_{ADX}\right) \times (A \to B,\, D \to C) \\
= & -\frac{1}{2}\left(g_{AD,X} - g_{XA,D} - g_{DX,A}\right)\lambda_{BCX} + [(A,D) \leftrightarrow (B,C)] + \mathcal{O}(s^{-1}). \qquad (3.78)
\end{aligned}$$

From the above expressions, it is clear that the S-wave amplitude can be categorised into three types of contributions up to $\mathcal{O}(s^0)$: i.e., (i) terms proportional to $s\,\xi$, (ii) terms proportional to $s^0\xi^0$ and (iii) terms proportional to $s^0\xi$. The contributions (i) and (ii) come only from the $g_{AB,CD}$ and λ_{ABCD} coupling, respectively, in the scalar contact interaction diagram as it is seen in Eq. (3.75). The contribution (iii) comes from the cross term $g_{A,BC} \times \lambda_{ABC}$ in the s-, t- and u-channel diagrams and also from the contact diagram in Eq. (3.65). When we neglect the contribution (iii), the calculation of the S-wave amplitude becomes extremely simple for the following reason. In this approximation, the propagator of (pseudo)scalar bosons and the invariant mass term from the product of the momentum p_{ij} do not enter the calculations. We thus can choose any basis of scalar states. In other words, the eigenvalues of the S-wave matrix do not depend on the mixing angles β and θ for the scalar bosons[6]. Clearly, the simplest way to calculate the S-wave matrix is by using the weak eigenbasis and we adopt it to calculate the S-wave amplitudes for all the scattering states in the next subsection.

Before calculating all the scattering amplitudes, let us discuss another particular process, e.g., $H^+H^- \to H^+H^-$, again in the active case, in order to see if the $\mathcal{O}(\xi s^0)$ term can be relevant.

[6]Even the shift of scalar fields given in Eq. (3.21) is not needed in this calculation, because the ξ factor from the shift provides $\mathcal{O}(\xi^2 s)$ or $\mathcal{O}(\xi s^0)$ contributions.

Using Eqs. (3.65)–(3.67), we obtain the amplitude for the $H^+H^- \to H^+H^-$ process as follows:

$$\mathcal{M}(H^+H^- \to H^+H^-) = \frac{s}{2v_{\rm SM}^2}\xi(1+c_\phi) - \frac{m_{H^\pm}^2}{v_{\rm SM}^2}\xi\left(\frac{2}{3}+4c_\phi\right) + \lambda_{H^+H^-H^+H^-} - \sum_{\varphi=h,H}\lambda_{H^+H^-\varphi}^2\left(\frac{1}{s-m_\varphi^2}+\frac{1}{t-m_\varphi^2}\right) \tag{3.79}$$

$$= \frac{s}{2v_{\rm SM}^2}\xi(1+c_\phi) - \frac{m_{H^\pm}^2}{v_{\rm SM}^2}\xi\left(\frac{2}{3}+4c_\phi\right) + \lambda_{H^+H^-H^+H^-} + \mathcal{O}(s^{-1}), \tag{3.80}$$

and the couplings associated with this process are defined by

$$\lambda_{H^+H^-H^+H^-} = \frac{2}{v_{\rm SM}^2}\left(1-\frac{\xi}{3}\right)\left[4\cot^2 2\beta\, M^2 - (c_\theta + 2\cot 2\beta s_\theta)^2\, m_h^2 - (s_\theta - 2\cot 2\beta c_\theta)^2\, m_H^2\right] + \frac{4c_{2\beta}}{3v_{\rm SM}^2 s_{2\beta}^2}\xi\Big[(c_\theta s_{2\beta}+2s_\theta c_{2\beta})s_\theta\, m_h^2 + (2c_\theta c_{2\beta} - s_\theta s_{2\beta})c_\theta\, m_H^2\Big], \tag{3.81}$$

$$\lambda_{H^+H^-h} = \frac{1}{v_{\rm SM}}\left[\frac{2s_{2\beta+\theta}}{s_{2\beta}}M^2 - (c_\theta + 2s_\theta\cot 2\beta)m_h^2 - 2c_\theta m_{H^\pm}^2\right] + \frac{\xi}{v_{\rm SM}}\left[-\frac{c_\theta}{3}M^2 + \frac{1}{6}(c_\theta + 4s_\theta\cot 2\beta)m_h^2 + \frac{c_\theta}{3}m_{H^\pm}^2\right], \tag{3.82}$$

$$\lambda_{H^+H^-H} = \frac{1}{v_{\rm SM}}\left[\frac{2c_{2\beta+\theta}}{s_{2\beta}}M^2 + (s_\theta - 2c_\theta\cot 2\beta)m_H^2 + 2s_\theta m_{H^\pm}^2\right] + \frac{\xi}{v_{\rm SM}}\left[\frac{s_\theta}{3}M^2 + \frac{1}{6}(-s_\theta + 4c_\theta\cot 2\beta)m_H^2 - \frac{s_\theta}{3}m_{H^\pm}^2\right], \tag{3.83}$$

and

$$g_{H^+H^-,H^+H^-} = -\frac{\xi}{3v_{\rm SM}^2}, \quad g_{H^\pm H^\pm,H^\mp H^\mp} = \frac{2\xi}{3v_{\rm SM}^2}, \tag{3.84}$$

$$g_{H^+H^-,h} = g_{H^\pm h,H^\mp} = g_{H^+H^-,H} = g_{H^\pm H,H^\mp} = 0. \tag{3.85}$$

Notice that the contribution from the s and t channels with h and H mediation only give the $\mathcal{O}(s^{-1})$ term in the $H^+H^- \to H^+H^-$ amplitude due to the absence of the trilinear $g_{a,bc}$ couplings as shown in Eq. (3.85). In contrast, the s- and t-channel contributions to the $G^+G^- \to G^+G^-$ amplitude do give $\mathcal{O}(\xi s^0)$ terms. Moreover, the second term in Eq. (3.80) is obtained from the mass dependence of the product of the four momenta [see Eqs. (3.70)–(3.73)] in the contact interaction diagram.

Let us now indicate some numerical results for the S-wave amplitudes of the $G^+G^- \to G^+G^-$ and $H^+H^- \to H^+H^-$ scatterings. First, we indicate the results by neglecting the $\mathcal{O}(s^{-1})$ terms in order to see fully the effect of the $\mathcal{O}(\xi s^0)$ contributions. In Figs. 3.2 and 3.3, we plot the absolute value of $a_0(G^+G^- \to G^+G^-)$ as a function of $\sqrt{s}$ in the case of $\cos\theta = 1$ and $\cos\theta = 0.99$, respectively. In the both figures, the solid (dashed) curves show the case with (without) $\mathcal{O}(\xi s^0)$ contributions and the scale f is taken to be 500 GeV (black), 750 GeV (blue) and 1000 GeV (red).

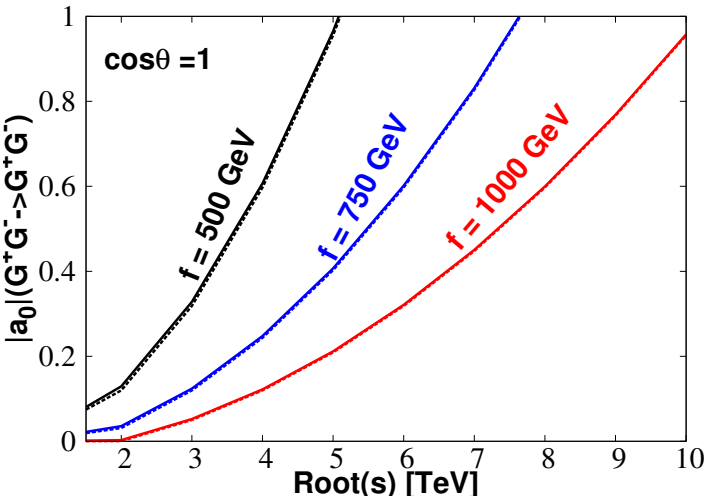

Figure 3.2: S-wave amplitude for the $G^+G^- \to G^+G^-$ process as a function of $\sqrt{s}$ in the case where $\cos\theta = 1$ and $f = 500$ GeV (black), 750 GeV (blue), 1000 GeV (red). The solid (dashed) curves are the result with (without) $\mathcal{O}(\xi s^0)$ terms. A similar figure is seen in Ref. [31].

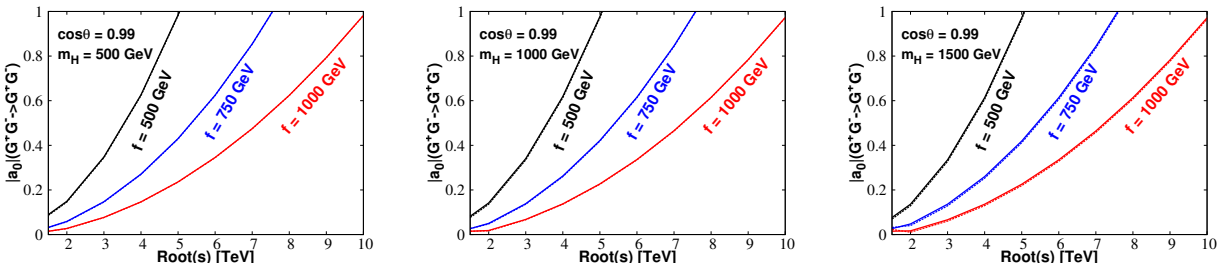

Figure 3.3: S-wave amplitude for the $G^+G^- \to G^+G^-$ process as a function of $\sqrt{s}$ for the case with $\cos\theta = 0.99$ and $f = 500$ GeV (black), 750 GeV (blue), 1000 GeV (red). The solid (dashed) curves are the result with (without) $\mathcal{O}(\xi s^0)$ terms. The left, centre and right panels display the result for $m_H = 500$, 1000 and 1500 GeV, respectively. A similar figure is seen in Ref. [31].

In Fig. 3.3, we set m_H =500, 1000 and 1500 GeV in the left, center and right panels, respectively. As expected, the S-wave amplitude grows as $\sqrt{s}$ increases because of the $\mathcal{O}(\xi\, s)$ terms, so that the unitarity constraint will give an upper limit on $\sqrt{s}$ for a given set of the parameters with $\xi \neq 0$. We see that the difference between the solid and dashed curves for each fixed value of f is negligibly small for $\cos\theta = 1$ because the difference only comes from the m_h^2 term, as shown in Eq. (3.54), whereas the m_H dependence vanishes. For the case with $\cos\theta = 0.99$, a slightly larger difference appears, especially for a larger value of m_H, as expected from Eq. (3.54). Although a further larger difference is expected to appear as θ increases for a fixed value of m_H, such a scenario is disfavored by the current LHC data [100, 101], which causes a large deviation in the hVV coupling from the SM value. So, in summary, we can safely neglect the $\mathcal{O}(\xi s^0)$ contributions in the S-wave amplitude for the $G^+G^- \to G^+G^-$ process.

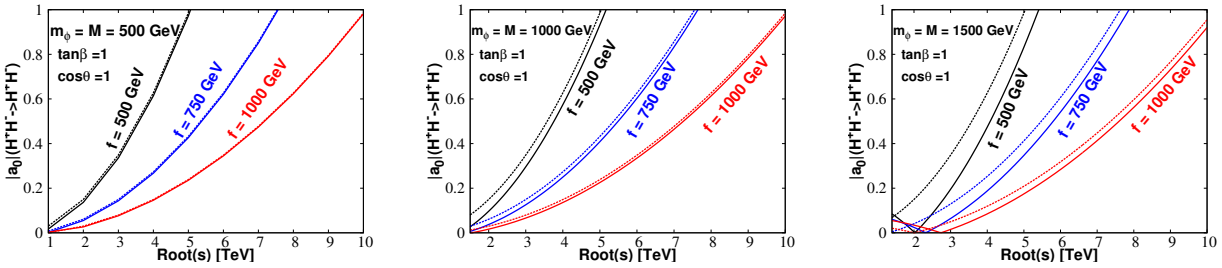

Figure 3.4: S-wave amplitude for the $H^+H^- \to H^+H^-$ process as a function of $\sqrt{s}$ in the case of $\cos\theta = 1$, $\tan\beta = 1$ and $f = 500$ (black), 750 (blue) and 1000 GeV (red). The solid (dashed) curves are the results with (without) $\mathcal{O}(\xi s^0)$ terms. The left, centre and right panels display the results for $m_\Phi (= m_A = m_H = m_{H^\pm}) = M = 500$, 1000 and 1500 GeV, respectively. A similar figure is seen in Ref. [31].

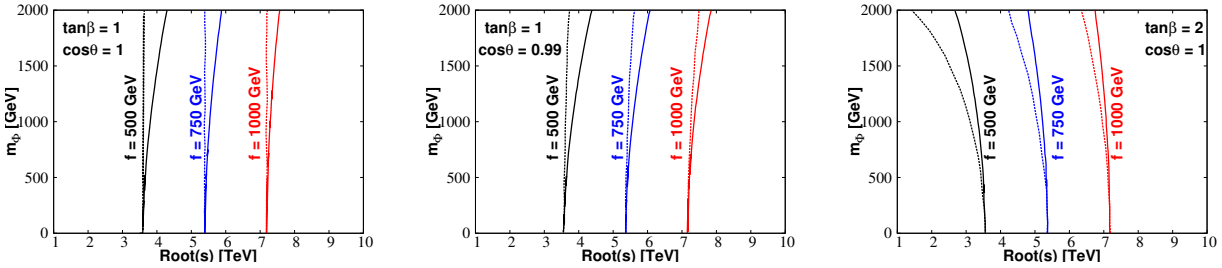

Figure 3.5: Unitarity bound on the $(\sqrt{s},\, m_\Phi)$ plane from the condition $|a_0(H^+H^- \to H^+H^-)| < 1/2$ in the case of $M = m_\Phi (= m_A = m_H = m_{H^\pm})$. In the left, centre and right panels, we choose $(\cos\theta, \tan\beta) = (1,1)$, (0.99,1) and (1,2), respectively. The solid (dashed) curves show the results with (without) $\mathcal{O}(\xi s^0)$ terms. A similar figure is seen in Ref. [31].

In Fig. 3.4, we show the S-wave amplitude for the $H^+H^- \to H^+H^-$ scattering as a function of $\sqrt{s}$ in the case of $\cos\theta = 1$, $\tan\beta = 1$ and $M = m_\Phi (= m_A = m_H = m_{H^\pm})$. Similarly to Fig. 3.2, the solid and dashed curves show the cases with and without $\mathcal{O}(\xi s^0)$ terms, respectively. Because of the $m^2_{H^\pm}\,\xi$ term in Eq. (3.80), the difference between these two cases becomes larger when we take larger values of m_Φ and small f.

In Fig. 3.5, we indicate the constraints on the $(\sqrt{s},\, m_\Phi)$ plane by the requirement that the magnitude of $a_0(H^+H^- \to H^+H^-)$ does not exceed 1/2. When we include the $\mathcal{O}(\xi s^0)$ contribution, the constraints get slightly weaker because of the destructive contributions between the $\xi\, s$ and $\xi\, m^2_{H^\pm}$ terms.

From the above results shown in Figs. 3.2-3.5, we can conclude that the $\mathcal{O}(\xi s^0)$ contributions are not so significant as long as we consider the case $m_\Phi \lesssim 1000$ GeV. Since we expect the same holds true for the other two-to-two-body scalar scattering amplitudes participating the S-wave amplitude matrix, we will in the following neglect the $\mathcal{O}(\xi s^0)$ terms and we will focus our analysis on the region $m_\Phi \lesssim 1000$ GeV where this approximation is safe. Notice also that this is the region of the C2HDM parameters that we are interested in for the phenomenology at the LHC.

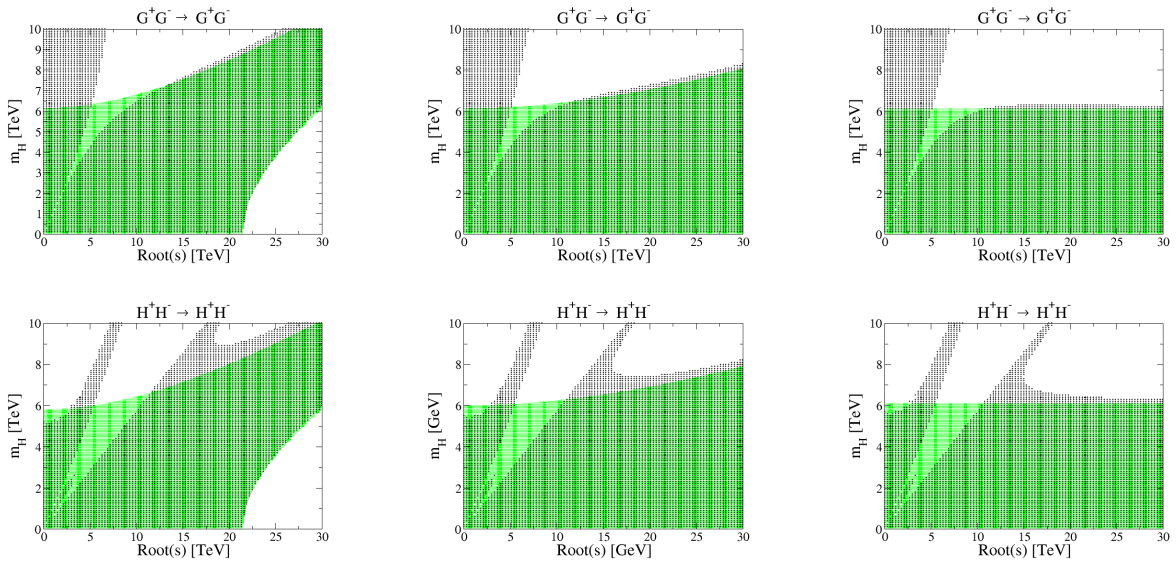

Figure 3.6: Allowed regions from perturbative unitarity in the $(\sqrt{s}, m_H)$ plane from $G^+G^- \to G^+G^-$ (upper panels) and from $H^+H^- \to H^+H^-$ (lower panels) scattering amplitudes within the C2HDM. We take $\cos\theta = 0.99$, $\tan\beta = 1$ and $m_\Phi (= m_H = m_A = m_{H^\pm}) = M$. The grey regions are obtained by employing the exact formulae, and the green ones by neglecting $\mathcal{O}(1/s)$ terms. The left, centre and right panels represent the cases with $f = 3$ TeV, 5 TeV, and infinity (corresponding to the E2HDM). A similar figure is seen in Ref. [31].

Next, we consider the effect of the $\mathcal{O}(1/s)$ terms on the S-wave amplitudes which were neglected in the above numerical calculations. In Fig. 3.6, we indicate the regions allowed by the unitarity bound using the $G^+G^- \to G^+G^-$ (upper panels) and $H^+H^- \to H^+H^-$ (lower panels) scattering amplitudes in the case of $\tan\beta = 1$, $\cos\theta = 0.99$ and $M = m_\Phi$. The black shaded regions show the allowed parameter space using the exact formulae given in Eqs. (3.55), (3.56), (3.57) and (3.79) while the green shaded regions do so using the approximate formulae given in Eq. (3.54) by neglecting the $\mathcal{O}(1/s)$ terms. The value of f is taken to be 3000 GeV, 5000 GeV and infinity (corresponding to the E2HDM) in the left, center and right panels, respectively. We see that these two results are in good agreement for values of $\sqrt{s}$ large as compared to m_H. In the complementary region of $m_H \gtrsim \sqrt{s}$, we find somewhat significant differences between these two results. In particular, the region with $\sqrt{s} \simeq m_H$ is excluded if we look at the result using the exact formula, which is due to the resonant/divergent effect of the s- and t-channel diagrams that makes the S-wave amplitude quite large. Consequently, as long as we consider the phenomenologically interesting case, i.e., the mass of the extra Higgs boson is set to be 1 TeV or below and $\sqrt{s} > 1$ TeV, the differences due to the $\mathcal{O}(1/s)$ terms are not important either and we can use the approximate formulae to study the unitarity bounds of our model.

Fig. 3.6 also allows a direct comparison between the C2HDM (left and center panels) and the E2HDM (right panels). Given a finite value to f, there is an energy scale over which the theory is

no longer valid and an UV completion is required (for example for $f = 3$ TeV we get $\sqrt{s} \lesssim 20$ TeV). But, for energies below this cut-off, the bound on the mass of the extra Higgs boson is less stringent than the one in the E2HDM. This is due to a partial cancellation between the term growing with s and the one proportional to m_H^2 in the scattering amplitudes here considered (or to a squared Higgs mass in general in all other channels). This property will be confirmed by the forthcoming analysis of the unitarity bounds via the complete S-wave amplitude matrix.

Moreover, in Fig. 3.6 one may notice that (e.g., in the left two panels, for $f = 3$ TeV, where the effect is most evident) the C2HDM remains perturbative for very large values of $\sqrt{s}$, if m_Φ is also set to be large. On the one hand, this corresponds to a very fine-tuned region where perturbativity is accomplished via a strong cancellation between the large scalar mass term and the contribution increasing with energy proportional to ξ, the two thereby compensating for each other. On the other hand, over the same region, we obtain stronger bounds on m_Φ appearing from the $HH \to Hh$ and/or $Hh \to hh$ channels, particularly when $\tan\beta \simeq 1$ and $\sin\theta \simeq 0$. This is mainly because a larger value of the $Hhhh$ and $HHHh$ quartic couplings is obtained as compared to the $G^+G^-G^+G^-$ and $H^+H^-H^+H^-$ ones. For the same configuration provided in Fig. 3.6, the above neutral (pseudo)scalar channels give an upper limit on m_Φ of about 2 TeV for $f = 3$ TeV and $\sqrt{s} \simeq 0$, i.e., several TeV less than in the charged (pseudo)scalar scattering cases, with the 'funnel region' onsetting as $\sqrt{s} \to \infty$ fading away. Generally, the upper bound on m_Φ gets stronger when we combine all the scattering channels together and impose the constraint from vacuum stability as well, as we will study later on in Sec. 3.3.4.

In conclusion, despite not presented explicitly here, we confirm that the results of the inert case does not differ substantially from the active case, so we shall adopt the same approximations in both constructions.

3.3.3 Diagonalisation of the S-wave amplitude matrix

In this subsection, we calculate all the two-to-two-body (pseudo)scalar boson scattering amplitudes by keeping the $\mathcal{O}(\xi\, s)$ and $\mathcal{O}(\xi^0\, s^0)$ contributions only. In this case, the diagonalisation of the S-wave amplitude matrix is analytically done as we will explain below. (We note that the following discussion is valid in both the active and inert case.)

In the C2HDM there are 14 neutral, 8 singly-charged and 3-doubly charged states as in the E2HDM. In the weak eigenbasis presented in Eq. (3.5), the 14 neutral channels are defined by

$$\omega_i^+\omega_i^-,\ \frac{z_i z_i}{\sqrt{2}},\ \frac{h_i h_i}{\sqrt{2}},\ h_i z_i,\ h_1 h_2,\ z_1 z_2,\ h_1 z_2,\ h_2 z_1,\ \omega_1^+\omega_2^-,\ \omega_2^+\omega_1^- \quad (i = 1, 2). \tag{3.86}$$

The eight (positive) singly-charged channels are given by

$$\omega_i^+ z_i,\ \omega_i^+ h_i,\ \omega_1^+ z_2,\ \omega_2^+ z_1,\ \omega_1^+ h_2,\ \omega_2^+ h_1 \quad (i = 1, 2). \tag{3.87}$$

The three (positive) doubly-charged channels are given by

$$\frac{\omega_i^+\omega_i^+}{\sqrt{2}},\ \omega_1^+\omega_2^+ \quad (i=1,2). \tag{3.88}$$

The negative charged states are simply obtained by taking the charge conjugation of the corresponding positive states.

Although each neutral, singly-charged and doubly-charged state respectively gives a 14×14, 8×8 and 3×3 S-wave amplitude matrix, respectively, they can all be simplified into a block-diagonal form with maximally 2×2 sub-matrices by taking appropriate unitary transformations of the scattering states. As discussed in Ref. [97], such an appropriate basis can be systematically obtained by using the conserved quantum numbers, e.g., the hypercharge Y, the weak isospin I, its third component I_3 and the Z_2 charge of two-to-two-body scattering states.

First of all, by using the Z_2 charge, the 14 neutral channels can be divided into eight Z_2-even and six Z_2-odd channels:

$$\omega_i^+\omega_i^-,\ \frac{z_iz_i}{\sqrt{2}},\ \frac{h_ih_i}{\sqrt{2}},\ h_iz_i \quad (i=1,2)\ \ [Z_2\text{-even states}], \tag{3.89}$$

$$h_1h_2,\ z_1z_2,\ h_1z_2,\ h_2z_1,\ \omega_1^+\omega_2^-,\ \omega_2^+\omega_1^-\ \ [Z_2\text{-odd states}]. \tag{3.90}$$

Next, the eight Z_2-even states are further separated into the following orthogonal states:

$$\frac{1}{\sqrt{2}}\left(\omega_i^+\omega_i^- + \frac{1}{2}z_iz_i + \frac{1}{2}h_ih_i\right),\ \frac{1}{\sqrt{2}}\left(\omega_i^+\omega_i^- - \frac{1}{2}z_iz_i - \frac{1}{2}h_ih_i\right),\ \frac{1}{2}\left(z_iz_i - h_ih_i\right),\ z_ih_i. \tag{3.91}$$

The corresponding 8×8 S-wave matrix in the above basis is expressed by

$$a_0^0(Z_2\text{-even}) = \mathrm{diag}(\mathcal{A}_1,\mathcal{A}_2,\mathcal{A}_3,\mathcal{A}_4), \tag{3.92}$$

where

$$\mathcal{A}_1 = \frac{s\xi}{2v_{\rm SM}^2}\begin{pmatrix}3 & 1\\ 1 & 3\end{pmatrix} - \begin{pmatrix}3\lambda_1 & 2\lambda_3+\lambda_4\\ 2\lambda_3+\lambda_4 & 3\lambda_2\end{pmatrix}, \tag{3.93}$$

$$\mathcal{A}_2 = \frac{s\xi}{2v_{\rm SM}^2}\begin{pmatrix}-1 & 1\\ 1 & -1\end{pmatrix} - \begin{pmatrix}\lambda_1 & \lambda_4\\ \lambda_4 & \lambda_2\end{pmatrix},\quad \mathcal{A}_3=\mathcal{A}_4 = \frac{s\xi}{2v_{\rm SM}^2}\begin{pmatrix}-1 & 1\\ 1 & -1\end{pmatrix} - \begin{pmatrix}\lambda_1 & \lambda_5\\ \lambda_5 & \lambda_2\end{pmatrix}. \tag{3.94}$$

The six Z_2-odd states are further separated into the following orthogonal states:

$$\begin{aligned}
&\frac{1}{\sqrt{2}}\left(-z_1z_2+h_1h_2\right),\ \frac{1}{\sqrt{2}}\left(h_1z_2+h_2z_1\right),\\
&\frac{1}{2}\left(-z_1z_2-h_1h_2+\omega_1^+\omega_2^-+\omega_2^+\omega_1^-\right),\ \frac{1}{2}\left(ih_1z_2-ih_2z_1-\omega_1^+\omega_2^-+\omega_2^+\omega_1^-\right),\\
&\frac{1}{2}\left(z_1z_2+h_1h_2+\omega_1^+\omega_2^-+\omega_2^+\omega_1^-\right),\ \frac{1}{2}\left(-ih_1z_2+ih_2z_1-\omega_1^+\omega_2^-+\omega_2^+\omega_1^-\right).
\end{aligned} \tag{3.95}$$

The corresponding 6×6 S-wave matrix in the above basis is defined by

$$a_0^0(Z_2\text{-odd}) = \frac{s\xi}{v_{\rm SM}^2}\text{diag}(-1,-1,-1,1,1,1) \\ - \text{diag}(\lambda_3+\lambda_4,\, \lambda_3+\lambda_4,\, \lambda_3+\lambda_5,\, \lambda_3-\lambda_5,\, \lambda_3+2\lambda_4+3\lambda_5,\, \lambda_3+2\lambda_4-3\lambda_5). \tag{3.96}$$

In a similar way to the neutral states, we can split the singly-charged states into four Z_2-even and four Z_2-odd states:

$$\omega_i^+ z_i,\ \omega_i^+ h_i,\quad [Z_2\text{-even states}], \\ \omega_1^+ z_2,\ \omega_2^+ z_1,\ \omega_1^+ h_2,\ \omega_2^+ h_1\quad [Z_2\text{-odd states}]. \tag{3.97}$$

The four Z_2-even states are further separated into the following orthogonal states:

$$\frac{1}{\sqrt{2}}\left(iz_i\omega_i^+ + h_i\omega_i^+\right),\ \frac{1}{\sqrt{2}}\left(-iz_i\omega_i^+ + h_i\omega_i^+\right), \tag{3.98}$$

and the corresponding 4×4 S-wave matrix in the above basis is expressed by

$$a_0^{\pm}(Z_2\text{-even}) = \text{diag}(\mathcal{A}_3,\, \mathcal{A}_2). \tag{3.99}$$

The four Z_2-odd states are further separated into the following orthogonal states:

$$\frac{1}{2}\left(i\omega_1^+ z_2 + i\omega_2^+ z_1 + \omega_1^+ h_2 + \omega_2^+ h_1\right),\ \frac{1}{2}\left(-i\omega_1^+ z_2 + i\omega_2^+ z_1 - \omega_1^+ h_2 + \omega_2^+ h_1\right), \\ \frac{1}{2}\left(-i\omega_1^+ z_2 - i\omega_2^+ z_1 + \omega_1^+ h_2 + \omega_2^+ h_1\right),\ \frac{1}{2}\left(i\omega_1^+ z_2 - i\omega_2^+ z_1 - \omega_1^+ h_2 + \omega_2^+ h_1\right), \tag{3.100}$$

and the corresponding 4×4 S-wave matrix in the above basis is expressed by

$$a_0^{\pm}(Z_2\text{-odd}) = \frac{s\xi}{v_{\rm SM}^2}\text{diag}(-1,\, 1,\, -1,\, 1) - \text{diag}(\lambda_3+\lambda_4,\, \lambda_3-\lambda_4,\, \lambda_3+\lambda_5,\, \lambda_3-\lambda_5). \tag{3.101}$$

Finally, the three doubly-charged states can be divided into two Z_2-even ($\omega_i^+\omega_i^+/\sqrt{2}$) and one Z_2-odd state ($\omega_1^+\omega_2^+$). They give

$$a_0^{\pm\pm}(Z_2\text{-even}) = \mathcal{A}_3, \quad a_0^{\pm\pm}(Z_2\text{-odd}) = -\frac{s\xi}{v_{\rm SM}^2} - (\lambda_3+\lambda_4). \tag{3.102}$$

As a result, we obtain the analytic formulae of all the independent eigenvalues by diagonalizing

the 2×2 sub-matrices as

$$16\pi x_1^{\pm} = \frac{3}{2}\frac{s\,\xi}{v_{\rm SM}^2} - \frac{3}{2}(\lambda_1+\lambda_2) \pm \frac{1}{2}\sqrt{9(\lambda_1-\lambda_2)^2 + \left(\frac{s\,\xi}{v_{\rm SM}^2} - 4\lambda_3 - 2\lambda_4\right)^2}, \tag{3.103}$$

$$16\pi x_2^{\pm} = -\frac{1}{2}\frac{s\,\xi}{v_{\rm SM}^2} - \frac{1}{2}(\lambda_1+\lambda_2) \pm \frac{1}{2}\sqrt{(\lambda_1-\lambda_2)^2 + \left(\frac{\xi\,s}{v_{\rm SM}^2} - 2\lambda_4\right)^2}, \tag{3.104}$$

$$16\pi x_3^{\pm} = -\frac{1}{2}\frac{s\,\xi}{v_{\rm SM}^2} - \frac{1}{2}(\lambda_1+\lambda_2) \pm \frac{1}{2}\sqrt{(\lambda_1-\lambda_2)^2 + \left(\frac{\xi\,s}{v_{\rm SM}^2} - 2\lambda_5\right)^2}, \tag{3.105}$$

$$16\pi x_4^{\pm} = \frac{s\,\xi}{v_{\rm SM}^2} - (\lambda_3 + 2\lambda_4 \pm 3\lambda_5), \tag{3.106}$$

$$16\pi x_5^{\pm} = \pm\frac{s\,\xi}{v_{\rm SM}^2} - (\lambda_3 \mp \lambda_5), \tag{3.107}$$

$$16\pi x_6^{\pm} = \pm\frac{s\,\xi}{v_{\rm SM}^2} - (\lambda_3 \mp \lambda_4). \tag{3.108}$$

It is significant to note here that the above eigenvalues can be applied in both the active and inert cases, as already mentioned. However, once the λ parameters are defined in terms of physical parameters (such as, e.g., the masses of extra Higgs bosons), then we get different expressions for the active and inert cases. For this reason, the constraints on the physical parameters induced by the unitarity bound can be different in these two cases even if we use the same expressions for the eigenvalues given in Eqs. (3.103)–(3.108).

3.3.4 Limits on the parameter space from all channels

We now perform the numerical evaluations of the theoretical constraints on the C2HDM parameter space induced by the requirement of perturbative unitarity using all the eigenvalues given in Eqs. (3.103)–(3.108). In addition to the unitarity constraints, we also impose the vacuum stability condition, where we require that the scalar potential is bounded from below in any direction of the scalar field space with a large field value. The vacuum stability is guaranteed by satisfying the following inequalities [102, 103]:[7]

$$\lambda_1 > 0, \quad \lambda_2 > 0, \quad \sqrt{\lambda_1\lambda_2} + \lambda_3 + \mathrm{MIN}(0, \lambda_4 \pm \lambda_5) > 0. \tag{3.109}$$

We first consider the constraints for the active C2HDM. Fig. 3.7 displays the allowed parameter

[7] It should be noted that, in general, higher-order dimensional terms emerge in the scalar potential due to its nonlinear nature, and these can modify the its shape for large values of the scalar fields, particularly when f is not very large. In total, eight independent dimension-six operators, such as $|\phi_1|^6$, can be written besides the terms defined in Eq. 3.23, which are proportional to $1/f^2$. In our approach, as we clarified in Sec. 3.3.3, we assume the same structure of the potential as in the E2HDM, thus we do not take into account the effect of such higher-order operators on the bound from vacuum stability. Indeed, the potential breaking the EW symmetry in a generic CHM is produced by loops so that such terms, in spite of being present and participating in the tree-level expansion, are not liable for mass generation and for generating a nonzero VEV of the Higgs fields.

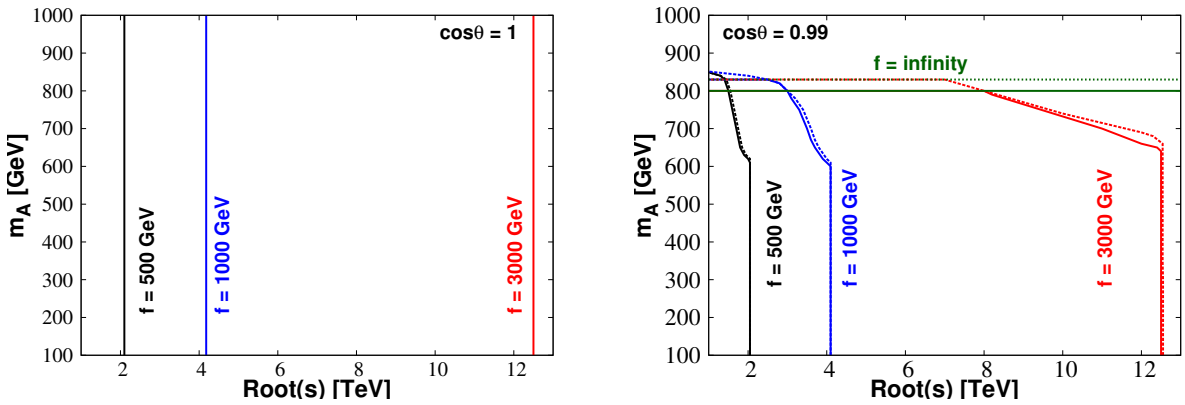

Figure 3.7: Bound on the parameter space of the C2HDM from the unitarity and the vacuum stability in the case where $\tan\beta = 1$ and $m_{H^\pm} = m_A$ for various fixed values of f. The left and right panels display the case of $\cos\theta = 1$ and 0.99, respectively. The lower left region of each curve is allowed. We take the value of m_H to be equal to m_A for the solid curves, while we scan within the region of $m_A \pm 500$ GeV for the dashed curves. For all plots, M is scanned. A similar figure is seen in Ref. [31].

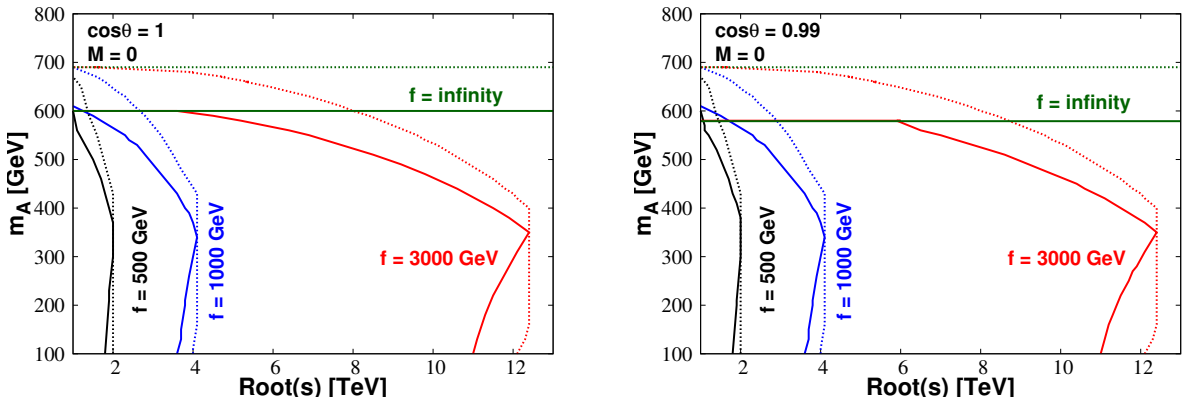

Figure 3.8: As per Fig. 3.7, but with M set to be 0. A similar figure is seen in Ref. [31].

regions on the $(\sqrt{s},\, m_A)$ plane for each fixed value of f, i.e., 500, 1000 and 3000 GeV, and infinity (only for the right panel), where $f = \infty$ corresponds to the limit of the E2HDM. We set $\cos\theta$ to be 1 (left) and 0.99 (right). In both panels, we take $m_{H^\pm} = m_A$ and $\tan\beta = 1$ while M is scanned over a sufficiently wide range so as to obtain the maximum allowed parameter region. The solid and dashed curves, respectively, indicate the case with $m_H = m_A$ and m_H scanned within $m_A \pm 500$ GeV. It can be seen from the left panel that there is an upper limit on $\sqrt{s}$, about 2, 4 and 13 TeV in the cases of $f = 500$, 1000 and 3000 GeV, respectively. The dependence on m_A for these limits is negligible in the range $m_A \leq 1$ TeV. If we look at the right panel, we find the limits not only on $\sqrt{s}$ but also on m_A, except for the case of $f = \infty$ in which the limit on $\sqrt{s}$ vanishes as we expect in the E2HDM. It is also observed that a bit milder bound on $\sqrt{s}$ and m_A is given in the case where we relax the mass degeneracy between m_A and m_H (dashed curves).

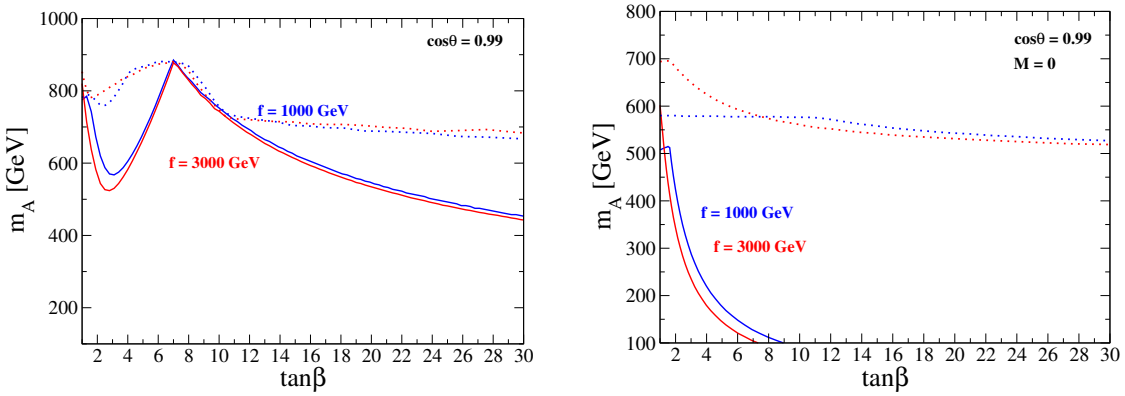

Figure 3.9: Constraint on the parameter space on the $(\tan\beta,\ m_A)$ plane from the unitarity and the vacuum stability in the case where $\cos\theta = 0.99$, $\sqrt{s} = 3000$ GeV and $m_{H^\pm} = m_A$ for $f = 1000$ GeV (blue) and $f = 3000$ GeV (red). The lower left region of each curve is allowed. The left panel represents the case where M is to be scanned, while the right one represents the case where $M = 0$. We take the value of m_H to be equal to m_A for the solid curves, while scan this value within the region of $m_A \pm 500$ GeV for the dashed curves. A similar figure is seen in Ref. [31].

In Fig. 3.8, we display the case for $M = 0$ by retaining the same configuration used in Fig. 3.7. Clearly, a stronger constraint on the $(\sqrt{s},\ m_A)$ plane is given as compared to the case with scanned M. According to [45], no M term can be generated by the C2HDM potential if the fermions fill the fundamental 6-plet representation of the $SO(6)$ group while and a non-zero value of M can be obtained in the C2HDM with traceless symmetric 20-plet fermion representations.

In Fig. 3.9, we display the allowed parameter space on the $(\tan\beta,\ m_A)$ plane in the case where $\cos\theta = 0.99$, $m_A = m_{H^\pm}$ and $\sqrt{s} = 3$ TeV. The value of M is scanned in the left panel whereas we take $M = 0$ in the right panel. In a similar way to Fig. 3.7, the solid and dashed curves indicate the case of $m_H = m_A$ and m_H scanned within $m_A \pm 500$ GeV, respectively. The case $f \to \infty$ is almost identical to the case with $f = 3000$ GeV. We find in the left panel that the case $\tan\beta \simeq 8$ gives the weakest bound on m_A while for $\tan\beta \gtrsim 10$ the bound gets stronger. For the case $M = 0$, the bound is stronger than the case shown in the left panel.

In Fig. 3.10, we indicate the allowed parameter region on the $(m_A,\ m_H)$ plane in the case of $m_{H^\pm} = m_A$ and $\sqrt{s} = 3000$ GeV. The values of $(\cos\theta, M)$ are set to be $(1, m_A)$ for the upper-left, $(0.99, m_A)$ for the upper-right, (1,0) for the lower-left and $(0.99, 0)$ for the lower-right panel. For the upper two panels, the region inside the two curves is allowed by unitarity and vacuum stability, where the lower (upper) curve is given by the constraint from vacuum stability (unitarity). From the upper two panels, we learn that a too large mass difference between m_A and m_H is not allowed by either the unitarity or vacuum stability constraint. Moreover, if we consider the case for $\cos\theta = 0.99$ (upper-right panel), only the region with small masses of m_A and m_H, i.e., less than 1 TeV, is allowed (we already saw this behavior in the right panel of Fig. 3.7). Regarding to the lower panels, we only have an upper bound on m_H and m_A from the unitarity requirement,

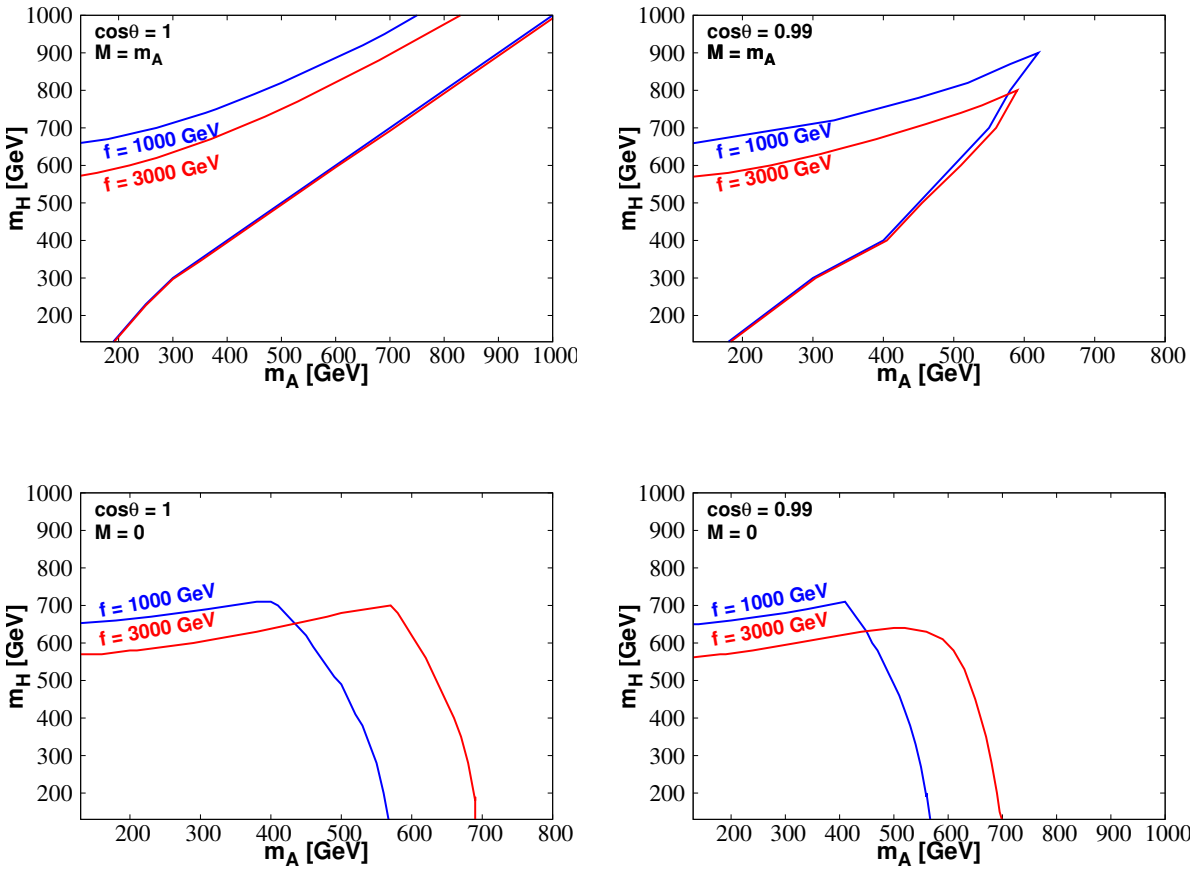

Figure 3.10: Constraint on the parameter space on the (m_A, m_H) plane by unitarity and vacuum stability in the case of $m_{H^\pm} = m_A$, $\tan\beta = 1$ and $\sqrt{s} = 3000$ GeV. The upper-left, upper-right, lower-left and lower-right panels present the case ofs $(\cos\theta, M) = (1, m_A)$, $(0.99, m_A)$, $(1, 0)$ and $(0.99, 0)$, respectively. A similar figure is seen in Ref. [31].

whereas the vacuum stability bound does not give a lower limit because setting $M = 0$ render the $\lambda_{1\text{-}5}$ parameters positive [see Eqs. (3.36)–(3.40)]. Fig. 3.11 is the same as Fig. 3.10 with the only difference that we take $\sqrt{s} = 1000$ GeV where also the case $f = 500$ GeV is allowed. The distributions here are similar to the case at higher energy, with the effect that more parameter space becomes available to the C2HDM with respect to the E2HDM, for smaller f values.

Fig. 3.12 is generated in the same manner as Fig. 3.10 but in the case of $m_{H^\pm} = m_H$. Here, we notice that the distributions of parameter space available in the C2HDM follow an opposite trend for the same f value. We trace this back to a change of sign in λ_4, which therefore induces a destructive(constructive) interference (in the case $m_{H^\pm} = m_H$) when it was instead constructive(destructive) one (in the case $m_{H^\pm} = m_A$). A similar pattern appears also for $\sqrt{s} = 1000$ GeV.

Finally, we briefly discuss the constraints in the inert case. In Fig. 3.13, we indicate the allowed parameter region on the (m_A, m_H) plane in the case of $m_{H^\pm} = m_A = m_2$ and $\sqrt{s} = 3000$ GeV. We

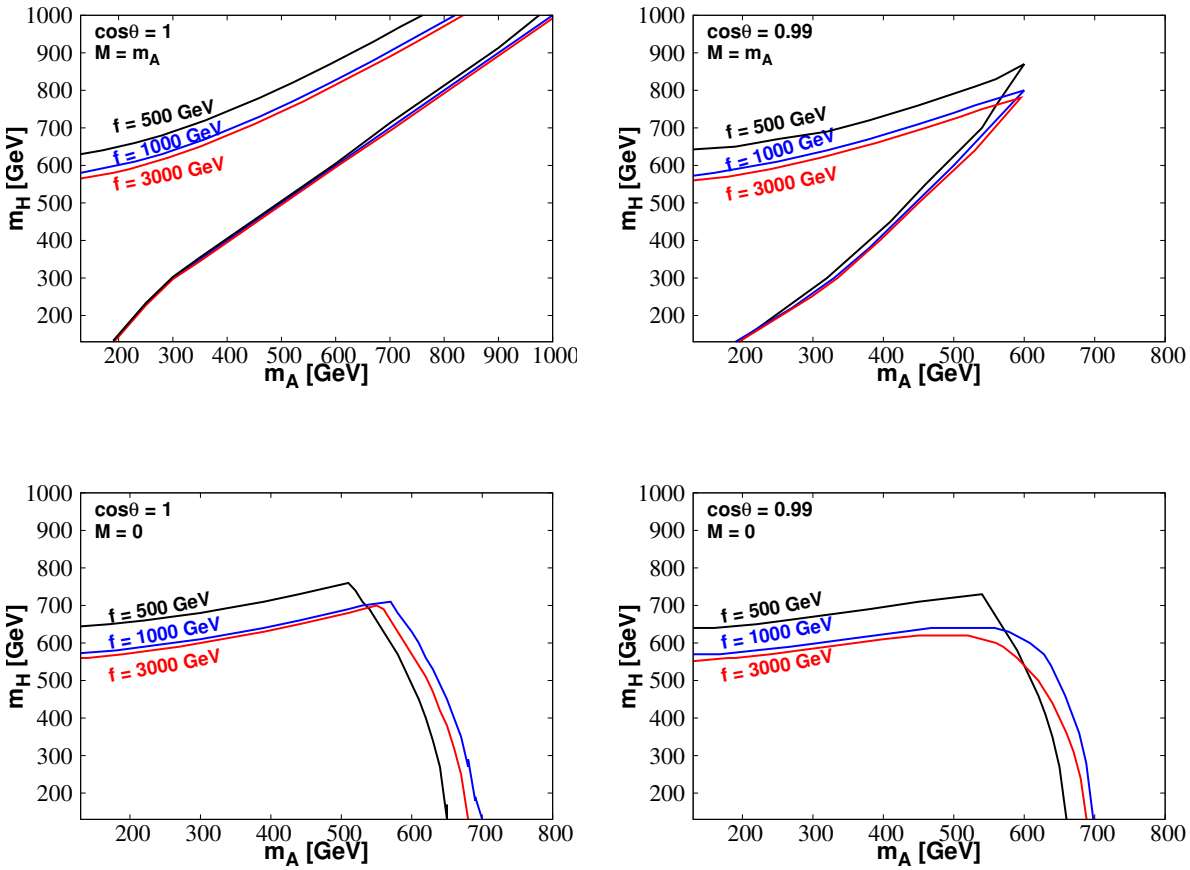

Figure 3.11: Same as Fig. 3.10 with $\sqrt{s} = 1000$ GeV. A similar figure is seen in Ref. [31]

.

take $\lambda_2 = 0.1$ (left), 2 (center) and 4 (right). Similarly to the upper panels in Fig. 3.10, the lower and upper curves are respectively determined by the bounds from vacuum stability and unitarity while the regions inside the two curves are allowed. We see that the vacuum stability bound becomes slightly milder in the case of a larger value of λ_2 while the unitarity bound is not changed importantly. Again, we have here swapped the role of A and H (by requiring $m_{H^\pm} = m_H = m_2$) as well as lowered $\sqrt{s}$ to 1000 GeV, like in the case of the active C2HDM, and have found similar patterns to those previously described.

In Fig. 3.13, we have considered h as the lightest Higgs, but a choice of parameters leading to a different mass spectrum is possible. For example, we have checked that for $m_H = m_2 = 100$ GeV the upper limit from unitarity on m_A $(= m_{H^\pm})$ is about 700 GeV. So, a DM motivated scenario is available as it is consistent with the unitarity bounds derived in this chapter.

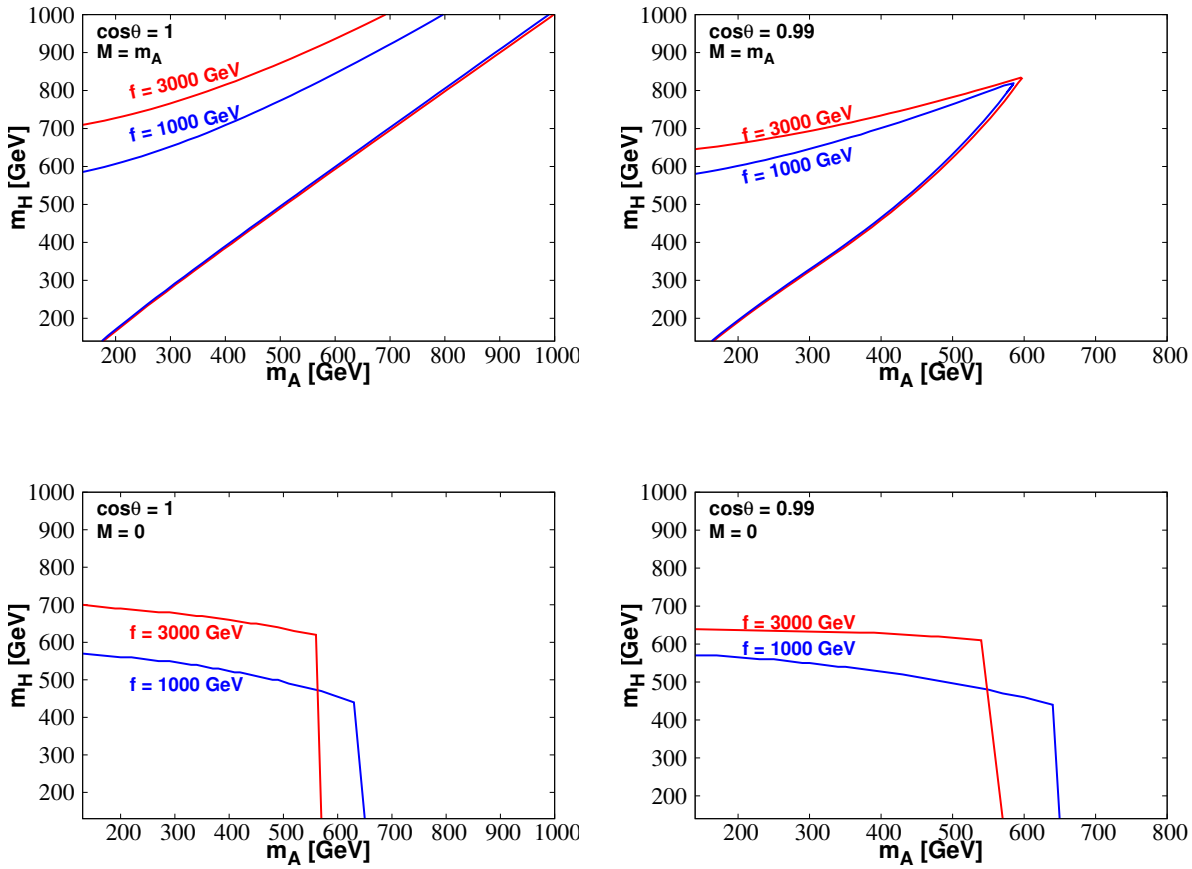

Figure 3.12: Constraint on the parameter space on the (m_A, m_H) plane by unitarity and vacuum stability in the case where $m_{H^\pm} = m_H$, $\tan\beta = 1$ and $\sqrt{s} = 3000$ GeV. The upper-left, upper-right, lower-left and lower-right panels displays the case of $(\cos\theta, M) = (1, m_H)$, $(0.99, m_H)$, $(1, 0)$ and $(0.99, 0)$, respectively. A similar figure is seen in Ref. [31].

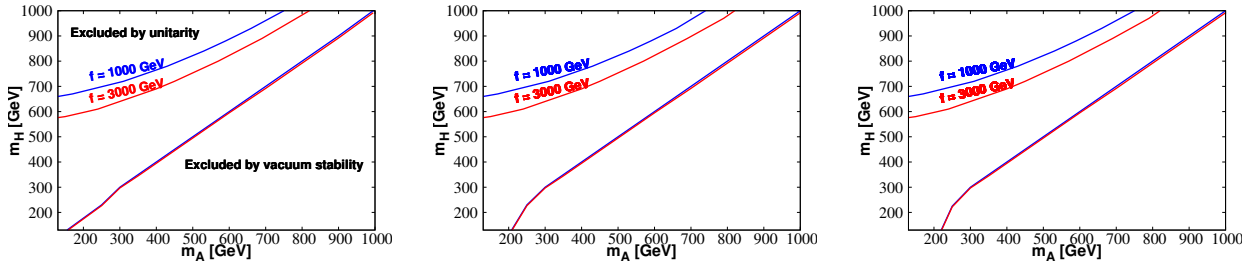

Figure 3.13: Constraint on the parameter space on the (m_A, m_H) plane by unitarity and vacuum stability in the inert case for $m_{H^\pm} = m_A = m_2$ and $\sqrt{s} = 3000$ GeV. λ_2 is fixed to be 0.1, 2 and 4 in the left, centre and right panels, respectively. A similar figure is seen in Ref. [31].

3.4 Conclusions

We have considered the bounds from perturbative unitarity as well as vacuum stability in a C2HDM based on the coset $SO(6) \to SO(4) \times SO(2)$ at the compositeness scale f. We have indicated that the ensuing eight PNGBs can be regarded as two-Higgs doublet fields and have derived from the kinetic Lagrangian according to the CCWZ method. We have assumed that the structure of the Higgs potential in the C2HDM is identical to that in the E2HDM with the softly-broken or exact Z_2 symmetry, where all the parameters in the potential are taken to be free.

In this construction, we have calculated the S-wave amplitude for the elastic two-to-two-body (pseudo)scalar boson scattering processes. We have explicitly shown that the amplitude grows with $\sqrt{s}$ in the $W_L^+W_L^- \to W_L^+W_L^-$ (equivalently $G^+G^- \to G^+G^-$) and the $H^+H^- \to H^+H^-$ processes as examples, so that unitarity is broken at a certain energy scale depending on the scale f. We have compared the allowed parameter region from the perturbative unitarity bound in these particular channels using the exact formulae and those neglecting $\mathcal{O}(1/s)$ and/or $\mathcal{O}(s^0\xi)$ terms. We have found that the results using the exact and the approximate formulae well agree in the region of $\sqrt{s} \gtrsim m_\Phi$ ($\Phi = H, A$ or $H^\pm$) and $m_\Phi \lesssim 1$ TeV which is motivated for the LHC phenomenology. Therefore, the contribution from $\mathcal{O}(s^0\xi)$ and $\mathcal{O}(s^{-1})$ terms can be safely neglected as long as we focus on this parameter region, and it allows us to get the explicit analytic expression for the eigenvalues of the S-wave amplitude for all the possible two-to-two-body (pseudo)scalar boson scattering, namely, 14 neutral, 8 singly-charged and 3 doubly-charged states.

We then have numerically demonstrated the allowed parameter space from the unitarity bound using all the aforementioned scattering channels and the vacuum stability bound as well. In this analysis, we set the mass of the SM-like Higgs boson h to be 125 GeV, the hVV coupling to be close to the SM value (as the discovered Higgs boson is consistent with the SM Higgs boson), and taken the masses of the CP-odd and charged Higgs bosons to be degenerate, i.e., $m_A = m_{H^\pm}$ (a condition compliant with EW precision data). We have also checked how results change by requiring $m_H = m_{H^\pm}$. We have discovered significant differences of the allowed parameter space in the E2HDM and C2HDM that can be exploited in order to separate phenomenologically the two Higgs scenarios. The main result that we have found is the following. If we take the no-mixing limit between h and H, i.e., $\cos\theta = 1$ and take the degenerate masses of all the extra Higgs bosons then we got the upper limit on $\sqrt{s}$ under the scan of M^2, e.g., $\sqrt{s} \lesssim 2$, 4 and 13 TeV for the case of $f = 500$, 1000 and 3000 GeV, respectively, as we have already seen this behavior in the particular scattering channels $G^+G^- \to G^+G^-$ and $H^+H^- \to H^+H^-$. If we consider the non-zero mixing case, e.g., $\cos\theta = 0.99$, we got the upper limit not only on $\sqrt{s}$ but also on m_Φ. Typically, we obtained the upper limit on m_Φ in the non-zero mixing case to be $\mathcal{O}(1)$ TeV, but this can become stronger depending on the choice of the value of $\tan\beta$ and M^2. We also have considered the case with relaxed mass degeneracy, i.e., $m_A \neq m_H$. In particular, for the case of $m_{H^\pm} = m_A = M$, we have observed that a somewhat larger mass region becomes available to the extra Higgs states H, A or $H^\pm$ in the C2HDM with respect to the E2HDM, the more so the smaller f. We have checked

that the similar behavior is seen in the case of $m_{H^\pm} = m_H = M$. However, if we take $m_{H^\pm} = m_H$ and $M = m_A$, a larger value of f gets a larger allowed parameter space. This is true irrespectively of whether we assume the additional doublet, with respect to the SM-like one, to be active or inert.

Finally, before closing, we would like to mention that our hybrid construction of the C2HDM, wherein we are using the same form of the scalar potential as in the E2HDM except for the "kinetic" term which is taken to be the first order of a chiral expansion, makes it difficult to extract trustable hints about the nature of the underlying dynamics of compositeness. In adopting such a choice for the scalar potential, we are clearly inducing a model dependence in our approach. However, by choosing the most general CP-conserving 2HDM potential which is phenomenologically viable and highlighting the parameter space regions where differences can be appeared between the E2HDM and C2HDM, our work will inform the choice of how to construct a realisation of a C2HDM (in terms of underlying gauge symmetries, their breaking patterns, and the ensuing new bosonic and fermionic spectra) that is notably different from the E2HDM. In essence, our findings will serve as a useful tool to take into account the constraints from perturbative unitarity in generic CHMs with two-Higgs-like doublets. Namely, if one calculates the CW potential in a given configuration of CHMs, then all the parameters in the Higgs potential can be written in terms of those belonging to the composite sector (such as masses and couplings of strong resonances). Using such parameters, one can then easily apply the formulae of the unitarity bounds given in this chapter to a C2HDM with a proper CW potential.

Chapter 4

Phenomenology of C2HDMs at the LHC

4.1 Overview

In this chapter, we analyse the LHC phenomenology of extra Higgs bosons in the C2HDM. We use the same kinetic Lagrangian and Higgs potential here as in Chapter 3, additionally, we introduce the effective Yukawa Lagrangian. First, we determine to deduce the necessary guidance in approaching this task from the study of theoretical (i.e., perturbativity, unitarity, vacuum stability, etc. – the subject of Ref. [31]) and experimental (one of the subjects of the present chapter) bounds, in particular by emphasising the parameter space regions where differences can be found between the E2HDM and C2HDM. This will inform the choice of how to build a phenomenologically feasible and different (from the E2HDM) realisation of a C2HDM in terms of fundamental gauge symmetries, their breaking patterns, and the ensuing new bosonic and fermionic spectrum, that is, in fact, to settle on a particular model dependence. Finally, we will discuss the LHC phenomenology by focusing on BRs and the production process of the extra Higgs bosons in the C2HDM, which we will then compare with the E2HDM [32].

4.2 Gauge couplings

As the kinetic Lagrangian for eight PNGB fields has already been determined in Chapter 3, we will show here the kinetic Lagrangian via an alternative formula. As already discussed in Chapter 3, the matrix U is transformed under $SO(6)$ non-linearly, i.e., $U \to gUh^{-1}$ with g and h being the transformation matrices for $SO(6)$ and $SO(4) \times SO(2)$, respectively. It is useful to define the linear representation of the PNGB fields from U to construct the $SO(6)$ invariant Lagrangian. In the following, we use the $SO(6)$ adjoint representation Σ, i.e., **15**-plet, which is reducible under the

$SO(4) \times SO(2)$ subgroup as $\mathbf{15} = (\mathbf{6}, \mathbf{1}) \oplus (\mathbf{4}, \mathbf{2}) \oplus (\mathbf{1}, \mathbf{1})$. Namely,

$$\Sigma = U \Sigma_0 U^T, \tag{4.1}$$

where Σ_0 is the $SO(4) \times SO(2)$ invariant VEV expressed as

$$\Sigma_0 = \begin{pmatrix} 0_{4\times4} & 0_{4\times2} \\ 0_{2\times4} & i\sigma_2 \end{pmatrix}. \tag{4.2}$$

Then, the field Σ is transformed linearly under $SO(6)$, i.e., $\Sigma \to g\Sigma g^T$.

The kinetic terms of the eight PNGB fields can then be written in terms of Σ as follows

$$\mathcal{L}_{\text{kin}} = \frac{f^2}{4} \text{tr}[D_\mu \Sigma \, (D^\mu \Sigma)^T]. \tag{4.3}$$

The covariant derivative D_μ is defined by

$$D_\mu \Sigma = \partial_\mu \Sigma - i[V_\mu, \Sigma], \tag{4.4}$$

where

$$V_\mu \equiv g(T_L^+ W_\mu^+ + T_L^- W_\mu^-) + \frac{g}{\cos\theta_W}(T_L^3 - \sin^2\theta_W Q) Z_\mu + g \sin\theta_W Q A_\mu, \tag{4.5}$$

with $T_L^\pm = (T_L^1 \pm i T_L^2)/\sqrt{2}$, $Q = T_L^3 + T_R^3$.

The formulae given in Eqs. (4.3 and 3.6) are, in fact, equivalent. In Appendix E, we present all the Feynman rules related to the discussion on Higgs phenomenology, which are obtained from the kinetic term given in Eqs. (4.3, 3.6)

4.2.1 Effective Yukawa Lagrangian

In this subsection, the low-energy (below the scale f) Yukawa Lagrangian is derived. In order to achieve this, we need to establish the embedding scheme of the SM fermions into $SO(6)$ multiplets. This embedding can be justified via the mechanism based on the partial compositeness assumption [82], where elementary SM fermions mix with composite fermions in the invariant form under the SM $SU(2)_L \times U(1)_Y$ gauge symmetry but not under the global $SO(6)$ symmetry. Through the mixing, the $SO(6)$ invariant Yukawa Lagrangian given in terms of Σ and composite fermions turns out to be the SM-like Yukawa Lagrangian after integrating out the (heavy) composite fermions.

4.2.1.1 Fermion embeddings

We consider the embeddings of the SM quarks and leptons employing **6**-plet representations of $SO(6)$. In order to regenerate the correct electric charge of the SM fermions, we introduce an additional $U(1)_X$ symmetry and assign its appropriate charge to **6**-plets. The electric charge Q is hence defined by[1] $Q = T_3^L + T_3^R + X$.

In order to understand the relation between the $SO(6)$ basis described in Eq. (3.1) and the $SU(2)_L \times SU(2)_R$ basis (T_L^3 and T_R^3 being diagonal), we introduce the unitary matrix V as

$$V = \frac{1}{\sqrt{2}} \begin{pmatrix} -i & -i & 0 & 0 & 0 & 0 \\ -1 & 1 & 0 & 0 & 0 & 0 \\ 0 & 0 & i & -i & 0 & 0 \\ 0 & 0 & 1 & 1 & 0 & 0 \\ 0 & 0 & 0 & 0 & \sqrt{2} & 0 \\ 0 & 0 & 0 & 0 & 0 & \sqrt{2} \end{pmatrix}. \tag{4.6}$$

This diagonalises the T_L^3 and T_3^R matrices as

$$V^\dagger T_L^3 V = \text{diag}\left(-\frac{1}{2}, \frac{1}{2}, -\frac{1}{2}, \frac{1}{2}, 0, 0\right), \quad V^\dagger T_R^3 V = \text{diag}\left(-\frac{1}{2}, \frac{1}{2}, \frac{1}{2}, -\frac{1}{2}, 0, 0\right). \tag{4.7}$$

In this $SU(2)_L \times SU(2)_R$ basis, we can allocate the charges of $T_{L,R}^3$ for the multiplet ψ_X (with X charge) as

$$\psi_X = (\psi_{--}, \psi_{++}, \psi_{-+}, \psi_{+-}, \psi_{00}, \psi'_{00})_X^T. \tag{4.8}$$

In the $SO(6)$ basis, we attain the **6**-plet fermion Ψ_X, with the $U(1)_X$ charge X expressed as a mixture of the states in the $SU(2)_L \times SU(2)_R$ basis, as follows:

$$\begin{aligned} \Psi_X &= V\psi_X \\ &= \left[-i\frac{\psi_{++} + \psi_{--}}{\sqrt{2}}, \frac{\psi_{++} - \psi_{--}}{\sqrt{2}}, i\frac{\psi_{-+} - \psi_{+-}}{\sqrt{2}}, \frac{\psi_{-+} + \psi_{+-}}{\sqrt{2}}, \psi_{00}, \psi'_{00}\right]_X^T, \end{aligned} \tag{4.9}$$

where ψ_{++}, ψ_{+-}, ψ_{-+} and ψ_{--} denote the $(+1/2, +1/2)$, $(+1/2, -1/2)$, $(-1/2, +1/2)$ and $(-1/2, -1/2)$ state for (T_L^3, T_R^3), while ψ_{00} and ψ'_{00} are singlets under $SU(2)_L$ and $SU(2)_R$, respectively. From this relation, the SM quarks and leptons can be embedded into the **6**-plet representation Ψ_X

[1] The $U(1)_X$ charge for the Higgs doublets Φ_α must be equal to zero to have a neutral component.

as follows:

$$(\Psi_{2/3})_L \equiv Q_L^u = (-id_L, -d_L, -iu_L, u_L, 0, 0)^T, \tag{4.10}$$
$$(\Psi_{-1/3})_L \equiv Q_L^d = (-iu_L, u_L, id_L, d_L, 0, 0)^T, \tag{4.11}$$
$$(\Psi_{2/3})_R \equiv U_R = (0, 0, 0, 0, 0, u_R)^T, \tag{4.12}$$
$$(\Psi_{-1/3})_R \equiv D_R = (0, 0, 0, 0, 0, d_R)^T, \tag{4.13}$$
$$(\Psi_{-1})_L \equiv L_L = (-i\nu_L, \nu_L, ie_L, e_L, 0, 0)^T, \tag{4.14}$$
$$(\Psi_{-1})_R \equiv E_R = (0, 0, 0, 0, 0, e_R)^T. \tag{4.15}$$

4.2.1.2 Yukawa Lagrangian

The Yukawa Lagrangian at low energy is introduced in terms of the **15**-plet of PNGB fields Σ and the **6**-plet of fermions determined in the previous subsection:

$$\mathcal{L}_Y = f\left[\overline{Q}_L^u(a_u\Sigma - b_u\Sigma^2)U_R + \overline{Q}_L^d(a_d\Sigma - b_d\Sigma^2)D_R + \overline{L}_L(a_e\Sigma - b_e\Sigma^2)E_R\right] + \text{h.c.} \tag{4.16}$$

Note that the Σ^3 term is equivalent to the $-\Sigma$ term, hence the terms with the cubic and more than cubic power of Σ do not provide any extra independent contributions to the Yukawa Lagrangian. The parameters a_f and b_f should be understood as being 3×3 complex matrices in flavour space. The a_f and b_f terms are expanded as follows (e.g., for the up-type Yukawa interaction)

$$\begin{aligned}
&f\overline{Q_L^u}a_u\Sigma U_R \\
&= fa_u(\overline{q_L^u})_{\hat{a}}(\Sigma_{4\times2})_{\hat{a}\alpha}(u_R)_\alpha \\
&= a_u(\overline{q_L^u})_{\hat{a}}\left\{(-\phi_2^{\hat{a}}, \phi_1^{\hat{a}})_\alpha - \frac{1}{f^2}\left[\frac{\phi_1\cdot\phi_2}{3}\phi_1^{\hat{a}} - \left(\frac{\phi_1^2}{2} + \frac{\phi_2^2}{6}\right)\phi_2^{\hat{a}}, \left(\frac{\phi_1^2}{6} + \frac{\phi_2^2}{2}\right)\phi_1^{\hat{a}} - \frac{\phi_1\cdot\phi_2}{3}\phi_2^{\hat{a}}\right]_\alpha\right\}(u_R)_\alpha \\
&= a_u(\overline{q_L^u})_{\hat{a}}\left[\phi_1^{\hat{a}} - \frac{1}{f^2}\left(\frac{\phi_1^2}{6} + \frac{\phi_2^2}{2}\right)\phi_1^{\hat{a}} + \frac{1}{f^2}\frac{\phi_1\cdot\phi_2}{3}\phi_2^{\hat{a}}\right]u_R, \\
&f\overline{Q_L^u}b_u\Sigma^2U_R \\
&= fb_u(\overline{q_L^u})_{\hat{a}}\Big[(\Sigma_{4\times4})_{\hat{a}j}(\Sigma_{4\times2})_{j\alpha} + (\Sigma_{4\times2})_{\hat{a}\beta}(\Sigma_{2\times2})_{\beta\alpha}\Big](u_R)_\alpha \\
&= b_u(\overline{q_L^u})_{\hat{a}}\left\{-(\phi_1^{\hat{a}}, \phi_2^{\hat{a}})_\alpha + \frac{2}{3f^2}\left[\phi_1^2\phi_1^{\hat{a}} + (\phi_1\cdot\phi_2)\phi_2^{\hat{a}}, \phi_2^2\phi_2^{\hat{a}} + (\phi_1\cdot\phi_2)\phi_1^{\hat{a}}\right]_\alpha\right\}(u_R)_\alpha \\
&= b_u(\overline{q_L^u})_{\hat{a}}\left\{-\phi_2^{\hat{a}} + \frac{1}{f^2}\frac{2}{3}\left[(\phi_1\cdot\phi_2)\phi_1^{\hat{a}} + \phi_2^2\phi_2^{\hat{a}}\right]\right\}u_R,
\end{aligned} \tag{4.17}$$

where $\phi_{1,2}^2 = \Sigma_{\hat{a}}\phi_{1,2}^{\hat{a}}\phi_{1,2}^{\hat{a}}$ and $\phi_1.\phi_2 = \Sigma_{\hat{a}}\phi_1^{\hat{a}}\phi_2^{\hat{a}}$.

We also expand the Yukawa interactions with the right-handed down-type quark and the charged lepton in a similar way because of the similar structure of the embeddings in the $SO(6)$ **6**-plet. Hence, the expanded form of the whole Yukawa Lagrangian is given by

$$\mathcal{L}_Y = \sum_{f=u,d,e} (\overline{\psi_L^f})_{\hat{a}} \Bigg\{ a_f \left[\phi_1^{\hat{a}} - \frac{1}{f^2}\left(\frac{\phi_1^2}{6} + \frac{\phi_2^2}{2}\right)\phi_1^{\hat{a}} + \frac{1}{f^2}\frac{\phi_1\cdot\phi_2}{3}\phi_2^{\hat{a}} \right] + b_f \left[\phi_2^{\hat{a}} - \frac{1}{f^2}\frac{2}{3}\left[(\phi_1\cdot\phi_2)\phi_1^{\hat{a}} + \phi_2^2\phi_2^{\hat{a}} \right] \right] \Bigg\} \psi_R^f. \tag{4.18}$$

This Lagrangian is rewritten up to the order $1/f^2$ by using the complex doublet form of the Higgs field defined in Eq. (3.5), as

$$\begin{aligned}
\mathcal{L}_Y =& \sqrt{2}a_u\overline{Q_L}\left[\tilde{\Phi}_1 - \frac{1}{f^2}\tilde{\Phi}_1\left(\frac{1}{3}\Phi_1^\dagger\Phi_1 + \Phi_2^\dagger\Phi_2\right) + \frac{1}{3f^2}\tilde{\Phi}_2(\Phi_1^\dagger\Phi_2 + \text{h.c.})\right] u_R \\
&+ \sqrt{2}b_u\overline{Q_L}\left[\tilde{\Phi}_2 - \frac{2}{3f^2}\left(\tilde{\Phi}_1(\Phi_1^\dagger\Phi_2 + \text{h.c.}) + 2\tilde{\Phi}_2(\Phi_2^\dagger\Phi_2)\right)\right] u_R \\
&+ \sqrt{2}a_d\overline{Q_L}\left[\Phi_1 - \frac{1}{f^2}\Phi_1\left(\frac{1}{3}\Phi_1^\dagger\Phi_1 + \Phi_2^\dagger\Phi_2\right) + \frac{1}{3f^2}\Phi_2(\Phi_1^\dagger\Phi_2 + \text{h.c.})\right] d_R \\
&+ \sqrt{2}b_d\overline{Q_L}\left[\Phi_2 - \frac{2}{3f^2}\left(\Phi_1(\Phi_1^\dagger\Phi_2 + \text{h.c.}) + 2\Phi_2(\Phi_2^\dagger\Phi_2)\right)\right] d_R \\
&+ \sqrt{2}a_e\overline{L_L}\left[\Phi_1 - \frac{1}{f^2}\Phi_1\left(\frac{1}{3}\Phi_1^\dagger\Phi_1 + \Phi_2^\dagger\Phi_2\right) + \frac{1}{3f^2}\Phi_2(\Phi_1^\dagger\Phi_2 + \text{h.c.})\right] e_R \\
&+ \sqrt{2}b_e\overline{L_L}\left[\Phi_2 - \frac{2}{3f^2}\left(\Phi_1(\Phi_1^\dagger\Phi_2 + \text{h.c.}) + 2\Phi_2(\Phi_2^\dagger\Phi_2)\right)\right] e_R,
\end{aligned} \tag{4.19}$$

where $\tilde{\Phi}_\alpha = i\sigma_2\Phi_\alpha^*$. The fermion mass terms, at the same order, are then derived to be:

$$m_f = v_{\text{SM}}\left[a_f c_\beta + b_f s_\beta\left(1 - \frac{\xi}{2}\right)\right]. \tag{4.20}$$

The interaction terms for h, H, A and $H^\pm$ are extracted as follows:

$$\begin{aligned}
\mathcal{L}_Y =& \sum_{f=u,d,e} \bar{f}(X_f^h h + X_f^H H - 2iI_f X_f\gamma_5 A)f \\
&+ \sqrt{2}\bar{u}(X_d^A P_R - X_u^A P_L)d\,H^+ + \sqrt{2}\bar{\nu}X_e^A P_R\, e\, H^+ + \text{h.c.},
\end{aligned} \tag{4.21}$$

where $I_f = +1/2$ $(-1/2)$ for $f = u(d,e)$, and

$$X_f^h = \left[a_f c_\beta\left(1 - \frac{\xi}{2}\right) + b_f s_\beta(1-2\xi)\right]c_\theta + \left[-a_f s_\beta + b_f c_\beta\left(1 - \frac{\xi}{2}\right)\right]s_\theta, \tag{4.22}$$

$$X_f^H = -\left[a_f c_\beta\left(1 - \frac{\xi}{2}\right) + b_f s_\beta(1-2\xi)\right]s_\theta + \left[-a_f s_\beta + b_f c_\beta\left(1 - \frac{\xi}{2}\right)\right]c_\theta, \tag{4.23}$$

$$X_f^A = -a_f s_\beta\left(1 - \frac{\xi}{2}\right) + b_f c_\beta, \quad (f = u,d,e). \tag{4.24}$$

	U_R	D_R	E_R	(a_u, b_u)	(a_d, b_d)	(a_e, b_e)	$\bar{X}_u^h$	$\bar{X}_d^h$	$\bar{X}_e^h$	$\bar{X}_u^H$	$\bar{X}_d^H$	$\bar{X}_e^H$	$\bar{X}_u^A$	$\bar{X}_d^A$	$\bar{X}_e^A$
Type-I	$-$	$-$	$-$	$(0, \surd)$	$(0, \surd)$	$(0, \surd)$	ζ_h	ζ_h	ζ_h	ζ_H	ζ_H	ζ_H	ζ_A	ζ_A	ζ_A
Type-II	$-$	$+$	$+$	$(0, \surd)$	$(\surd, 0)$	$(\surd, 0)$	ζ_h	ξ_h	ξ_h	ζ_H	ξ_H	ξ_H	ζ_A	ξ_A	ξ_A
Type-X	$-$	$-$	$+$	$(0, \surd)$	$(0, \surd)$	$(\surd, 0)$	ζ_h	ζ_h	ξ_h	ζ_H	ζ_H	ξ_H	ζ_A	ζ_A	ξ_A
Type-Y	$-$	$+$	$-$	$(0, \surd)$	$(\surd, 0)$	$(0, \surd)$	ζ_h	ξ_h	ζ_h	ζ_H	ξ_H	ζ_H	ζ_A	ξ_A	ζ_A

Table 4.1: Classification in charge assignments of the C_2 symmetry in the C2HDM. All the left-handed fermions Q_L^u, Q_L^d and L_L are even under C_2 symmetry. In the third column, the symbol $\surd$ indicates non-zero a_f or b_f. A similar table is seen in Ref. [32]

Again, note that the above X_f^ϕ ($\phi = h, H, A$) couplings are 3×3 matrices in flavor space. In general, these matrices are non-diagonal in the mass eigenbasis of fermions, so that FCNCs appear at the tree level because of the presence of two independent 3×3 Yukawa couplings a_f and b_f. In short, the FCNC problem results from the fact that both of the doublets Φ_1 and Φ_2 couple to each fermion type, i.e., up-type quarks, down-type quarks and charged leptons. This feature is kept even if we set the E2HDM limit $f \to \infty$. As a result, our Yukawa Lagrangian introduced in Eq. (4.19) reproduces the so-called Type-III E2HDM. In the next subsection, we focus on the case without tree level FCNCs.

4.2.1.3 C_2 symmetric Yukawa Lagrangian

In order to eliminate FCNCs at the tree level, we implement a C_2 symmetry [45] as the following:

$$U(\pi_1^{\hat{a}}, \pi_2^{\hat{a}}) \to C_2 U(\pi_1^{\hat{a}}, \pi_2^{\hat{a}}) C_2 = U(\pi_1^{\hat{a}}, -\pi_2^{\hat{a}}), \tag{4.25}$$

where

$$C_2 = \mathrm{diag}(1, 1, 1, 1, 1, -1). \tag{4.26}$$

By this definition, $\pi_1^{\hat{a}}$ and $\pi_2^{\hat{a}}$ have a C_2-even and C_2-odd charge, respectively, i.e., $(\pi_1^{\hat{a}}, \pi_2^{\hat{a}}) \to (\pi_1^{\hat{a}}, -\pi_2^{\hat{a}})$. Relying on C_2 the charge assignment of the right-handed fermions, we can determine four independent types of Yukawa interactions, similar to the Z_2 symmetric version of the E2HDM [57, 67, 104], as indicated in Tab. 4.1. The Yukawa Lagrangian for each type of fermion is described through a_f or b_f, e.g., the Type-I Yukawa interaction is obtained by taking $a_f = 0$.

Under C_2 symmetry, we obtain the following interaction terms in the mass eigenbasis of the fermions:

$$\begin{aligned}\mathcal{L}_Y = &\sum_{f=u,d,e} \frac{m_f}{v_{\rm SM}} \bar{f}\Big(\bar{X}_f^h h + \bar{X}_f^H H - 2i I_f \bar{X}_f^A \gamma_5 A\Big) f \\ &+ \frac{\sqrt{2}}{v_{\rm SM}} \bar{u} V_{ud} (m_d \bar{X}_d^A P_R - m_u \bar{X}_u^A P_L) d\, H^+ + \frac{\sqrt{2}}{v_{\rm SM}} \bar{\nu} m_e \bar{X}_e^A P_R\, e\, H^+ + \text{h.c.},\end{aligned} \tag{4.27}$$

where $I_f = +1/2$ $(-1/2)$ for $f = u$ (d, e), V_{ud} are the CKM matrix elements and $P_{L,R}$ are the projection operators for left- and right-handed fermions. The coefficients $\bar{X}_f^\phi$ are diagonal in the mass eigenbasis of fermions, which is obtained from X_f^ϕ by the following method:

$$\bar{X}_f^\phi = \frac{v_{\rm SM}}{m_f} V_L^\dagger X_f^\phi V_R, \tag{4.28}$$

where V_L and V_R are the diagonalisation matrices obtained from the left-handed and right-handed fermions, respectively. The coefficients $\bar{X}_f^{h,H,A}$ can be either $\zeta_{h,H,A}$ or $\xi_{h,H,A}$, as presented in Tab. 4.1, and their expressions, at the first order in ξ, are defined by

$$\zeta_h = \left(1 - \frac{3}{2}\xi\right) c_\theta + s_\theta \cot\beta, \quad \xi_h = \left(1 - \frac{\xi}{2}\right) c_\theta - s_\theta \tan\beta, \tag{4.29}$$

$$\zeta_H = -\left(1 - \frac{3}{2}\xi\right) s_\theta + c_\theta \cot\beta, \quad \xi_H = -\left(1 - \frac{\xi}{2}\right) s_\theta - c_\theta \tan\beta, \tag{4.30}$$

$$\zeta_A = \left(1 + \frac{\xi}{2}\right) \cot\beta, \quad \xi_A = -\left(1 - \frac{\xi}{2}\right) \tan\beta. \tag{4.31}$$

In the limit of $\xi \to 0$, these coefficients get the same form as the corresponding ones in a softly-broken Z_2 symmetric version of the E2HDM [67].

4.3 Phenomenology

In this section, we discuss how we can discriminate the C2HDM from the E2HDM. Firstly, we discuss the constraints on the parameter space in the C2HDM from various (null) searches of extra Higgs bosons at collider experiments (Sec. 4.3.1). Secondly, we focus on deviations in the SM-like Higgs boson (h) couplings from the SM predictions (Sec. 4.3.2). Thirdly, we discuss the difference in the properties of the decay (Sec. 4.3.3) and production mechanisms at the LHC (Sec. 4.3.4) of the extra Higgs bosons.

Before proceeding further though, we ought to note now that CHMs usually also predict heavy spin-1 and spin-1/2 states via the partial compositeness mechanism. These extra particles can potentially enter the ensuing phenomenological analysis through loop induced couplings of the composite Higgs bosons to Z, photons and gluons. Contributions from these particles to loop-induced Higgs production and/or decay modes were studied in detail in Ref. [105] (albeit for a single doublet realisation of a CHM). It was found therein that the individual extra gauge boson contributions to the loop induced couplings of the SM-like h state are always negligible while this is not the case for the extra fermion ones. However, the extra fermion effects are not dramatically large, i.e., at the $\mathcal{O}(1\%)$ level in the $h \to \gamma\gamma, \gamma Z$ cases and $\mathcal{O}(10\%)$ in the $h \to gg$ case. Thus, Ref. [105] indicates that all such contributions to h phenomenology at the LHC are not crucial for our purposes. Similarly, we expect that these extra resonances (both bosons and fermions) will not affect significantly the $H, A \to gg, \gamma\gamma$ and $Z\gamma$ partial widths either. Hence, in our forthcoming

Model Type	$\xi = 0.08$	$\xi = 0.04$	$\xi = 0$
Type I	$pp \to H \to ZZ \to 4\ell$ [106] $qQ \to q'Q'h \to WW \to 2\ell 2\nu$ [108]	$pp \to H \to ZZ \to 4\ell$ [106] $qQ \to q'Q'h \to WW \to 2\ell 2\nu$ [108]	$pp \to H \to ZZ \to 4\ell$ [106] $qQ \to q'Q'h \to WW \to 2\ell 2\nu$ [108]
Type II	$pp \to H \to ZZ \to 4\ell$ [106] $pp \to h \to ZZ \to 4\ell$ [109]	$pp \to H \to ZZ \to 4\ell$ [106] $qQ \to q'Q'h \to WW \to 2\ell 2\nu$ [108] $pp \to h \to ZZ \to 4\ell$ [109]	$pp \to H \to ZZ \to 4\ell$ [106] $qQ \to q'Q'h \to WW \to 2\ell 2\nu$ [108] $pp \to h \to ZZ \to 4\ell$ [109] $pp \to h \to WW^* \to \ell\nu\ell\nu$ [113]
Type X	$pp \to H \to ZZ \to 4\ell$ [106] $qQ \to q'Q'h \to WW \to 2\ell 2\nu$ [108] $gg \to \phi(h, H) \to \tau\tau$ [110] $pp \to h \to \tau\tau$ [111] $pp \to Vh \to V\tau\tau$ [112]	$pp \to H \to ZZ \to 4\ell$ [106] $qQ \to q'Q'h \to WW \to 2\ell 2\nu$ [108] $gg \to \phi(h, H) \to \tau\tau$ [110] $pp \to h \to \tau\tau$ [111] $pp \to Vh \to V\tau\tau$ [112]	$pp \to H \to ZZ \to 4\ell$ [106] $pp \to h \to \tau\tau$ [111]
Type Y	$pp \to H \to ZZ \to 4\ell$ [106] $pp \to H \to hh \to 4b$ [107] $pp \to h \to ZZ \to 4\ell$ [109]	$pp \to H \to ZZ \to 4\ell$ [106] $pp \to H \to hh \to 4b$ [107] $pp \to h \to ZZ \to 4\ell$ [109]	$pp \to H \to ZZ \to 4\ell$ [106] $pp \to H \to hh \to 4b$ [107] $pp \to h \to ZZ \to 4\ell$ [109] $pp \to h \to WW^* \to \ell\nu\ell\nu$ [113]

Table 4.2: Higgs search channels generally give excluding parameter points in Fig. 4.1. A similar table is seen in Ref. [32].

C2HDM analysis at the LHC, we will not include all such effects.

4.3.1 Bounds from collider experiments

Let us discuss constraints on the parameter space of the E2HDM and C2HDM from data gathered at LEP, Tevatron and LHC by using the `HiggsBounds` [114–119] (v4.3.1) package. This tells us if a given set of model parameters is allowed at 95% Confidence Level (CL) by various (null) searches of Higgs bosons.

In Fig. 4.1, we display the allowed parameter space (green shaded) in the $(\sin\theta, \tan\beta)$ plane using `HiggsBounds`. We can see that larger values of ξ give more excluded regions in the Type-I C2HDM, but in the other three models the ξ dependence is not so crucial. In particular, in the Type-I C2HDM with $\xi = 0.08$, negative values of $\sin\theta$ are mostly excluded, mainly because of the positive deviation of the signal strength for the vector boson fusion production of h (the SM-like state) decaying into W^+W^- [108], as compared to the Type-I E2HDM (related to $\xi = 0$ and presented in the first column of Fig. 4.1). In the Type-X C2HDM, additional exclusion parameter regions emerge for larger ξ, which is mostly due to the same reasons as in the Type-I C2DHM. In the Type-II and -Y C2HDMs, the excluded regions almost do not depend upon the ξ value. In Tab. F.1 we list the Higgs search channels most responsible for the exclusions.

In Fig. 4.1 we also present the compatibility of the signal strengths of the SM-like Higgs boson h based on a $\Delta\chi^2$ analysis by using the `HiggsSignals` [120] (v1.4.0) package. In this figure, the black, red and blue contours respectively show the compatibility with 68.27% CL, 95.45% CL and 99.73% CL from the value of $\Delta\chi^2 = \chi^2 - \chi^2_{\rm min}$ in the $(\sin\theta, \tan\beta)$ plane. Apart from the Type-I case, which reveals a better compliance with the LHC data (this is after all the scenario which more closely resembles the SM), the other three types respond similarly to the LHC Higgs data.

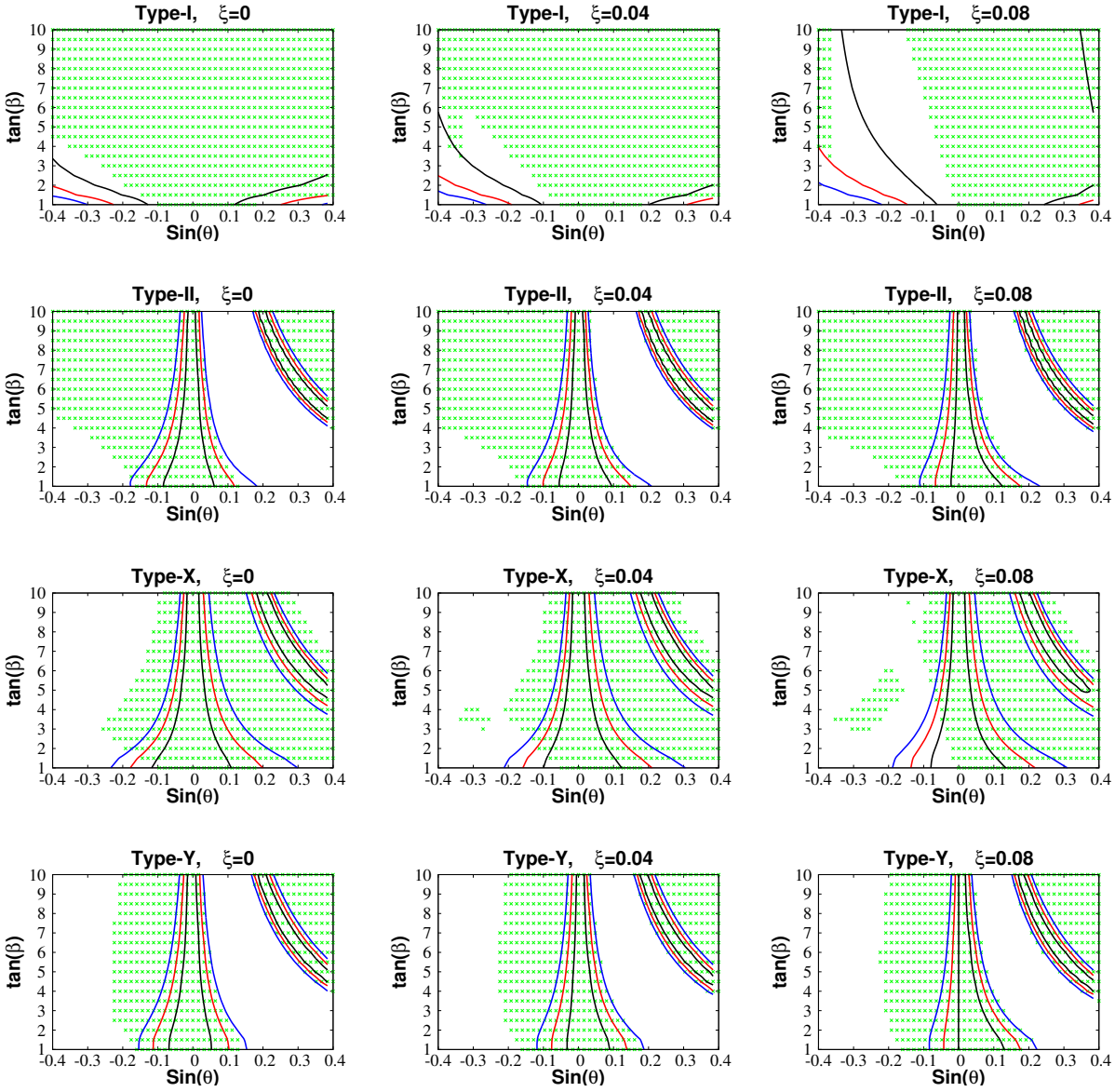

Figure 4.1: Regions allowed at 95% CL from LEP, Tevatron and LHC experiments in the Type-I, -II, -X and -Y C2HDMs (green shaded). The black, red and blue curves represent the contours for $\Delta\chi^2 = 2.30$ (68.27% CL), 6.18 (95.45% CL) and 11.83 (99.73% CL), respectively. The reference input values are taken as $m_h = 125$ GeV, $m_H = m_{H^\pm} = m_A = 500$ GeV and $M = 0.8\ m_A$. The first, second, and third column of the panels display the results with $\xi = 0,\ 0.04,\ 0.08$, respectively. A similar figure is seen in Ref. [32].

Overall, the ξ dependence is only marginally evident, being more pronounced for Type-I.

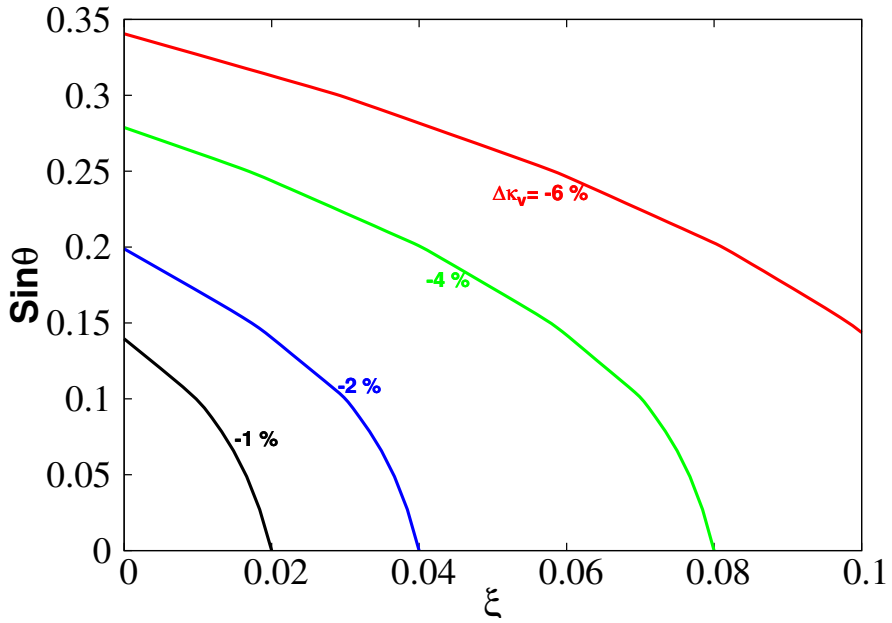

Figure 4.2: Contour plot shows the deviation in the hVV couplings $\Delta\kappa_V = \kappa_V - 1$ from the SM prediction. A similar figure is seen in Ref. [32].

4.3.2 Modification of the Higgs boson couplings

In both the E2HDM and the C2HDM, the Higgs boson couplings can deviate from the predictions in the SM. However, the patterns of deviations can be distinct between these two scenarios. In order to discuss these, it is convenient to introduce the scaling factor κ_X for the hXX couplings by $\kappa_X = g^{\rm NP}_{hXX}/g^{\rm SM}_{hXX}$ and $\Delta\kappa_X = \kappa_X - 1$. In the C2HDM, these deviations are given at the tree level by

$$\kappa_V = \left(1 - \frac{\xi}{2}\right) c_\theta \quad (V = W, Z), \qquad \kappa_f = X^h_f = \zeta_h \ \text{ or } \ \xi_h \quad (f = u, d, e). \tag{4.32}$$

We can easily derive those for the E2HDM by taking $\xi \to 0$ corresponding to $f \to \infty$. We can see that two sources contribute to $\kappa_X \neq 1$ in the C2HDM, i.e., non-zero values of ξ and θ. By contrast, only $\theta \neq 0$ yields $\kappa_X \neq 1$ in the E2HDM[2]. Hence, for a given measured value of κ_X, the value of θ is determined in the E2HDM while only the combination (θ, ξ) is determined in the C2HDM.

Fig. 4.2 shows the contour for $\Delta\kappa_V$ as a function of ξ and $\sin\theta$. Note that there is no sign dependence of $\sin\theta$ in this plot. From this figure, it can be seen that one can reproduce a fixed value of the deviation $\Delta\kappa_V$ at $\xi = 0$ which corresponds to the E2HDM in the C2HDM by using a different parameter with a non-zero θ and/or ξ. For example, we can reproduce the deviation $|\Delta\kappa_V| = -2\%$ by setting (ξ, θ) to be $(0.04, 0)$, $(0.03, 0.1)$ and $(0, 0.2)$. This result suggests an

[2]The hVV couplings can also be altered by radiative corrections, but their typical magnitude is less than 1% [91, 121] according to the tree level prediction in the E2HDM.

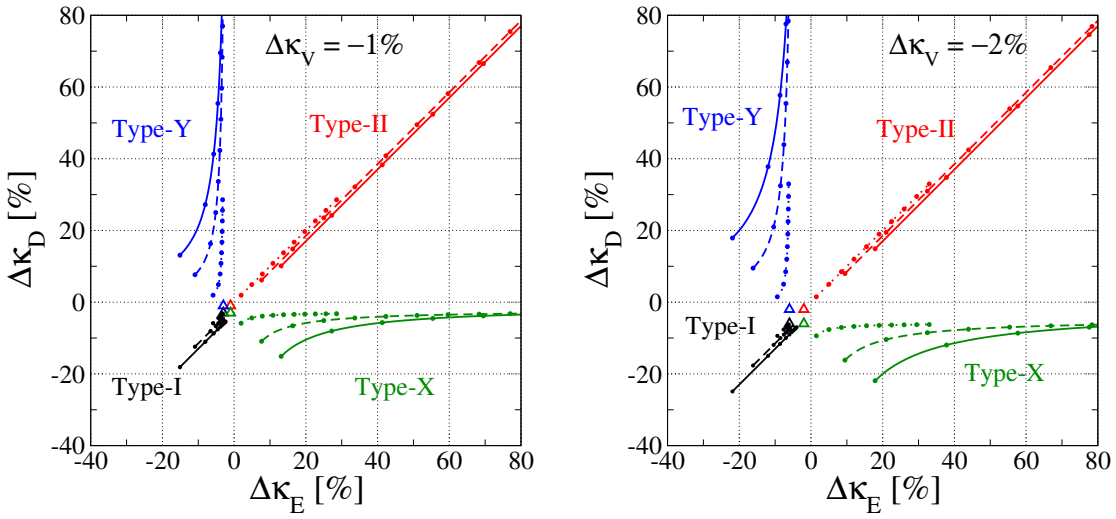

Figure 4.3: We plot the correlation between the Yukawa coupling deviations of the $\Delta\kappa_E$ (E represents a charged lepton) and $\Delta\kappa_D$ (D represents a down-type quark) in the C2HDMs with $s_\theta < 0$. The left (right) panel shows the case for $\Delta\kappa_V = -1(-2)\%$. The black, red, green and blue curves display the results in the Type-I, -II, -X and -Y C2HDM, respectively, while the solid, dashed and dotted curves display the case for $f = \infty$, 2200 (1500) GeV and 1780 (1250) GeV, respectively, for the left (right) panel. Each dot on the curve indicates the prediction with $\tan\beta = 1$ to 10 with an interval of 1, and the dot at the left edge on each curve corresponds to $\tan\beta = 1$. The triangles represent the prediction with $\theta = 0$. A similar figure is seen in Ref. [32].

interesting consequence, namely, even if there is no mixing between the CP-even Higgs bosons h and H, in the C2HDM, we can have a non-zero deviation in the hVV couplings. As a result, we will find a significant difference in the two scenarios for the decay BRs of the extra Higgs bosons for a given value of $\Delta\kappa_V$, which will be discussed in the succeeding subsections.

As it has been discussed in Ref. [122], the type of Yukawa interactions can be determined by looking at the correlation between $\Delta\kappa_E$ and $\Delta\kappa_D$ in the E2HDM, where E and D stand for a charged lepton and a down-type quark, respectively. Now, let us discuss the correlation between $\Delta\kappa_E$ and $\Delta\kappa_D$ in the C2HDM.

Fig. 4.3 shows the prediction for the four types of Yukawa interaction on the $\Delta\kappa_E$ and $\Delta\kappa_D$ plane with the settled value of $\Delta\kappa_V$ being -1% (left panel) and -2% (right panel). We set the range of the $\tan\beta$ from 1 to 10. In these plots, we determine the value of θ by fixing $\Delta\kappa_V$ and f (or equivalently ξ). For each type of Yukawa interaction, we set $f = 1780$ GeV (dotted curve), 2200 GeV (dashed curve) and ∞ (solid curve) for the left panel, when $f = 1250$ GeV (dotted curve), 1500 GeV (dashed curve) and ∞ (solid curve) for the right panel. From this figure, we can extract two essential aspects: (i) the models with a different type of Yukawa interaction can be separated by looking at $\Delta\kappa_E$ and $\Delta\kappa_D$ and (ii) for a fixed value of $\Delta\kappa_V$ and the type of Yukawa interaction, predicted regions on the $\Delta\kappa_E$-$\Delta\kappa_D$ plane can be different depending on the value of f. It is also shown that the magnitude of $\Delta\kappa_{E,D}$ with a smaller value of f tends to be small for a given value

of $\tan\beta$ as compared to that with a larger f. As an extreme case $f = 1740\,(1230)$ GeV, where the deviation $\Delta\kappa_V = -1\%\,(-2\%)$ comes only via the non-zero ξ (or equivalently the case with $s_\theta = 0$), the prediction is given as a point indicated by the triangle, because the $\tan\beta$ dependence vanishes in this case. In addition, the predicted region with a fixed range of $\tan\beta$ shrinks when the value of f is getting small, because the $\tan\beta$ dependent part of κ_f is proportional to s_θ as seen in Eq (4.29).

As a result, if a non-zero value of $\Delta\kappa_V$ is measured at collider experiments, we have an indirect evidence for a non-minimal Higgs sector, possibly belonging to a E2HDM or C2HDM. Furthermore, by looking at the pattern of the deviations in $\Delta\kappa_E$ and $\Delta\kappa_D$, we can discriminate between the four types of Yukawa interactions. In particular, if the Type-X or Type-Y Yukawa interaction is realised, the composite dynamics can also be extracted from the different allowed regions of the predictions on the $\Delta\kappa_E$–$\Delta\kappa_D$ plane. For the Type-I and Type-II cases, a prediction with a non-zero value of ξ corresponds to the case with a different value of $\tan\beta$ in the E2HDM, so that we need to use other information, such as the decay properties of the additional Higgs bosons as we will discuss below. We note that making use of information from $\Delta\kappa_U$ with U being an up-type quark is also helpful to extract the sign of s_θ as long as $\tan\beta$ and/or ξ are not very large.

4.3.3 Decays of extra Higgs bosons

Next, we study the decay properties of the additional Higgs bosons H, A and $H^\pm$ in both the E2HDM and C2HDM with the four types of Yukawa interaction. In particular, we compare the BRs of the additional Higgs bosons in the two models with the same value of $\Delta\kappa_V$. As examples, the following three benchmark points giving $\Delta\kappa_V = -2\%$ are considered:

$$\text{BP1} : (s_\theta, \xi) = (-0.2, 0), \quad \text{BP2} : (s_\theta, \xi) = (-0.1, 0.03), \quad \text{BP3} : (s_\theta, \xi) = (0, 0.04). \tag{4.33}$$

BP1 represents the E2HDM case, whereas BP2 and BP3 are two possible C2HDM cases, the latter relating to the zero-mixing angle.

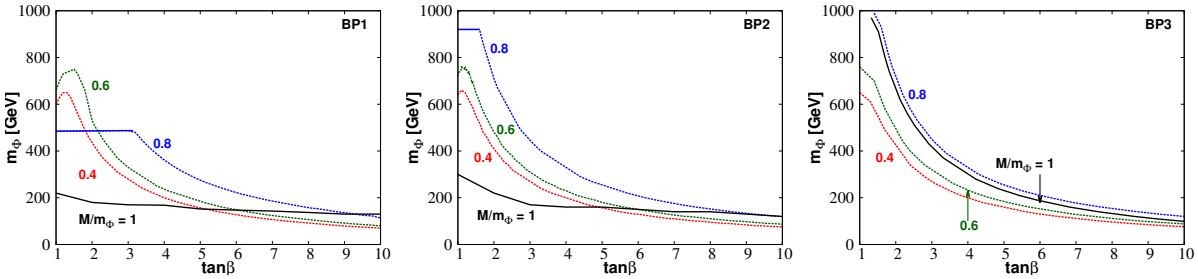

Figure 4.4: Upper bound on the mass parameter $m_\Phi (= m_{H^\pm} = m_A = m_H)$ from the perturbative unitarity (denoted by the dashed curves) and the vacuum stability bounds (denoted by the solid curves) as a function of $\tan\beta$ in BP1 (left), BP2 (centre) and BP3 (right). We determine several fixed values of the ratio M/m_Φ and $\sqrt{s} = 1$ TeV for the unitarity bound. A similar figure is seen in Ref. [32].

Before discussing the BRs, we survey the allowed parameter regions by constraints from the perturbative unitarity and the vacuum stability. Details of these bounds have been already studied in Chapter 3. Regarding to the unitarity bound, we take into account all the elastic scatterings of two-body to two-body scalar boson processes up to $\mathcal{O}(s^0)$ dependences, where $\sqrt{s}$ is the scattering energy. Differently from E2HDMs, the s-wave amplitude matrix has terms proportional to $s\,\xi$, thus showing that an UV completion of the theory is needed at high energy. Here we set $\sqrt{s}$ to be 1 TeV.

Fig. 4.4 indicates the allowed parameter region on the $(\tan\beta, m_\Phi)$ plane for the three benchmark points, where $m_\Phi = m_{H^\pm} = m_A = m_H$. The region above each curve is ruled out by perturbative unitarity or vacuum stability, so that this figure displays the absolute theoretical upper limit on m_Φ. Different colours of each curves represent different choices of the ratio M/m_Φ, being 1, 0.8. 0.6 and 0.4. We can see that, typically, the unitarity and/or the vacuum stability bounds get stronger as the value of $\tan\beta$ grows. Moreover, the case with $M/m_\Phi \lesssim 1$ tends to have a larger allowed value of m_Φ as compared to the case with $M/m_\Phi = 1$. Following this result, we take $\tan\beta = 2$, $m_\Phi \leq 500$ GeV and $M/m_\Phi = 0.8$ for the following analysis.

In Figs. 4.5, 4.6 and 4.7, we respectively present the BRs as a function of m_Φ for H, A and $H^\pm$ for BP1 (left), BP2 (centre) and BP3 (right) in the Type-I, -II, -X and -Y patterns, respectively.

When we look at the left and center panels of Fig. 4.5, we can observe the two thresholds at $m_H \simeq 250$ GeV and 350 GeV which correspond to the $H \to hh$ and $H \to t\bar{t}$ channel, respectively. If we compare them and the right panels of Fig. 4.5, we find important differences in the H decay modes. Namely, the $H \to VV$ ($V = W^+W^-$, ZZ) and $H \to hh$ modes do not appear in the right panels, as they are proportional to s_θ^2. Furthermore, in the BP3 case, the difference among the four types of Yukawa interactions becomes more clear, because only the fermionic final states of the H decay mode are dominant.

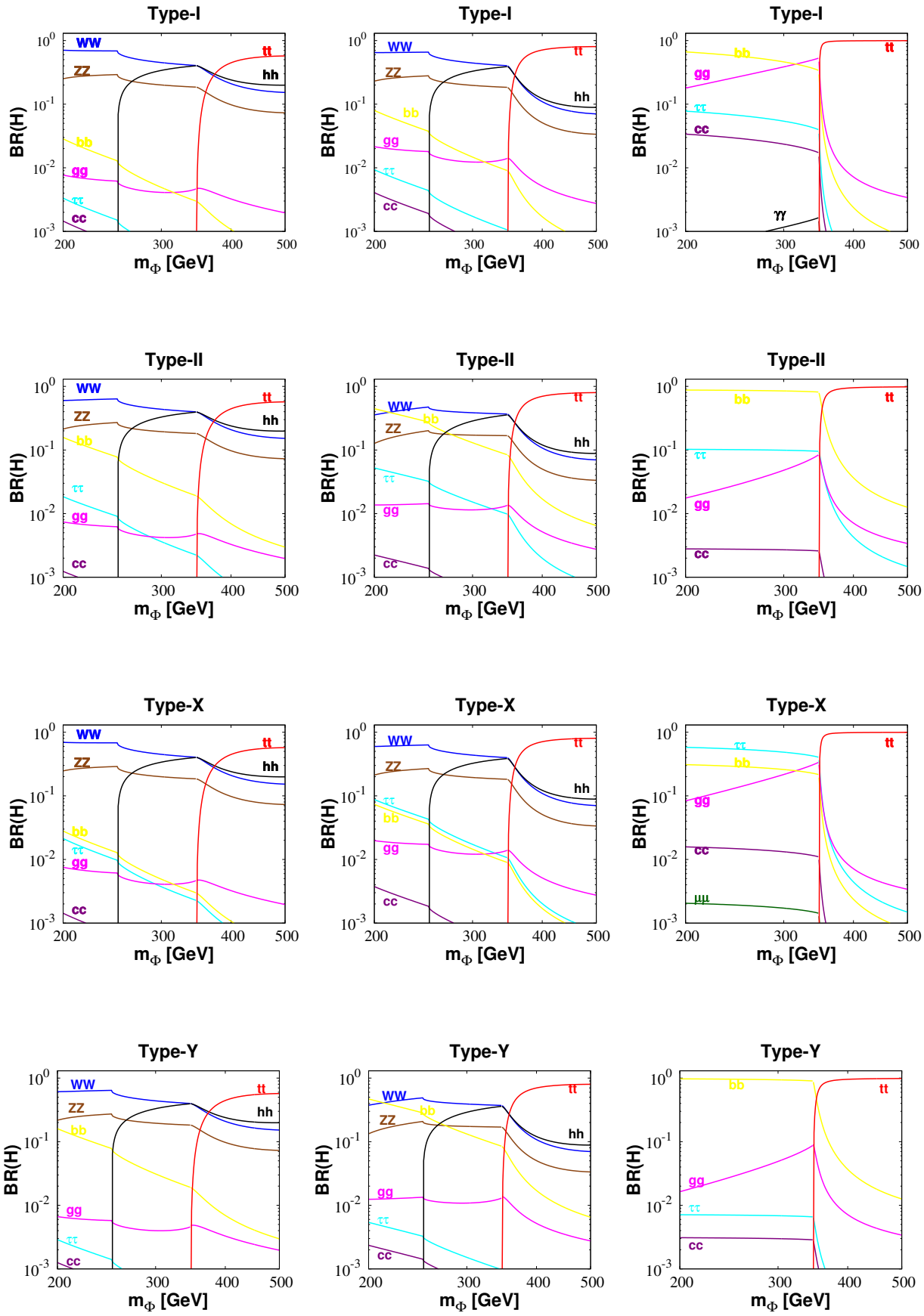

Figure 4.5: We display the BRs of H as a function of $m_\Phi (= m_H = m_A = m_{H^\pm})$ with $\tan\beta = 2$ and $M = 0.8 \times m_\Phi$ for the cases of BP1, BP2 and BP3, respectively. A similar figure is seen in Ref. [32].

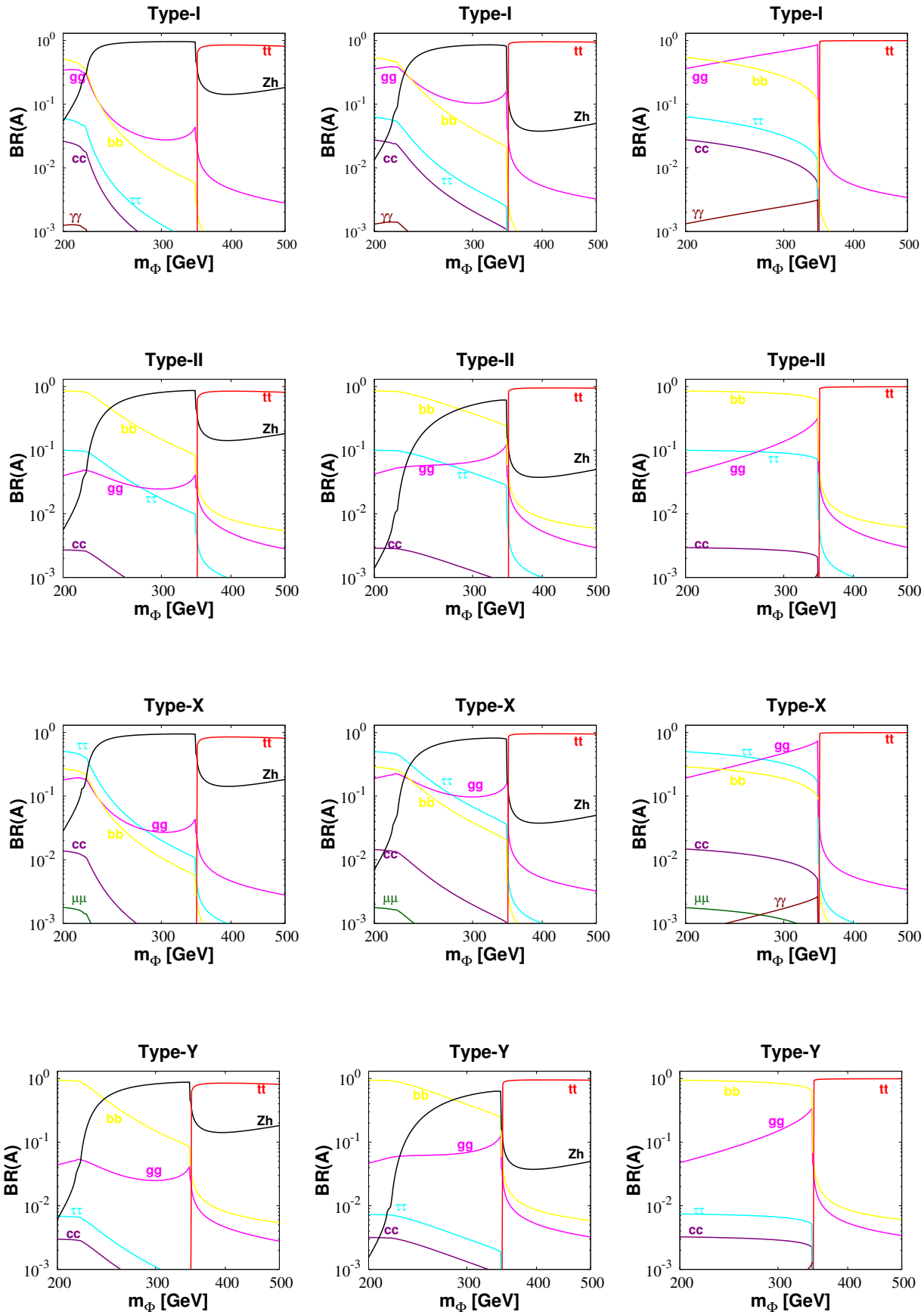

Figure 4.6: Identical to Fig. 4.5, but for the BRs of A. A similar figure is seen in Ref. [32].

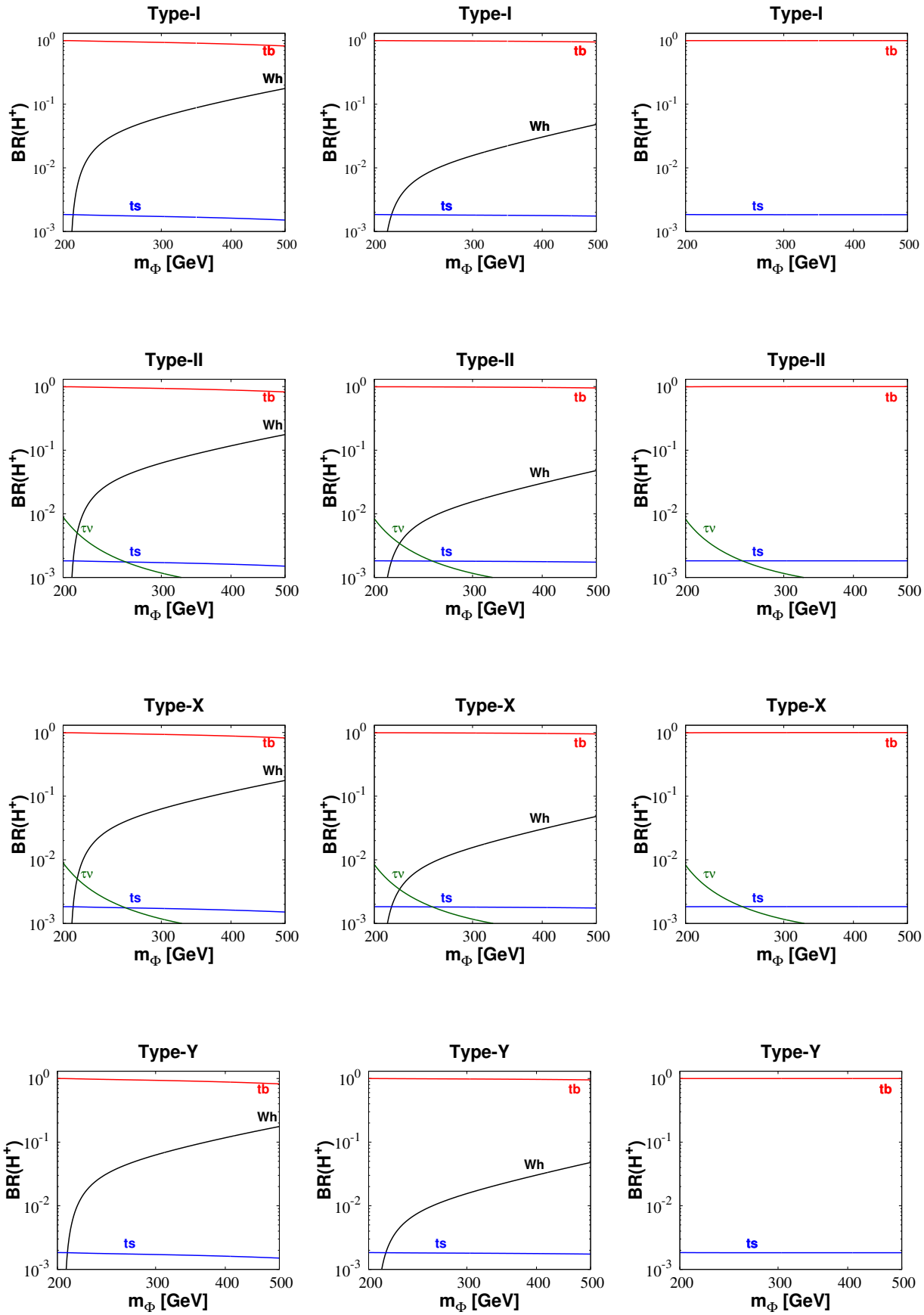

Figure 4.7: Identical to Fig. 4.5, but for the BRs of $H^{\pm}$. A similar figure is seen in Ref. [32].

Regarding the BRs of A (Fig. 4.6), it is seen that their behaviour is drastically changed at $m_A \simeq 350$ GeV. Namely, below $m_A \simeq 350$ GeV, the $A \to Z^{(*)}h$ channel can be dominant in BP1 and BP2 depending on m_Φ, while the $A \to b\bar{b}$, $\tau^+\tau^-$ and/or gg modes are dominant in BP3 depending on the type of Yukawa interactions. Notice that we have taken into account the three body decay process $A \to Z^*h \to f\bar{f}h$, which becomes important when $m_A < m_Z + m_h \simeq 215$ GeV. Conversely, above $m_A \simeq 350$ GeV, $A \to t\bar{t}$ becomes dominant in all four type models and all three benchmark points. In BP1 (BP2) with $m_A \simeq 350$ GeV, $A \to Z^{(*)}h$ can be 10–20% (a few %) level depending on m_Φ and the type of Yukawa interactions. Regarding the results for BP3, the behaviour of the BRs of A is almost the same as those of H, where the $A \to Z^{(*)}h$ mode does not appear, because its decay rate is proportional to s_θ^2. Only for the BR of the $A \to gg$ mode, it is slightly larger than that of the $H \to gg$ mode when we compare them with the same configuration, because of the difference in the loop function.

The mass dependence on the BRs of $H^\pm$ is shown in Fig. 4.7. We see that the $H^+ \to t\bar{b}$ mode is dominant in all the four types of Yukawa interactions and all the three benchmark points. In BP1 (BP2), the $H^+ \to W^{+(*)}h$ mode can be about 20% (5%) at $m_\Phi \simeq 500$ GeV.

4.3.4 Production of extra Higgs bosons at the LHC

Finally, we study on the production cross sections of the extra Higgs bosons at the LHC. We here consider the gluon fusion process $gg \to H/A$, the bottom quark-associated process $gg \to b\bar{b}H/A$ and the gluon-bottom fusion process $g\bar{b} \to H^+\bar{t}$. Indeed, the cross sections for the vector boson fusion ($qq' \to qq'H$) and vector boson-associated ($q\bar{q} \to ZH$ and $q\bar{q}' \to W^\pm H^\mp$) processes are negligibly small, since they are suppressed by the gauge-gauge-Higgs couplings (by s_θ).

In order to calculate the gluon fusion cross section, we adopt the following formalism:

$$\sigma(gg \to \phi^0) = \frac{\Gamma(\phi^0 \to gg)}{\Gamma(h_{\rm SM} \to gg)} \times \sigma(gg \to h_{\rm SM}), \quad (\phi^0 = H \text{ or } A), \tag{4.34}$$

where $h_{\rm SM}$ is the SM Higgs boson with the mass artificially fixed at m_{ϕ^0}. The value of the gluon fusion cross section $\sigma(gg \to h_{\rm SM})$ in the SM is taken from Ref. [123]. In order to calculate the other production cross section, we employ `CalcHEP` [124] and adopt the `CTEQ6L` [125] for the parton distribution functions with factorisation/renormalisation scale fixed at $Q = \sqrt{\hat{s}}$. We note that since the lepton Yukawa coupling is irrelevant for the calculation of the production cross sections, the result in the Type-I (Type-II) and Type-X (Type-Y) models are identical to each other. As in the previous subsection, we use BP1, BP2 and BP3 given in Eq. (4.33) and $\tan\beta = 2$ for the numerical analysis.

In Fig. 4.8, we plot the gluon fusion production cross section as a function of the mass of the produced Higgs boson. In this process, the dependence of the type of Yukawa interactions is almost negligible, because only the top Yukawa coupling is important to determine the size of the cross

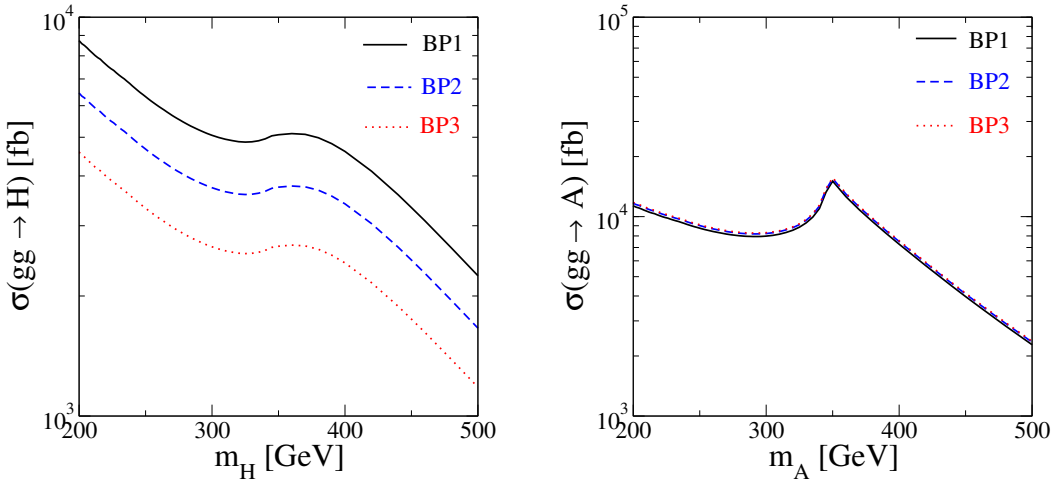

Figure 4.8: Cross section of the gluon fusion process for H (left) and A (right) as a function of the extra neutral Higgs boson mass at $\sqrt{s} = 13$ TeV in BP1, BP2 and BP3 with $\tan\beta = 2$. A similar figure is seen in Ref. [32].

section. We present the results for BP1, BP2 and BP3 as the solid, dashed, and dotted curves, respectively. We obtain differences in the cross section of $gg \to H$ among the three benchmark points, which emerges from the s_θ term in ζ_H or ξ_H given in Eq. (4.30). Conversely, the cross section for A is significantly the same for the three benchmark points because of the absence of the s_θ term in ζ_A or ξ_A given in Eq. (4.30).

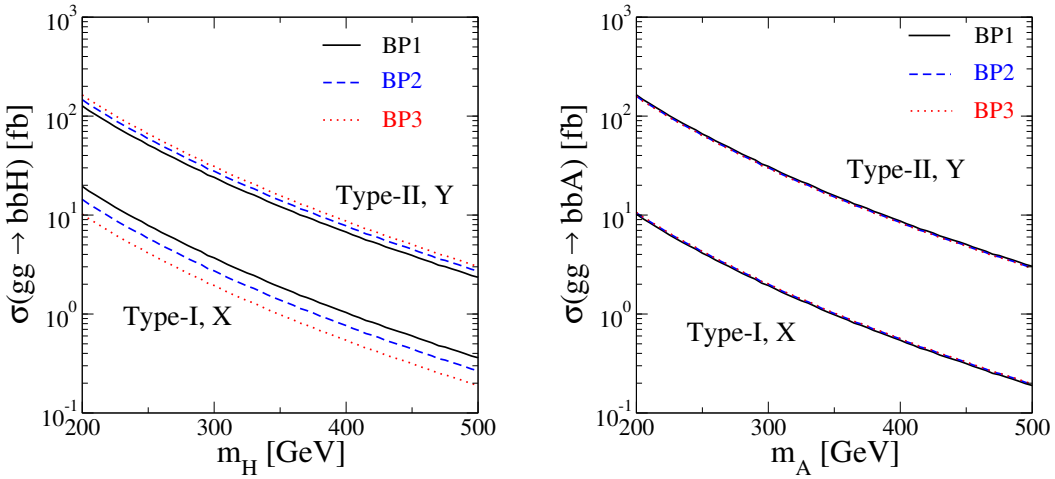

Figure 4.9: We plot the cross section for the bottom quark-associated production process for H (left) and A (right) as a function of the extra neutral Higgs boson mass at $\sqrt{s} = 13$ TeV in BP1, BP2 and BP3 with $\tan\beta = 2$. A similar figure is seen in Ref. [32].

In Fig. 4.9, we plot the cross section of the bottom quark-associated production as a function of the mass of the produced Higgs boson. Typically, the cross section is more than one order of magnitude smaller than the gluon fusion production process because of the smallness of the

bottom Yukawa coupling and the three body phase space. Differently from the gluon fusion, the dependence of the type is important, because the bottom Yukawa coupling determines the size of the cross section. In fact, the cross section in Type-II and Type-Y is almost one order of magnitude greater than that in Type-I and Type-X. Similar to the case for the gluon fusion, a larger discrepancies of the cross section among BP1, BP2 and BP3 is seen for the production of H state, as for the A one differences are marginal.

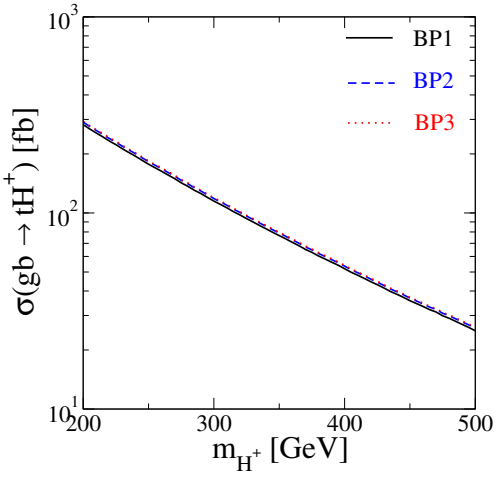

Figure 4.10: Plot of the cross section of the gluon bottom fusion process of $H^{\pm}$ as a function of the extra neutral Higgs boson mass at $\sqrt{s} = 13$ TeV in BP1, BP2 and BP3 with $\tan\beta = 2$. A similar figure is seen in Ref. [32].

In Fig. 4.10, we plot the gluon-bottom fusion production cross section for the $H^{\pm}$ state. Similar to the gluon fusion process, the dependence of the type of Yukawa interactions is almost negligible, because of containing the top Yukawa coupling. The differences among the three benchmark points are negligibly small.

To conclude, in this section, we have compared the differences between the E2HDM and C2HDM by focusing on the deviations in the SM-like Higgs boson couplings from the SM predictions in addition to the decay BRs and production cross sections at the LHC. It has been indicated that, even if both the E2HDM and C2HDM produce the same value of deviation in the hVV coupling, crucial differences can be found in the correlation of $\Delta\kappa_E$-$\Delta\kappa_D$ in the two scenarios (elementary and composite). Furthermore, through the combination of the differences in the decay BRs and production cross sections for the additional Higgs bosons, one may be able to distinguish these two hypotheses by the nature of the Higgs bosons liable for EWSB.

4.4 Conclusions

In this chapter, we have continued with our exploration of C2HDM scenarios that started with Chapter 3, assuming four different types of Yukawa interactions, wherein the nature of all Higgs states are composite objects. Particularly, they appear as the PNGBs from the global symmetry breaking $SO(6) \to SO(4) \times SO(2)$, induced explicitly by interactions between a new strong sector and the SM fields at the compositeness scale f. Such PNGBs for which, we use the same scalar potential as in the E2HDM for our PNGBs, then trigger EWSB governed by the SM gauge group. Under the assumption of partial compositeness, it is rather natural that one of the appearing physical Higgs states, the lightest one, is the 125 GeV state, h, discovered at CERN.

Within this construct, we then proceed to carry out a phenomenological study aiming at establishing the potential of the LHC in disentangling the two hypotheses, E2HDM versus C2HDM, by exploiting the fact that drastically different production and decay patterns for the four heavy Higgs states (H, A and $H^\pm$) may onset in the composite scenario with respect to the elementary one, even when the properties of SM-like Higgs state are the same (within experimental accuracy) in the two scenarios. We have completed this after imposing both theoretical (as already discussed in Chapter 3) and experimental (attained here by suitably altering the numerical toolboxes used in the E2HDM investigation to also embed the C2HDM option) bounds, the latter showing an obvious dependence upon ξ only in the case with Type-I Yukawa interactions. Practically, the most dramatic situation could occur when, e.g., in the presence of an established deviation of a few percents from the SM prediction for the hVV ($V = W^\pm, Z$) coupling (in fact, possibly the most precisely determined one at the LHC), the E2HDM would require the mixing between the h and H states to be non-zero whereas in the C2HDM compliance with such a measurement could be achieved also for the zero mixing case. Thus, in this situation, the $H \to W^+W^-$ and ZZ decays would be forbidden in the composite case, while still being allowed in the elementary one. (Similarly, Higgs-strahlung and vector-boson-fusion would be nullified in the C2DHM scenario, unlike in the E2HDM, while potentially large differences also appear in the case of gluon-gluon fusion and associated production with $b\bar{b}$ pairs.) Clearly, also intermediate situations can be realised. Therefore, a close scrutiny of the possible signatures of a heavy CP-even Higgs boson, H, would be a key to assess the viability of either model. Regarding the CP-odd Higgs state, A, in the extreme case of non-zero(zero) mixing in the E2HDM(C2HDM), again, it is the absence of a decay, i.e., $A \to Zh$, in the C2HDM that would distinguish it from the E2HDM. In the case of the $H^\pm$ state, a similar role is played by the $H^\pm \to W^\pm h$ decay. Obviously, for both these states too, intermediate situations are also possible, so that a precise study of these two channels would be a further strong handle to use in order to disentangle the two hypotheses. As far as A and $H^\pm$ production modes which are accessible at the LHC, i.e., gluon-gluon fusion and associate production with $b\bar{b}$ pairs (for the A) and associated production with $b\bar{t}$ pairs (for the H^+), are concerned though, practically no difference appears. The actual size of all these differences between the E2HDM and C2HDM is governed by the value of the $\xi = v^2_{\rm SM}/f^2$ parameter, the larger the latter the more significant the former. Finally, although there

are quantitative differences between the usual four Yukawa types (I, II, X and Y, in our notation) when predicting the yield of both the E2HDM and C2HDM, the qualitative pattern we described would generally persist. In fact, a similar phenomenology would emerge if deviations were instead (or in addition) established in the Yukawa couplings of the h state to b-quarks and/or τ-lepton.

Chapter 5

Single and double SM-like Higgs boson production at future electron-positron colliders in C2HDMs

5.1 Overview

In this chapter [33], differences in single- and double-h production cross sections at future e^+e^- colliders between E2HDMs and C2HDMs are investigated by using the same model construction as in Chapters 3 and 4. For single-h production, three relevant modes exist: (i) Higgs-Strahlung (HS) off a Z boson via $e^+e^- \to Zh$, (ii) Vector Boson Fusion (VBF) via $e^+e^- \to e^+e^-h$[1] and (iii) associated production with top quarks via $e^+e^- \to t\bar{t}h$. The double-h production can be categorised likewise by including one more Higgs boson h in the final state, namely, we have: $e^+e^- \to Zhh$, $e^+e^- \to e^+e^-hh$ and $e^+e^- \to t\bar{t}hh$.

The single-h production modes are useful to obtain the hZZ coupling through (i) and (ii) plus the $ht\bar{t}$ coupling through (iii). Due to the small background cross sections typical of a future e^+e^- machine as compared to those at the LHC, it is expected to measure these Higgs boson couplings with a good precision. For instance, in Ref. [126] the 1σ error on the measurement of the hZZ and $ht\bar{t}$ couplings at the International Linear Collider (ILC) are anticipated to be 0.5% and 2.5%,

[1]Herein, we neglect considering $W^\pm$ caused VBF as the hW^+W^- coupling scales in all scenarios considered in the same way as hZZ. Moreover, while W^+W^- fusion is the favoured channel for h searches, above ZZ fusion, it should be recalled that we are here primarily concerned with distinguishing the C2HDM from the E2HDM via the several production modes. From this point of view then, it should be noted that the ZZ fusion process can be separated by the Zhh one followed by $Z \to e^+e^-$ decay by reconstructing the invariant mass of the e^+e^- system around M_Z, thus we can compare the deviations in the cross sections of the Zhh and ZZ fusion processes separately. This would not be feasible in the case of WW fusion and $Z \to$ neutrino decays.

respectively, for an energy of $\sqrt{s} = 500$ GeV and integrated luminosity of $\mathcal{L} = 500$ fb^{-1}. Notice that, in the $e^+e^- \to t\bar{t}h$ mode, one can also attain the AZh coupling.

The double-h production modes have natural sensitivity not only to the hZZ and $ht\bar{t}$ couplings but also to the triple Higgs boson coupling λ_{hhh}. Particularly, the measurement of λ_{hhh} is rather significant to rebuild the shape of the Higgs potential, which has been known to be a really challenging task at the LHC [127, 128]. The expected precision obtainable at future e^+e^- colliders in the measurement of λ_{hhh} is of $\mathcal{O}(10\%)$ [126]. This should be compared with the much more limited precision expected at the LHC, wherein λ_{hhh} can be constrained only within a factor of 3 or so [129] of the SM value. Moreover, the heavier CP-even Higgs boson H can enter the double-Higgs boson production process via their propagators, consequently enabling sensitivity to the Hhh vertex, which is anticipated to be with in a factor of 10 or so [130] in E2HDMs. Furthermore, the AHZ coupling becomes reachable alongside the AhZ one in associated production with top quarks. Ultimately, quartic couplings of the type $hhZZ$ also mediate. (Notice that AhZ and $hhZZ$ are related to the fundamental gauge structure and as such are not independent couplings.) As a result, the measurement of the aforementioned double-Higgs boson cross sections at future e^+e^- colliders is significant to also obtain information about extra Higgs bosons such as their masses and couplings.

We will display in this chapter that there are measurable deviations induced in C2HDMs by the dependence upon the compositeness scale in various Higgs couplings which cannot be defined in E2HDMs, no matter the choice of parameters in either scenario. Particularly, assuming a fixed value of κ_V [given by the hVV ($V = W^\pm, Z$) coupling normalised to the SM value], the distinction between predictions in the two hypotheses can be even larger than 50% for the double-Higgs production processes. Thus, a future electron-positron machine potentially discriminates between the E2HDMs and the C2HDMs.

5.2 C2HDMs and their interaction terms

5.2.1 Lagrangian

In Chapter 3 and 4, as we have already discussed the kinetic, Yukawa and the potential part of the Lagrangian in the C2HDM, herein we only present the following Lagrangian relevant to single- and double-h production:

$$\begin{aligned}\mathcal{L}^{\rm int} = {} & g_{\phi_i VV}\phi_i V_\mu V^\mu + g_{\phi_i\phi_j VV}\phi_i\phi_j V_\mu V^\mu + g^\mu_{\phi_i\phi_j V}\phi_i\phi_j V_\mu + y_{\phi_i\psi\psi}\phi_i\bar{\psi}\psi + \tilde{y}_{\phi_i\psi\psi}\phi_i\bar{\psi}\gamma_5\psi \\ & + y_{\phi_i\phi_j\psi\psi}\phi_i\phi_j\bar{\psi}\psi + \lambda_{\phi_i\phi_j\phi_k}\phi_i\phi_j\phi_k, \end{aligned} \tag{5.1}$$

where $V_\mu = W_\mu(Z_\mu)$, $\psi(\bar{\psi})$ stands for a SM fermion(anti-fermion) and ϕ_i symbolises a (pseudo)scalar Higgs boson. We note that the dimension five term $\phi_i\phi_j\bar{\psi}\psi$ emerges in C2HDMs, which comes from

the $1/f^2$ term in Eqs. 4.17. Employing this notation, one attains the (pseudo)scalar Higgs boson couplings with the gauge bosons as (afterwards, we adopt the shorthand notations $s_y \equiv \sin y$ and $c_y \equiv \cos y$):

$$g_{hVV} = \left(1 - \frac{\xi}{2}\right) c_\theta g^{\rm SM}_{hVV}, \quad g_{HVV} = -\left(1 - \frac{\xi}{2}\right) s_\theta g^{\rm SM}_{hVV}, \tag{5.2}$$

$$g_{hhVV} = \left[1 - \frac{\xi}{3}(1 + 5c_\theta^2)\right] g^{\rm SM}_{hhVV}, \tag{5.3}$$

$$g^\mu_{AhZ} = -i\frac{g_Z}{2} s_\theta \left[\left(1 - \frac{5}{6}\xi\right) p^\mu_h - \left(1 - \frac{1}{6}\xi\right) p^\mu_A\right], \tag{5.4}$$

$$g^\mu_{AHZ} = -i\frac{g_Z}{2} c_\theta \left[\left(1 - \frac{5}{6}\xi\right) p^\mu_H - \left(1 - \frac{1}{6}\xi\right) p^\mu_A\right], \tag{5.5}$$

where θ represents the the mixing angle between two CP-even Higgs bosons given in Eq. 3.22. For the $AhZ(AHZ)$ coupling, $p^\mu_\phi(\phi = h, H, A)$ stands for the incoming four-momentum. The relevant Yukawa couplings are defined by

$$y_{htt} = \left[\left(1 - \frac{3\xi}{2}\right) c_\theta + s_\theta \cot\beta\right] y^{\rm SM}_{htt}, \quad y_{Htt} = \left[-\left(1 - \frac{3\xi}{2}\right) s_\theta + c_\theta \cot\beta\right] y^{\rm SM}_{htt}, \tag{5.6}$$

$$\tilde{y}_{Att} = \left(1 + \frac{\xi}{2}\right) \cot\beta \times \tilde{y}^{\rm SM}_{Gtt}, \tag{5.7}$$

$$y_{hhtt} = -\frac{2\xi}{3v_{\rm SM}} \left(2 + \frac{s_{\beta+2\theta}}{s_\beta}\right) y^{\rm SM}_{htt}. \tag{5.8}$$

In the limit $\xi \to 0$, the coupling y_{hhtt} disappears, since E2HDMs do not generate $hht\bar{t}$ coupling in tree level. Note that the above formulations of the top Yukawa couplings are common to all the four types of Yukawa interactions, therefore type dependence does not exist in the cross section of the process where only h is mediated such as $e^+e^- \to Zh$ and $e^+e^- \to e^+e^-h$. If we discuss processes containing the propagators of H and/or A, the type dependence emerges in these cross sections via their widths. However, we have confirmed that such dependence is neglected as long as $\tan\beta$ is small (state, below 5 or so), which is a condition we will assume in our investigation.

Lastly, the related trilinear Higgs self-couplings are defined by

$$\begin{aligned}\lambda_{hhh} = {} & \frac{1}{4v_{\rm SM}s_{2\beta}} \left[(s_{2\beta+3\theta} - 3s_{2\beta+\theta})m_h^2 + 4s_\theta^2 s_{2\beta+\theta} M^2\right] \\ & + \frac{\xi}{12v_{\rm SM}} \left[c_\theta m_h^2 + 2s_\theta^2 M^2 (c_\theta + 2s_\theta \cot 2\beta)\right],\end{aligned} \tag{5.9}$$

$$\begin{aligned}\lambda_{Hhh} = {} & \frac{s_\theta}{2v_{\rm SM}s_{2\beta}} \left[-s_{2(\beta+\theta)}(2m_h^2 + m_H^2) + (s_{2\beta} + 3s_{2(\beta+\theta)})M^2\right] \\ & + \frac{\xi}{12v_{\rm SM}} s_\theta \left[m_H^2 - 2m_h^2 + (1 + 3c_{2\theta} + 6\cot 2\beta s_{2\theta})M^2\right],\end{aligned} \tag{5.10}$$

In the above formulae, the ξ dependence is obtained by redefining the scalar fields given in Eq. 3.21. Note that Ref. [131] has indicated that λ_{hhh} coupling can receive $\mathcal{O}(100\%)$ radiative corrections

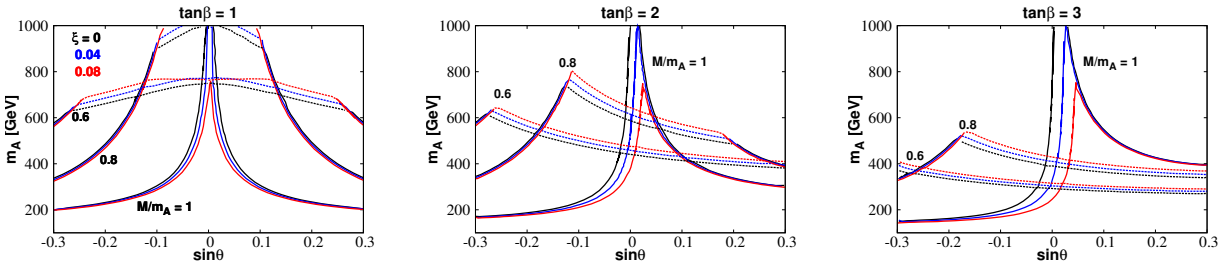

Figure 5.1: Upper limit on m_A ($= m_H = m_{H^\pm}$) from unitarity (displayed as the dashed part of each curve) and vacuum stability (indicated as the solid part of each curve) bounds in the case of $\sqrt{s} = 1000$ GeV and $\tan\beta = 1$ (left), 2 (center) and 3 (right). The value of ξ is set to be 0 (black), 0.04 (blue) and 0.08 (red). We also adopt the three different values of the ratio M/m_A (1, 0.8 and 0.6) as shown in the figures. A similar figure is seen in Ref. [33].

at the one-loop level without violating perturbative unitarity in E2HDMs. They are due to non-decoupling effects of the extra Higgs boson loops, which become crucial when the Higgs masses are mostly obtained by the Higgs VEV, i.e., the value of the M^2 is not so large as compared to that of the (squared) masses of the extra Higgs bosons. In our numerical analysis, we do not take into account the non-decoupling case.

5.2.2 Bounds on parameters in C2HDMs

We first discuss bounds arising from theoretical studies, particularly, perturbative unitarity and vacuum stability bounds through the approach introduced in Chapter 3 [31]. In Fig. 5.1, we demonstrate the upper limit on m_A ($= m_H = m_{H^\pm}$) as a function of $\sin\theta$ and take $\tan\beta$ fixed at 1 (left), 2 (center) and 3 (right). The black, blue and red curves represents the case with $\xi = 0$, 0.04 and 0.08, respectively. To calculate the unitarity bound, we set $\sqrt{s} = 1000$ GeV. We determine that the allowed region dramatically depends upon the choice of the ratio M/m_A, which is set to be 1, 0.8 and 0.6. For instance, when $m_A, M/m_A$ and ξ are set to be 500 GeV, 0.8 and 0 respectively, we obtain the allowed region of $\sin\theta$ to be between $-0.20 \lesssim \sin\theta \lesssim +0.20$ (for $\tan\beta = 1$), $-0.19 \lesssim \sin\theta \lesssim +0.14$ (for $\tan\beta = 2$) and $-0.19 \lesssim \sin\theta \lesssim -0.18$ (for $\tan\beta = 3$). For a larger value of ξ, the unitarity constraint gives slightly additional parameter space with respect to the case $\xi = 0$ in the case of $M/m_A \neq 1$, as it was already discussed in Chapter 3 [31], whereas the vacuum stability constraint does not change dramatically. We note that since the vacuum stability bound highly dislikes the case of $M \gtrsim m_A$, which induces us to establish the illustrative relation $M = 0.8 m_A$ ($= m_H = m_{H^\pm}$) for the rest of the chapter.

Next, we consider the bounds from collider experiments. We discuss the situation which will rise at the end of the LHC era regarding the investigation of the already discovered 125 GeV Higgs state and that of potential extra signals from an extended Higgs sector. Here, we assume that no extra Higgs bosons will have been discovered by the LHC, either in standard luminosity

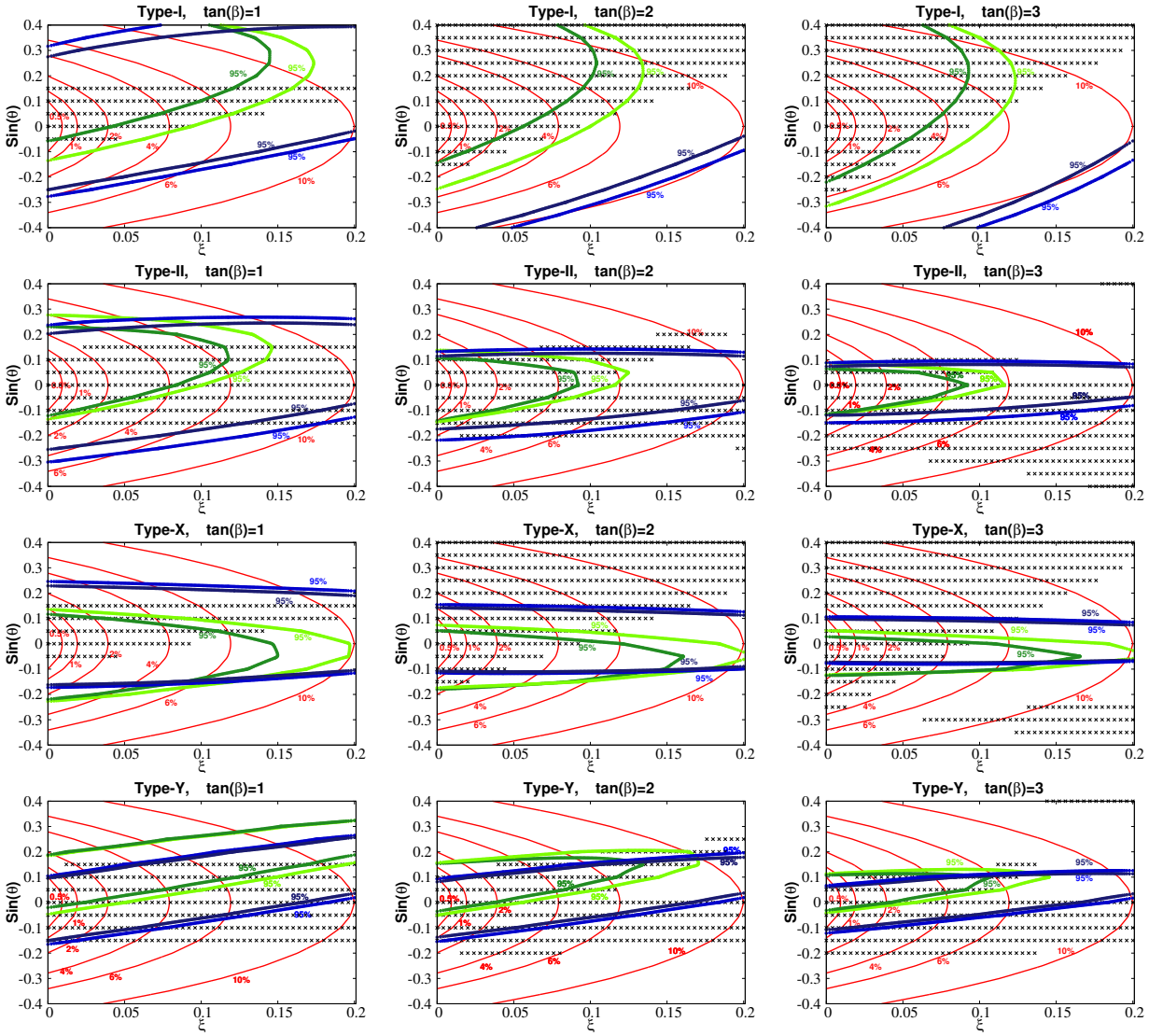

Figure 5.2: Regions marked by x are allowed by the LHC data at 95% CL by using the HiggsBounds tool. The four rows display the results in the C2HDM of Type-I, Type-II, Type-X and Type-Y. The light- and dark-green (light- and dark-blue) curves indicate the compatibility with observed Higgs signals (SM signal strengths) at $\Delta\chi^2$ =6.18 (95.45% CL) extrapolated to 300 fb^{-1} and 3000 fb^{-1} of luminosity respectively. Red curves are contours of $|\Delta\kappa_V| = |g_{hVV}/g^{\rm SM}_{hVV} - 1|$. The input parameters are fixed to be $m_H = m_A = m_{H^\pm} = 500$ GeV and $M = 0.8m_A$. The left, center and right panels show tan β=1, 2 and 3, respectively. A similar figure is seen in Ref. [33].

conditions (i.e., after 300 fb^{-1}) or in high luminosity ones (i.e., after 3000 fb^{-1}). Even so, we need to determine whether, after such luminosity values will have been arisen, the measurements of the couplings to SM objects of the Higgs discovered state will be as at current (with, of course, a higher precision obtaining from the higher statistics) or different. From this point of view, we will here discuss two possible scenarios. On the one hand, we will assume that present central values of

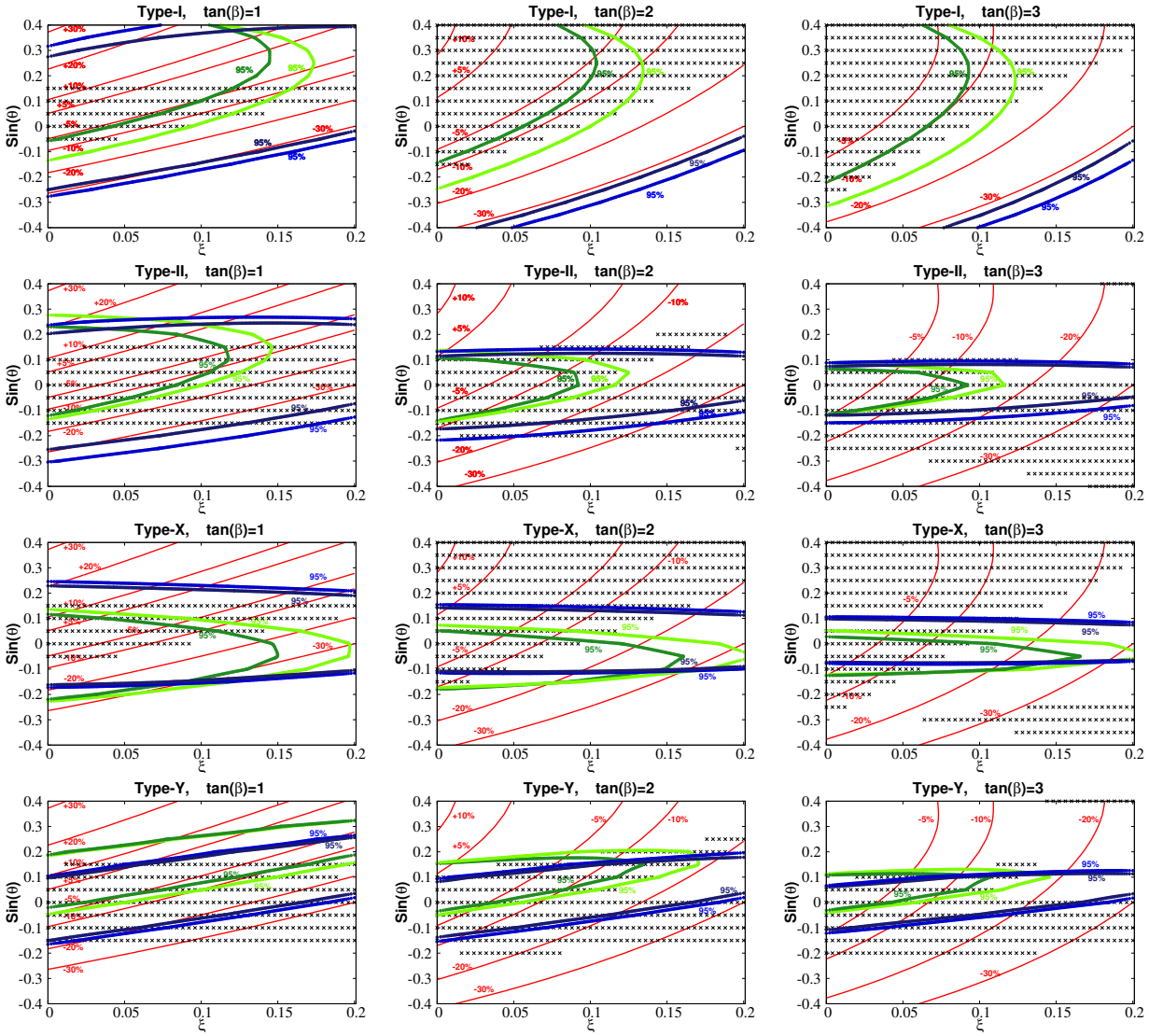

Figure 5.3: Same of Fig. 5.2. Here the red curves are contours of $\Delta\kappa_t = y_{htt}/y_{htt}^{\rm SM} - 1$. A similar figure is seen in Ref. [33].

such measurements will have been verified. On the other hand, we will assume that SM central values will ultimately have been established. We will indicate that, under either case, a future e^+e^- collider will be in a position to distinguish a C2HDM from an E2HDM, via the study of single- and double-h production modes.

In Figs. 5.2–5.3 the Higgs sector predictions in C2HDMs (and their E2HDM limits) are compared with the present exclusion bounds from the LHC experiments at 95% CL via the HiggsBounds tool (v4.3.1) [114–119] on the $(\xi, \sin\theta)$ plane. We study the ordinary Yukawa Type-I, -II, -X and -Y configurations for $\tan\beta = 1, 2, 3$. Moreover, we make a $\Delta\chi^2$ evaluation via the HiggsSignal package (v1.4.0) [120] to study compatibility of the projected exclusion limits from measurements of signal

ξ	$\tan\beta = 1$	$\tan\beta = 2$	$\tan\beta = 3$
$\xi = 0$	Type-I $-0.05 \leq s_\theta \leq 0.15$	Type-I $-0.14 \leq s_\theta \leq 0.52$	Type-I $-0.22 \leq s_\theta \leq 0.51$
	Type-II $-0.12 \leq s_\theta \leq 0.10$	Type-II $-0.14 \leq s_\theta \leq 0.10$	Type-II $-0.12 \leq s_\theta \leq 0.05$
	Type-X $-0.05 \leq s_\theta \leq 0.12$	Type-X $-0.15 \leq s_\theta \leq 0.05$	Type-X $-0.13 \leq s_\theta \leq 0.03$
	Type-Y $-0.02 \leq s_\theta \leq 0.10$	Type-Y $-0.04 \leq s_\theta \leq 0.10$	Type-Y $-0.03 \leq s_\theta \leq 0.05$
$\xi = 0.04$	Type-I $0.00 \leq s_\theta \leq 0.15$	Type-I $-0.05 \leq s_\theta \leq 0.47$	Type-I $-0.10 \leq s_\theta \leq 0.45$
	Type-II $-0.07 \leq s_\theta \leq 0.15$	Type-II $-0.10 \leq s_\theta \leq 0.09$	Type-II $-0.08 \leq s_\theta \leq 0.05$
	Type-X $-0.05 \leq s_\theta \leq 0.10$	Type-X $-0.10 \leq s_\theta \leq 0.04$	Type-X $-0.12 \leq s_\theta \leq 0.02$
	Type-Y $0.00 \leq s_\theta \leq 0.15$	Type-Y $0.00 \leq s_\theta \leq 0.15$	Type-Y $0.00 \leq s_\theta \leq 0.10$
$\xi = 0.08$	Type-I $0.06 \leq s_\theta \leq 0.15$	Type-I $0.08 \leq s_\theta \leq 0.39$	Type-I $0.08 \leq s_\theta \leq 0.34$
	Type-II $-0.01 \leq s_\theta \leq 0.15$	Type-II $-0.03 \leq s_\theta \leq 0.06$	Type-II $-0.03 \leq s_\theta \leq 0.02$
	Type-X $0.00 \leq s_\theta \leq 0.07$	Type-X $0.00 \leq s_\theta \leq 0.02$	Type-X $0.00 \leq s_\theta \leq 0.01$
	Type-Y $0.06 \leq s_\theta \leq 0.15$	Type-Y $0.05 \leq s_\theta \leq 0.15$	Type-Y $0.04 \leq s_\theta \leq 0.10$

Table 5.1: Allowed values of $\sin\theta$ in a Type-I, -II,-X and -Y C2HDM with fixed values of ξ and $\tan\beta$ achieved by performing both a 95% CL fit using the measurements given in Tab. F.1 in the Appendix F and current data at the LHC. For the former fit, statistical errors are rescaled to an integrated luminosity of 3000 fb^{-1} . Here we select $m_H = m_A = m_{H^\pm} = 500$ GeV and $M = 0.8m_A$. A similar table is seen in Ref. [33].

strengths assuming the (currently) measured central values (green), as summarised in Tab. F.1 in the Appendix F from ATLAS data[2], besides the SM ones (blue), with the E2HDM ($\xi = 0$) and C2HDM ($\xi \neq 0$) predictions after 300 fb^{-1} (light-green and -blue curves) and 3000 fb^{-1} (dark-green and -blue curves) of LHC luminosity. Here, the green and blue contours display the $\Delta\chi^2$=6.18 (95.45% CL) regions. To be specific, we report in Tab. 5.1 the constraints on $\sin\theta$ in a Type-I, -II, -X and -Y C2HDM achieved by performing a 95% CL fit employing the measurements listed in Tab. F.1 in the Appendix F with statistical errors rescaled to an integrated luminosity of 3000 fb^{-1} and current data at the LHC. Here we study in the case with $\xi = 0,\ 0.04,\ 0.08$ (the first one regarding to the E2HDM limit) and $\tan\beta = 1, 2, 3$.

Specifically , more parameter space with positive values of $\sin\theta$ takes part in the 95% CL contours of the Type-I C2HDM, compared to those of the Type-II, -X and -Y C2HDMs, for both luminosity data sets. In general, 95% CL contours achieved under the assumption of SM central values for the Higgs signal strength measurements (blue curves) include larger parameter regions compared to those achieved adopting (currently) measured central values of the latter (green curves), for all Yukawa types. (We list the experimental channels excluding most parameter regions in Figs. 5.2–5.3 in Tab. F.2 in the Appendix F.)

In Figs. 5.2-5.3 we also display (in red) the contours of κ_V and κ_t given by $\kappa_V = g_{hVV}/g^{\rm SM}_{hVV}$ and $\kappa_t = y_{htt}/y^{\rm SM}_{htt}$. These red lines specify the coupling deviations possible in the relevant C2HDM (with respect to the SM) as a function of $\sin\theta$ and ξ (plus $\tan\beta$ for the Yukawa coupling) that we plan to investigate using the described single- and double-h production modes, within the limits

[2]We could not employ CMS data in this extrapolation since the public sources that we could access did not describe the statistic and systematic errors on the measurements separately.

imposed by Tab. 5.1. We note that the latter receive the most stringent constraints possible at 95% CL following the High Luminosity LHC (HL-LHC) runs (i.e., after 3000 fb^{-1} of luminosity). Needless to say, in the remainder, we will use the parameter configurations which will not testable for the aforementioned LHC conditions.

Before processing to e^+e^- phenomenology, we also should discuss double-h production at the CERN machine. Whereas this is potentially reachable at the HL LHC [132, 133] in E2HDMs (and consequently in C2HDMs), it is clear that due to the poor signal rate and background contamination, separation between the elementary and composite hypotheses is barely possible, particularly at the level we will envisage in the forthcoming analysis.

5.3 Single-Higgs boson production

In this section, we study the three single-Higgs boson production processes, namely, HS, VBF and associated production with top quarks ($t\bar{t}h$). We compute all the cross sections for the Type-I Yukawa interaction, but, as already emphasised, for our $\tan\beta$ choices, the results are also valid for the other Yukawa types.

The reference SM cross sections for these processes are presented in Fig. 5.4, as a function of the centre-of-mass energy of the collider $\sqrt{s}$. Here, we can notice that the HS and $t\bar{t}h$ production cross sections can reach maximal at just above their thresholds, i.e., $\sqrt{s} \sim 215$ and ~ 425 GeV, respectively. When $\sqrt{s}$ becomes larger, the cross sections monotonically reduce because of the s-channel topology in both cases. Conversely, for the VBF process, the cross section grow according to $\log\sqrt{s}$ due to the t-channel topology. Recall that precision on such cross sections at future e^+e^- colliders, quite irrespective of the machine configuration and energy, is anticipated to be at the percent level or even less (particularly for HS and VBF).

We first discuss the HS and VBF processes, where, in both E2HDMs and C2HDMs, only one diagram containing the hZZ vertex exists, just like in the SM. Hence, we simply obtain these production cross sections from the corresponding ones in the SM upon multiplying for the squared scaling factor of the hZZ coupling κ_V^2. As a result, by measuring these cross sections, κ_V^2 can be extracted.

In all C2HDM types, κ_V relies on two parameters, $|\sin\theta|$ and ξ, as we can see in Eq. (5.2), whereas in the corresponding E2HDM cases ($\xi = 0$) only one parameter is included. Namely, if κ_V is measured at e^+e^- colliders, the allowed combinations of $|\sin\theta|$ and ξ are determined via Eq. (5.2). Fig. 5.5 displays the contour of κ_V^2 on the $(|\sin\theta|, \xi)$ plane. For example, if $\kappa_V^2 = 0.94$ (the green solid curve), the value of $|\sin\theta|$ is determined to be around 0.245 at $\xi = 0$, which corresponds to the E2HDM case, whereas this can vary from 0 to 0.245 in the C2HDM one by varying ξ from about 0.06 to 0. Hence, in order to distinguish ξ and $|\sin\theta|$ in C2HDMs, further inputs are required from experiment. Particularly, once κ_V is fixed, one can then predict the deviations expected in

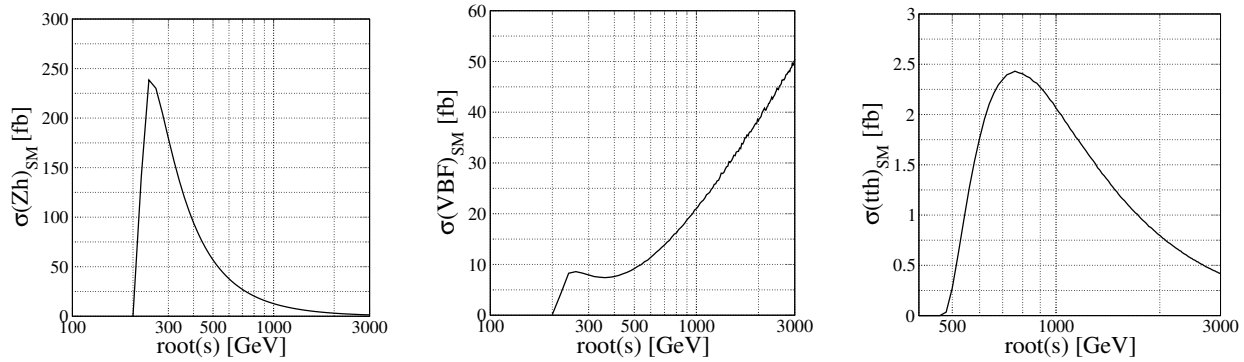

Figure 5.4: Cross sections for $e^+e^- \to Zh$ (left), $e^+e^- \to e^+e^-h$ (center) and $e^+e^- \to t\bar{t}h$ (right) processes as functions of $\sqrt{s}$ in the SM. A similar figure is seen in Ref. [33].

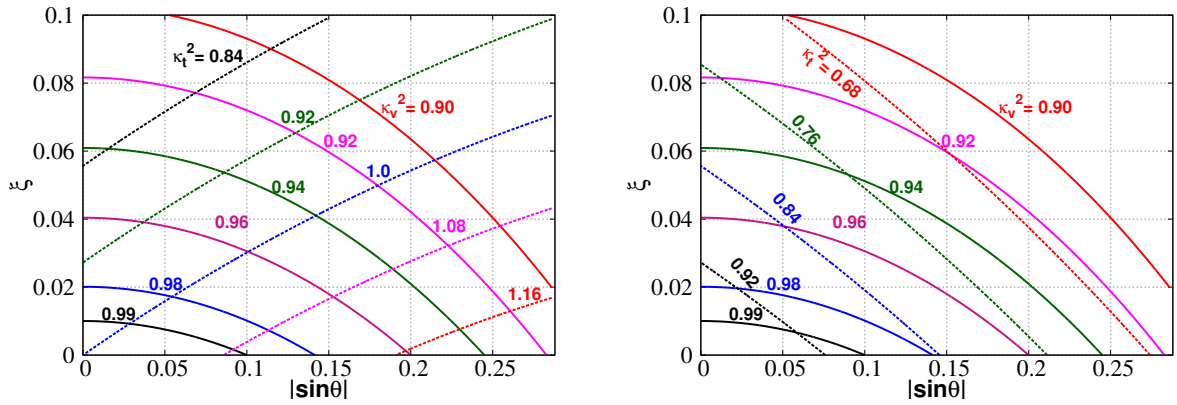

Figure 5.5: Contour plots of $\kappa_V^2 = (g_{hVV}/g_{hVV}^{\rm SM})^2$ (solid) and $\kappa_t^2 = (y_{htt}/y_{htt}^{\rm SM})^2$ (dashed) in the $(|\sin\theta|, \xi)$ plane for $\sin\theta < 0$ (left) and $\sin\theta > 0$ (right). Contour plots of κ_t^2 are for $\tan\beta = 2$. A similar figure is seen in Ref. [33].

κ_t by fixing the sign of $\sin\theta$ and the value of $\tan\beta$. This way, indeed, one can obtain κ_t from Eq. (5.6). The κ_t contours are also indicated in Fig. 5.5. Conversely, in the E2HDM case, once κ_V and $\tan\beta$ are known, only two values of κ_t, depending on the sign of $\sin\theta$, are uniquely achieved. This delineates hence a strategy to follow in order to possibly distinguish the two assumptions of 2HDMs, elementary and composite, i.e., through the simultaneous extraction of κ_V from HS and VBF and measurement of the event rates for associated production with top quarks. In short, at fixed κ_V^2, there could well be values of the $t\bar{t}h$ cross section achievable in C2HDMs which are instead unachievable in E2HDMs.

Before doing so though, we first consider the $t\bar{t}h$ production cross section as a function of $\sin\theta$, ξ and $\tan\beta$. In contrast to the HS and VBF processes, this process requires a more complicated treatment. As is clear from Fig. 5.6, there are three representative diagrams entering such a process, namely, (i) $e^+e^- \to t\bar{t}$ production followed by h emission from t and $\bar{t}$ (first diagram of Fig. 5.6), (ii) $e^+e^- \to Z^*h$ production followed by $Z^* \to t\bar{t}$ (second diagram of Fig. 5.6) and (iii) $e^+e^- \to A^{(*)}h$

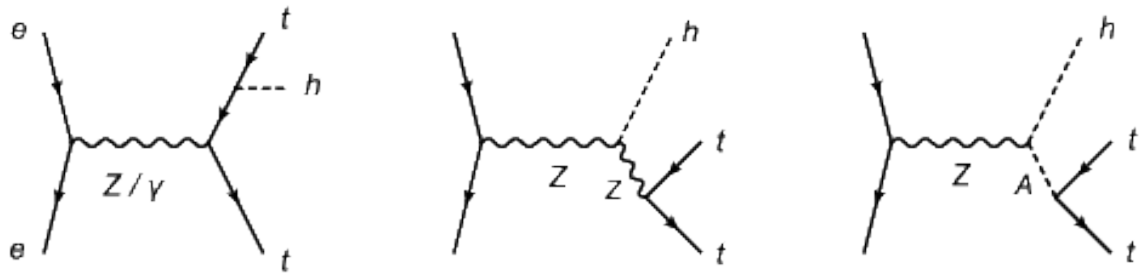

Figure 5.6: Representative Feynman diagrams for the $e^+e^- \to t\bar{t}h$ process. A similar figure is seen in Ref. [33].

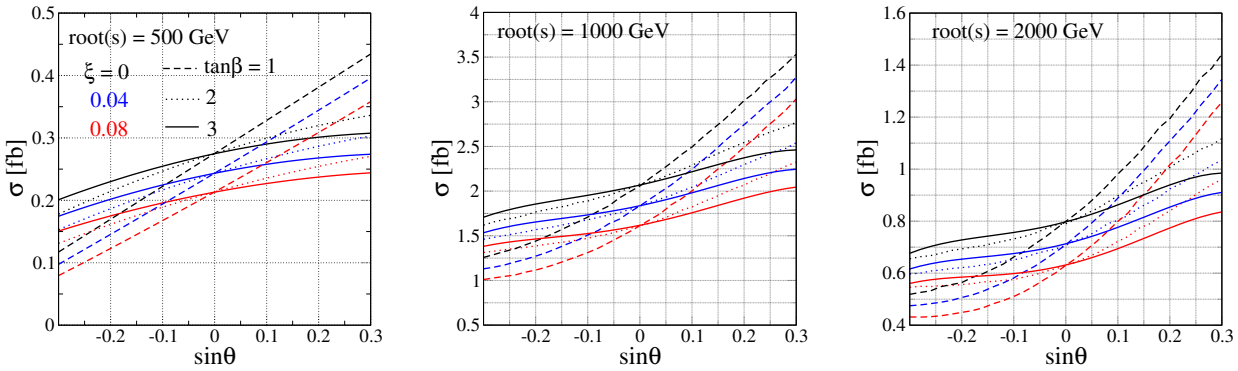

Figure 5.7: Cross section for the $e^+e^- \to t\bar{t}h$ process as a function of $\sin\theta$. The value of $\tan\beta$ is fixed to be 1 (dashed), 2 (dotted) and 3 (solid), and that of ξ is taken to be 0 (black), 0.04 (blue) and 0.08 (red). The collision energy and the mass of A $(\sqrt{s}, m_A)$ is fixed to be (500, 400), (1000, 500) and (2000,500) in GeV unit for the left, center and right panels, respectively. A similar figure is seen in Ref. [33].

production followed by $A^{(*)} \to t\bar{t}$ (third diagram of Fig. 5.6). We can see from the functional form of g_{hVV} and g_{AhZ} in Eq. (5.2) and y_{htt} and $\tilde{y}_{Att}$ in Eq. (5.6), it is clear that the cross section for $e^+e^- \to t\bar{t}h$ does not scale trivially with respect to the SM in either the E2HDM or the C2HDM case.

Fig. 5.7 displays the cross section for the $t\bar{t}h$ production process as a function of $\sin\theta$ for various fixed values of $\tan\beta$ and ξ. The collision energy $\sqrt{s}$ is set to be 500 (left), 1000 (center) and 2000 GeV (right). It can be seen that the cross section gets smaller when we take a smaller value of $\sin\theta$. Moreover, when we fix $\sqrt{s}$ to be 1 TeV or 2 TeV, the on-shell production of A is realised. This importantly enhances the cross section as it is realised by comparing the case for $\sqrt{s} = 500$ and 1000 or 2000 GeV. Regarding the differences between the E2HDM and C2HDM cases, parametrised by ξ, we see that the cross section becomes smaller for larger values of ξ. It is also found that the ratio of the cross section with $\xi = 0$ to that with $\xi = 0.04$ (or 0.08) for a fixed value of $\tan\beta$, $\sin\theta$ and $\sqrt{s}$ does not depend much on the choice of $\tan\beta$, $\sin\theta$ and $\sqrt{s}$. The ξ dependence acts rather like an overall rescaling of the $t\bar{t}h$ cross section. Crucial deviations possibly occur between the

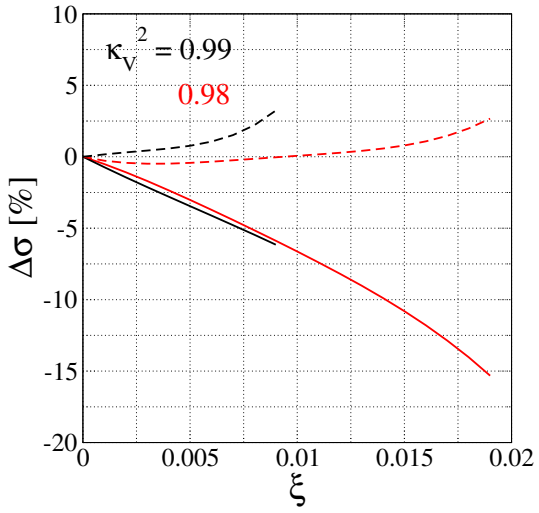

Figure 5.8: Deviations in the cross section $\Delta\sigma \equiv (\sigma_{\rm C2HDM}/\sigma_{\rm E2HDM} - 1)$ for the $e^+e^- \to t\bar{t}h$ process at fixed $\kappa_V^2 = 0.99$ (black curves) and 0.98 (red curves). We take $\tan\beta = 2$ and $\sqrt{s} = 1000$ GeV. For each κ_V^2, we indicate the case of $\sin\theta > 0$ (solid lines) and $\sin\theta < 0$ (dashed lines). We only indicate the result permitted by the unitarity and vacuum stability constraints and by the future LHC data assuming 3000 fb^{-1} with 95% CL. The latter constraint is for the Type-I C2HDM. A similar figure is seen in Ref. [33].

E2HDM and C2HDM cases. If we contrast two scenarios for the same value of $\sin\theta$, the difference is $\mathcal{O}(20\%)$ or so in all Yukawa types, for $\sin\theta$ and ξ combinations permitted by Tab. 5.1.

However, as intimated, what we really need to compute is the $e^+e^- \to t\bar{t}h$ cross section for a fixed value of κ_V^2, as this will immediately be measured at future electron-positron machines through the HS and VBF processes. As emphasised already, the choice of the type of Yukawa interactions does not have an impact on the $t\bar{t}h$ results. Conversely, as indicated in Figs. 5.2–5.3, the constraints from collider data are different for the several 2HDM types. In Tab. 5.1 we have reported the 95% CL constraints on $\sin\theta$ after 3000 fb^{-1} of LHC collected data, for fixed ξ and $\tan\beta$. Under the scenario of having measured κ_V^2, this information states the allowed $\sin\theta$ values that can be related to ξ, as displayed in Fig. 5.5.

Fig. 5.8, we thus indicate the deviation in the $t\bar{t}h$ cross section in C2HDMs relative to E2HDMs, i.e., $\Delta\sigma \equiv (\sigma_{\rm C2HDM}/\sigma_{\rm E2HDM} - 1)$, as a function of ξ for two values of $\kappa_V^2 = 0.99$ and 0.98. We here set $\sqrt{s} = 1000$ GeV, $m_A = 500$ GeV and $\tan\beta = 2$. Now, $|\sin\theta|$ is determined for each fixed value of ξ (see Fig. 5.5). As the sign of $\sin\theta$ cannot be determined by measuring κ_V^2, we indicate the cases for $\sin\theta > 0$ (solid curves) and $\sin\theta < 0$ (dashed curves) separately. The result is that there can still be a very large variation between the elementary and composite $e^+e^- \to t\bar{t}h$ cross section. For instance, if the measured value of κ_V^2 were 0.98, then $\Delta\sigma$ can be up to -15% for $\sin\theta > 0$. We can interpret this behaviour as follows. Once κ_V^2 is determined, this fixes $|\sin\theta|$ in the E2HDM. Contrarily, in the C2HDM the value of $|\sin\theta|$ can be lower depending on ξ. In the case of $\sin\theta > 0$,

when the value of ξ becomes large, $\sin\theta$ decreases (approaching 0). Fig. 5.7 shows that the cross section gets small when $\sin\theta(\xi)$ decreases(increases), thus the ratio gets smaller. In contrast, in the case of $\sin\theta < 0$, a larger value of ξ corresponds to a larger value of $\sin\theta$, therefore the reduction of the cross section by a larger value of ξ can be cancelled via a larger value of $\sin\theta$. Either way, large values for $\Delta\sigma$, well beyond the expected accuracy of the $e^+e^- \to t\bar{t}h$ cross sections can be achieved for allowed values of $\sin\theta$ and ξ (for a given $\tan\beta$).

In summary, we find that, after having imposed theoretical constraints and experimental limits from the high luminosity option of the LHC, there are parameter space regions of C2HDMs predicting cross sections for $t\bar{t}h$ production that cannot be attained in E2HDMs for a given value of $\tan\beta$ when κ_V^2 is precisely determined via the HS and VBF processes. This also suggests that we can obtain the value of ξ from the measurement of the $t\bar{t}h$ yield if $\tan\beta$ is known via the investigation of other observables. Indeed, such a parameter can be attained at the LHC, e.g., through the precise measurement of the Yukawa couplings of the h state. In actuality, one may also need to know the values of m_A, Γ_A and the $At\bar{t}$ coupling, whenever the third topology in Fig. 5.6 contributes crucially to the $e^+e^- \to t\bar{t}h$ cross section, e.g., when it is resonant, as is the case in Fig. 5.7, because herein m_A is greater than $2m_t$. (Note that the AhZ coupling is determined by the gauge structure, which is common to both the elementary and composite Higgs hypotheses we are studying, so that, different m_A, Γ_A and $\tilde{y}_{Att}$, it is not an independent parameter.) As we are working under the circumstance (already spelled out in the introduction) that the LHC will have not generated any proof of extra Higgs bosons other than the SM-like h state (assumption which is in fact encoded in Figs. 5.2–5.3), access to these extra parameters can be obtained via the study of the $e^+e^- \to hA$ cross section and decay rates, which are promptly reachable at a future e^+e^- collider whenever $\sqrt{s} > m_h + m_A$. Finally, understanding of m_A, Γ_A and the $At\bar{t}$ coupling would gain access to κ_t in C2HDMs, for which large deviations from the E2HDMs' counterpart are possible over allowed parameter regions, at the level of tens of percent; see red lines in Fig. 5.3.

5.4 Double-Higgs boson production

In this section, we discuss the case of double-Higgs production, wherein the pair of final state Higgs bosons is made up by two h (SM-like) states. The production modes are those already studied, i.e., HS ($e^+e^- \to Zhh$), VBF ($e^+e^- \to e^+e^-hh$) and associated production with top quarks ($e^+e^- \to t\bar{t}hh$). For reference, Fig. 5.9 presents the cross sections for these processes in the SM . Generally, in each case, the production cross section is smaller than the corresponding cross section for single-h production by a factor of more than hundred because of the phase space suppression. Thanks to double-Higgs production, one can access triple-Higgs self-couplings, particularly, in the case of h pairs, the hhh and Hhh vertices. As stated earlier, while the constraints that can be obtained from these couplings at the LHC are rather poor, with the accuracy of $\mathcal{O}(100\%)$, the precision achievable at future e^+e^- colliders can be less close to 10%.

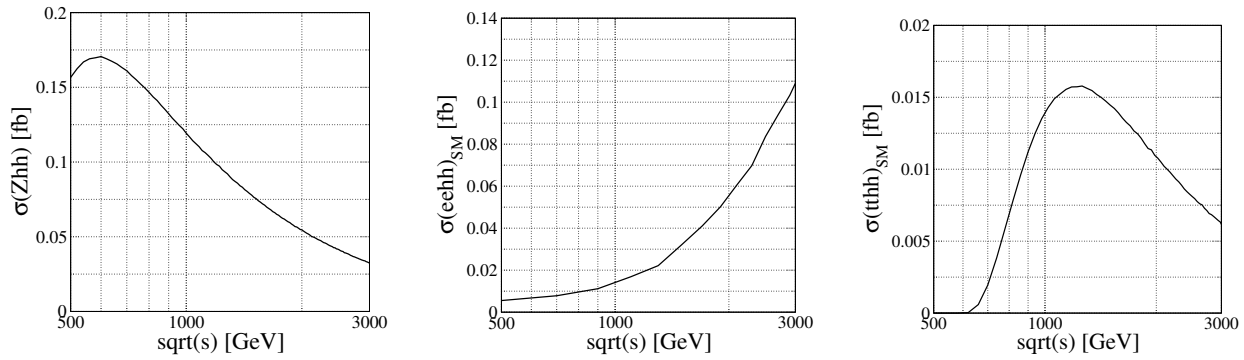

Figure 5.9: Cross section of the $e^+e^- \to Zhh$ (left), $e^+e^- \to e^+e^-hh$ (center) and $e^+e^- \to t\bar{t}hh$ (right) as a function of $\sqrt{s}$ in the SM. A similar figure is seen in Ref. [33].

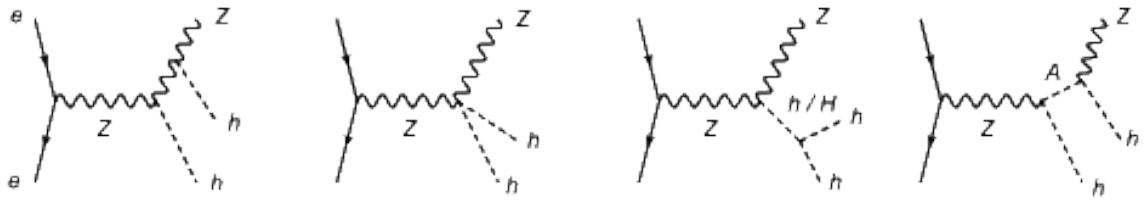

Figure 5.10: Representative Feynman diagram for the $e^+e^- \to Zhh$ process. A similar figure is seen in Ref. [33].

Firstly, we study the Zhh production mode. The representative Feynman diagrams are indicated in Fig. 5.10. Different from the single-h production process, there are interactions depending on λ_{hhh} and λ_{Hhh} (in the third diagram), where the formulae for these couplings are defined in Eqs. (5.9) and (5.10). Moreover, the fourth diagram includes the propagation of A. It is significant to discuss here that the $\tan\beta$ dependence of the cross section for this process only comes from the λ_{hhh} and λ_{Hhh} couplings and they are very weakly sensitive to this parameter for small θ values. Indeed, for $\theta \to 0$, one has

$$\lambda_{hhh} = -\frac{m_h^2}{2v_{\rm SM}}\left(1 - \frac{\xi}{6}\right) + \mathcal{O}(\theta^2), \tag{5.11}$$

$$\lambda_{Hhh} = -\frac{\theta}{2v_{\rm SM}}\left[m_H^2 - 2m_h^2 + 4M^2 - \frac{\xi}{6}(m_H^2 - 2m_h^2 - 4M^2)\right] + \mathcal{O}(\theta^2), \tag{5.12}$$

wherein the $\tan\beta$ dependence only emerges at the $\mathcal{O}(\theta^2)$ level.

Fig. 5.11 displays the production cross section of the $e^+e^- \to Zhh$ process as a function of $\sin\theta$ for three fixed values of ξ, i.e, 0, 0.04 and 0.08. We here set $\tan\beta = 2$ (in fact, we have checked that the $\tan\beta$ dependence is significantly negligible for $|\sin\theta| \lesssim 0.2$). We find that the $\sin\theta$ dependence of the cross section is rather dissimilar in the case of $\sqrt{s} = 500$ GeV from those when $\sqrt{s} = 1000$ and 2000 GeV. This can be explained depending upon whether on-shell A production is possible or not. Clearly, in the case of $\sqrt{s} = 500$ GeV, the diagram including A is not significant because

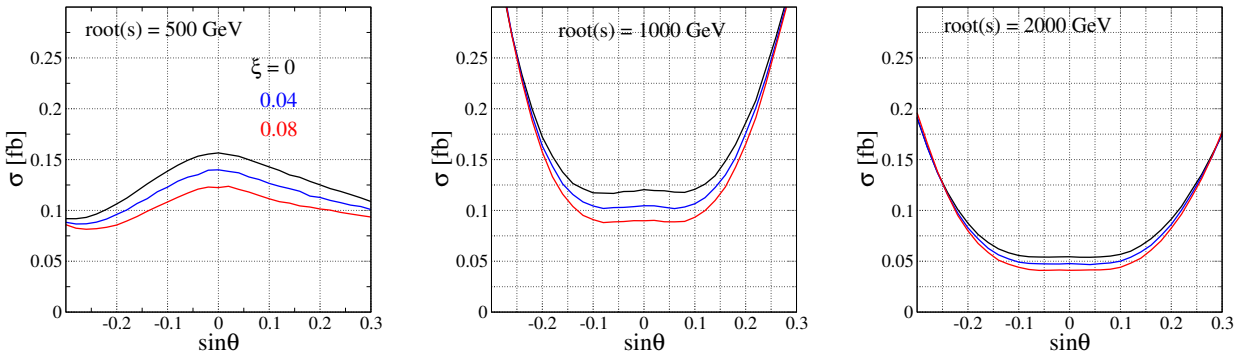

Figure 5.11: Cross section for the $e^+e^- \to Zhh$ process as a function of $\sin\theta$ in the C2HDM with $\tan\beta = 2$ and $M = 0.8m_A$. The collision energy and the mass $(\sqrt{s}, m_A)$ with $m_H = m_A$ is fixed to be (500, 400), (1000, 500) and (2000, 500) in GeV unit for the left, center and right panels, respectively. A similar figure is seen in Ref. [33].

of its off-shell feature, since $m_A = 400$ GeV is larger than $\sqrt{s} - m_h$. Contrary, for the cases with $\sqrt{s} = 1000$ and 2000 GeV, a non-zero value of $\sin\theta$ permits one to have on-shell production of both H and A followed by the decays $H \to hh$ and $A \to hZ$, respectively, because λ_{Hhh} and g_{AhZ} are proportional to $\sin\theta$, as defined in Eqs. (5.10) and (5.2). As a result, at these two energies, the cross section can be increased due to their resonant productions. Regarding the ξ dependence, we notice that deviations between the C2HDM and E2HDM case remain comparable at all energies, typically being in the 20–30% range, a result of the interplay between the fact that the aforementioned $H \to hh$ and $A \to hZ$ decays are not the dominant ones at $m_A = m_H = 500$ GeV with the ξ dependence of the HZZ and AhZ couplings.

Fig. 5.12 displays the deviations in the $e^+e^- \to Zhh$ cross section from the E2HDM case arising in the C2HDM one by considering fixed values of $\kappa_V^2 = 0.99$ and 0.98. We here set $\sqrt{s} = 1000$ GeV, $m_H = m_A = 500$ GeV, $M = 0.8m_A$ and $\tan\beta = 2$. We notice that negative deviations up to around -18% observed in the case of $\kappa_V^2 = 0.98$ and $\sin\theta > 0$ are predicted also after imposing the constraints from the high luminosity data at the LHC. The main reason for this is a decreasing $|\sin\theta|$ as ξ becomes larger. As already clarified above, this result is almost independent of the choice of $\tan\beta$, so this process could be appropriate to separate the values of ξ and $\sin\theta$ once the masses of H and A are known, e.g., from studies of the $e^+e^- \to HA$ cross section.

Next, we consider double-h production through the VBF process. The representative Feynman diagrams are indicated in Fig. 5.13. The HS topologies (last diagram in Fig. 5.13) perform a subdominant role due to the tiny BR of $Z \to e^+e^-$. Identically to Zhh production, the $\tan\beta$ dependence only comes from the λ_{hhh} and λ_{Hhh} couplings, thus it is very small for small $\sin\theta$ values. The most significant difference compared to Zhh production is the fact that A resonance does not exist, since only the H one is possible, in the VBF case. Thus, it is not surprising to see the rather different dependence of the cross sections upon $\sin\theta$ and ξ, with respect to Fig. 5.11.

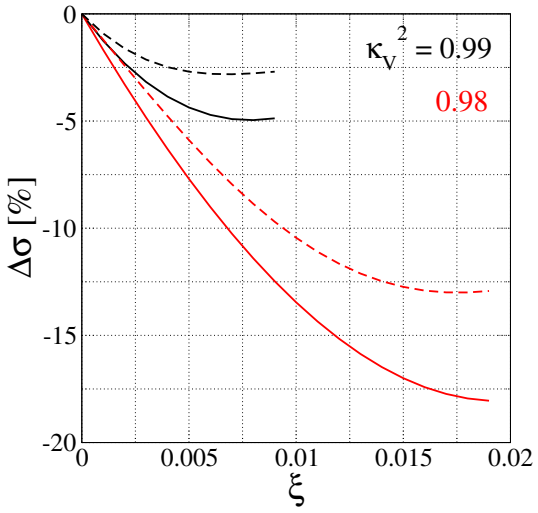

Figure 5.12: Deviations in the cross section $\Delta\sigma \equiv (\sigma_{\rm C2HDM}/\sigma_{\rm E2HDM} - 1)$ for the $e^+e^- \to Zhh$ process at fixed $\kappa_V^2 = 0.99$ (black curves) and 0.98 (red curves). We select $\tan\beta = 2$ and $\sqrt{s} = 1000$ GeV. For each κ_V^2, we display the case with $\sin\theta > 0$ (solid lines) and $\sin\theta < 0$ (dashed lines). We only display the result permitted by the unitarity and vacuum stability constraints and by the future LHC data assuming 3000 fb^{-1} with 95% CL The latter constraint is for the Type-I C2HDM. A similar figure is seen in Ref. [33].

In Fig. 5.14, we plot the cross section for the VBF process as a function of $\sin\theta$ with $\tan\beta = 2$. The characteristic behaviour is quite similar to that emerged in Zhh production. Nevertheless, the distinction between the C2HDM and the E2HDM evaluated for the same value of $\sin\theta$ is not so important as compared to the Zhh case, although the A resonance does not exist (in the existence of which the coupling dependence can be washed out through the BR).

In Fig. 5.15, we present the deviations in the VBF cross section as attained in the E2HDM case relative to the C2HDM one by adopting again $\kappa_V^2 = 0.99$ and 0.98, in line with previous examples. The behaviour is similar to that emerged in Fig. 5.12 , but the the magnitude of the deviation can be around -50% in the case of $\kappa_V^2 = 0.98$ and $\sin\theta > 0$. Here, according to Fig. 5.13, it would be possible to study the hhh, Hhh and $hhZZ$ couplings in presence of the knowledge of the Zhh one (recall that the AhZ vertex is fixed by the gauge structure).

Finally, we study the $t\bar{t}hh$ production process, for which the representative Feynman diagrams are presented in Fig. 5.16. We note (again) that the third diagram emerges at the tree level only in C2HDMs, not E2HDMs, since it comes from the non-linear nature of the composite Higgs interaction. Its effect is, however, negligibly small, because the y_{hhtt} coupling defined in Eq. (5.6) is proportional to ξ. The $\tan\beta$ dependence is significant here compared to the previous two double-h production modes , i.e., it appears not only in λ_{hhh} and λ_{Hhh} but also in several Yukawa couplings such as y_{htt}, y_{Htt} and $\tilde{y}_{Att}$ (other than indirectly via the Higgs widths). As a result, this process is useful to get independent information on $\tan\beta$ or to check its consistency with other processes

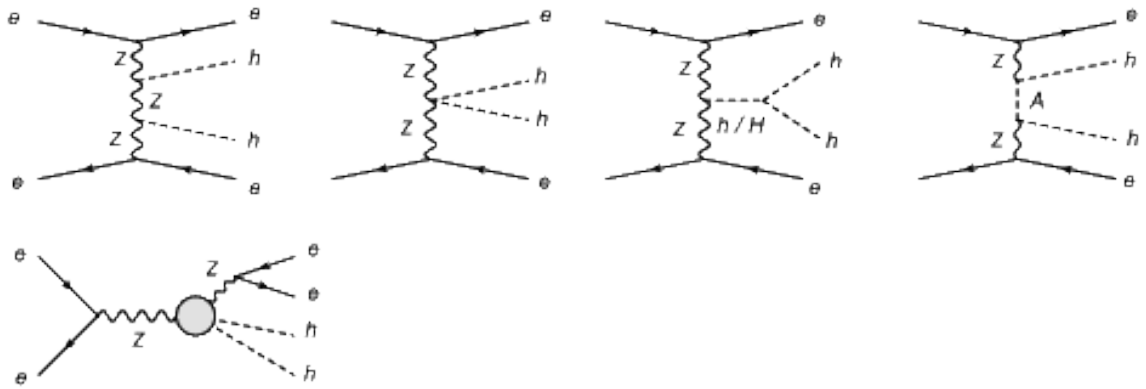

Figure 5.13: Representative Feynman diagrams for the $e^+e^- \to e^+e^-hh$ process. The last diagram corresponds to the process $e^+e^- \to Zhh \to e^+e^-hh$ (see Fig. 5.10). A similar figure is seen in Ref. [33].

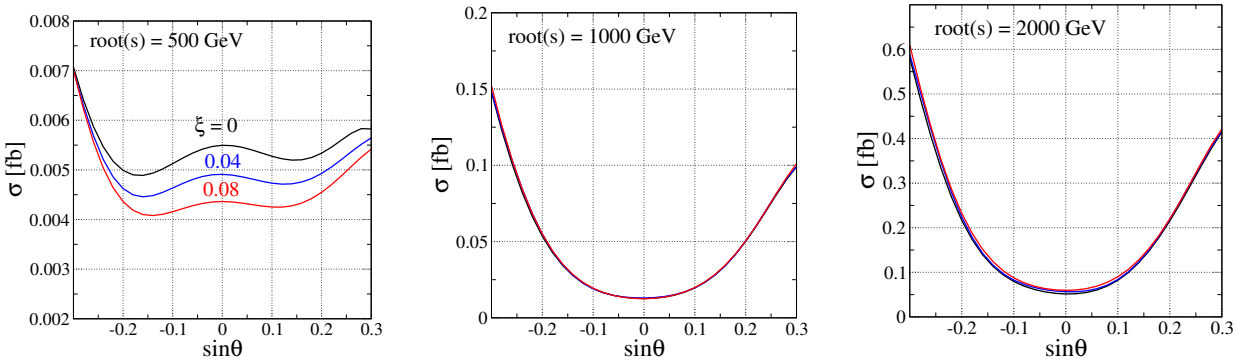

Figure 5.14: Cross section of the $e^+e^- \to e^+e^-hh$ process as a function of $\sin\theta$ in the C2HDM with $\tan\beta = 2$ and $M = 0.8m_A$. The collision energy and the mass ($\sqrt{s}$,m_A) with $m_H = m_A$ is fixed to be (500,400), (1000,500) and (2000,500) in GeV unit for the left, center and right panels, respectively. A similar figure is seen in Ref. [33].

if $\xi, \sin\theta, \tan\beta$ and the masses (plus possibly widths) of the additional Higgs bosons are known to some extent.

Fig. 5.17 indicates the cross section of the $t\bar{t}hh$ process as a function of $\sin\theta$ with $m_A = m_H =$ 500 GeV and $M = 0.8m_A$. We set $\tan\beta$ to be 1, 2 and 3 for the left, center and right panels, respectively. The cross section grows when $\sin\theta \gtrsim 0$ since the $H \to hh$ decay mode opens up and diagrams including the AhZ vertex, e.g., the fourth topology in Fig. 5.16, become nonzero. Comparing the top ($\sqrt{s} = 1$ TeV) and bottom ($\sqrt{s} = 2$ TeV) panels we find that the cross section at $\sqrt{s} = 1$ TeV is approximately 1 order of magnitude smaller than that at $\sqrt{s} = 2$ TeV when $\sin\theta \neq 0$. This can be clarified with the opening of on-shell HA production (again, see the fourth diagram in Fig. 5.16) with the subsequent decays of $H \to hh$ and $A \to t\bar{t}$.

Even if in both previous figures differences between the E2HDM ($\xi = 0$) and C2HDM ($\xi \neq 0$)

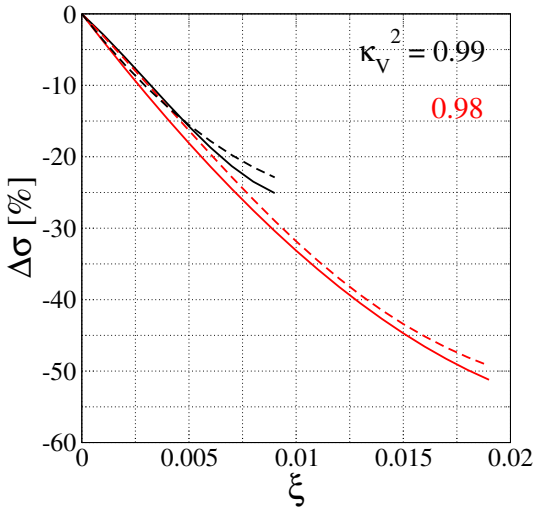

Figure 5.15: Deviations in the cross section $\Delta\sigma \equiv (\sigma_{\rm C2HDM}/\sigma_{\rm E2HDM} - 1)$ for the $e^+e^- \to e^+e^-hh$ process at fixed $\kappa_V^2 = 0.99$ (black curves) and 0.98 (red curves). We select $\tan\beta = 2$ and $\sqrt{s} = 1000$ GeV. For each κ_V^2, we show the case of $\sin\theta > 0$ (solid lines) and $\sin\theta < 0$ (dashed lines). We only display the result permitted by the unitarity and vacuum stability constraints and by the future LHC data assuming 3000 fb^{-1} with 95% CL. The latter constraint is for the Type-I C2HDM. A similar figure is seen in Ref. [33].

cases can be large, up to several tens of percent in the regions permitted by Tab. 5.1, again, they become very apparent if hVV is fixed. Hence, in Fig. 5.18, we indicate their relative cross sections of the $t\bar{t}hh$ process for a fixed value of κ_V^2=0.99 and 0.98. Here, we set $m_A = m_H = 500$ GeV, $M = 0.8m_A$, $\tan\beta = 2$ and $\sqrt{s} = 1000$ GeV. As we can see, the deviation is negative and can be more than 30% for $\kappa_V^2 = 0.98$ with positive $\sin\theta$. This is simply because of the fact that the cross section has a minimum at $\sin\theta = 0$ and important cancellations among the diagrams in Fig. 5.16 do not exist. Conversely, for positive values of $\sin\theta$ the deviation can be positive, thus relative sign differences among the mentioned graphs can offset the usually negative rescaling of all vertices via ξ.

In brief, the double-h productions can be useful to obtain the ξ and θ parameters by measuring the cross sections of the HS and VBF cases, because these are not easily defined by the factor of κ_V^2 yet they are little sensitive to $\tan\beta$. The $t\bar{t}hh$ production is instead useful to derive $\tan\beta$ and significant to examine the self-consistency of either Higgs scenario, elementary or composite, produced the diversity of particles and interactions intervening in it.

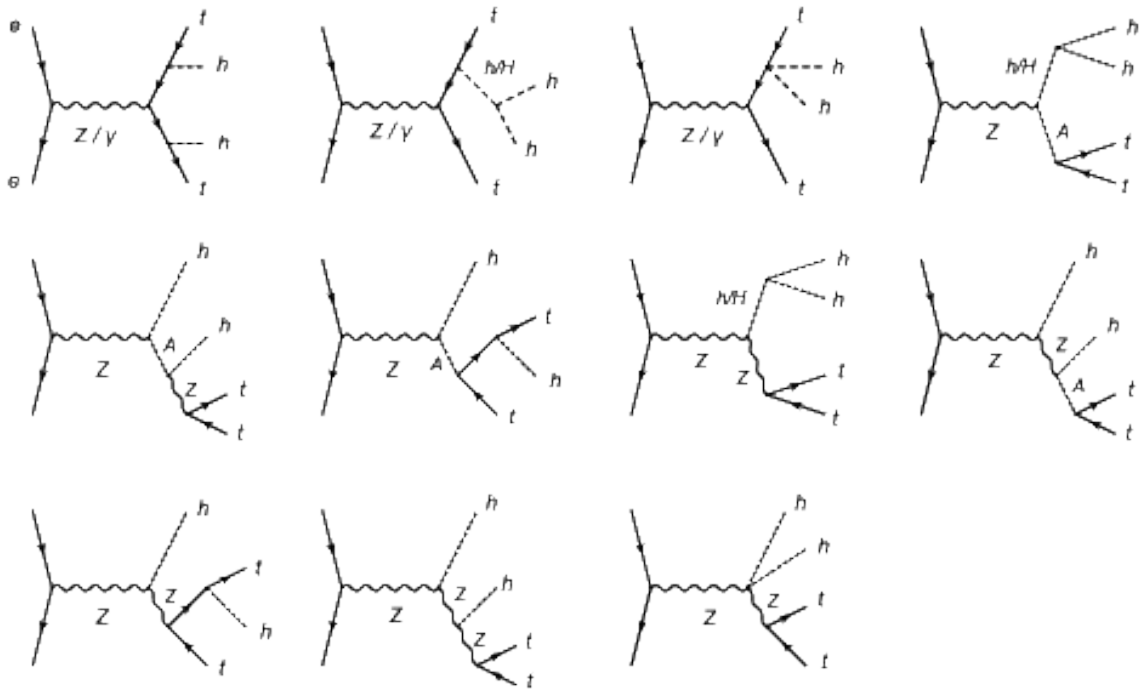

Figure 5.16: Representative Feynman diagrams for the $e^+e^- \to t\bar{t}hh$ process. A similar figure is seen in Ref. [33].

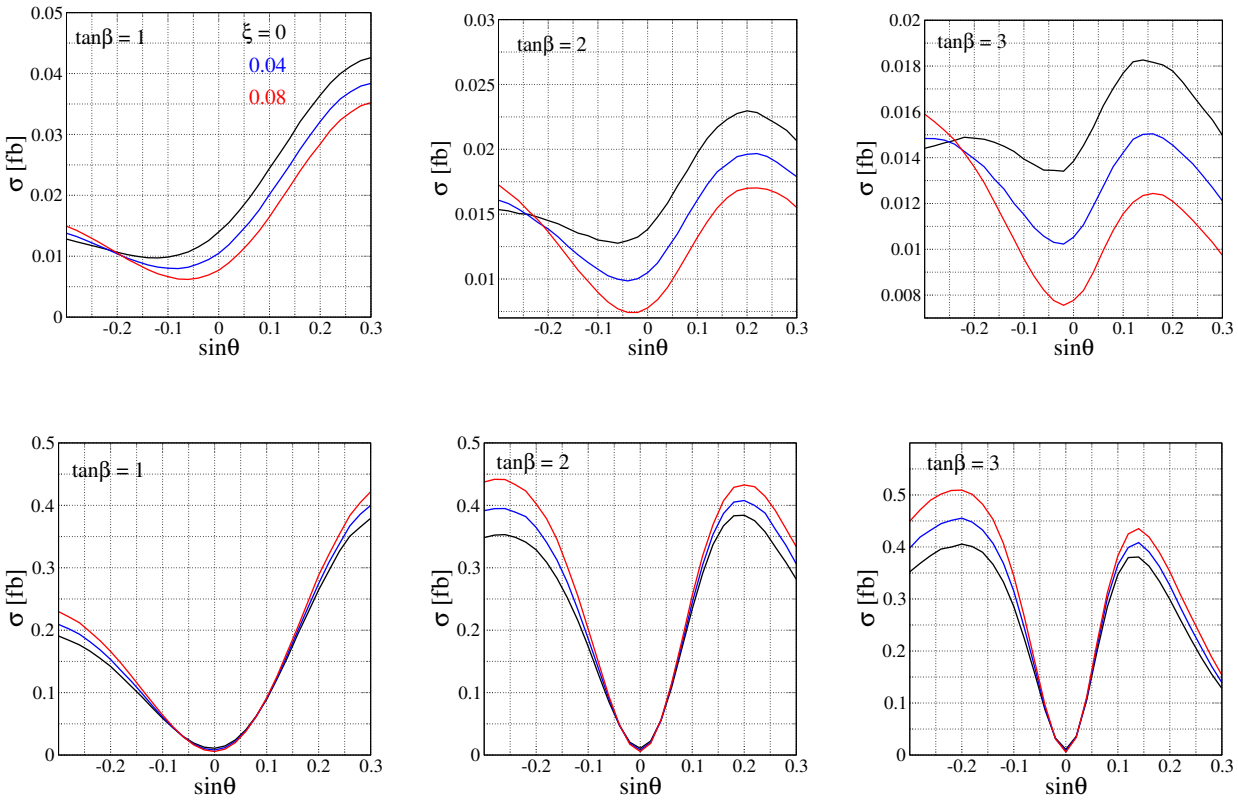

Figure 5.17: Cross section of the $e^+e^- \to t\bar{t}hh$ process as a function of $\sin\theta$ in the C2HDM with $m_A = m_H = 500$ GeV and $M = 0.8m_A$. We select $\tan\beta = 1$, 2 and 3 for the left, center and right panels, respectively. The collision energy $\sqrt{s}$ is fixed to be 1000 GeV (top) and 2000 GeV (bottom). A similar figure is seen in Ref. [33].

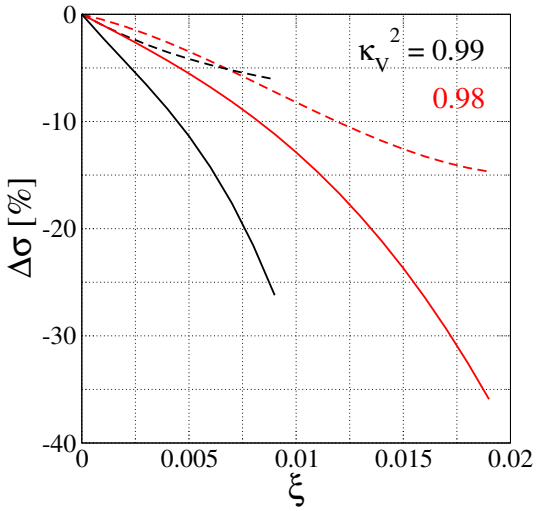

Figure 5.18: Deviations in the cross section $\Delta\sigma \equiv (\sigma_{\rm C2HDM}/\sigma_{\rm E2HDM} - 1)$ for the $e^+e^- \to t\bar{t}hh$ process at fixed $\kappa_V^2 = 0.99$ (black curves) and 0.98 (red curves). We select $\tan\beta = 2$ and $\sqrt{s} = 1000$ GeV. For each κ_V^2, we display the case of $\sin\theta > 0$ (solid lines) and $\sin\theta < 0$ (dashed lines). We only show the result allowed by the unitarity and vacuum stability constrains and by the future LHC data assuming 3000 fb^{-1} with 95% CL. The latter constraint is for the Type-I C2HDM. A similar figure is seen in Ref. [33].

5.5 Conclusions

In this chapter, we have continued our research on the C2HDM hypothesis, by adopting the same model structure as in Chapter 3 and 4. We have herein continued to carry out a phenomenological study intending to establish the potential of future e^+e^- colliders in distinguishing the two scenarios, E2HDM versus C2HDM. These machine environments provide one with a very high precision achievable in measuring the SM-like h production cross section in both single- and double-h mode, so that the rather different samples appearing in the composite scenario compared to the elementary one may effectively be tested. We have proven this to be the case for all available modes: i.e., HS, VBF and associated production with top quarks. Separation between the two non-minimal elementary and composite Higgs hypotheses can potentially (i.e., depending on the values of $\sin\theta$ and ξ but irrespectively of $\tan\beta$) be achieved in all channels. Indeed, for some combinations of $\sin\theta$ and ξ, the C2HDM generates large, and generally negative, corrections to the SM coupling strengths, up to order -20% or so, that cannot ever be attained in the E2HDM, consequently enabling one to promptly disentangle between the two hypotheses. In other cases, when one can achieve similar deviations in both hypotheses within expected precision for some (different in the two models) combination of inputs, one has to resort to a multidimensional fit evaluating the CL in either scenario. Yet, even in this case, we expect that the separation to be possible.

We have come to these conclusions assuming a Type-I setup in the Yukawa sector, even though we have argued that our results are independent of the interactions of the Higgs states with fermions, since the Yukawa dependence only appears in higher orders via the width of the heavy CP-even and CP-odd states, at least for the h production modes we have studied. Only the experimental bounds are in fact type dependent, but the above prospects about the possibility of distinguishing the two 2HDM realisation persist for all types.

This has been accomplished in existence of theoretical and experimental bounds, the latter extrapolated to the end of the LHC era, assuming both a standard (up to 300 fb^{-1}) and HL (up to 3000 fb^{-1}) setup for it. We are thus led to conclude that future electron-positron colliders performing between 500 and 2000 GeV, of which there exist various prototypes (such as the aforementioned ILC [134–144], but also the Compact Linear Collider (CLiC) [145] and Future Circular Collider e^+e^- (FCC-ee) [146]), are the ideal testing ground to confirm or disprove the presence in Nature of either a E2HDM or C2HDM as the fundamental dynamics of EWSB.

Chapter 6

Conclusion

The discovery of a Higgs boson with a mass of $\sim$ 125 GeV is an enormous success for particle physics. The Higgs boson can be recognised as a more special particle than all others since it is the origin of the hierarchy problem, relevant to EWSB, interacts with BSM particles to give them mass and is the only scalar in the SM. The current task is the accurate measurement of the properties of the last particle of the SM. Many BSM scenarios introduce altered Higgs couplings which may give rise to indirect signals of new physics. Investigation of properties of new signals for each model is also essential to discriminate between BSM frameworks at present and future collider experiments. So the thesis has presented some phenomenological studies relevant to the Higgs sector of BSM scenarios, namely, the C2HDM and 3HDM.

In Chapter 1 we briefly discussed the SM of particle physics. In particular, we focused on Higgs physics in the SM. We then gave a brief motivation for some extended Higgs models discussed in the main chapters.

In Chapter 2 we considered the phenomenology of charged Higgs bosons in 3HDMs. We found that the $H^{\pm}_{1,2} \to cb$ decay mode is dominant in the Type-Y and Type-Z 3HDMs when $m_{H^{\pm}_{1,2}} < m_t - m_b$. The $H^{\pm} \to cb$ decay mode can also be dominant in the Type-Y 2HDM when $m_{H^{\pm}} < m_t - m_b$, but the bound from $B \to X_s\gamma$ rules out such a light Higgs boson scenario. Conversely, in 3HDMs, the scenario with masses of $\mathcal{O}(100)$ GeV for the charged Higgs boson is allowed by $B \to X_s\gamma$. We found that the numerical values of the BR($B \to X_s\gamma$) in the Type-II, Type-Y and Type-Z 3HDMs are different from those in the Type-II and Type-Y 2HDMs for the case of a non-zero mixing and, e.g., $m_{H^{\pm}_2} - m_{H^{\pm}_1} = 20$, 50 and 80 GeV. In contrast, those in the Type-I and Type-X 3HDMs are not much different from those in Type-I and Type-X 2HDMs for the case of a non-zero mixing and, e.g., $m_{H^{\pm}_2} - m_{H^{\pm}_1} = 20$, 50 and 80 GeV. We have also considered the constraints from direct searches at the LHC for charged Higgs bosons from top quark decays. Our results showed that, in the Type-Y and Type-Z 3HDMs, the scenario with $m_{H^{\pm}_{1,2}} < m_t - m_b$ is extremely constrained from $B \to X_s\gamma$ and LHC direct searches, while the scenario with only $m_{H^{\pm}_1} < m_t - m_b$ is allowed. However, the special case $m_{H^{\pm}_1} \approx m_{W^{\pm}}$ with $m_{H^{\pm}_2} < m_t$ is permitted (also by Tevatron and LEP2),

but only in the Type-Y 3HDM. Thus, this multi charged Higgs signature enables us to distinguish between 2HDMs and 3HDMs.

Chapter 3 has been devoted to unitarity properties of the C2HDM. We calculated the scattering amplitude for all possible two-to-two body elastic pseudo(scalar) boson scatterings at energy scales $\sqrt{s}$ accessible at the LHC and beyond it. We then made a numerical analysis of the parameter space from unitarity employing all the possible scattering channels in addition to vacuum stability constraints. We found important discriminations between the allowed parameter space in the C2HDM and that in the E2HDM. The overall results are the following. We obtained the upper limit on $\sqrt{s}$ following a scan on M^2, e.g., $\sqrt{s} \lesssim 2$, 4 and 13 TeV for the case of $f = 500$, 1000 and 3000 GeV, respectively, in the case of no-mixing between h and H, i.e., $\cos\theta = 1$ and $m_A = m_{H^\pm} = m_H$. The upper limit was obtained not only on $\sqrt{s}$ but also on m_Φ (a generic heavy Higgs mass) in the non-zero mixing case, e.g., $\cos\theta = 0.99$. In the case of $m_{H^\pm} = m_A = M$, we have found that the extra Higgs states H, A or $H^\pm$ produce a somewhat larger mass region in the C2HDM compared to the E2HDM, the more so the smaller f. A similar behaviour is valid for the case of $m_{H^\pm} = m_H = M$. Thus, a thorough investigation of the Higgs mass samples that may appear at the LHC could allow us to find hints of a C2HDM hypothesis and disentangle it from the E2HDM one.

In Chapter 4 we presented a phenomenological study aimed at establishing the potential of the LHC in distinguishing two hypotheses, E2HDM versus C2HDM, by employing the different decay and production samples for the four heavy Higgs states (H, A and $H^\pm$). Particularly, the most interesting situation could appear when, e.g., in the presence of a fixed deviation of a few percents from the SM value for the $hVV (V = W^\pm, Z)$ coupling, the E2HDM(C2HDM) would demand the non-zero(zero) mixing case between h and H states. Thus, in this situation, $H \to W^+W^-$ and ZZ decays would be a discriminator between the two hypotheses since they would be absent in the composite case. Furthermore, the $A \to Zh$ and $H^\pm \to W^\pm h$ decays would also be discriminators between the two scenarios due to the absence of these decays in the C2HDM. In summary, if deviations will be detected during Run 2 of the LHC in the couplings of the discovered Higgs state with either SM gauge bosons or matter fermions, then, not only a thorough investigation of the 2HDM scenarios is required (as one of the simplest non-minimal versions of EWSB produced by the Higgs mechanism via *doublet* states, like the one already discovered) but also a dedicated investigation of the decay samples of all potentially reachable heavy Higgs states could allow one to distinguish the E2HDM from the C2HDM.

Finally, in Chapter 5 we presented a phenomenological study aimed at establishing the potential of future e^+e^- colliders in distinguishing the two hypotheses, E2HDM versus C2HDM. A very high accuracy achievable in measuring the SM-like h production cross section in both single- and double-h mode is provided by these machine environments, i.e., via the HS, VBF and associated production with top quarks modes, so that we may effectively test the rather different samples appearing in the composite scenario with respect to the elementary one. All channels can potentially accomplish

to distinguish E2HDM realisations from C2HDM ones (depending on the values of $\sin\theta$ and ξ but irrespectively of $\tan\beta$). In short, future electron-positron colliders running between 500 and 2000 GeV, of which there exist various prototypes (such as the ILC, CLIC, FCC-ee), are the perfect machines to verify or disprove the presence in Nature of either an E2HDM or C2HDM as the underlying dynamics of EWSB.

Overall, in this thesis, we focused on the phenomenology of extended Higgs models determining the patterns of Higgs bosons in a C2HM and 3HDM. As we have studied in this thesis, the discovered Higgs boson can still belong to an extended Higgs model, as for instance one of the CP-even Higgs bosons of the C2HDM or the 3HDM, or it can be a composite or an elementary Higgs boson. As a result, Higgs physics is one of the essential tasks of future collider experiments. The data collected herein will enable us to assess more precisely Higgs boson properties. Thus, extended Higgs sectors are currently an exciting topic of research. In the future, we hope we can find physics beyond the SM and our study of extended Higgs models will have contributed to this goal.

Appendix A

Mass matrix elements

We show here the analytic formulae for the mass matrices of the singly-charged ($\mathcal{M}_C^2$), CP-odd ($\mathcal{M}_A^2$) and CP-even ($\mathcal{M}_H^2$) scalar states in the Higgs basis of 3HDMs. The matrix elements of $\mathcal{M}_C^2$ and $\mathcal{M}_A^2$ are defined by

$$(\mathcal{M}_C^2)_{11} = -\frac{v^2}{2}\left[(\rho_2+\rho_3)c_\gamma^2 + (\kappa_2+\kappa_3)s_\gamma^2\right] + \mu_{12}^2\frac{c_\gamma}{s_\beta c_\beta} + \mu_{23}^2\frac{s_\gamma}{s_\beta c_\beta}, \tag{A.1}$$

$$\begin{aligned}(\mathcal{M}_C^2)_{22} = &-\frac{v^2}{2}\left[(\rho_2+\rho_3)s_\beta^2 s_\gamma^2 + (\sigma_2+\sigma_3)c_\beta^2 + (\kappa_2+\kappa_3)s_\beta^2 c_\gamma^2\right] \\ &+ \mu_{12}^2 t_\beta s_\gamma t_\gamma + \frac{\mu_{13}^2}{s_\gamma c_\gamma} + \mu_{23}^2\frac{t_\beta c_\gamma}{t_\gamma},\end{aligned} \tag{A.2}$$

$$(\mathcal{M}_C^2)_{12} = -\frac{v^2}{4}(\rho_2+\rho_3-\kappa_2-\kappa_3)s_\beta s_{2\gamma} + \mu_{12}^2\frac{s_\gamma}{c_\beta} - \mu_{23}^2\frac{c_\gamma}{c_\beta}, \tag{A.3}$$

$$(\mathcal{M}_A^2)_{11} = -v^2\left(\rho_3 c_\gamma^2 + \kappa_3 s_\gamma^2\right) + \mu_{13}^2\frac{c_\gamma}{s_\beta c_\beta} + \mu_{23}^2\frac{s_\gamma}{s_\beta c_\beta}, \tag{A.4}$$

$$(\mathcal{M}_A^2)_{22} = -v^2\left(\rho_3 s_\beta^2 s_\gamma^2 + \sigma_3 c_\beta^2 + \kappa_3 s_\beta^2 c_\gamma^2\right) + \mu_{12}^2 t_\beta s_\gamma t_\gamma + \mu_{13}^2\frac{s_\gamma}{s_\gamma c_\gamma} + \mu_{23}^2\frac{t_\beta c_\gamma}{t_\gamma}, \tag{A.5}$$

$$(\mathcal{M}_A^2)_{12} = -\frac{v^2}{2}(\rho_3-\kappa_3)s_\beta s_{2\gamma} + \mu_{12}^2\frac{s_\gamma}{c_\beta} - \mu_{23}^2\frac{c_\gamma}{c_\beta}. \tag{A.6}$$

Those for $\mathcal{M}_H^2$ are defined by

$$(\mathcal{M}_H^2)_{11} = \frac{v^2}{2}(2\lambda_1 c_\beta^4 c_\gamma^4 + 2\lambda_2 s_\beta^4 + 2\lambda_3 c_\beta^4 s_\gamma^4 + \rho_{123} s_{2\beta}^2 c_\gamma^2 + \sigma_{123} c_\beta^4 s_{2\gamma}^2 + \kappa_{123} s_{2\beta}^2 s_\gamma^2), \tag{A.7}$$

$$(\mathcal{M}_H^2)_{22} = \frac{v^2}{8}(2\lambda_1 s_{2\beta}^2 c_\gamma^4 + 2\lambda_2 s_{2\beta}^2 + 2\lambda_3 s_{2\beta}^2 s_\gamma^4 - 4\rho_{123} c_\beta^2 s_{2\gamma}^2 + \sigma_{123} s_{2\beta}^2 s_{2\gamma}^2 - 4\kappa_{123} s_{2\beta}^2 s_\gamma^2) + \mu_{12}^2 \frac{c_\gamma}{s_\beta c_\beta} + \mu_{23}^2 \frac{s_\gamma}{s_\beta c_\beta}, \tag{A.8}$$

$$(\mathcal{M}_H^2)_{33} = \frac{v^2}{4}(\lambda_1 + \lambda_3 - 2\sigma_{123}) c_\beta^2 s_{2\gamma}^2 + \mu_{12}^2 t_\beta s_\gamma t_\gamma + \frac{\mu_{13}^2}{s_\gamma c_\gamma} + \mu_{23}^2 \frac{c_\gamma t_\beta}{t_\gamma}, \tag{A.9}$$

$$(\mathcal{M}_H^2)_{12} = -\frac{v^2}{2}\Big[2\lambda_1 s_\beta c_\beta^3 c_\gamma^4 - 2\lambda_2 s_\beta^3 c_\beta + 2\lambda_3 s_\beta c_\beta^3 s_\gamma^4 - (c_\beta + c_{3\beta}) s_\beta c_\gamma^2 \rho_{123} + s_\beta c_\beta^3 s_{2\gamma}^2 \sigma_{123} - (c_\beta + c_{3\beta}) s_\beta s_\gamma^2 \kappa_{123}\Big], \tag{A.10}$$

$$(\mathcal{M}_H^2)_{13} = -\frac{v^2}{4}\left(2\lambda_1 c_\beta^3 s_{2\gamma} c_\gamma^2 - 2\lambda_3 c_\beta^3 s_{2\gamma} s_\gamma^2 + 2\rho_{123} s_\beta^2 c_\beta s_{2\gamma} - \sigma_{123} c_\beta^3 s_{4\gamma} - 2\kappa_{123} s_\beta^2 c_\beta s_{2\gamma}\right), \tag{A.11}$$

$$(\mathcal{M}_H^2)_{23} = \frac{v^2}{4}[4\lambda_1 s_\gamma c_\gamma^3 - 4\lambda_3 s_\gamma^3 c_\gamma - 2(\rho_{123} - \kappa_{123}) s_{2\gamma} - \sigma_{123} s_{4\gamma}] s_\beta c_\beta^2 + \mu_{12}^2 \frac{s_\gamma}{c_\beta} - \mu_{23}^2 \frac{c_\gamma}{c_\beta}. \tag{A.12}$$

In the above formulae, we adopted the shorthand notations $c_Y = \cos Y$, $s_Y = \sin Y$ and $t_Y = \tan Y$.

Appendix B

Input parameters

For the numerical calculations, we have adopted the following input values for the SM parameters [147]:

$$\begin{aligned} &m_{W^\pm} = 80.385 \text{ GeV},\ m_Z = 91.1876 \text{ GeV},\ G_F = 1.1663787 \times 10^{-5} \text{ GeV}^{-2}, \\ &m_\tau = 1.77684 \text{ GeV},\ m_\mu = 0.105658367 \text{ GeV}, \\ &\alpha_s(m_Z) = 0.1185,\ m_t^{\text{pole}} = 174.6 \text{ GeV},\ m_b^{\text{pole}} = 4.89 \text{ GeV},\ m_c^{\text{pole}} = 1.64 \text{ GeV}, \end{aligned} \tag{B.1}$$

where m_t^{pole}, m_b^{pole} and m_c^{pole} are, respectively, the pole masses of the top, bottom and charm quark. For the $\overline{\text{MS}}$ masses of the quarks, we use the following values [147]:

$$\bar{m}_b(\bar{m}_b) = 4.18 \text{ GeV},\ \bar{m}_c(\bar{m}_c) = 1.275 \text{ GeV},\ \bar{m}_s(2 \text{ GeV}) = 0.0935 \text{ GeV}. \tag{B.2}$$

Using these $\overline{\text{MS}}$ masses, we attain the running masses of the quarks at, e.g., $\mu = 100$ GeV to be $\bar{m}_b = 3.01$ GeV, $\bar{m}_c = 0.701$ GeV and $\bar{m}_s = 0.0489$ GeV. As for the other inputs, we use

$$|V_{tb}V_{ts}/V_{cb}|^2 = 0.9626,\ \text{BR}(B \to X_c \ell \nu) = 0.1065. \tag{B.3}$$

for the calculation of $\text{BR}(B \to X_s\gamma)$ and

$$|V_{cb}| = 0.0409 \tag{B.4}$$

for that of the charged Higgs boson decays.

Appendix C

Kinetic term

According to the formulae constructed by Callan, Coleman, Wess and Zumino [49, 50], the kinetic Lagrangian in non-linear sigma models is given in Eq. (3.6). In this expression, each of d_μ's defined in Eq. (3.7) are determined in the $SO(6) \to SO(4) \times SO(2)$ model by

$$\begin{aligned}(d^{\hat{1}}_\alpha)_\mu &= -\frac{\sqrt{2}}{f}\partial_\mu h^1_\alpha - \frac{g}{2f}[(h^4_\alpha - ih^3_\alpha)W^+_\mu + (h^4_\alpha + ih^3_\alpha)W^-_\mu] \\ &\quad - \frac{\sqrt{2}g_Z}{f}\left(\frac{1}{2} - \sin^2\theta_W\right)h^2_\alpha Z_\mu - \frac{\sqrt{2}e}{f}h^2_\alpha A_\mu + \mathcal{O}(1/f^3), \qquad \text{(C.1)} \\ (d^{\hat{2}}_\alpha)_\mu &= -\frac{\sqrt{2}}{f}\partial_\mu h^2_\alpha - i\frac{g}{2f}[(h^4_\alpha - ih^3_\alpha)W^+_\mu - (h^4_\alpha + ih^3_\alpha)W^-_\mu] \\ &\quad + \frac{\sqrt{2}g_Z}{f}\left(\frac{1}{2} - \sin^2\theta_W\right)h^1_\alpha Z_\mu + \frac{\sqrt{2}e}{f}h^1_\alpha A_\mu + \mathcal{O}(1/f^3), \qquad \text{(C.2)} \\ (d^{\hat{3}}_\alpha)_\mu &= -\frac{\sqrt{2}}{f}\partial_\mu h^3_\alpha + \frac{g}{2f}[(h^2_\alpha - ih^1_\alpha)W^+_\mu + (h^2_\alpha + ih^1_\alpha)W^-_\mu] - \frac{g_Z}{\sqrt{2}f}h^4_\alpha Z_\mu + \mathcal{O}(1/f^3), \qquad \text{(C.3)} \\ (d^{\hat{4}}_\alpha)_\mu &= -\frac{\sqrt{2}}{f}\partial_\mu h^4_\alpha + i\frac{g}{2f}[(h^2_\alpha - ih^1_\alpha)W^+_\mu - (h^2_\alpha + ih^1_\alpha)W^-_\mu] + \frac{g_Z}{\sqrt{2}f}h^3_\alpha Z_\mu + \mathcal{O}(1/f^3). \qquad \text{(C.4)}\end{aligned}$$

These expressions can be rewritten as

$$i(d^{\hat{1}}_\alpha)_\mu + (d^{\hat{2}}_\alpha)_\mu = -\frac{2}{f}\left[\partial_\mu\omega^+_\alpha - i\frac{g}{\sqrt{2}}\phi^0_\alpha W^+_\mu - ig_Z\left(\frac{1}{2} - \sin^2\theta_W\right)\omega^+_\alpha Z_\mu - ie\omega^+_\alpha A_\mu\right] + \mathcal{O}(1/f^3), \qquad \text{(C.5)}$$

$$-i(d^{\hat{3}}_\alpha)_\mu + (d^{\hat{4}}_\alpha)_\mu = \frac{2}{f}\left[\partial_\mu\phi^0_\alpha - i\frac{g}{\sqrt{2}}\omega^+_\alpha W^-_\mu + i\frac{g_Z}{2}\phi^0_\alpha Z_\mu\right] + \mathcal{O}(1/f^3), \qquad \text{(C.6)}$$

where $\phi^0_\alpha = (h^4_\alpha - ih^3_\alpha)/\sqrt{2}$.

Appendix D

Antisymmetric representation, $\Sigma(15)$

As already mentioned, under $SO(6)$, the matrix U is transformed as non-linearly, i.e., $U \to gUh^{-1}$ with g and h being the transformation matrices for $SO(6)$ and $SO(4)\times SO(2)$, respectively. We can build a linear representation of the NG fields, e.g., the antisymmetric (adjoint) **15**-plet representation of $SO(6)$, by introducing a maxtrix $\Sigma_0 \equiv \sqrt{2}T_S$ which is invariant under the transformation of the $SO(4) \times SO(2)$ subgroup:

$$\Sigma = U\,\Sigma_0\,U^T. \tag{D.1}$$

Taking the Taylor expansion of the matrix U and summing up all the terms, the matrix Σ is expressed by four submatrices:

$$\begin{aligned}\Sigma &= \begin{pmatrix} \Sigma_{4\times4} & \Sigma_{4\times2} \\ -\Sigma_{4\times2}^T & \Sigma_{2\times2} \end{pmatrix} \\ &= \begin{pmatrix} \det\left[\sin\sqrt{\omega}(\sqrt{\omega})^{-1}\right]\frac{\Phi}{f}(i\sigma_2)\frac{\Phi^T}{f} & \frac{\Phi}{f}\sin\sqrt{\omega}(\sqrt{\omega})^{-1}(i\sigma_2)\cos\sqrt{\omega} \\ -\cos\sqrt{\omega}(i\sigma_2)\sin\sqrt{\omega}(\sqrt{\omega})^{-1}\frac{\Phi^T}{f} & \det[\cos\sqrt{\omega}](i\sigma_2) \end{pmatrix},\end{aligned} \tag{D.2}$$

where

$$\phi \equiv (\phi_1^{\hat{a}}, \phi_2^{\hat{a}}) \quad \text{and} \quad \omega \equiv \frac{\phi^T\phi}{f^2}. \tag{D.3}$$

By expanding the sine and cosine functions up to $\mathcal{O}(1/f^3)$, we obtain

$$(\Sigma_{4\times4})_{\hat{a}\hat{b}} = \frac{1}{f^2}\left[1 - \frac{1}{3!f^2}(\phi_1^2+\phi_2^2)\right](\phi_1^{\hat{a}}\phi_2^{\hat{b}} - \phi_1^{\hat{b}}\phi_2^{\hat{a}}) + \mathcal{O}\left(\frac{1}{f^6}\right), \tag{D.4}$$

$$(\Sigma_{4\times2})_{\hat{a}\alpha} = \frac{1}{f}[-\phi_2^{\hat{a}}, \phi_1^{\hat{a}}]_\alpha \tag{D.5}$$

$$+ \frac{1}{f^3}\left[-\frac{\phi_1\cdot\phi_2}{3}\phi_1^{\hat{a}} + \left(\frac{\phi_1^2}{2}+\frac{\phi_2^2}{6}\right)\phi_2^{\hat{a}}, -\left(\frac{\phi_1^2}{6}+\frac{\phi_2^2}{2}\right)\phi_1^{\hat{a}} + \frac{\phi_1\cdot\phi_2}{3}\phi_2^{\hat{a}}\right]_\alpha + \mathcal{O}\left(\frac{1}{f^5}\right), \tag{D.6}$$

$$(\Sigma_{2\times2})_{\alpha\beta} = \left[1 - \frac{1}{2f^2}(\phi_1^2+\phi_2^2) + \frac{1}{4!f^4}(\phi_1^4+\phi_2^4)\right](i\sigma_2)_{\alpha\beta} + \mathcal{O}\left(\frac{1}{f^6}\right). \tag{D.7}$$

Appendix E

Feynman rules

We present the trilinear couplings of the Higgs bosons which relate to the discussion of the C2HDM phenomenology given in Chapter 4. First, the Gauge-Gauge-Scalar type interactions are introduced by

$$\mathcal{L}_{\text{kin}} = \left(1 - \frac{\xi}{2}\right)(h\cos\theta - H\sin\theta)\left(g m_W W_\mu^+ W^{-\mu} + \frac{g_Z}{2} m_Z Z_\mu Z^\mu\right). \tag{E.1}$$

Second, the coefficients of the Scalar-Scalar-Gauge type interactions are defined in Table E.1, where we introduce

$$X \overleftrightarrow{\partial}_\mu Y = X(\partial_\mu Y) - (\partial_\mu X)Y. \tag{E.2}$$

Lastly, the scalar trilinear Hhh and H^+H^-h couplings given by

$$\mathcal{L} = +\lambda_{Hhh} Hhh + \lambda_{H^+H^-h} H^+H^-h + \cdots \tag{E.3}$$

are extracted as

$$\begin{aligned}\lambda_{Hhh} = {} & \frac{s_\theta}{v_{\text{SM}} s_{2\beta}}\left[-\frac{s_{2(\beta+\theta)}}{2}(2m_h^2 + m_H^2) + \frac{1}{2}(s_{2\beta} + 3s_{2(\beta+\theta)})M^2\right] \\ & + \frac{\xi}{12 v_{\text{SM}}} s_\theta\left[m_H^2 - 2m_h^2 + (1 + 3c_{2\theta} + 6\cot 2\beta s_{2\theta})M^2\right], \end{aligned} \tag{E.4}$$

$$\begin{aligned}\lambda_{H^+H^-h} = {} & \frac{c_\theta}{v_{\text{SM}}}\left[-(1 + 2\cot 2\beta\tan\theta)m_h^2 - 2m_{H^\pm}^2 + \frac{2}{s_{2\beta} c_\theta} s_{2\beta+\theta} M^2\right] \\ & + \frac{\xi}{6 v_{\text{SM}}} c_\theta\left[(1 + 4\cot 2\beta\tan\theta)m_h^2 + 2(m_{H^\pm}^2 - M^2)\right]. \end{aligned} \tag{E.5}$$

Vertex	Coefficient
$H^{\pm} \overleftrightarrow{\partial}_{\mu} A W^{\mp\mu}$	$\frac{g}{2}$
$H^{\pm} \partial_{\mu} h W^{\mp\mu}$	$\mp i \frac{g}{2}(1 - \frac{5}{6}\xi) \sin\theta$
$h \partial_{\mu} H^{\pm} W^{\mp\mu}$	$\pm i \frac{g}{2}(1 - \frac{1}{6}\xi) \sin\theta$
$H^{\pm} \partial_{\mu} H W^{\mp\mu}$	$\mp i \frac{g}{2}(1 - \frac{5}{6}\xi) \cos\theta$
$H \partial_{\mu} H^{\pm} W^{\mp\mu}$	$\pm i \frac{g}{2}(1 - \frac{1}{6}\xi) \cos\theta$
$A \partial_{\mu} h Z^{\mu}$	$-\frac{g_Z}{2}(1 - \frac{5}{6}\xi) \sin\theta$
$h \partial_{\mu} A Z^{\mu}$	$\frac{g_Z}{2}(1 - \frac{1}{6}\xi) \sin\theta$
$A \partial_{\mu} H Z^{\mu}$	$-\frac{g_Z}{2}(1 - \frac{5}{6}\xi) \cos\theta$
$H \partial_{\mu} A Z^{\mu}$	$\frac{g_Z}{2}(1 - \frac{1}{6}\xi) \cos\theta$
$H^{+} \overleftrightarrow{\partial}_{\mu} H^{-} Z^{\mu}$	$-i \frac{g_Z}{2} c_{2W}$
$H^{+} \overleftrightarrow{\partial}_{\mu} H^{-} A^{\mu}$	$-ie$

Table E.1: Vertices among Higgs and gauge bosons and their corresponding coefficients. A similar table is seen in Ref. [32].

Appendix F

Higgs search channels

Channel	Refs.
$\tau_{\rm had}\tau_{\rm had}$ (VBF, 8 TeV) $\tau_{\rm lep}\tau_{\rm had}$ (boosted, 8 TeV) $\tau_{\rm lep}\tau_{\rm had}$ (VBF, 8 TeV) $\tau_{\rm lep}\tau_{\rm lep}$ (boosted, 8 TeV) $\tau_{\rm lep}\tau_{\rm lep}$ (VBF, 8 TeV)	[148]
WW (VBF enhanced, 8TeV)	[149]
ZZ (VBF, 8TeV)	[150]
multilepton $1\ell 2\tau_{\rm had}$ ($t\bar{t}H$, 8 TeV) $2\ell 0\tau_{\rm had}$ ($t\bar{t}H$, 8 TeV) $2\ell 1\tau_{\rm had}$ ($t\bar{t}H$, 8 TeV) 3ℓ ($t\bar{t}H$, 8 TeV)	[151]
$b\bar{b}$ (Vh, 8 TeV) with 1-lepton and 2-lepton channels	[152]
$b\bar{b}$ (Vh, 13 TeV) with 0-lepton, 1-lepton and 2-lepton channels	[153]

Table F.1: List of the Higgs data patterns employed in the $\Delta\chi^2$ calculations in Figs. 5.2–5.3. A similar figure is seen in Ref. [33].

Model Type	$\tan\beta = 1$	$\tan\beta = 2$	$\tan\beta = 3$
Type I	$pp \to H \to ZZ \to 4\ell$ [106] $qQ \to q'Q'h \to WW \to 2\ell 2\nu$ [108]	$pp \to H \to ZZ \to 4\ell$ [106] $qQ \to q'Q'h \to WW \to 2\ell 2\nu$ [108]	$pp \to H \to ZZ \to 4\ell$ [106] $qQ \to q'Q'h \to WW \to 2\ell 2\nu$ [108]
Type II	$pp \to H \to ZZ \to 4\ell$ [106] $qQ \to q'Q'h \to WW \to 2\ell 2\nu$ [108]	$pp \to H \to ZZ \to 4\ell$ [106] $pp \to h \to WW^* \to \ell\nu\ell\nu$ [113] $qQ \to q'Q'h \to WW \to 2\ell 2\nu$ [108] $pp \to h \to ZZ \to 4\ell$ [109]	$pp \to H \to ZZ \to 4\ell$ [106] $qQ \to q'Q'h \to WW \to 2\ell 2\nu$ [108] $pp \to h \to ZZ \to 4\ell$ [109]
Type X	$pp \to H \to ZZ \to 4\ell$ [106] $qQ \to q'Q'h \to WW \to 2\ell 2\nu$ [108]	$pp \to H \to ZZ \to 4\ell$ [106] $qQ \to q'Q'h \to WW \to 2\ell 2\nu$ [108]	$pp \to H \to ZZ \to 4\ell$ [106] $qQ \to q'Q'h \to WW \to 2\ell 2\nu$ [108]
Type Y	$pp \to H \to ZZ \to 4\ell$ [106] $qQ \to q'Q'h \to WW \to 2\ell 2\nu$ [108] $gg \to \phi(h, H) \to \tau\tau$ [110]	$pp \to H \to ZZ \to 4\ell$ [106] $pp \to H \to hh \to 4b$ [107] $pp \to H \to WW^* \to \ell\nu\ell\nu$ [113] $pp \to h \to ZZ \to 4\ell$ [109]	$pp \to H \to hh \to 4b$ [107] $qQ \to q'Q'h \to WW \to 2\ell 2\nu$ [108] $pp \to h \to ZZ \to 4\ell$ [109]

Table F.2: Higgs search channels most reliable for excluding parameter regions in Figs. 5.2–5.3. A similar figure is seen in Ref. [33].

Appendix G

List of publications

This thesis is based on the following research papers.

[1] *Light charged Higgs boson scenario in 3-Higgs doublet models*
A. G. Akeroyd, S. Moretti, K. Yagyu and E. Yildirim
Int. J Mod. Phys. A32 (2017), 1750145

[2] *Perturbative unitarity bounds in composite two-Higgs doublet models*
S. De Curtis, S. Moretti, K. Yagyu and E. Yildirim
Phys. Rev. D94 (2016) 055017

[3] *LHC Phenomenology of Composite 2-Higgs Doublet Models*
S. De Curtis, S. Moretti, K. Yagyu and E. Yildirim
Eur. Phys. J. C77 (2017) 513

[4] *Single and double SM-like Higgs boson production at future electron-positron colliders in composite 2HDMs*
S. De Curtis, S. Moretti, K. Yagyu and E. Yildirim
Phys. Rev. D95 (2017) 095026

[5] *Prospects for charged Higgs searches at the LHC*
A. G. Akeroyd *et al.*,
Eur. Phys. J. C77 (2017) 276
Ref. [30] was captured by this review paper that I co-authored.

Bibliography

[1] G. Aad *et al.* [ATLAS Collaboration], "Observation of a new particle in the search for the Standard Model Higgs boson with the ATLAS detector at the LHC," Phys. Lett. **B716**, 1 (2012); S. Chatrchyan *et al.* [CMS Collaboration], "Observation of a new boson at a mass of 125 GeV with the CMS experiment at the LHC," Phys. Lett. **B716**, (2012) 30.

[2] P. W. Higgs, "Broken Symmetries and the Masses of Gauge Bosons", Phys. Rev. Lett. **13** (1964) 508–509.

[3] P. Higgs, "Broken symmetries, massless particles and gauge fields", Physics Phys. Lett. **12** (1964) 132.

[4] F. Englert and R. Brout, "Broken symmetry and the mass of gauge vector mesons", Phys. Rev. Lett. **13** (1964) 321.

[5] G. S. Guralnik, C. R. Hagen, and T. W. B. Kibble, "Global Conservation Laws and Massless Particles", Phys. Rev. Lett. **13** (1964) 585.

[6] T. Kibble, "Symmetry breaking in non Abelian gauge theories", Phys. Rev. **155** (1967) 1554.

[7] P. W. Higgs, "Spontaneous symmetry breakdown without massless bosons", Phys. Rev. **145** (1966) 1156.

[8] T. P. Cheng and L. F. Li, "Gauge theory of elementary particle physics: Problems and solutions," Oxford, UK: Clarendon (2000).

[9] S. F. Novaes, "Standard model: An Introduction," In "Sao Paulo 1999, Particles and fields" [hep-ph/0001283].

[10] C. Burgess and G. Moore, "The Standard Model: A Primer," Cambridge (2012).

[11] S. L. Glashow, "Partial Symmetries of Weak Interactions", Nucl. Phys. **22** (1961) 579.

[12] S. Weinberg, "A Model of Leptons", Phys. Rev. Lett. **19** (1967) 1264.

[13] A. Salam, "Weak and Electromagnetic Interactions", Conf. Proc. **C680519** (1968) 367.

[14] G. S. Franz Mandl and Graham Shaw, "Quantum Field Theory", John Wiley and Sons Ltd, (1984).

[15] H. Fritzsch, M. Gell-Mann and H. Leutwyler, "Advantages of the Color Octet Gluon Picture", Phys. Lett. **B47** (1973) 365.

[16] M. Gell-Mann, "A schematic model of baryons and mesons", Phys. Lett. **8** (1964) 214.

[17] G. Zweig, "An $SU(3)$ model for strong interaction symmetry and its breaking; Version 1", Technical Report CERN-TH-401, CERN, Geneva, (Jan, 1964).

[18] M. Baak, R. Kogler, "The global electroweak Standard Model fit after the Higgs discovery", arXiv:1306.0571v2.

[19] H. Yukawa, "On the Interaction of Elementary Particles I", Proc. Phys. Math. Soc. Jap. **17** (1935) 48.

[20] B. W. Lee, C. Quigg and H. B. Thacker, "Weak interactions at very high energies: The role of the Higgs-boson mass", Phys. Rev. **D16** (1977) 1519.

[21] J. M. Cornwall, D. N. Levin and G. Tiktopoulos, "Uniqueness of spontaneously broken gauge theories", Phys. Rev. Lett. **30** (1973) 1268; J. M. Cornwall, D. N. Levin and G. Tiktopoulos, "Derivation of gauge invariance from high-energy unitarity bounds on the S matrix", Phys. Rev. **D10** (1974) 1145.

[22] A. Djouadi, "The Anatomy of electro-weak symmetry breaking. I: The Higgs boson in the standard model", Phys. Rept. **457** (2008) 1.

[23] M. Lindner, M. Sher and H. W. Zaglauer, "Probing vacuum stability bounds at the fermilab collider", Phys. Lett. **B228**, (1989) 139.

[24] G. Altarelli and G. Isidori, "Lower limit on the Higgs mass in the standard model: An update", Phys. Lett. **B337**, (1994) 141.

[25] J. A. Casas, J. R. Espinosa and M. Quiros, "Standard model stability bounds for new physics within LHC reach," Phys. Lett. **B382**, (1996) 374.

[26] O. Matsedonskyi, G. Panico, and A. Wulzer, "Light Top Partners for a Light Composite Higgs", JHEP **1301** (2013) 164.

[27] M. Redi and A. Tesi, "Implications of a Light Higgs in Composite Models", JHEP **1210** (2012) 166.

[28] G. Panico, M. Redi, A. Tesi, and A. Wulzer, "On the Tuning and the Mass of the Composite Higgs", JHEP **1303** (2013) 051.

[29] S. Weinberg, "Implications of dynamical symmetry breaking", Phys. Rev. **D13** (1976) 974; L. Susskind, "Dynamics of spontaneous symmetry breaking in the Weinberg-Salam theory", Phys. Rev. **D20** (1979) 2619.

[30] A. G. Akeroyd, S. Moretti, K. Yagyu and E. Yildirim, "Light charged Higgs boson scenario in 3-Higgs doublet models", Int. J. Mod. Phys. **A**32 (2017) 1750145.

[31] S. De Curtis, S. Moretti, K. Yagyu and E. Yildirim, "Perturbative unitarity bounds in composite two-Higgs doublet models", Phys. Rev. **D94** (2016) 055017.

[32] S. De Curtis, S. Moretti, K. Yagyu and E. Yildirim, "LHC Phenomenology of Composite 2-Higgs Doublet Models", Eur. Phys. J. **C77** (2017) 513.

[33] S. De Curtis, S. Moretti, K. Yagyu and E. Yildirim, "Single and double SM-like Higgs boson production at future electron-positron colliders in composite 2HDMs", Phys. Rev. **D95** (2017) 095026.

[34] V. Keus, S. F. King and S. Moretti, "Three-Higgs-doublet models: symmetries, potentials and Higgs boson masses," JHEP **1401** (2014) 052.

[35] I. P. Ivanov and E. Vdovin, "Classification of finite reparametrization symmetry groups in the three-Higgs-doublet model", Eur. Phys. J. **C73** 2309 (2013); I. P. Ivanov and C. C. Nishi, "Symmetry breaking patterns in 3HDM" JHEP **1501** (2015) 021; D. Das and U. K. Dey, "Analysis of an extended scalar sector with S_3 symmetry", Phys. Rev. **D89** (2014) 095025; V. Keus, S. F. King and S. Moretti, "Phenomenology of the inert (2+1) and (4+2) Higgs doublet models", Phys. Rev. **D90** (2014) 075015.

[36] M. Maniatis and O. Nachtmann, "Stability and symmetry breaking in the general three-Higgs-doublet model," JHEP **1502** (2015) 058 [Erratum-ibid. JHEP **1510** (2015) 149].

[37] R. Barbieri, L. J. Hall and V. S. Rychkov, "Improved naturalness with a heavy Higgs: An Alternative road to LHC physics", Phys. Rev. **D74** (2006) 015007.

[38] A. Zee, "A theory of lepton number violation and neutrino Majorana masses", Phys. Lett. **B93**, (1980) 389 [Erratum-ibid. B 95 (1980) 461.] and "Charged scalar field and quantum number violations", Phys. Lett. **B161** (1985) 141.

[39] A. I. Bochkarev, S. V. Kuzmin and M. E. Shaposhnikov, "Electroweak baryogenesis and the Higgs boson mass problem", Phys. Lett. **B244** (1990) 275; A. E. Nelson, D. B. Kaplan and A. G. Cohen, "Why there is something rather than nothing: Matter from weak interactions", Nucl. Phys. **B373** (1992) 453; N. Turok and J. Zadrozny, "Phase transitions in the two doublet model", Nucl. Phys. **B369** (1992) 729.

[40] D. B. Kaplan and H. Georgi, "$SU(2) \times U(1)$ Breaking by Vacuum Misalignment", Phys.Lett. **B136** (1984) 183.

[41] S. R. Coleman and E. J. Weinberg, "Radiative Corrections as the Origin of Spontaneous Symmetry Breaking", Phys. Rev. **D7** 1888 (1973).

[42] J. R. Espinosa, C. Grojean and M. Muhlleitner, "Composite Higgs Search at the LHC", JHEP **1005** (2010) 065.

[43] K. Agashe, R. Contino, and A. Pomarol, "The Minimal composite Higgs model", Nucl. Phys. **B719** (2005) 165.

[44] R. Contino, L. Da Rold and A. Pomarol, "Light custodians in natural composite Higgs models", Phys. Rev. **D75** (2007) 055014.

[45] J. Mrazek, A. Pomarol, R. Rattazzi, M. Redi, J. Serra and A. Wulzer, "The Other Natural Two Higgs Doublet Model", Nucl. Phys. **B853** (2011) 1.

[46] N. Fonseca, R.Z. Funchal, A. Lessa and L. Lopez-Honorez, "Dark Matter Constraints on Composite Higgs Models", JHEP **1506** (2015) 154.

[47] M. Frigerio, A. Pomarol, F. Riva and A. Urbano, "Composite Scalar Dark Matter", JHEP **1207** (2012) 015.

[48] S. L. Glashow and S. Weinberg, "Natural Conservation Laws for Neutral Currents", Phys. Rev. **D15** (1977) 1958.

[49] J. Callan, G. Curtis, S. R. Coleman, J. Wess, and B. Zumino, "Structure of phenomenological lagrangians. 2.", Phys. Rev. **177** (1969) 2247.

[50] S. R. Coleman, J. Wess, and B. Zumino, "Structure of phenomenological lagrangians. 1.", Phys. Rev. **177** (1969) 2239.

[51] M. Ciuchini, E. Franco, G. Martinelli, L. Reina and L. Silvestrini, "$b \to s\gamma$ and $b \to sg$: A Theoretical reappraisal", Phys. Lett. **B334** (1994) 137.

[52] M. Ciuchini, G. Degrassi, P. Gambino and G. F. Giudice, "Next-to-leading QCD corrections to $B \to X(s)\gamma$: Standard model and two Higgs doublet model", Nucl. Phys. **B527** (1998) 21.

[53] F. Borzumati and C. Greub, "2HDMs predictions for $B \to X(s)\gamma$ gamma in NLO QCD", Phys. Rev. **D58** (1998) 074004.

[54] P. Gambino and M. Misiak, "Quark mass effects in $B \to X(s)\gamma$," Nucl. Phys. **B611** (2001) 338.

[55] T. Hermann, M. Misiak and M. Steinhauser, "$\bar{B} \to X_s\gamma$ in the Two Higgs Doublet Model up to Next-to-Next-to-Leading Order in QCD," JHEP **1211** (2012) 036.

[56] M. Misiak, H. M. Asatrian, R. Boughezal, M. Czakon, T. Ewerth, A. Ferroglia, P. Fiedler and P. Gambino *et al.*, "Updated NNLO QCD predictions for the weak radiative B-meson decays," Phys. Rev. Lett. **114** (2015) 221801.

[57] Y. Grossman, "Phenomenology of models with more than two Higgs doublets," Nucl. Phys. **D426** (1994) 355.

[58] A. G. Akeroyd and W. J. Stirling, "Light charged Higgs scalars at high-energy e^+e^- colliders," Nucl. Phys. **D447** (1995) 3.

[59] G. Cree and H. E. Logan, "Yukawa alignment from natural flavor conservation," Phys. Rev. **D84** (2011) 055021.

[60] A. G. Akeroyd, S. Moretti and J. Hernandez-Sanchez, "Light charged Higgs bosons decaying to charm and bottom quarks in models with two or more Higgs doublets," Phys. Rev. **D85** (2012) 115002.

[61] A. G. Akeroyd, "Three body decays of Higgs bosons at LEP-2 and application to a hidden fermiophobic Higgs," Nucl. Phys. **B544** (1999) 557.

[62] D. J. Miller, S. Moretti, D. P. Roy and W. J. Stirling, "Detecting heavy charged Higgs bosons at the CERN LHC with four b quark tags," Phys. Rev. **D61** (2000) 055011.

[63] O. Eberhardt, U. Nierste and M. Wiebusch, "Status of the two-Higgs-doublet model of type II," JHEP **1307** (2013) 118.

[64] I. P. Ivanov, "Properties of the general NHDM. II. Higgs potential and its symmetries," JHEP **1007** (2010) 020.

[65] I. P. Ivanov and E. Vdovin, "Discrete symmetries in the three-Higgs-doublet model," Phys. Rev. **D86** (2012) 095030.

[66] S. Moretti and K. Yagyu, "Constraints on Parameter Space from Perturbative Unitarity in Models with Three Scalar Doublets," Phys. Rev. **D91** (2015) 055022.

[67] M. Aoki, S. Kanemura, K. Tsumura and K. Yagyu, "Models of Yukawa interaction in the two Higgs doublet model, and their collider phenomenology," Phys. Rev. **D80** (2009) 015017.

[68] J. L. Hewett, "Top ten models constrained by $b \to s\gamma$," In "Stanford 1993, Proceedings, Spin structure in high energy processes" 463-475, and SLAC Stanford - SLAC-PUB-6521.

[69] Y. Amhis *et al.* [Heavy Flavor Averaging Group (HFAG) Collaboration], "Averages of b-hadron, c-hadron, and τ-lepton properties as of summer 2014," arXiv:1412.7515 [hep-ex].

[70] G. Aad *et al.* [ATLAS Collaboration], "Search for charged Higgs bosons decaying via $H^\pm \to \tau^\pm\nu$ in fully hadronic final states using pp collision data at $\sqrt{s} = 8$ TeV with the ATLAS detector," JHEP **1503** (2015) 088.

[71] V. Khachatryan *et al.* [CMS Collaboration], "Search for a charged Higgs boson in pp collisions at $\sqrt{s} = 8$ TeV," JHEP **1511** (2015) 018.

[72] V. Khachatryan *et al.* [CMS Collaboration], "Search for a light charged Higgs boson decaying to $c\bar{s}$ in pp collisions at $\sqrt{s} = 8$ TeV," JHEP **1512** (2015) 178.

[73] G. Aad *et al.* [ATLAS Collaboration], "Search for a light charged Higgs boson in the decay channel $H^+ \to c\bar{s}$ in $t\bar{t}$ events using pp collisions at $\sqrt{s} = 7$ TeV with the ATLAS detector," Eur. Phys. J. **C73** (2013) 2465.

[74] S. Moretti, A.G. Akeroyd and J. Hernandez-Sanchez, "$H^{\pm} \to cb$ in models with two or more Higgs doublets," PoS Charged **2014** (2014) 025.

[75] G. Abbiendi *et al.* [ALEPH and DELPHI and L3 and OPAL and LEP Collaborations], "Search for Charged Higgs bosons: Combined Results Using LEP Data," Eur. Phys. J. **C73** (2013) 2463.

[76] V. M. Abazov *et al.* [D0 Collaboration], "Search for Charged Higgs Bosons in Top Quark Decays," Phys. Lett. **B682** (2009) 278.

[77] M. Guchait and S. Moretti, "Improving the discovery potential of charged Higgs bosons at Tevatron run II," JHEP **0201** (2002) 001.

[78] K. A. Assamagan, M. Guchait and S. Moretti, "Charged Higgs bosons in the transition region $M(H^{\pm}) \sim m(t)$ at the LHC," hep-ph/0402057.

[79] H. L. Lai, J. Huston, S. Kuhlmann, F. I. Olness, J. F. Owens, D. E. Soper, W. K. Tung and H. Weerts, "Improved parton distributions from global analysis of recent deep inelastic scattering and inclusive jet data," Phys. Rev. **D55** (1997) 1280.

[80] A. E. Cárcamo Hernández, S. Kovalenko and I. Schmidt, "Precision measurements constraints on the number of Higgs doublets," Phys. Rev. **D91** (2015) 095014.

[81] M. J. Dugan, H. Georgi and D. B. Kaplan, "Anatomy of a Composite Higgs Model", Nucl. Phys. **B254**, (1985) 299.

[82] D. B. Kaplan, "Flavor at SSC energies: A New mechanism for dynamically generated fermion masses", Nucl. Phys. **B365** (1991) 259.

[83] R. Contino, T. Krame, M. Son and R. Sundrum, "Warped/composite phenomenology simplified", JHEP **0705** (2007) 074.

[84] N. Fonseca, R.Z. Funchal, A. Lessa and L. Lopez-Honorez, "Dark Matter Constraints on Composite Higgs Models," JHEP **1506** (2015) 154.

[85] G.F. Giudice, C. Grojean, A. Pomarol and R. Rattazzi, "The Strongly-Interacting Light Higgs", JHEP **0706** (2007) 045.

[86] G. C. Branco, P. M. Ferreira, L. Lavoura, M. N. Rebelo, M. Sher and J. P. Silva, "Theory and phenomenology of two-Higgs-doublet models," Phys. Rept. **516** (2012) 1.

[87] S. Kanemura, K. Kaneta, N. Machida and T. Shindou, "New resonance scale and fingerprint identification in minimal composite Higgs models," Phys. Rev. **D91** (2015) 115016.

[88] S. Davidson and H. E. Haber, "Basis-independent methods for the two-Higgs-doublet model", Phys. Rev. **D72** (2005) 035004 [Erratum-ibid. Phys. Rev. **D72** (2005) 099902].

[89] S. R. Coleman and E. J. Weinberg, "Radiative Corrections as the Origin of Spontaneous Symmetry Breaking," Phys. Rev. **D7**, 1888 (1973).

[90] K. Agashe, R. Contino and A. Pomarol, Nucl. Phys. B **719**, (2005) 165. [hep-ph/0412089].

[91] S. Kanemura, Y. Okada, E. Senaha and C.-P. Yuan, "Higgs coupling constants as a probe of new physics," Phys. Rev. **D70** (2004) 115002.

[92] E. Bertuzzo, T. S. Ray, H. de Sandes, and C. A. Savoy, "On Composite Two Higgs Doublet Models," JHEP **1305** (2013) 153.

[93] S. Kanemura, T. Kubota and E. Takasugi, "Lee-Quigg-Thacker bounds for Higgs boson masses in a two doublet model," Phys. Lett. **B313** (1993) 155.

[94] A. G. Akeroyd, A. Arhrib and E. M. Naimi, "Note on tree-level unitarity in the general two Higgs doublet model," Phys. Lett. **B490** (2000) 119.

[95] S. Kanemura and K. Yagyu, "Unitarity bound in the most general two Higgs doublet model," Phys. Lett. **B751** (2015) 289.

[96] I. F. Ginzburg and I. P. Ivanov, "Tree-level unitarity constraints in the 2HDM with CP-violation," Phys. Rev. **D72** (2005) 115010.

[97] I. F. Ginzburg and I. P. Ivanov, "Tree level unitarity constraints in the 2HDM with CP violation," hep-ph/0312374.

[98] J. F. Gunion, H. E. Haber, G. L. Kane and S. Dawson, "The Higgs Hunter's Guide," Front. Phys. **80**, (2000) 1.

[99] J. M. Cornwall, D. N. Levin and G. Tiktopoulos, "Derivation of Gauge Invariance from High-Energy Unitarity Bounds on the s Matrix," Phys. Rev. **D10**, (1974) 1145. [Phys. Rev. **D11**, (1975) 972].

[100] G. Aad *et al.* [ATLAS Collaboration], "Measurements of Higgs boson production and couplings in the four-lepton channel in pp collisions at center-of-mass energies of 7 and 8 TeV with the ATLAS detector," Phys. Rev. **D91** (2015) 012006.

[101] V. Khachatryan *et al.* [CMS Collaboration], "Precise determination of the mass of the Higgs boson and tests of compatibility of its couplings with the standard model predictions using proton collisions at 7 and 8 TeV," Eur. Phys. J. **C75** (2015) 212.

[102] N. G. Deshpande and E. Ma, "Pattern Of Symmetry Breaking With Two Higgs Doublets," Phys. Rev. **D18** (1978) 2574.

[103] M. Sher, "Electroweak Higgs Potentials And Vacuum Stability," Phys. Rept. **179** (1989) 273; S. Nie and M. Sher, "Vacuum stability bounds in the two-Higgs doublet model," Phys. Lett. **B449** (1999) 89; S. Kanemura, T. Kasai and Y. Okada, "Mass bounds of the lightest CP even Higgs boson in the two Higgs doublet model," Phys. Lett. **B471** (1999) 182.

[104] V. D. Barger, J. L. Hewett and R. J. N. Phillips, "New Constraints on the Charged Higgs Sector in Two Higgs Doublet Models," Phys. Rev. **D41**, (1990) 3421.

[105] D. Barducci, A. Belyaev, M. S. Brown, S. De Curtis, S. Moretti and G. M. Pruna, "The 4-Dimensional Composite Higgs Model (4DCHM) and the 125 GeV Higgs-like signals at the LHC", JHEP **1309** (2013) 047.

[106] G. Aad *et al.* [ATLAS Collaboration], "Search for an additional, heavy Higgs boson in the $H \to ZZ$ decay channel at $\sqrt{s} = 8$ TeV in pp collision data with the ATLAS detector," Eur. Phys. J. **C76** (2016) 45.

[107] CMS Collaboration, 'Search for di-Higgs resonances decaying to 4 bottom quarks," CMS-PAS-HIG-14-013.

[108] CMS Collaboration, "Update of the search for the Standard Model Higgs boson decaying into WW in the vector boson fusion production channel," CMS-PAS-HIG-13-022.

[109] CMS Collaboration, "Properties of the Higgs-like boson in the decay H to ZZ to 4l in pp collisions at $\sqrt{s} = 7$ and 8 TeV," CMS-PAS-HIG-13-002.

[110] CMS Collaboration,"Search for additional neutral Higgs bosons decaying to a pair of tau leptons in pp collisions at $\sqrt{s} = 7$ and 8 TeV," CMS-PAS-HIG-14-029.

[111] CMS Collaboration, "Search for the standard model Higgs boson decaying to tau pairs," CMS-PAS-HIG-12-043.

[112] CMS Collaboration, "Search for the standard model Higgs boson decaying to tau pairs produced in association with a W or Z boson," CMS PAS HIG-12-051.

[113] ATLAS Collaboration, "Search for the Standard Model Higgs boson in the $H \to WW \to l\nu l\nu$ decay mode with 4.7 fb^{-1} of ATLAS data at sqrt(s) = 7 TeV," ATLAS-CONF-2012-012.

[114] P. Bechtle, O. Brein, S. Heinemeyer, G. Weiglein and K. E. Williams, "HiggsBounds: Confronting Arbitrary Higgs Sectors with Exclusion Bounds from LEP and the Tevatron," Comput. Phys. Commun. **181** (2010) 138.

[115] P. Bechtle, O. Brein, S. Heinemeyer, G. Weiglein and K. E. Williams, "HiggsBounds 2.0.0: Confronting Neutral and Charged Higgs Sector Predictions with Exclusion Bounds from LEP and the Tevatron," Comput. Phys. Commun. **182** (2011) 2605.

[116] P. Bechtle, O. Brein, S. Heinemeyer, O. Stal, T. Stefaniak, G. Weiglein and K. E. Williams, "HiggsBounds-4: Improved Tests of Extended Higgs Sectors against Exclusion Bounds from LEP, the Tevatron and the LHC," Eur. Phys. J. **C74** (2014) 2693.

[117] P. Bechtle, O. Brein, S. Heinemeyer, O. Stal, T. Stefaniak, G. Weiglein and K. Williams, "Recent Developments in HiggsBounds and a Preview of HiggsSignals," PoS CHARGED **2012** (2012) 024.

[118] P. Bechtle, S. Heinemeyer, O. Stal, T. Stefaniak and G. Weiglein, "Applying Exclusion Likelihoods from LHC Searches to Extended Higgs Sectors," Eur. Phys. J. **C75** (2015) 421.

[119] O. Stal and T. Stefaniak, "Constraining extended Higgs sectors with HiggsSignals," PoS EPS **-HEP2013** (2013) 314.

[120] P. Bechtle, S. Heinemeyer, O. Stal, T. Stefaniak and G. Weiglein, "*HiggsSignals*: Confronting arbitrary Higgs sectors with measurements at the Tevatron and the LHC," Eur. Phys. J. **C74** (2014) 2711.

[121] S. Kanemura, M. Kikuchi and K. Yagyu, "Fingerprinting the extended Higgs sector using one-loop corrected Higgs boson couplings and future precision measurements," Nucl. Phys. **B896** (2015) 80.

[122] S. Kanemura, K. Tsumura, K. Yagyu and H. Yokoya, "Fingerprinting nonminimal Higgs sectors," Phys. Rev. **D90** (2014) 075001.

[123] https://twiki.cern.ch/twiki/bin/view/LHCPhysics/CERNYellowReportPageAt1314TeV.

[124] A. Pukhov, E. Boos, M. Dubinin, V. Edneral, V. Ilyin, D. Kovalenko, A. Kryukov and V. Savrin *et al.*, "CompHEP: A Package for evaluation of Feynman diagrams and integration over multiparticle phase space," hep-ph/9908288.

[125] P. M. Nadolsky, H. L. Lai, Q. H. Cao, J. Huston, J. Pumplin, D. Stump, W. K. Tung and C.-P. Yuan, "Implications of CTEQ global analysis for collider observables," Phys. Rev. **D78** (2008)) 013004.

[126] D. M. Asner *et al.*, "ILC Higgs White Paper," arXiv:1310.0763 [hep-ph].

[127] F. Gianotti *et al.*, "Physics potential and experimental challenges of the LHC luminosity upgrade," Eur. Phys. J. **C39** (2005) 293.

[128] J. Baglio, A. Djouadi, R. Gröber, M. M. Mühlleitner, J. Quevillon and M. Spira, "The measurement of the Higgs self-coupling at the LHC: theoretical status," JHEP **1304** (2013) 151.

[129] See, e.g., ATLAS Collaboration, ATL-PHYS-PUB-2016-024, ATL-PHYS-PUB-2015-046 and ATL-PHYS-PUB-2014-019.

[130] V. Barger, L. L. Everett, C. B. Jackson, A. D. Peterson and G. Shaughnessy, "Measuring the two-Higgs doublet model scalar potential at LHC14," Phys. Rev. **D90** (2014) 095006.

[131] S. Kanemura, S. Kiyoura, Y. Okada, E. Senaha and C. P. Yuan, "New physics effect on the Higgs self-coupling," Phys. Lett. **B558** (2003) 157; S. Kanemura, Y. Okada, E. Senaha and C.-P. Yuan, "Higgs coupling constants as a probe of new physics," Phys. Rev. **D70** (2004) 115002; S. Kanemura, M. Kikuchi and K. Yagyu, "Fingerprinting the extended Higgs sector using one-loop corrected Higgs boson couplings and future precision measurements," Nucl. Phys. **B896** (2015) 80.

[132] F. Gianotti *et al.*, "Physics potential and experimental challenges of the LHC luminosity upgrade," Eur. Phys. J. **C39** (2005) 293.

[133] J. Baglio, A. Djouadi, R. Gröber, M. M. Mühlleitner, J. Quevillon and M. Spira, "The measurement of the Higgs self-coupling at the LHC: theoretical status," JHEP **1304** (2013) 151.

[134] N. Phinney, "ILC reference design report: Accelerator executive summary," ICFA Beam Dyn. Newslett. **42** (2007) 7.

[135] G. Aarons *et al.* [ILC Collaboration], "International Linear Collider Reference Design Report Volume 2: Physics at the ILC," arXiv:0709.1893 [hep-ph].

[136] N. Phinney, N. Toge and N. Walker, "ILC Reference Design Report Volume 3 - Accelerator," arXiv:0712.2361 [physics.acc-ph].

[137] T. Behnke *et al.* [ILC Collaboration], "ILC Reference Design Report Volume 4 - Detectors," arXiv:0712.2356 [physics.ins-det].

[138] J. Brau *et al.* "International Linear Collider reference design report. 1: Executive summary. 2: Physics at the ILC. 3: Accelerator. 4: Detectors," ILC-REPORT-2007-001, AAI-PUB-2007-002, BNL-79150-2007, CERN-2007-006, CHEP-A07-001, CLNS-07-1991, COCKCROFT-07-04, DESY-07-046, FERMILAB-TM-2382, JAI-2007-001, JINR-E9-2007-039, JLAB-R-2007-01, KEK-REPORT-2007-2, LBNL-62867, LNF-07-9-NT, SLAC-R-857.

[139] J. Brau *et al.* [ILC Collaboration], "ILC Reference Design Report: ILC Global Design Effort and World Wide Study," arXiv:0712.1950 [physics.acc-ph].

[140] T. Behnke *et al.* "The International Linear Collider Technical Design Report - Volume 4: Detectors," arXiv:1306.6329 [physics.ins-det].

[141] C. Adolphsen *et al.* "The International Linear Collider Technical Design Report - Volume 3.II: Accelerator Baseline Design," arXiv:1306.6328 [physics.acc-ph].

[142] C. Adolphsen *et al.* "The International Linear Collider Technical Design Report - Volume 3.I: Accelerator & in the Technical Design Phase," arXiv:1306.6353 [physics.acc-ph].

[143] T. Behnke *et al.* "The International Linear Collider Technical Design Report - Volume 1: Executive Summary," arXiv:1306.6327 [physics.acc-ph].

[144] H. Baer *et al.* "The International Linear Collider Technical Design Report - Volume 2: Physics," arXiv:1306.6352 [hep-ph].

[145] M. Aicheler *et al.* "A Multi-TeV Linear Collider Based on CLIC Technology: CLIC Conceptual Design Report," preprint CERN-2012-007.

[146] M. Bicer *et al.* [TLEP Design Study Working Group], "First Look at the Physics Case of TLEP," JHEP **1401** (2014) 164.

[147] K. A. Olive *et al.* [Particle Data Group Collaboration], "Review of Particle Physics," Chin. Phys. **C38** (2014) 090001.

[148] ATLAS Collaboration,"Evidence for the Higgs-boson Yukawa coupling to tau leptons with the ATLAS detector," JHEP **04** (2015) 117.

[149] ATLAS Collaboration, "Observation and measurement of Higgs boson decays to WW* with the ATLAS detector," Phys. Rev. **D92** (2015) 012006.

[150] ATLAS Collaboration, "Measurements of Higgs boson production and couplings in the four-lepton channel in pp collisions at center-of-mass energies of 7 and 8 TeV with the ATLAS detector," Phys. Rev. **D91** (2015) 012006.

[151] ATLAS Collaboration, "Search for the associated production of the Higgs boson with a top quark pair in multilepton final states with the ATLAS detector," Phys. Lett. B **749** (2015) 519.

[152] ATLAS Collaboration, "Search for the $b\bar{b}$ decay of the Standard Model Higgs boson in associated $(W/Z)H$ production with the ATLAS detector," JHEP **01** (2015) 069.

[153] ATLAS Collaboration, "Search for the Standard Model Higgs boson produced in association with a vector boson and decaying to a $b\bar{b}$ pair in pp collisions at 13 TeV using the ATLAS detector," ATLAS-CONF-2016-091.